Pliocene-Pleistocene evolution of the Laurentide Ice Sheet and North Atlantic ocean circulation

Submitted by Rebecca Louise Parker

To the University of Exeter as a thesis for the degree of

Doctor of Philosophy

In Geology

March 2022

I certify that all material in this thesis which is not my own work has been identified and that any material that has previously been submitted and approved for the award of a degree by this or any other University has been acknowledged.

(Signature) 

Abstract

The high sensitivity of the North Atlantic to climate change makes it an ideal region to study in palaeoclimate research to understand better the workings our planet's climate system. To this end, this thesis reports new authigenic lead (Pb) isotope and fish debris neodymium (Nd isotope; ε_{Nd}) records from northwest North Atlantic IODP sites U1302/3 (~50˚N) and IODP Site U1313 (~41˚N), which are used to investigate the evolution of the North American Laurentide Ice Sheet (LIS) and North Atlantic ocean circulation during the Plio-Pleistocene. Authigenic Pb isotope records from sites U1302/3 track chemical weathering on North America, which varies as a function of LIS extent. In Chapters 3 and 4, data of this sort spanning the past ~500 kyr are used to demonstrate that the timescale of LIS retreat during each of the largest three glacial terminations of the mid- to late-Pleistocene – Terminations (T) 5 (~424 ka), T2 (~130 ka) and T1 (~14 ka) – is different; a fact that should be taken into consideration when using models of glacio-isostatic adjustment to correct estimates of sea-level highstand during interglacial marine isotope stages (MIS) 11 (~410 ka) and 5e (~124 ka), which are widely considered to represent the most recent geological analogues for near-future changes in Earth's climate. The early timing inferred in Chapter 4 for LIS (and Greenland Ice Sheet) break-up during T5 (by ~ 418 ka) also makes it likely that the sea-level highstand associated with MIS 11 (by ~405 ka) reflects ice loss from Antarctica, and thus lies in the upper end of estimates (~+1–13 m above present). In Chapter 5, a new ε_{Nd} record from Site U1313 is used to track the evolution of the end-member composition of Northern Sourced Waters bathing the deep North Atlantic during the Last Glacial Cycle (~124–0 ka). The history of high-latitude changes in climate inferred here to be responsible for this evolution is applied to older ε_{Nd} records from this region to infer climate changes in the high northern latitude during the last two major transitions in Earth's climate – the intensification of Northern Hemisphere Glaciation (3.6–2.5 Ma) and the Mid-Pleistocene Transition (1.2–0.8 Ma).

Acknowledgments

First and foremost, a huge thank you to Ian Bailey, my main supervisor, for giving me the opportunity to move to the UK and work on this project four years ago. His guidance, advice and encouragement was invaluable and I am still amazed by how fast I received my drafts back. I am sincerely grateful for his understanding and faith that I would (eventually) complete my PhD back home in New Zealand in the midst of a global pandemic. The late night and early morning zoom meetings were a treat. Thanks also to Kate Littler who stepped in as my main supervisor towards the final stages of my PhD.

A big thank you to my co-supervisor Paul Wilson and collaborator Gavin Foster at NOCS for sharing their expertise, discussing project ideas and making me feel so welcome when I moved to Southampton. A special thanks to Marcus at MARUM for his invaluable discussions, especially for my very first publication.

To everyone in the labs in Southampton, thank you for being so accommodating. I thank Matt, Agnes and Andy for teaching me to prep, run and process radiogenic isotopes and answer any questions I had along the way. A further thanks to Tom who put up with my questions in the middle of the Norwegian night. Finally, a big thank you to Vicki, who has provided never-ending laughs, help in the labs and proper (and not so proper) science chat for the past four years.

Thank you to the University of Exeter for my International Excellence Scholarship. My project would not have been possible without your support and I am grateful for all of the opportunities to conduct exciting research and develop as a scientist. I also thank the CSM Trust and ECORD for financially supporting science travel.

Love to all my friends at both the Penryn Campus and NOCS. You made my time in the UK unforgettable, and I will always look back fondly at our terrible science jokes and for always reminding me that I'm the 'token Kiwi' with the accent.

Finally, I am very thankful to my parents who have given me so much moral support and encouragement during not only the past 4 years, but my entire academic journey. Thanks for taking me in as your new flatmate in the final few months of writing my thesis.

Contents

List of figures

List of tables

Abbreviations

AABW	Antarctic Bottom Water
AMOC	Atlantic Meridional Overturning Circulation
DSOW	Denmark Strait Overflow Water
DWUC	Deep Western Boundary Undercurrent
IODP	International Ocean Discovery Program
Fe-Mn	Ferro-manganese
GIA	Glacio-isostatic adjustment
H-	Heinrich
HE	Heinrich event
HREE	Heavy Rare Earth Elements
IRD	Ice-rafted debris
ka	Thousand years
kyr	Thousands of years
LC	Labrador Current
LGC	Last Glacial Cycle
LGM	Last Glacial Maximum
LIS	Laurentide Ice Sheet
LNADW	Lower North Atlantic Deep Water
HREE	Heavy Rare Earth Elements (terbium (Tb), dysprosium (Dy), holmium (Ho), erbium (Er), thulium (Tm), ytterbium (Yb), lutetium (Lu), scandium (Sc), and yttrium (Y)
LREE	Light Rare Earth Elements (lanthanum (La), cerium (Ce), praseodymium (Pr), neodymium (Nd), and promethium (Pm)

MREE	Mid Rare Earth Elements (samarium (Sm), europium (Eu), and gadolinium (Gd)
LSW	Labrador Sea Water
Myr	Millions of years ago
MIS	Marine Isotope Stage
MPT	Mid-Pleistocene Transition
MREE	Mid Rare Earth Elements
NAC	North Atlantic Current
NADW	North Atlantic Deep Water
NPS	*Neogloboquadrina pachyderma* (sinistral)
NSW	Northern Sourced Waters
(i)NHG	(intensification of) Northern Hemisphere Glaciation
NSOW	Norwegian (Nordic) Overflow Water
pCO_2	Atmospheric concentration of carbon dioxide
PGM	Penultimate Glacial Maximum
REE	Rare Earth Element
SP	Superior Province
SPMW	Subpolar Mode Waters
SST	Sea Surface Temperature
SSW	South Sourced Waters
T-	Termination

Chapter 1: Introduction

1.1 Motivation

Palaeoclimate research enhances our ability to understand and predict climate change. It allows us to appreciate better the full range of states of Earth's climate system and contributes to our understanding of natural feedbacks and processes that will drive future changes in climate and our environment in the face of human-induced carbon emissions (Lear et al., 2021). Palaeoclimate reconstructions are also essential for evaluating Earth System Model predictions of climate change by testing their ability to reproduce large-scale climate changes from the geological past (Haywood et al., 2019)

Complex and interlinked, Earth's climate system consists of multiple components (i.e., oceans, atmosphere, biosphere, the land surface and cryosphere) and thresholds (e.g., tipping points; Lenton et al., 2019) that are interdependent and interact over different timescales (from decades to multiple millions of years). Geologists can investigate the behaviour of these components and their temporal evolution by generating what are known as proxy records. Proxies are indirect measures of past climates or environments preserved in natural archives such as marine and terrestrial sediments, rocks and ice cores. Proxy data are generated either by examining the sedimentological or geochemical nature of these geological archives. Geochemical proxies, which are the focus of this thesis, are most commonly based on measuring the stable (e.g., of oxygen and carbon) and radiogenic (e.g., lead or neodymium) isotope and geochemical compositions (e.g., wt.% inorganic and organic carbon) of rocks and sediments or of biogenic components they contain.

Three aspects of our planet's climate system and environment that are widely reconstructed by geologists using geochemical proxies are changes in global mean sea-level (GMSL), continental ice-sheet extent and ocean circulation. Future rise of GMSL will be dominated by ocean thermal expansion and the melting of glaciers and ice sheets (Oppenheimer et al., 2019). An estimated 0.70–1 m of GMSL rise is projected by 2100 in the most extreme Representative Concentration Pathway 8.5, outlined by the Intergovernmental Panel on Climate Change (Kopp et al., 2014; Stocker et al., 2013; Jackson and Jevrejeva, 2016). Understanding the rates and magnitudes of change in GMSL in the geological past is therefore of particular importance, as ~230 million people live on land less than 1 m above current high tide lines (Kulp and Strauss, 2019). Accurate reconstructions of past ice-sheet extents are needed to understand better regional ice-mass contributions to GMSL change. They are also required to correct interglacial sea-level reconstructions accurately for glacial-isostatic adjustment (GIA; so crustal loading and unloading) when ice-sheets grow or melt (e.g., Dendy et al., 2017; Mitrovica et al., 2001; 2011; Gregory et al., 2019). It is important to understand past changes in Atlantic Meridional Overturning Circulation (AMOC) because it helps to redistribute heat from the tropics to high northern latitudes and changes in its vigour are widely implicated in amplifying abrupt suborbital-climate shifts during past glacials (e.g. Broecker, 1982; Imbrie et al., 1992; Bond et al., 1999; Maslin et al., 2001).

The two most recent interglacials that are likely to have featured GMSL above modern are MIS 11 (~400 ka) and MIS 5e (~125 ka). Relative sea-level estimates for MIS 11 range between +1 m (Rohling et al., 2010) to between +6-13 m (e.g., Raymo and Mitrovica, 2012) relative to present, while the sea-level highstand during MIS 5e may have ranged between +6-9 m (Dutton et al., 2015). These GMSL high-stands were ultimately the product of ice-sheet melt on Greenland and/or Antarctica under warmer than present climate conditions. Yet, volumetrically speaking, North American Laurentide Ice Sheet (LIS) melting contributed the most to the glacial termination events (Termination (T) 5, ~424 ka, and T2, ~130 ka) that led to these sea-level rises. The LIS held the equivalent of 76–85 m of GMSL during the Last Glacial Maximum (LGM, ~26–19 ka; Clark et al., 2009; Clark & Mix, 2002). Yet our understanding of its history prior to this time is markedly limited (e.g., Dyke et al., 2002; Batchelor et al., 2019; Dalton et al., 2020) but is required for accurate GIA modeling of Termination (T) 5 and 2.

The traditional view of AMOC configuration during the LGM invokes a reduction in its vigour (Böhm et al., 2015; Ng et al., 2018), a shoaling of its overturning cell, North Atlantic Deep Water, and an expansion of Antarctic Bottom Waters into the deep North Atlantic (>2.5 km depth) compared to the present day (Lynch-Stieglitz et al., 2007; Curry and Oppo, 2005; Chalk et al., 2019). Past changes in Atlantic Ocean water-mass geometry are most commonly reconstructed using benthic $\delta^{13}C$ and ε_{Nd} data and require a detailed understanding of the end-member compositions of Northern- and Southern-sourced waters (e.g., Du et al., 2020; Abbott et al., 2021; Pöppelmeier et al., 2021). Despite decades of progress, we still lack such information even for the LGC.

This thesis presents authigenic Pb isotope and fish debris Nd isotope data generated from two marine sediment cores recovered in the North Atlantic. These data are used here to reconstruct: (1) the history of LIS extent during key intervals of the late Quaternary - MIS 12 and 11, T5 (~424 ka), T2 (~130 ka) and the LGC and, (2) to extend our understanding of the ε_{Nd} composition of the Northern Sourced Waters (NSW) end-member back to ~130 ka. This chapter provides an introduction to the key themes of this thesis including an overview of Plio-Pleistocene climate evolution with a focus on the LIS and North Atlantic Ocean circulation and how they interacted and responded to past changes in climate. The outline and aims of each chapter are also summarised in Section 2.4.

1.2 Setting the scene: the North Atlantic of the Plio-Pleistocene epochs

1.2.1 Brief introduction to the Plio-Pleistocene

Over the past ~5.3 Myr, Earth has slowly evolved from a planet that was globally warmer than present with a single glaciated southern pole, to a world that was often colder than today and characterised by repeated bipolar glaciations (Zachos et al., 2008). Clear orbitally-paced glacial-interglacial (G-IG) cycles first became a significant feature of Earth's climate system during the late Pliocene-early Pleistocene intensification of Northern Hemisphere glaciation (iNHG, ~3.6–2.4 Ma, Fig. 1.1a-b,e; Lisiecki and Raymo, 2005; Mudelsee and Raymo, 2005). At this time, ice-sheets waxed and waned on ~41 kyr timescales and responded

linearly to insolation forcing (Fig. 1.1c; Imbrie et al., 1992). However, it was not until the mid-Pleistocene that the large and long, ~100 kyr duration, asymmetric G-IG cycles that are well documented for the late Pleistocene and especially so for the Last Glacial Cycle (Imbrie et al., 1992; Raymo, 1997; Ridgwell et al., 1999), first emerged during the Mid Pleistocene Transition (MPT, ~1.5-0.8 Ma, Fig. 1.1e; Clark et al., 2006; McClymont et al., 2013; Barker et al., 2019).

The quasi-periodic ~100-kyr (inter)glacial cycles over the past ~1 Ma are associated with large-amplitude variations in atmospheric CO_2 and corresponding changes in temperature, ice volume and AMOC structure and vigour (Jouzel et al., 2007; Lisiecki and Raymo, 2005; Deaney et al., 2017). In contrast to the ~41-kyr (inter)glacial world, the asymmetric nature of changes in benthic foraminiferal $\delta^{18}O$ (Lisiecki and Raymo, 2005) and sea-level records (Elderfield et al., 2012; Rohling et al., 2014; Grant et al., 2014) over the past ~1 Myr reveals that large continental ice-sheets grew slowly during this time (over ~80–90 kyr) but collapsed rapidly (over ~20–10-kyr) during what are known as abrupt 'terminaton' events (Fig. 1.1e; e.g. Broecker and van Donk, 1970; Barker et al., 2021).

The MPT occurred in the absence of substantial changes in astronomical climate forcing (Quinn et al., 2018). The quasi ~100-kyr periodicity of G-IG cycles following the MPT (Hays et al., 1976) are therefore thought to be a product of an enhanced ability of non-linearities within the climate system to amplify relatively modest changes in insolation forcing due variations in orbital precession and obliquity (Huybers, 2011; Tzedakis et al., 2017; Bajo et al., 2020). Suggested amplifiers include: (1) long-term global cooling and associated atmospheric CO_2 reductions (Fig. 1.1d; Chalk et al., 2017; Hönisch et al., 2009; Dyez et al., 2018); (2) Southern and/or Northern Hemisphere sea-ice expansion (Lear et al., 2016; Raymo, 1997) and (3) changes in AMOC (Pena and Goldstein, 2014); (4) change from a soft-bedded to a hard-bedded LIS through glacial erosion of a thick chemically weathered regolith that developed on North America prior to NHG that allowed ice-sheets to build up for longer (Clark and Pollard, 1998; 2006; Yehudai et al., 2021). The MPT is revisited in Chapters 5 and 6.

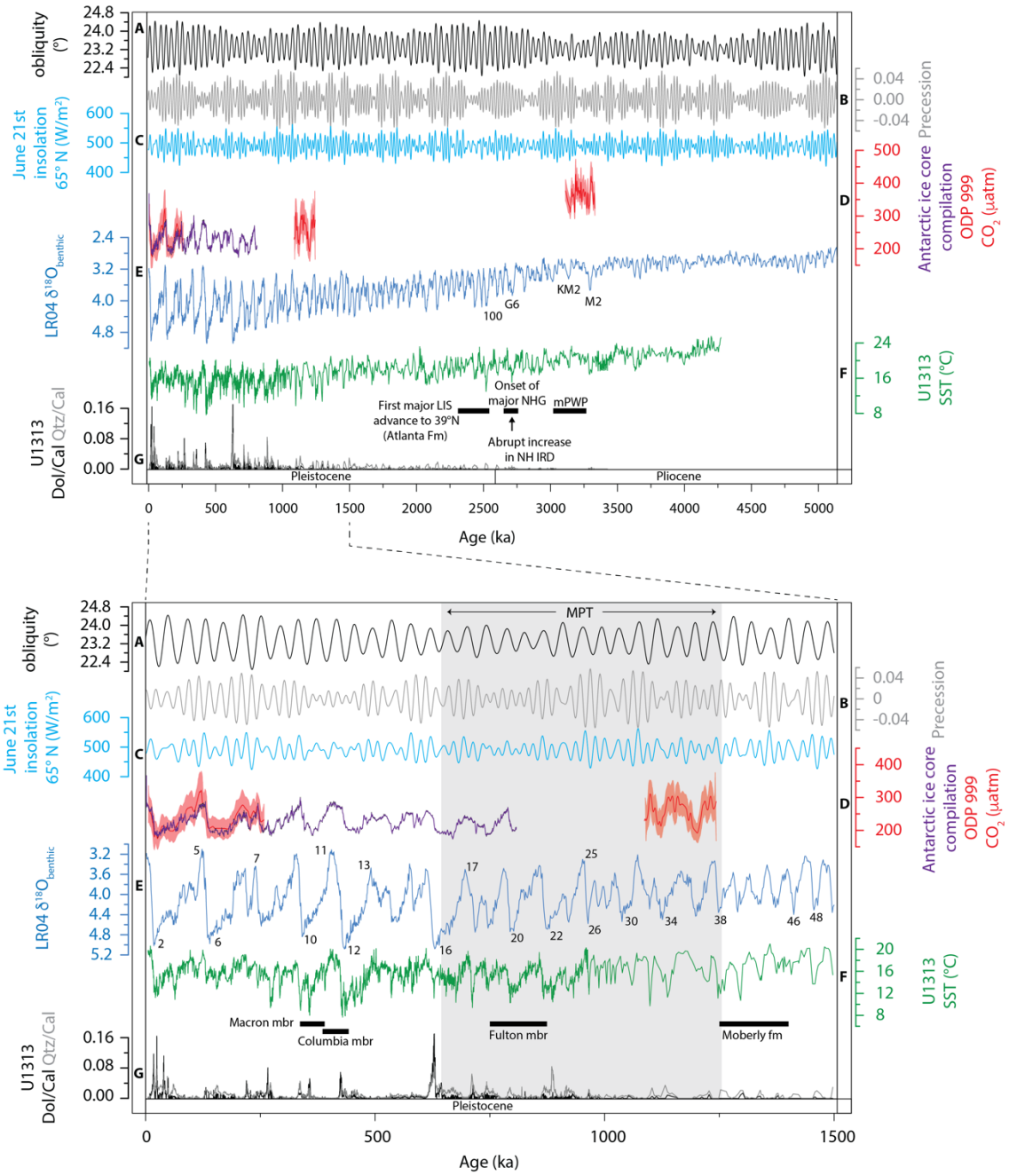

Figure 1.1: Plio-Pleistocene climate change with zoom in of the past ~1500 ka below: **(A)** Obliquity; **(B)** Precession; **(C)** Insolation forcing at 21st June 65°N (W/m^2; Laskar et al., 2004); **(D)** δ^{11}B-derived CO_2 record from *Globigerinoides ruber* at ODP Site 999 with 2σ error bars/envelopes. mid-Piacenzian warm period (MPWP; ~3100-3350 ka from de la Vega et al., 2020 and Martinez-Boti et al. 2015), early mid Pleistocene Transition and late Pleistocene (~1050-1250 and 0-250 ka respectively; from Chalk et al., 2017), Late Pleistocene (~0-800 ka Antarctic ice core compilation; Bereiter et al., 2015). **(E)** LR04 benthic δ^{18}O stack (Lisiecki and Raymo, 2005. **(F)** IODP Site U1313 alkenone-derived sea surface temperature (SST °C; Naafs et al., 2013b; 2020). **(G)** IODP Site U1313 Dolomite/Calcite (black line) and Quartz/Calcite (grey line) ratios (Naafs et al., 2013b). Plio-Pleistocene panel: Key features labelled include the onset of major Northern Hemisphere glaciation (NHG) and the duration of the mPWP labelled (Lisiecki and Raymo, 2005), abrupt increase in Northern Hemisphere (NH) ice-rafted debris (IRD; Bailey et al., 2013), first major Laurentide Ice Sheet advance to mid continental United States (~39°N; Balco and Rovey, 2010). Past ~1500 ka panel: Black horizontal bars highlight ages for central Missouri tills (width reflects 1σ uncertainty; Balco and Rovey, 2010; Rovey and Siemens, 2021).

1.2.2 Plio-Pleistocene History of the Laurentide Ice Sheet

Large ice-sheets are unlikely to have existed on North America during the Cenozoic prior to the onset of significant NHG, ~2.7 Ma. Yet our ability to reconstruct the history of glaciation of this landmass is strongly influenced by the available geological evidence, which becomes increasingly fragmentary in both space and time the further back in time we investigate (Naafs et al., 2014; Batchelor et al., 2019).

1.2.2.1 Pliocene and early to mid Pleistocene

Widespread deposition of ice rafted debris (IRD) in the Nordic Seas and subpolar North Atlantic ~2.72 Ma during MIS G6 fingerprints a significant expansion in Northern Hemisphere ice sheets during the late Pliocene (Kleiven et al., 2002). It reflects a time from which these ice-sheets became large enough to interact with the coast and calve abundant icebergs (and the IRD they contain) to the marine realm. The relative contributions that the Greenland, Scandinavian and North American ice sheets made to this depositional event is still relatively poorly constrained. A large LIS-like ice-sheet was unlikely, however, to have existed on North America until during MIS 100, 2.52 Ma. This cold stage marks the first time during iNHG that abundant IRD deposition is found to have occurred across all of the subpolar North Atlantic (Fig. 1.1g; so down to ~41˚N as recorded at Site U1313; Bolton et al., 2010; 2018). It also overlaps in time with the oldest evidence (dated at 2.40 ± 0.14 Ma) of mid-latitude glaciation on North America in the form of cosmogenic nuclide-dated glacial tills in central Missouri (Tab. 1.1; at ~39ºN, the Atlanta Formation; Balco and Rovey, 2010) and seawater δ^{18}O-based evidence for meltwater discharge from a mid-latitude proto-LIS into the Gulf of Mexico from ~2.5 Ma (Shakun et al., 2016). It is argued that iceberg calving from Greenland and European ice sheets dominated IRD deposition in the subpolar North Atlantic prior to this time (Bailey et al., 2013). While glaciation of North America was likely significant ~2.52 Ma, sea-level reconstructions and benthic foraminiferal δ^{18}O records reveal, however, that the first late Pleistocene-like glacial maxima in continental glaciation of the high northern latitudes did not occur until ~2.1 Ma (Rohling et al., 2014; Lisiecki and Raymo, 2005). It is argued that earlier Quaternary North American ice-sheets reached the mid latitudes because they had relatively low profiles, likely facilitated by lower basal friction,

most likely because they were positioned on a soft, deformable regolith during this time (Clark and Pollard, 1998; Bailey et al., 2010).

Table 1.1: Age constraints for glacial tills located at ~39°N in Missouri, mid continental United States.

Unit	Age (Balco and Rovey, 2010)	Age (Rovey and Siemens, 2021)	Revised MIS Stage
Macon mbr	0.21 ± 0.18	Older than 0.30–0.24 Ma	MIS 10
Columbia mbr	0.22 ± 0.16	Older than 0.48–0.42 Ma	MIS 12
Fulton mbr	0.80 ± 0.06		
Moberly fm	1.31 ±0.09		
Atlanta fm	2.42 ± 0.14		

1.2.2.2 Mid to late Pleistocene

Only snippets of evidence exist in the terrestrial geological record of North America that can be used to constrain LIS extent prior to the LGM (Balco and Rovey, 2010; Rovey and Siemens, 2021; Batchelor et al., 2019). In central Missouri, the terrestrial record of mid-latitude glacial till deposition records the southernmost advances of the LIS during the Quaternary (Tab. 1.1). This record shows that the Atlanta Formation, that marks the first major LIS advance on North America to ~39˚N ~2.40 ± 0.14 Ma, is only overlain by four younger tills - the Moberly Formation till and the McCredie Formation, the latter of which is composed of three till members (Tab. 1.1; Balco and Rovey, 2010). Cosmogenic nuclide-dating of these tills seemingly reveals that no continental ice on North America advanced south of ~45-47°N again until 1.30 ± 0.09 Ma during the deposition of the Moberly Formation (Balco and Rovey, 2010; Rovey and McLouth, 2015). The overlying glacial Fulton till was seemingly emplaced 0.80 ± 0.06 Ma (Balco and Rovey, 2010; Rovey and McLouth, 2015), and thus may document the significant increase in ice volume associated with the MPT during MIS 22 or 20 (Tab.1.1, Fig. 1.1e; Elderfield et al., 2012). Cosmogenic nuclide-dating of the two youngest tills in this sequence suggest that the Columbia and Macon members were formed during MIS 12 and 8, respectively (Tab. 1.1). A

recent reinterpretation of the age relations of these units using new pedostratigraphic constraints provides a more likely minimum age of the Macon Member till to MIS 10 (Tab. 1.1; Rovey and Siemens, 2021). While this new stratigraphic framework highlights that the LIS may have had a larger footprint in the mid-continent of the US during MIS 12 and 10 than its LGM counterpart, nothing is known about LIS coverage on other sectors of North America during the mid to late Pleistocene glaciations. Relatively little is also known about the timing and magnitude of LIS retreat during most mid to late Pleistocene glacial terminations.

The history of ice-sheet decay in the Northern Hemisphere during T1 of the last deglaciation is mapped out accurately in space and time (e.g., Dalton et al., 2020; discussed in detail in Section 2.2.3). The history of ice-sheet retreat on southern Greenland during glacial T5–1 and the associated interglacials MIS 11, 9, 7 and 5e is also well constrained by studies of marine cores adjacent to this landmass (de Vernal and Hillaire-Marcel, 2008; Colville et al., 2011; Reyes et al., 2014; Hatfield et al., 2016). Collectively, these records show that the collapse of the LIS Hudson Bay Ice Saddle (Carlson et al., 2008; Dalton et al., 2020) and southern Greenland Ice Sheet retreat (Colville et al., 2011; Hatfield et al., 2016) culminated at the same time during the last deglaciation (~8.4 ka; Fig. 1.1). The collapse of the Hudson Bay Ice Saddle during the early Holocene caused the final outburst of glacial Lake Agassiz-Ojibway south of Hudson Bay (Brouard et al., 2021) and the deposition of a red detrital marker bed in Hudson Straits sediments (Fig. 1.1; Kerwin, 1996; Barber et al., 1999; Lajeunesse and St-Onge, 2008; Jennings et al., 2015). A similar red (hematite-rich) detrital layer has been found in sediments deposited at Northwest North Atlantic IODP Site U1302/3 during T2 (Fig. 1.1; ~126 ka) and is argued to be the product of extensive deglaciation of the Hudson Bay region following a last deglacial-like collapse of the Hudson Bay Ice Saddle and a subsequent Lake Agassiz-like glacial outburst flood (Nicholl et al., 2012). It shows that during MIS 5e, southern Greenland Ice Sheet retreat continued for ~10 kyr (Hatfield et al., 2016) following LIS Hudson Bay Ice Saddle collapse (Nicholl et al., 2012). Little to nothing is known, however, about LIS retreat during T5 and the longest and warmest interglacial of the last ~500 kyr that followed – MIS 11, ~424-395 ka (Loutre and Berger, 2003; Rohling et al., 2010), widely considered by many, from the perspective of astronomically-driven insolation, to represent the most recent analogue in the geological past for near-future changes

in Earth's climate (e.g., Droxler and Farrell, 2000; Loutre and Berger, 2000, 2003). To shed new light on this important unknown, I explore the timing and duration of LIS deglaciation during T5 in Chapter 4.

1.2.2.3 The Last Glacial Cycle

The LGC (~130-10 ka), is the most recent ~100-kyr-long (inter)glacial cycle of the Quaternary (Lisiecki and Raymo, 2005). Although the spatial extent of the LIS is well mapped for the LGM-Holocene (~26–0 ka; e.g., Dyke et al., 2002; Carlson et al., 2007; Carlson et al., 2007; 2008; Dalton et al., 2019; 2020), few constraints exist for this ice-sheet for earlier times during the LGC. This gap in our knowledge exists because most geological evidence for LIS extent during the LGC was destroyed by its advance towards the mid-latitudes. This fact has led to a reliance on numerical modeling of the LIS for its pre-LGM configurations during the LGC (e.g. Batchelor et al., 2019; Lambeck et al., 2006; 2010; 2017; Abe-Ouchi et al., 2013; de Boer et al., 2014; Colleoni et al., 2016).

Following the Eemian (~129-116 ka), the LIS on North America is thought to have initially occurred in the form of largely isolated Quebec-Labrador, Keewatin and Baffin Island domes (Fig. 1.2b; Vincent and Prest, 1987; Forsström and Punkari, 1997). While the existence of the Quebec-Labrador dome during MIS 5 is supported by glacial landform swarm patterns in Quebec (Kleman et al., 2010), the age of these features is relatively poorly constrained, and are assumed to have formed during MIS 5d or 5b (Kleman et al., 2010). Regardless, the most recent review of the available evidence (Batcheler et al, 2019) infers that Hudson Bay and much of the region south of it remained ice-free throughout MIS 5 (Fig. 1.2b,c).

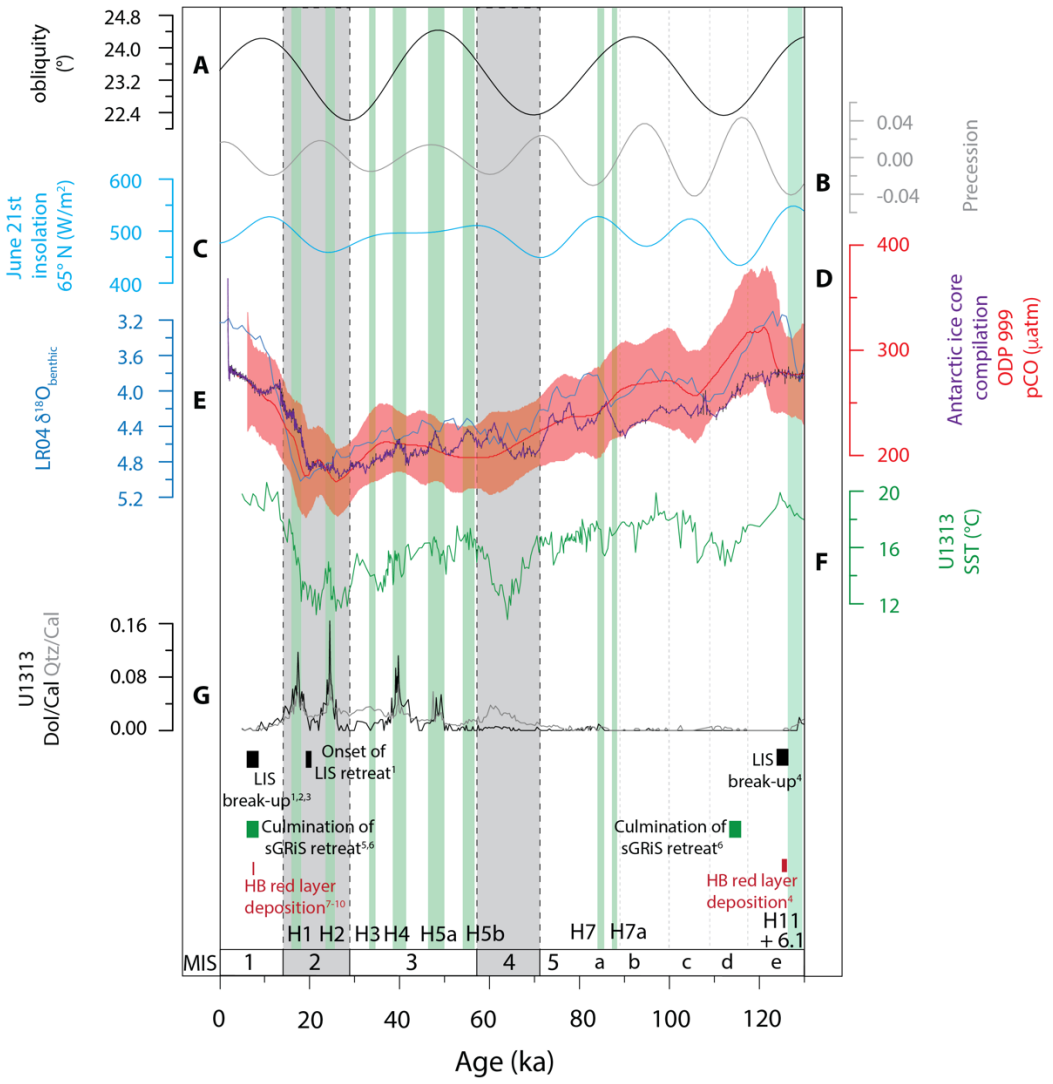

Figure 1.2: Last Glacial Cycle climate change: **(A)** Obliquity; **(B)** Precession; **(C)** Insolation forcing at 21st June 65°N (W/m^2; Laskar et al., 2004); **(D)** δ^{11}B-derived CO_2 record from *Globigerinoides ruber* at ODP Site 999 with 2σ error bars/envelopes. MPWP (~3100-3350 ka from de la Vega et al., 2020 and Martinez-Boti et al. 2015), early mid Pleistocene Transition and late Pleistocene (~1050-1250 and 0-250 ka respectively; from Chalk et al., 2017), Late Pleistocene (~800-0 ka Antarctic ice core compilation; Bereiter et al., 2015). **(E)** LR04 benthic δ^{18}O stack (Lisiecki and Raymo, 2005. **(F)** IODP Site U1313 alkenone-derived sea surface temperature (SST °C; Naafs et al., 2013b; 2020). **(G)** IODP Site U1313 Dol/Cal (black line) and Qtz/Cal (grey line) ratios (Naafs et al., 2013b). Black horizontal bars and associated superscript numbers highlight timing of major events that characterise Laurentide Ice Sheet retreat during T1, (1 = Dalton et al., 2020, 2 = Brouard et al., 2021, 3 = Margold et al., 2018) and T2 (4 = Nicholl et al., 2012). Inferred timing of southern Greenland Ice Sheet (sGRiS) retreat ceased during T1 (5 = Hatfield et al., 2016; 6 = Colville et al., 2011), T2 (6 = Colville et al., 2011) Also shown is timing of the deposition of a red layer in Hudson Bay (HB; red horizontal bar) during T1 (7 = Barber et al., 1999, 8 = Lajeunesse and St-Onge, 2008, 9 = Jennings et al., 2015, 10 = Lochte et al., 2019) and T2 (Nicholl et al., 2012).

MIS 4 (~57-71 ka) is thought to represent the first stage during the LGC that the Hudson Bay region of North America was covered by a proto-LIS (Fig. 1.3d; Kleman et al., 2010; Batchelor et al., 2019). Most of its estimated aerial extent at this time is, however, based on numerical models (Batchelor et al., 2019; Gowan

et al., 2021). These indicate that the LIS during MIS 4 was less spatially extensive than its LGM counterpart (Stokes et al., 2012; Batchelor et al., 2019), but a westward advance of the Quebec-Labrador dome at this time is supported by till fabrics and lineation swarms from the Hudson Bay Lowlands (Fig. 1.3d; Kleman et al., 2010; Gauthier et al., 2019).

Controversy also exists around whether the Quebec-Labrador dome in the east and the Keewatin dome in the west were connected during MIS 3 (~57-27 ka; Fig. 1.3e), i.e. whether Hudson Bay was glaciated during this time by the Hudson Bay Ice Saddle, or whether the Quebec-Labrador dome even existed during this interstadial (e.g., Dalton et al., 2016; 2019; Pico et al., 2017; Miller and Andrews, 2019; Kerr et al., 2021). I will explore the features of the LIS history outlined above in Chapter 3.

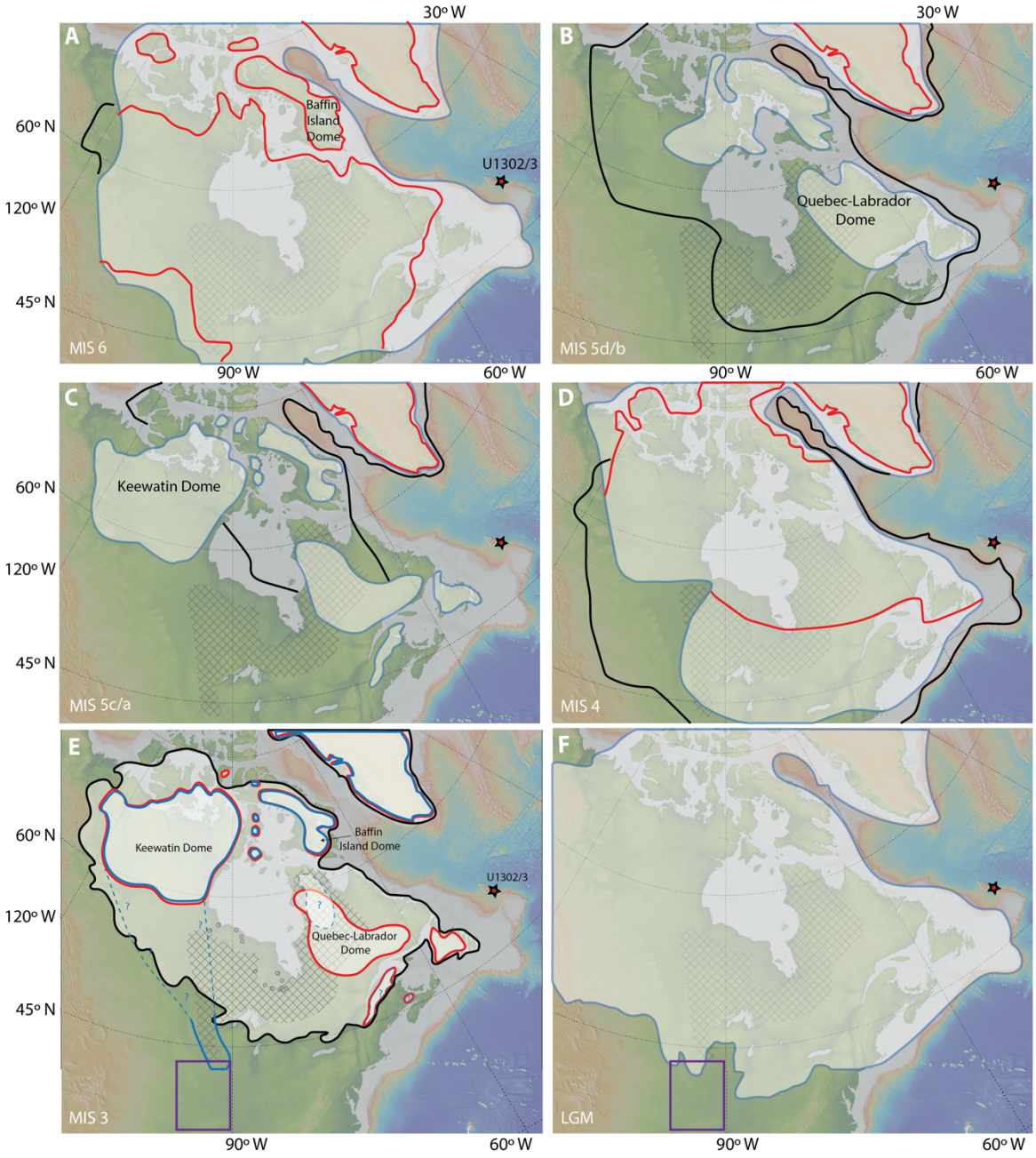

Figure 1.3: Reconstructions of Laurentide Ice Sheet and Greenland Ice Sheet extents following Batchelor et al. (2019). Maximum (black line), minimum (red line) and best-estimate (blue) ice-sheet extents for: **(A)** marine isotope stage (MIS) 6 (132-140 ka); **(B)** MIS 5d/b (108-117; 86-92 ka, respectively); **(C)** MIS 5c/a (92-108; 72-86 ka); **(D)** MIS 4 (58-72 ka); **(E)** MIS 3 (29-57 ka) where minimum estimate is at peak warmth (40-45 ka; red line), maximum estimate achieved following a period of LIS growth (30 ka; black line); most recent reconstruction for peak warmth (40-45 ka; blue line) following Pico et al. (2017), Dalton et al. (2019) and Kerr et al. (2021) where dashed blue line is inferred ice extent; **(F)** Last Glacial Maximum (26-19 ka). Black cross-hatched area denotes geographical extent of Superior Province craton (Montsion et al., 2018). Red stars highlight location of IODP Site U1302/3 on Orphan Knoll. Black cross-hatched area denotes geographical extent of Superior Province (Montsion et al., 2018). Grey circles (n = 35) represent locations of ^{14}C and optically stimulated luminescence geochronological dates of marine and fluvial strata from the Hudson Bay Lowlands used by Dalton et al. (2016; 2019) to infer a marine incursion into this area (and its deglaciation) between 52-42 ka. Main glacial till sites in Missouri that indicate maximum LIS extent during the past ~2.4 Ma are located within the purple rectangle (Balco and Rovey, 2010; Rovey and Siemens, 2021).

1.2.3 Plio-Pleistocene North Atlantic water mass geometry

One prominent theory proposed to help explain a drop of ~90 ppm in the atmospheric concentration of CO_2 during the LGC involves enhanced oceanic carbon storage via deep water stratification due to a "two-cell" circulation structure in the Atlantic Ocean (e.g., Sigman et al., 2010). This theory is supported by benthic foraminiferal carbon isotope ($\delta^{13}C$ and $\Delta^{14}C$) and B/Ca-based reconstructions of water-mass provenance which are traditionally believed to indicate that, unlike for the modern, old, carbon-rich and nutrient-depleted SSW occupied depths greater than ~2500 m in both the western and eastern North Atlantic during the LGM (Fig. 1.4a; e.g., Curry and Oppo, 2005; Yu et al., 2008; Chalk et al., 2019). It has been further argued that this view of the LGM oceans is broadly supported by studies of the Nd isotope (ε_{Nd}) composition of bottom waters bathing the deep Atlantic during this time (e.g., Böhm et al., 2015).

Together, benthic $\delta^{13}C$ and ε_{Nd} records spanning the past ~3.3 Ma from deep northwestern North Atlantic IODP Site U1313 (Lang et al., 2016; Kirby et al., 2020) and its predecessor Site 607 (Kim et al., 2021; Yehudai et al., 2021) have been suggested to record a major LGM-like SSW incursion to the deep North Atlantic during prominent cold stages from MIS 100, ~2.52 Ma, but that they were not a persistent feature of Quaternary glaciations until following the MPT. Yet it has recently been argued that the distribution of Nd in the LGM Atlantic Ocean is better explained by a change in the preformed NSW ε_{Nd} signature (Du et al., 2020; Zhao et al., 2019; Pöppelmeier et al., 2021; Abbott et al., 2022) and that the more negative LGM values in North Atlantic $\delta^{13}C$ records reflects greater remineralisation of carbon in deep waters (Howe et al., 2016) under a more sluggish glacial deep Atlantic circulation (Fig. 1.4b; Böhm et al., 2015; Ng et al., 2018). Seen in this light, changes in ε_{Nd} data from the deep northwestern North Atlantic track the evolution of the Nd isotope composition of NSW rather than changes in water-mass mixing. No records spanning the entire LGC exist from this region of the North Atlantic. In Chapter 5, I present a new record of fish debris ε_{Nd} from Site U1313 spanning the past ~130 kyr and discuss the likely changes in high latitude climate that are responsible for the evolution in NSW ε_{Nd}. These observations are then used to explore changes in high latitude climate over the past ~3.3 Ma using previously published ε_{Nd} records from sites U1313 and 607.

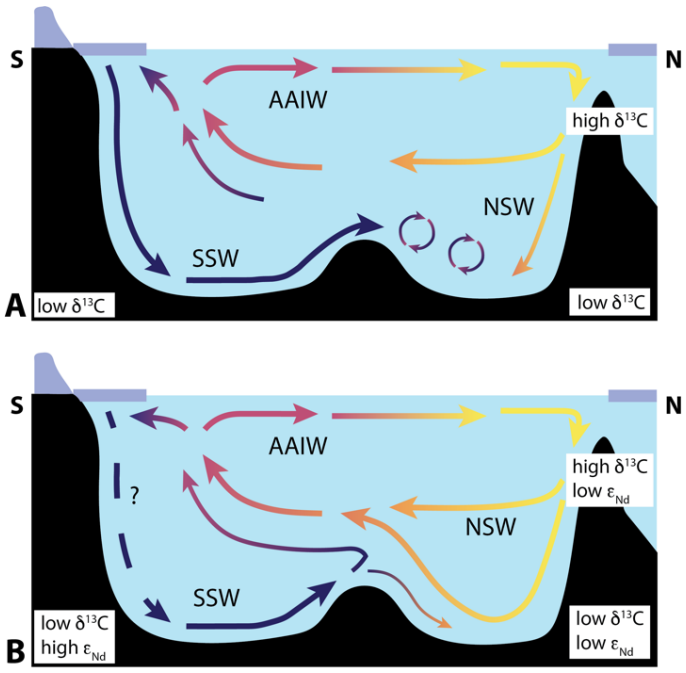

Figure 1.4: Proposed circulation regimes in the Atlantic Ocean during the Last Glacial Maximum based on: **(A)** $\delta^{13}C$ records and **(B)** ε_{Nd} records. The width of the arrows roughly corresponds to proposed volume of each water mass. SSW = Southern Sourced Waters, NSW = Northern Sourced Waters, AAIW = Antarctic Intermediate Waters. Modifed from Howe et al., (2016) and Pöppelmeier et al., (2020).

1.3 Thesis aims and outline

In this thesis I use a two-pronged approach to investigate two major aspects of Earth's climate during the Plio-Pleistocene using two marine records recovered during Integrated Ocean Drilling Program (IODP) Expeditions 303 and 306:

the mid to late Pleistocene evolution of the North American LIS using authigenic Pb isotope records from IODP sites U1302/3 from Orphan Knoll; specifically during most extreme termination of the Quaternary, T5, during MIS 12–11 (~430 ka) and T2 (~130 ka) and the LGC (124–0 ka);

Changes in high-latitude climate over the past ~3.3 Myr using deep North Atlantic ε_{Nd} data from deep northwest North Atlantic Site U1313, with a focus on iNHG, the MPT and LGC.

In **Chapter 2**, I begin by outlining the methodologies employed in undertaking the research for this thesis, focusing on radiogenic isotopes of lead (Pb) and neodymium (Nd) to reconstruct continent ice sheet extent, ocean circulation and water mass mixing, respectively. The specific questions posed as part of this thesis within Chapters 3 to 5 are outlined below.

Chapter 3: "History of the Laurentide Ice Sheet extent over the last 130 thousand years traced by the Pb isotope signature of weathering inputs to the Labrador Sea"

The study addresses the following questions about the history of the LIS:

1) *How can marine-core authigenic Pb isotope records from Site U1302/3 be used to track LIS extent on North America during the mid and late Pleistocene?*
2) *What do such data reveal about LIS evolution during the LGC?*
3) *How do the deglacial histories of the LIS differ during T2 and T1?*

Chapter 4: "Ice-sheet evolution on North America and southern Greenland during Termination 5"

The study addresses the following questions about the history of the LIS using authigenic Pb isotope records from Site U1302/3:

1) *When did LIS retreat begin during T5?*
2) *What is the relationship between the timing of Hudson Bay Ice Saddle collapse and the two weak precessional-paced maxima in insolation associated with MIS 11?*
3) *Is there any evidence for LIS regrowth during the intervening insolation minima?*
4) *By what likely time was LIS deglaciation complete during MIS 11?*

Chapter 5: "The Nd isotope composition of the deep western North Atlantic during the Last Glacial Cycle: implications for the evolution of the preformed composition of northern sourced water"

The study addresses the following questions related to our understanding of the evolution of NSW ε_{Nd}:

1) *How does NSW ε_{Nd} evolve during the LGC at Site U1313?*
2) *What North Atlantic oceanographic and climatic factors are responsible for controlling the preformed composition of NSW that is recorded in this ε_{Nd} record? We examine in turn the contribution that the 'top-down' hypothesis*

(chemical weathering), Labrador Sea Water (LSW) production, southward migration of the polar front and the 'bottom-up' hypothesis may have played in explaining the trends in this new record.

3) *What do older Plio-Pleistocene ε_{Nd} records from sites U1313 and 607 reveal about changes in northern high-latitude climate during iNHG and the MPT?*

Chapter 6 outlines the main conclusions and provides a synthesis of this research, alongside a summary of potential future research resulting from this thesis. All thesis data chapters (3-5) have been written with the intention of them being independently published. As such, some unavoidable repetition of core information exists.

Chapter 2: Radiogenic isotopes as palaeoclimate proxies

This thesis focuses on the use of radiogenic lead (Pb) and neodymium (Nd) isotope data generated from North Atlantic marine sediments to track the Plio-Pleistocene history of Laurentide Ice Sheet (LIS) extent on North America and water mass mixing, respectively.

2.1 Pb isotopes as a glacial-extent tracer

The particle reactive nature and short seawater-residence time of Pb (20-30 years in the North Atlantic; Henderson and Maier-Reimer, 2002), makes the Pb isotope composition of seawater an excellent tracer of regional weathering intensity and runoff from continental landmasses (Fagel et al., 2002; Frank, 2002). Changes in seawater Pb isotope compositions are recorded in the geological record in ferro-manganese (Fe-Mn) crusts and authigenic Fe-Mn oxyhydroxide coatings of marine sediments, which co-precipitate Pb from the ambient seawater.

Lead is characterized by four naturally occurring isotopes. Three of these (^{206}Pb, ^{207}Pb, ^{208}Pb) are the radiogenic daughter products of ^{238}U ($t_{1/2}$= 4.5 Ga; ^{206}Pb), ^{235}U ($t_{1/2}$= 704 Ma; ^{207}Pb), or ^{232}Th ($t_{1/2}$= 14 Ga; ^{208}Pb), while the last (^{204}Pb) is a stable isotope of Pb (Steiger and Jaeger, 1977). The Pb isotope composition of circum-North Atlantic terranes depends primarily on the composition of the rocks they contain, their age and number of metamorphic events they have

experienced (Fig. 2.1; see e.g., Innocent et al., 1997; Fagel et al., 2002). During partial melting and fractional crystallisation of magma, U and Th concentrate in the liquid phase due to their lithophile characteristic and become incorporated into more acidic (silicate-rich) components. Consequently, granites are enriched in U and Th, when compared with rocks of basic (basaltic and ultramafic) composition (e.g., Zartman and Wasserburg, 1969). The primary signature can be altered by subsequent metamorphic (overprint) events, whereby the degree of overprint is controlled by the modification and destruction of datable mineral phases (Connelly, 2001; Parrish, 2001; Williams et al., 1999). On a continental scale, the distinctive U/Pb and Th/Pb ratios produced from the above processes can be used to delineate crustal boundaries that separate major lithotectonic blocks with coherent crustal growth histories (e.g., Zartman, 1974).

Common lead is found in potassium (K) minerals such as plagioclase and K-feldspar during magma cooling and crystallisation as the ionic radii of Pb and K are similar (Larsen et al., 1952). These minerals are characterised by low U/Pb and Th/Pb ratios and Pb isotopic values that have not evolved significantly by radioactive decay since the mineral formed. Radiogenic Pb is found mainly in accessory minerals that have high U/Pb and Th/Pb ratios, and are old enough so that a significant amount of Pb has been produced by the decay of uranium and thorium. Minerals that contain radiogenic Pb include zircon, apatite, epidote, monazite, sphene and uraninite. Because minerals that contain most of the radiogenic Pb are generally accessory phases, lead isotope ratios in most whole rock samples are much closer to the values in plagioclase and K-feldspar than to the radiogenic accessory minerals (Erel et al., 1994).

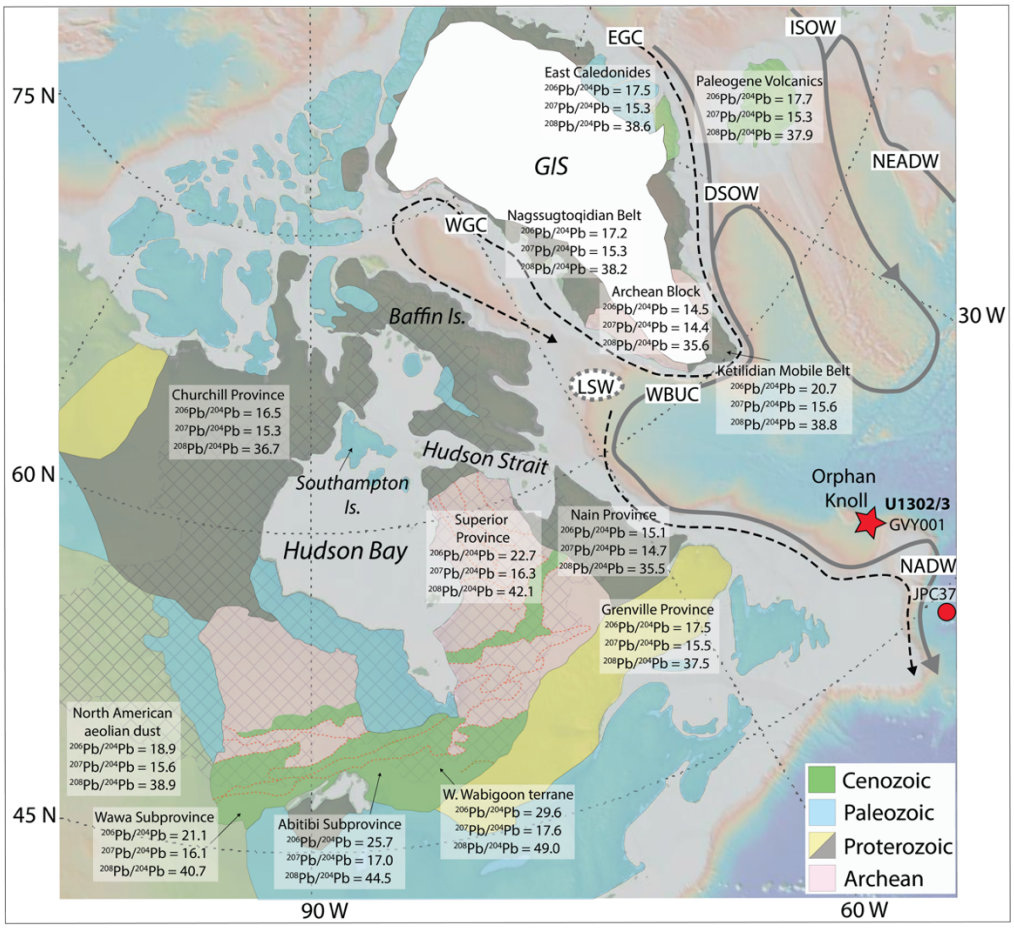

Figure 2.1: Map showing the relevant circum-North Atlantic Pb isotope signatures of surrounding bedrock geology based on continental whole rock data compiled in Chapter 3, Table 3.1. Refer to Table 3.1 for data sources. Geology of North America and Greenland redrawn from Reed et al. (2005) and White et al. (2016). Grey hatched region denotes modern area of watershed drainage into Hudson Bay and its straits (Natural Resources Canada, 2006). Arrows denote paths of key modern deep (solid grey) and surface (dashed grey) ocean currents relevant to this study (redrawn from Blake-Mizen et al., 2019). DSOW = Denmark-Scotland Overflow Water. EGC = East Greenland Current GIS = Greenland Ice Sheet ISOW = Iceland-Scotland Overflow Water. LC = Labrador Current. LSW = Labrador Sea Water. NADW = North Atlantic Deep Water. NEADW = Northeast Atlantic Deep Water. WBUC = Western Boundary Undercurrent. WGC = West Greenland Current.

Pb isotope data from Fe-Mn crusts (Foster and Vance, 2006) and the authigenic fraction of marine sediments (Gutjahr et al., 2009; von Blanckenburg, 1999; Crocket et al., 2012; Kurzweil et al., 2010) from the northwest North Atlantic have been utilised to track regional weathering intensity and solute flux associated with glacial extent on North America in high latitude settings. Fe-Mn crusts have been shown to trace continental weathering on long time scales of millions of years (e.g. Reynolds et al., 1999) and glacial-interglacial cycles (e.g. Foster and Vance, 2006), while the authigenic Fe-Mn oxyhydroxide fraction of marine sediment has more recently demonstrated continental weathering on orbital and at high

resolution millennial timescales (e.g. Gutjahr et al., 2009; Crocket et al., 2012). Chapter 3 focuses on the use of $^{206}Pb/^{204}Pb$, $^{207}Pb/^{204}Pb$ and $^{208}Pb/^{204}Pb$ ratios to track the influence of the history of continental glaciation of North American (the Laurentide Ice Sheet, LIS) on the Pb isotope composition of seawater bathing Labrador Sea IODP site U1302/3 on Orphan Knoll during the mid to late Pleistocene. This Pb was extracted from the authigenic Fe-Mn oxyhydroxide fraction in sediments from this location closely following Blaser et al. (2016). The remaining detrital fraction was digested and prepared for Pb isotope analysis following the same procedure as the authigenic fraction. An outline of these analytical techniques is presented in Section 1.3 of Chapter 3.

Two competing processes have been proposed to explain the influence of LIS extent on the Pb isotope composition of seawater bathing Orphan Knoll. These are: (1) incongruent weathering (Crocket et al., 2012) and, (2) changing provenance (Blaser et al., 2020). Both processes are discussed further in detail in Section 2.1 of Chapter 3, but are also briefly outlined below. Given the short residence time of Pb in seawater (20-30 years), Labrador Current vigour also helps to determine how much Pb supplied from continental runoff into the inner parts of the Labrador Sea makes it to Orphan Knoll. Finally, variations in subaerial deposition of aeolian dust also influences the Pb isotope composition of Labrador Sea seawater. Their combined roles are discussed in Chapter 3.

Historically, and argued by Crocket et al. (2012), it is thought that Pb is released incongruently during the early stages of chemical weathering on continental bedrock and soil during LIS retreat. The Pb isotope composition of these solutes drain into the ocean and it has been suggested that seawater Pb isotope records record this process. Freshly exposed soil and regolith bearing accessory mineral phases rich in uranium (U) and thorium (Th) preferentially release highly radiogenic ^{208}Pb and ^{207}Pb, respectively during incipient and early chemical weathering following ice sheet retreat. These phases tend to be much more radiogenic than the bulk rock Pb isotope composition. Once the accessory phases are depleted, the relatively unradiogenic ^{204}Pb dominates the Pb isotope composition of the weathered product, signalling complete deglaciation (Erel et al., 1994; Harlavan et al., 1998). The magnitude of incongruent chemical weathering is thought to be dependent on the abundance of U- and Th- mineral phases and the continental climatic conditions. Its influence, however, on

seawater composition is largely theoretical since studies of its impact are based on simplified lab experiments (e.g., Süfke et al., 2019) and observations based on the evolution of the chemical weathering signature of granites during only the Holocene Epoch (Dausmann et al., 2019). It has been shown that any incongruent weathering signal should take tens of thousands of years to decay (Harlavan et al., 1998; Süfke et al., 2019). Furthermore, if incongruent weathering dominated chemical weathering, a progressive increase in the $^{208}Pb/^{204}Pb$ ratios of the associated solute products should also lag those in $^{207}Pb/^{204}Pb$ because the main source of radiogenic ^{208}Pb (Th-bearing minerals) is more resistant to dissolution than (U-bearing) mineral sources of ^{206}Pb and ^{207}Pb (Dausmann et al., 2019; Süfke et al., 2019).

The competing, but also potentially complimentary, model to explain evolution of seawater Pb isotopes as a function of LIS extent invokes change in Pb provenance of solute runoff (Blaser et al., 2020). The continental landmasses surrounding the North Atlantic are composed of tectonic terranes with distinct Pb isotopic signatures that enter the ocean via runoff following chemical weathering, advected in water masses and precipitated on authigenic Fe-Mn oxyhydroxide sediment coatings (Fagel et al., 2002). The most radiogenic Pb end-member in this region is the Superior Provence of the Canadian Shield (mean $^{206}Pb/^{204}Pb$ = 21.13), while the Greenland Archean Craton is the most unradiogenic end-member (mean $^{206}Pb/^{204}Pb$ = 14.54). The Superior Province is the only relevant end-member with higher $^{206}Pb/^{204}Pb$ ratios than the authigenic record from Site U1302/3 presented by Blaser et al. (2020), suggesting that increased weathering of this terrane in the Hudson Bay region controls the seawater Pb isotope values at this site. The idea that changes in Pb provenance control the evolution of the Pb isotope composition of Labrador Sea seawater is supported by a recent Pb isotopic record of freshwater routing from North America into the Arctic Ocean. It shows meltwater events associated with a retreat LIS during the Bølling–Allerød argues against incongruent weathering. The major shift in both authigenic and detrital Pb isotope ratios at the onset of this event support congruent weathering and suggests that the radiogenic Pb isotopic signal reflects a change in sediment provenance as the LIS retreated (Süfke et al., 2022). This thesis provides a further test of the role of incongruent vs. congruent weathering in controlling seawater Pb isotopes in the Labrador Sea, which is discussed in detail in Chapter 3 and 4.

Any test of the role of (in)congruent chemical weathering in controlling regional signatures of the Pb isotope composition of freshwater discharge into the North Atlantic Ocean requires a detailed knowledge of the Pb isotope composition of the tectonic terranes that make up its adjacent landmasses. Some uncertainty exists, however, in this regard. In an ideal world, an estimate of the average Pb isotope weathering signal of a source would be made using data from all major units that characterize that source, normalized for, e.g., their Pb concentrations and aerial coverage. In reality, this is rarely possible to achieve in a geological study. An alternative approach comes from the measurement of the Pb isotope composition of the well-mixed fine fraction of glaciofluvial sediments from rivers and trough mouth fans. This approach has been used successfully to characterize the Pb isotope composition of southern Greenland tarranes (e.g., Reyes et al., 2014). In this thesis, I have utilized these datasets in Chapter 3 (Section 2.2) as part of an update in our understanding (e.g., Innocent et al., 1997; Fagel et al., 2002) of the isotope composition of regional sources of Pb runoff to the Labrador Sea (the study area focused on in Chapters 3 and 4). Whole rock bedrock data were used to refine our understanding of the Pb isotope composition of North American terranes.

One way to estimate the average weathering signal of a tectonic terrane is to determine the mean and median of the whole-rock Pb isotope composition of its bedrock. The degree of disparity between the mean and median can be used as a first-order estimate of uncertainty in each end-member's average Pb isotope composition (see, e.g., Fagel et al., 2002). The true average composition of a regional source is likely to fall somewhere between the mean and median of the available whole rock data (see Chapter 3). For most terranes (Archean Block, Ketilidian Mobile Belt, Nagssugtoqidian Mobile Belt, Paleogene Volcanics, Grenville, Churchill and Nain provinces), the mean and median are very similar so we can be relatively confident that averaging bedrock data for most circum-Atlantic terranes provides a useful measure of the average composition of them. The relatively large difference between the mean and median values for the Superior Province is likely due to undersampling of its diverse geology, which is composed of many geologically distinct terranes with continental and oceanic affinities (Gariepy and Allegre, 1985; Vervoort et al., 1993; Percival, 2007). It has recently been suggested that increased congruent weathering of a radiogenic Superior Province during times of LIS retreat may drive radiogenic signals in

Labrador Sea seawater (Blaser et al., 2020). This sampling bias undoubtedly influences our confidence in whether congruent chemical weathering of the SP (Blaser et al., 2020) or incongruent weathering (Crocket et al., 2012) drives radiogenic trends in the Pb isotope composition of Labrador Sea seawater, and is discussed in detail Chapter 3.

Finally, it is also important to assess the integrity of the seawater Pb isotope record extracted from the authigenic Fe-Mn oxyhydroxide sediment fraction, by testing whether non-seawater-derived Pb is released from the detrital sediment fraction. Chapter 3 and 4 employ the following tests: (1) examination of detrital and authigenic Pb isotope trends for evidence of covariance, (2) evaluation of rare earth element data to identify what material was leached (Haley et al., 2004; Martin et al., 2010) and, (3) comparison of Al/Nd, Al/Th and Al/Pb ratios of the authigenic and detrital fractions of our samples and abyssal ocean Fe-Mn crusts (Gutjahr et al., 2007).

2.2 Nd isotopes as a palaeo-water mass tracer

The Nd isotopic composition of seawater has been used extensively to trace ocean circulation on a variety of timescales, as the estimated residence time of Nd in oceans is shorter (~300-750 years; Tachikawa er al., 2017), but on the same order of magnitude as the homogenisation of the ocean (~1500 years; Broecker and Peng, 1982). Nd isotopic ratios (or ε_{Nd}-values) vary in rocks and oceanic water due to radioactive α–decay of ^{147}Sm to ^{143}Nd ($t_{1/2}$= 106 Ga) and the different behaviour of Sm compared to Nd during melting and crystallisation processes. Nd is less compatible for minerals in Earth's mantle than Sm due to its slightly larger ionic radius and is therefore enriched during the partial melting of mantle and the subsequent formation of igneous rocks that changes the Sm/Nd ratio in minerals which, over time, will change the relative abundance of ^{143}Nd and ^{144}Nd, although the long half-life of ^{147}Sm means the deviations in $^{143}Nd/^{144}Nd$ are small (Fig 2.2). Consequently, the Nd in older continental rock is unradiogenic due to the low Sm/Nd ratio in this material compared to mantle-derived and young continental rocks that have positive epsilon (ε_{Nd}) values (radiogenic), where ε_{Nd} is the deviation of the determined $^{143}Nd/^{144}Nd$ ratio from the composition

expected today for a hypothetical chondritic uniform reservoir 'CHUR 'in parts per 10,000 (Fig. 2.3; Eq. 1; Jacobsen and Wasserburg, 1980). CHUR is the model value for the evolution of $^{143}Nd/^{144}Nd$ as a function of time for an undifferentiated earth. This model assumes that terrestrial Nd has evolved in a uniform reservoir in which the Sm/Nd ratio equals that on chondritic meteorites (Fig 2.3; DePaolo and Wasserburg, 1976). The present day value of the $^{143}Nd/^{144}Nd$ ratio of this reservoir is 0.5126 relative to a $^{146}Nd/^{144}Nd$ ratio of 0.7219 (Vance and Thirlwall, 2002). Major minerals such as amphibole, garnet and pyroxene can host significant amounts of rare earth elements (including Nd), while accessory phases such as zircon, allanite, epidote, monazite, titanite and apatite appear to be the most important hosts of Sm and Nd (e.g. Bea, 1996; Hermann, 2002).

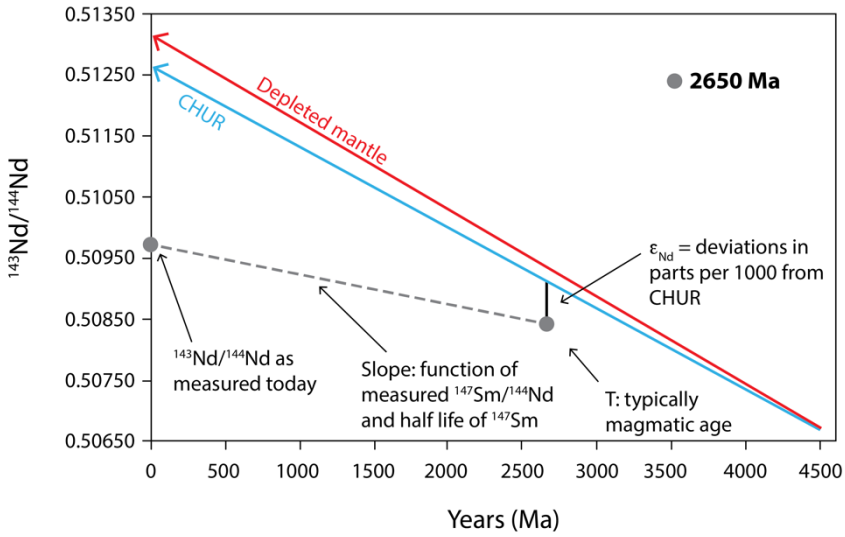

Figure 2.2: Evolution of $^{143}Nd/^{144}Nd$ through time, based on radioactive decay of ^{147}Sm. The change in $^{143}Nd/^{144}Nd$ through time is a function of the $^{147}Sm/^{144}Nd$ ratio. Variations of $^{143}Nd/^{144}Nd$ are small and are therefore typically reported as ε_{Nd} values (deviations from CHUR = blue line) using the formula in Eq. 1. Depleted mantle and CHUR evolution curves are shown in red and blue lines, respectively (modified from Champion, 2013).

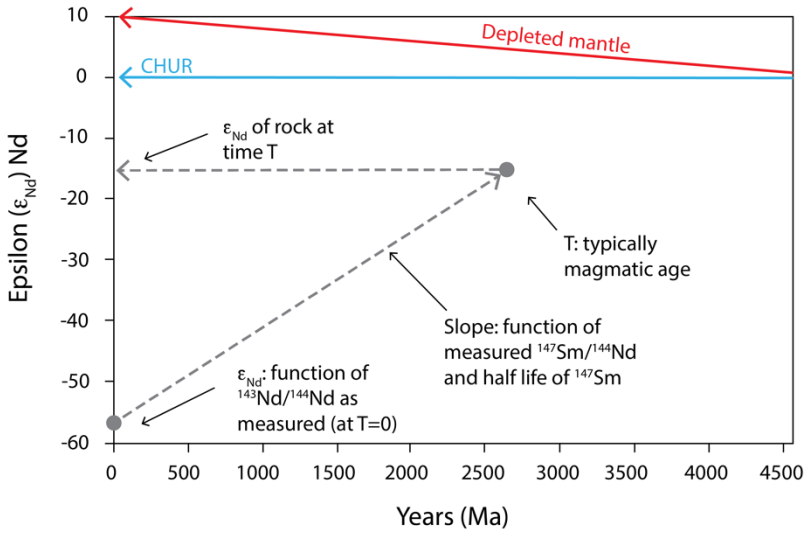

Figure 2.3: ε_{Nd} vs. time. The ε_{Nd} value of rock at time (T), typically the crystallisation age for a magmatic rock, requires present day (T=0), $^{143}Nd/^{144}Nd$ and $^{147}Sm/^{144}Nd$ values, a measure or estimate of T, and present day values of $^{147}Sm/^{144}Nd$ and $^{143}Nd/^{144}Nd$ for CHUR – 0.1967 and 0.51265, respectively. The line connection ε_{Nd} at time T and time = 0 tracks the ε_{Nd} evolution of the sample through time, and is useful for comparing samples of different ages (Modified from Champion, 2013).

$$\varepsilon_{Nd} = \left(\frac{\frac{^{143}Nd}{^{144}Nd}sample}{\frac{^{143}Nd}{^{144}Nd}CHUR} - 1 \right) \times 10^4 \qquad \text{Eq.1}$$

The seawater Nd signature reflects the surrounding continental rock sources (Fig. 2.4), whereby Nd enters the ocean via chemical weathering, dissolved solutes in runoff and dust deposition and is recorded in the authigenic coatings of seafloor sediments (Frank, 2002; Goldstein and Hemming, 2003; Tachikawa et al., 1999; van de Flierdt et al., 2016). However, partial dissolution of reactive detrital phases within sediments can release Nd to pore waters that are subsequently taken up into authigenic fractions and thus contaminate the source seawater signal. As a result, the Nd isotope composition of porewater and authigenic phases converge on that of the containment phases (Abbott et al., 2016; 2022; Blaser et al., 2019; Du et al., 2020; Haley et al., 2017; Roberts and Piotrowski, 2015). The magnitude of relabelling is determined by the reactivity of marine sediment (and the exposure time). Young radiogenic volcanic phases (e.g., Icelandic basalt with an ε_{Nd} composition of up to ~+7; Pearce et al., 2013) have, for example, been shown in some settings to release Nd readily (Elmore et al., 2011; Roberts and

Piotrowski, 2015), while unradiogenic Laurentian-sourced detrital carbonates (ε_{Nd} = ~–18; Roberts and Piotrowski et al., 2015) are another phase in North Atlantic marine sediments that have been shown to release Nd to sediment pore-waters and the water column (Blaser et al., 2019), thereby potentially overprinting the seawater ε_{Nd} signature.

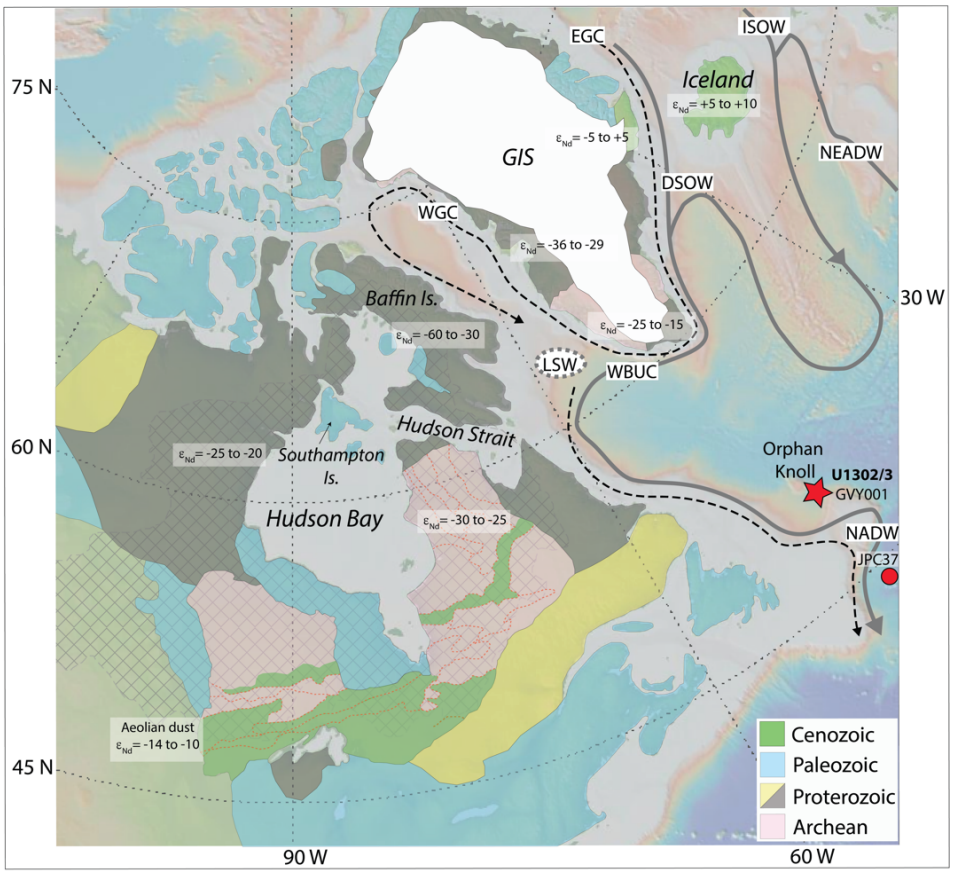

Figure 2.4: North Atlantic Nd isotope (ε_{Nd}) distribution based on continental whole rock and river sediment data for relevant terranes. Data sources from Robinson et al., (2021) and Jeandel et al., (2007) compilations and references therein. Geology of North America and Greenland redrawn from Reed et al. (2005) and White et al. (2016). Grey hatched region denotes modern area of watershed drainage into Hudson Bay and its straits (Natural Resources Canada, 2006). Arrows denote paths of key modern deep (solid grey) and surface (dashed grey) ocean currents relevant to this study (redrawn from Blake-Mizen et al., 2019). DSOW = Denmark-Scotland Overflow Water. EGC = East Greenland Current GIS = Greenland Ice Sheet ISOW = Iceland-Scotland Overflow Water. LC = Labrador Current. LSW = Labrador Sea Water. NADW = North Atlantic Deep Water. NEADW = Northeast Atlantic Deep Water. WBUC = Western Boundary Undercurrent. WGC = West Greenland Current.

The modern distribution of Nd in the ocean shows that ε_{Nd} deep-water relabelling increases as a function of water-mass age (Du et al., 2020). In the Pacific, where deep-waters are oldest, seawater and authigenic ε_{Nd} are higher than younger Atlantic deep-waters (Du et al., 2020). The degree of ε_{Nd} overprinting of water-

masses is likely to vary as a function of exposure time of sea water to these phases, which increases as bottom current speed decreases. This process is likely to be amplified in North Atlantic sediments during glacials when the Atlantic Meridional Overturning Circulation (AMOC) vigor was likely reduced (Böhm et al., 2015). Relabelling can also occur in the water column via reverse scavenging when phases rain down in pelagic aggregrates. This process probably only plays a minor role in comparison to seafloor sediment relabelling (Siddall et al., 2008; Haley et al., 2014; Du et al., 2020; Roberts and Piotrowski, 2015). Chapter 5 explores seafloor sediment relabelling in controlling the ε_{Nd} signature at the study site.

Today, the ocean's lowest ε_{Nd} values (~–10 to –20 epsilon units) are found in Baffin Bay (located between Baffin Island and the west coast of Greenland) and the Labrador Sea, where Nd is derived from old cratonic rocks that have originated in sources with a lower Sm/Nd ratio than the chondritic reservoir and become more negative as a function of the measured $^{147}Nd/^{144}Nd$ and half-life of ^{147}Sm. This mixes with waters derived from the Nordic/Iceland basins that are slightly more radiogenic. In comparison, the North Pacific is characterised by high ε_{Nd}-values (~0 to –4) from younger surrounding volcanic activity that are sourced from residual solids in the reservoir subsequent to earlier magma withdrawal and is now depleted in large ion lithophile elements that are preferentially partitioned into the liquid phase during partial melting. The admixture of ε_{Nd} signatures of water masses in the sub-polar North Atlantic represent Northern Sourced Water (NSW; ε_{Nd} = -12.8 ± 0.4; Lambelet et al., 2016) that is subsequently exported equatorwards. The Southern and Indian Ocean ε_{Nd}-values (~-7 to -9) are derived from a mixture of North Atlantic and Pacific values (von Blanckenburg, 1999). Because Nd isotopes are resistant to mass dependant fractionation by biological processes and considered quasi-conservative in the ocean, different water masses 'tagged' by varying but distinct ε_{Nd} signatures allow water masses to be traced very far from their source (Goldstein and Hemming, 2003; von Blanckenburg, 1999; Rutberg et al., 2000). Our understanding of the Nd isotope composition of circum-Atlantic terranes is subject to the same sampling bias discussed above for Pb isotopes. The uncertainties that may result in our understanding of terrane ε_{Nd} have, however, limited bearing on the interpretation of the U1313 fish-debris Nd isotope data reported in this thesis in Chapter 5 as a

record of the evolution of NSW ε_{Nd} during the Last Glacial Cycle. This is because Chapter 5 focuses on exploring the theoretical role that changes in the modern-day ε_{Nd} of regional water masses from the North Atlantic region (which is well documented; Lambelet et al., 2016) and oceanographic and climatic processes have in driving the evolution of NSW ε_{Nd} over the past ~130 kyr.

The Nd isotope signature of past deep water is preserved in various ways. One archive for the Nd isotopic signature is planktic foraminifera located within ocean floor sediment. Once dead, their shells sink to the ocean floor where the bottom water Nd signature is incorporated into Fe-Mn rich coatings surrounding the foraminifera shell near the sediment-water interface and preserved (Roberts and Piotrowski, 2015). Another important archive is fish debris apatite (the archive used in Chapter 5). This mineral incorporates trace elements during early diagenesis following sediment deposition. The high trace element concentrations (Wright et al., 1984) make this archive advantageous compared to foraminifera coatings, but fish debris is not always available in the sediment record (Huck et al., 2016). Finally, Fe-Mn crusts accumulate hydrogenous Fe-Mn oxides in the deep sea and incorporate Nd during this process (Rutberg et al., 2000). Verifying the seawater origin of the Nd in Fe-Mn crusts is challenging, but has been studied extensively, especially by applying various extraction techniques such as the “Sr test” (Rutberg et al., 2000; Piotrowski et al., 2004; 2005; 2008) and sequential leaching (Bayon et al., 2002; Gutjahr et al., 2007; Blaser et al., 2016). An increasing number of studies in the North Atlantic have called for the generation of detrital ε_{Nd} data alongside authigenic records to help determine the influence of sediment to pore-water Nd flux contamination of authigenic signatures (e.g. Du et al., 2020; Abbott et al., 2022).

Chapter 3: Laurentide Ice Sheet extent over the last 130 thousand years traced by the Pb isotope signature of weathering inputs to the Labrador Sea

Chapter 3 is based on a manuscript in revision for Quaternary Science Reviews. Rebecca L. Parker (R.L.P) led this project with contributions as follows: Ian Bailey (I.B.) was responsible for the project conception and supervised R.L.P. R.L.P acquired funding, performed Pb isotope and rare earth element analysis at the School of Ocean and Earth Science, University of Southampton, made the interpretations presented and co-wrote the manuscript with I.B. Paul A. Wilson (P.A.W) helped to finance the analyses. P.A.W., Gavin L. Foster, Marcus Gutjahr, and Kirsty C. Crocket contributed to manuscript writing and the ideas presented. Matthew J. Cooper, Agnes Mitchelik and James A. Milton helped R.L.P to generate Pb isotope and rare earth element data, oversaw instrumentation and helped with analysis. Kate Littler and P.A.W. co-supervised R.L.P.

3.1 Abstract

Understanding the history of continental ice-sheet growth on North America is important for palaeoclimate and sea-level reconstructions but information on ice-sheet extent pre-dating the Last Glacial Maximum (LGM) is heavily reliant on the outputs of numerical models underpinned by scant geological data. We present authigenic ferro-manganese (Fe-Mn) oxyhydroxide-derived high-resolution records of Pb isotope data and associated rare earth element profiles for samples spanning the past ~130 kyr from northwest North Atlantic Labrador Sea, IODP Site U1302/3. We use these new data to track chemical weathering intensity and solute flux to the Labrador Sea associated with Laurentide Ice Sheet (LIS) extent on the adjacent highly radiogenic (high Pb isotope ratios) North American Superior Province (SP) since the Penultimate Glacial Maximum (PGM). Our new records show that relatively high (radiogenic) ratios characterise warm marine isotope stages (MIS) 5, 3 and 1 and the lowest (most unradiogenic) ratios occurred during cold stages MIS 6, 4 and 2. The radiogenic Pb isotope excursion associated with Termination 2 is short-lived relative to the one documented for Termination 1, suggesting that the LIS retreat during the PGM was relatively fast compared to the LGM. Highly radiogenic inputs to the Labrador Sea during MIS 5d-a, ~116-71 ka, most likely reflect a spin-up in Labrador Current vigour, incipient glaciation and renewed glacial erosion of high grounds of the eastern SP craton by localised wet-based ice-caps, exposing fresh rock for chemical weathering. A large decrease in Pb isotope values towards unradiogenic LGM-like compositions between ~75-65 ka across the MIS 5/4 transition likely reflects a slow-down in Labrador Current vigour, an increase in subaerial deposition of aeolian dust and a strong reduction or even abandonment of Pb sourcing from the SP due to a westward advance of the LIS across Hudson Bay. The relatively radiogenic Pb isotope composition of bottom-waters bathing our study site during MIS 3 is unlikely to reflect a major reduction in LIS extent and is instead perhaps best explained by southern Greenland Ice Sheet retreat and increased chemical weathering of the Ketilidian Mobile Belt and Pb runoff from Greenland.

3.2 Introduction

The growth and decay of continental ice sheets has resulted in major fluctuations in global sea-level during the Quaternary (Rohling et al., 2014). Accurate reconstructions of past ice sheet extent are necessary to understand better the cause and timing of glacial terminations, rates of sea-level change and ice-sheet-ocean-atmosphere interactions. Knowledge of where ice-sheets grew during past glacials facilitates a firmer understanding of factors that drive their mass balance (e.g., astronomical cycles, atmospheric pCO_2 and associated feedbacks) and is also required to correct interglacial sea-level reconstructions accurately for glacial isostatic adjustment (GIA; crustal loading and unloading) when ice-sheets grow or melt (e.g., Dendy et al., 2017). Yet we have only a rudimentary understanding of northern hemisphere continental ice-sheet histories prior to the Last Glacial Maximum (LGM), especially for the largest of these ice sheets, the North American Ice Sheet complex (consisting of the Laurentide, Cordilleran and Innuitian ice sheets).

It has been shown that GIA-based corrections of Last Interglacial (MIS 5e, ~129-116 ka) sea-level records are highly sensitive to uncertainties in the distribution of Northern Hemisphere ice-sheets during preceding glacial maxima to the order of up to ~5 m (Dendy et al., 2017; Dwyer et al., 2021), a figure equivalent to the lower-end estimate and range of sea-level rise reported for this interglacial (+6.6 ± 2 m; Kopp et al., 2013; Hibbert et al., 2016). Yet GIA models used to correct MIS 5e records for such factors mainly assume LGM ice-sheet distributions and volumes for the Northern Hemisphere for the PGM (~155-140 ka) and older glacial maxima (Dendy et al., 2017). Multiple lines of indirect evidence suggest, however, that the North American Ice Sheet complex during the PGM may have been considerably smaller than its LGM counterpart (e.g., Potter and Lambeck, 2003; Svendsen et al., 2004a, b; Rabineau et al., 2006; Colleoni et al., 2011, 2016; Wainer et al., 2017; Rohling et al., 2017). Uncertainty in our knowledge of the North American Ice Sheet complex history is not just restricted to the PGM and older times. Our understanding, for instance, of when a large North American Ice Sheet Complex first grew during the Last Glacial Cycle (LGC) is poorly constrained by empirical data (compare Batchelor et al. (2019) to Pico et al. (2017)).

Considerable debate also exists about the extent of North American Ice Sheet complex reduction during the LGC warm interstadial MIS 3, ~29-57 ka (e.g., Pico et al., 2017; Dalton et al., 2019; Miller and Andrews, 2019; Gowan et al., 2021; Kerr et al., 2021). Uncertainty in MIS 3 ice-sheet extent is rooted in the sparsity of well dated terrestrial glaciomorphological evidence of pre-LGM age (e.g., Miller and Andrews, 2019). Thus, much of our knowledge of the history of the North American Ice Sheet complex prior to the LGM is reliant on either numerical modelling experiments (e.g., Lambeck et al., 2006; 2010; 2017; Abe-Ouchi et al., 2013; de Boer et al., 2014; Colleoni et al., 2016) or indirect sedimentological evidence from glacially-derived terrigenous sediments deposited in marine ice-proximal Quaternary settings (e.g., Hemming, 2004; Hodell et al., 2008; Bailey et al., 2013; Lang et al., 2014). One proxy that has great potential to reveal important new insights into these issues is the Pb isotope composition of oceanic waters recorded in the Fe-Mn oxyhydroxide fraction of marine sediments. Owing to the particle-reactive nature and short seawater residence time of Pb (20-30 years), the Pb isotope compositions of authigenic Fe-Mn oxyhydroxides have been proposed to track regional weathering intensity and solute flux associated with glacial extent on adjacent continental landmasses (e.g., Crocket et al., 2012; Foster and Vance, 2006; Gutjahr et al., 2009; Kurzweil et al., 2010). A short Pb isotope record from Integrated Ocean Drilling Program (IODP) Site U1302/3, recovered from North Atlantic Orphan Knoll proximal to northeast America, is most unradiogenic (so is characterised by its lowest $^{206}Pb/^{204}Pb$, $^{207}Pb/^{204}Pb$ and $^{208}Pb/^{204}Pb$) during the LGM and increases (thus becoming more radiogenic) in response to increased continental chemical weathering of highly reactive glacial debris as the Laurentide Ice Sheet (LIS) retreated in the Hudson Bay region of northeast North America during the last deglacial (Crocket et al., 2012). Yet, this record, and other available North American-proximal Pb isotope Fe-Mn oxyhydroxide datasets (e.g., Gutjahr et al., 2009; Kurzweil et al., 2010) are currently temporally limited to the past ~37 kyr.

To improve our understanding of LIS extent over the past ~130 kyr, we present new authigenic Fe-Mn oxyhydroxide-derived Pb isotope and rare earth element profiles of 87 samples from IODP Site U1302/3 reaching back to MIS 6. We examine the history of change in this new Pb isotope record and discuss the significance of its variability over this time in terms of LIS evolution.

3.3 Background

3.3.1 How are changes in Fe-Mn oxyhydroxide-derived Pb isotope ratios from Site U1302/3 related to changes in ice-sheet extent on North America?

The Pb isotope composition of seawater bathing Orphan Knoll in the geological past was controlled by input from three main sources – the Mid Atlantic Ridge and the adjacent continents through chemical weathering, runoff and dust generation and its subaerial deposition in the Labrador Sea (Frank, 2002; Klemm et al., 2007). Given the high particle reactivity of Pb (Henderson and Maier-Reimer, 2002), an influence from chemical weathering and runoff of continental landmasses further afield than North America and Greenland seems unlikely for this region of the North Atlantic Ocean.

The Pb isotope composition of seawater can be determined by analysing the authigenic fraction of marine sediments. Lead is characterized by four naturally occurring isotopes. Three of these (^{206}Pb, ^{207}Pb, ^{208}Pb) are the radiogenic daughter products of ^{238}U ($_{t1/2}$= 4.47 Ga; ^{206}Pb), ^{235}U ($_{t1/2}$= 704 Ma; ^{207}Pb), or ^{232}Th ($_{t1/2}$= 14.0 Ga; ^{208}Pb) while the other one (^{204}Pb) is a stable isotope of Pb (Steiger and Jaeger, 1977). In our study we focussed on using $^{206}Pb/^{204}Pb$, $^{207}Pb/^{204}Pb$ and $^{208}Pb/^{204}Pb$ ratios to track the Pb isotope composition of seawater bathing our study site. Relatively high ratios are described as being radiogenic, whereas low isotopic ratios are described as unradiogenic. Crocket et al. (2012) proposed that the relatively unradiogenic Pb isotope values bathing U1302/3 during LGM ($^{206}Pb/^{204}Pb \approx 19.2$) predominantly reflect a reduction in North American chemical weathering and runoff under a spatially extensive LIS and a dominance of a dust and Mid-Atlantic Ridge Pb isotope signal. They further argue that the subsequent trend towards more radiogenic values from ~19 ka records increased continental weathering intensity on this landmass as well as increasing runoff during Termination 1 as the LIS retreated under a warming climate. The peak radiogenic values obtained during the early Holocene (~8 ka, $^{206}Pb/^{204}Pb \approx 20.3$) are attributed by these authors to incongruent weathering of highly reactive weakly chemically altered glacial debris exposed following ice-sheet retreat. In this

model, the decay towards unradiogenic values of ~19.6 $^{206}Pb/^{204}Pb$ from ~7 ka is suggested to reflect an increase in weathering, attacking and releasing more of the unradiogenic Pb-hosting minerals, as the exposure age of this glacial debris increased (see also Harlavan et al., 1998; Foster and Vance, 2006). Crocket et al. (2012) argued that incongruent weathering processes must have a major control on the Pb isotopic composition of seawater bathing U1302/3 over the past ~37 ka because the values recorded are much too radiogenic to be controlled by regional variations in the chemical weathering of continental crust. This assertion is based on two observations: (1) the Pb isotope composition of U1302/3 detrital sediments, which may provide a well-mixed measure of the bulk composition of the potential weathering source(s) from the adjacent continents, is much less radiogenic (~16-17 $^{206}Pb/^{204}Pb$) than the seawater signal (~19-21 $^{206}Pb/^{204}Pb$); and (2) a lack of co-variance exists between authigenic and detrital Pb isotope ratios at this site (Crocket et al., 2012).

Blaser et al. (2020) suggest, however, that the Pb isotope composition of detrital sediments at U1302/3 is much less radiogenic than the authigenic record because outside of Heinrich (H) events the authigenic radiogenic Pb signal recorded at Orphan Knoll must be dominated by dissolved and colloidal transport and subsequent scavenging into deep water and not terrigenous inputs. Recent laboratory experiments and observations from an enclosed Alpine lake challenge the notion that incongruent weathering can account for highly radiogenic Pb isotope ratios reported for U1302/3 during Termination 1 (T1) and the early Holocene (see Dausmann et al., 2019; Süfke et al., 2019). It is difficult, however, to assess subpolar conditions using this experiment, given the boundary conditions of climate, topography and bedrock geology differ to that of the Hudson Bay region. Any incongruent weathering signal may take tens of thousands of years to decay (Harlavan et al., 1998, Süfke et al., 2019), which does not match the timescale of change observed during the Holocene at Orphan Knoll (~5 kyr) and elsewhere (e.g., Süfke et al., 2019). Instead, Blaser et al. (2020) argue that changing provenance may be a key factor. In other words, the Pb isotope signal recorded at Orphan Knoll could also be generated by continental runoff transporting a congruent chemical weathering signal to the Labrador Sea and NW Atlantic. Through reference to a compilation of whole-rock Pb isotope data for circum-North Atlantic cratons assembled by Fagel et al. (2002), they suggest that the only regional continental source with Pb isotope

ratios high enough to explain the variability in the U1302/3 Pb isotope record is the Superior Province (SP) of the Canadian Shield (mean $^{206}Pb/^{204}Pb$ = 25.7, median $^{206}Pb/^{204}Pb$ = 22.7; Tab. 1). During the LGM, the SP formed a central part of the foundation of the LIS south and east of Hudson Bay (Figs. 3.1 & 3.2). Today, the dissolved transport products of SP craton continental runoff are routed to the Labrador Sea through the Hudson Bay straits (see hatched area in Fig. 3.1). This source area of Pb would have been significantly diminished, however, when Hudson Straits was cut off from the Labrador Sea by advance of the LIS in northeast North America during the LGM, resulting in relatively unradiogenic seawater Pb isotope ratios at Site U1302/3. In this interpretation, the most radiogenic ratios characteristic of bottom waters bathing U1302/3 during T1 and the early Holocene are attributed to enhanced supply of dissolved and colloidal radiogenic weathered material from the SP craton exposed following LIS retreat (Blaser et al., 2020).

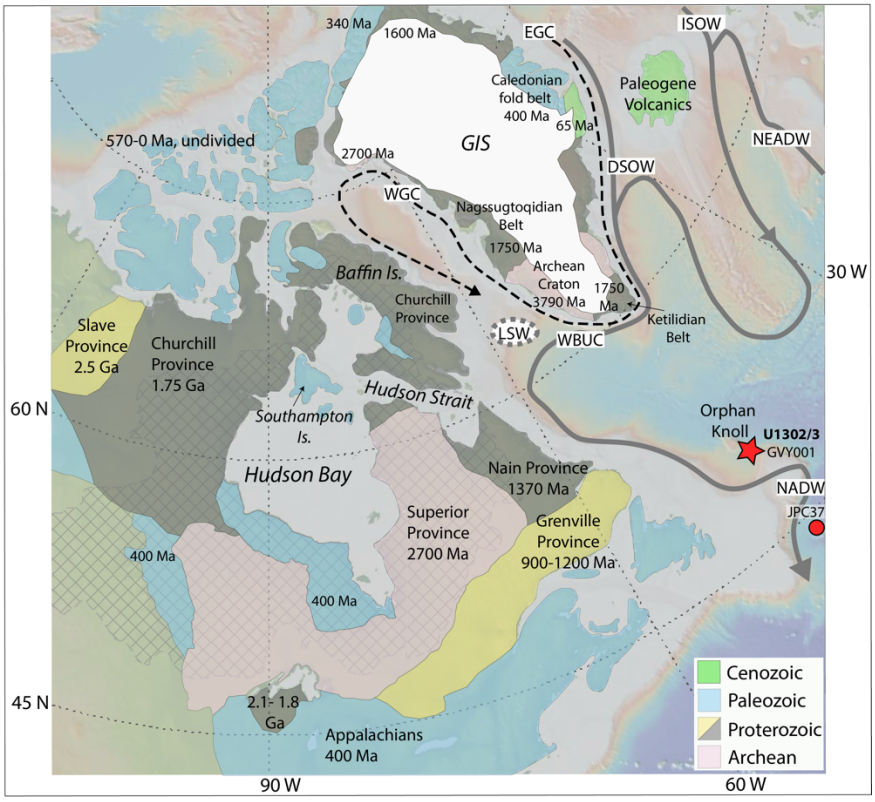

Figure 3.1: Map showing location of IODP Site U1302/3 and other sites discussed in the text, and relevant surrounding cratonic (bedrock) geology. Geology of North America and Greenland redrawn from Reed et al. (2005) and White et al. (2016). Grey hatched region denotes modern area of watershed drainage into Hudson Bay and its straits (Natural Resources Canada, 2006). Arrows denote paths of key modern deep (solid grey) and surface (dashed grey) ocean currents relevant to this study (redrawn from Blake-Mizen et al., 2019). DSOW = Denmark-Scotland Overflow Water. EGC = East Greenland Current GIS = Greenland Ice Sheet ISOW = Iceland-Scotland Overflow Water. LC = Labrador Current. LSW = Labrador Sea Water. NADW = North Atlantic Deep Water. NEADW = Northeast Atlantic Deep Water. WBUC = Western Boundary Undercurrent. WGC = West Greenland Current.

3.3.2 Updating our understanding of the isotope composition of regional sources of Pb runoff to the Labrador Sea

We followed Innocent et al. (1997) and Fagel et al. (1999; 2002; 2004; 2011) in using the mean and median of available whole-rock Pb isotope data to define regional source end-members of Pb runoff from North America and Greenland to the Labrador Sea. We used this approach because we want to compare authigenic Pb isotope data from U1302/3 to estimates of the average weathering signal of regional sources. The mean and median are two ways of estimating this average and the degree of disparity or agreement between them can be used as a first-order estimate of uncertainty in our understanding of each end-member's average Pb isotope composition (Fagel et al., 2002). Our update to the Fagel et al. (2002) whole-rock Pb isotope compilation (Tab. 1) refines, however, our understanding of the potential role that changes in Pb provenance may have played in influencing variability in the Pb isotope composition of Orphan Knoll seawater during the LGC.

The heterogeneous composition of SP geology reflects its origin as an accretionary orogen composed of many geologically distinct continental and oceanic terranes (Percival, 2007; Percival et al., 2012). The highly radiogenic Pb isotope signal for SP bedrock reported by Fagel et al. (2002) is based on whole-rock records from its southeastern Abitibi Subprovince (Gariepy and Allegre, 1985; Vervoot et al., 1993) - a greenstone-granite belt that has an oceanic-arc origin (Thurston et al. 1991) and is rich in gold and massive sulphide deposits (Mathieu et al., 2020). We lack whole-rock Pb isotope records from most subprovinces of the SP. An examination, though, of those that are available for its western and central regions (from the Abitibi, Wawa and Wabigoon subprovinces and Minnesota River Valley terrane) highlights the following: 1) A broad region of the southern SP is on average highly radiogenic ($^{206}Pb/^{204}Pb$ mean = ~22.6; median = ~19.4) in comparison to other North American and Greenland cratonic bedrock, but the SP as a whole is unlikely to be as radiogenic as the Abitibi Greenstone Belt (Fig. 3.2); 2) The average Pb isotope weathering signal of other SP greenstone belts with oceanic-arc affinities (e.g., the western Wabigoon terrane and Wawa Subprovince) may be as radiogenic as the Abitibi (Tab. 3.1).

Table 3.1: Average Pb isotope signature of regional end-members.

Regional source end members	Variable	$^{206}Pb/^{204}Pb$	$^{207}Pb/^{204}Pb$	$^{208}Pb/^{204}Pb$	Data Sources
Superior Province (SP)	No. of data	200			1–9
	Mean	22.7	16.3	42.1	
	Median	19.4	15.8	39.4	
Abitibi Subprovince (SP)	No. of data	55			1–2
(Greenstone Belt)	Mean	25.7	17.0	44.5	
	Median	22.7	16.2	42.8	
Wawa Subprovince (SP)	No. of data	62			3–4
(Greenstone Belt)	Mean	21.1	16.1	40.7	
	Median	17.5		37.5	
Western Wabigoon terrane (SP)	No. of data	25			5–6
(Greenstone Belt)	Mean	29.6	17.6	49.0	
	Median	20.4	15.8	40.4	
Minnesota River Valley terrane (SP)	No. of data	2			9
	Mean	18.5	15.8	42.1	
	Median	18.5	15.8	42.2	
Churchill Province	No. of data	24			4, 10–11
	Mean	16.5	15.3	36.7	
	Median	16.7	15.3	36.3	
Nain Province	No. of data	49			12–14
	Mean	15.1	14.7	35.5	
	Median	14.7	14.6	35.6	
Grenville Province	No. of data	185			14–17
	Mean	17.5	15.5	37.5	
	Median	17.4	15.5	37.2	
Ketilidian Mobile Belt	No. of data	76			18–19
	Mean	20.7	15.6	38.8	
	Median	20.3	15.6	38.0	

Table 3.1 continued

Regional source end members	Variable	$^{206}Pb/^{204}Pb$	$^{207}Pb/^{204}Pb$	$^{208}Pb/^{204}Pb$	Data Sources
Archean Block	No. of data	316			19–24
	Mean	14.5	14.4	35.6	
	Median	14.0	14.4	34.5	
Nagssugtoqidian Mobile Belt	No. of data	223			25–28
	Mean	17.2	15.3	38.2	
	Median	16.6	15.3	37.0	
East Caledonides	No. of data	12			29–32
	Mean	17.5	15.3	38.6	
	Median	18.0	15.4	38.6	
Paleogene Volcanics	No. of data	81			33–38
	Mean	17.7	15.3	37.9	
	Median	18.0	15.4	38.0	
North American aeolian dust	No. of data	52			39–40
	Mean	18.9	15.6	38.9	
	Median	18.9	15.7	39.1	

Here, we follow Innocent et al. (1997) and Fagel et al. (1999; 2002; 2004; 2011) in using the mean and median of whole-rock data to define the Pb isotope composition of regional source end-members (see Fig. 3.2, Appendix A1 & A5-A17). This approach provides us with two estimates of the average weathering Pb isotope signal of each source based on the available whole-rock data. The degree of disparity between the mean and the median can be used as a first-order estimate of uncertainty in our understanding of each end-member's average Pb isotope composition. The true average composition for each source likely falls somewhere between these two parameters. Data sources: (1) Gariepy and Allegre (1985); (2) Vervoort et al. (1993); (3) Smith (1988); (4) Thorpe (2008); (5) Wu et al. (2016); (6) Fowland (1982); (7) Richardson et al. (2005); (8) Stevenson et al. (1999); (9) Doe and Delevaux (1980); (10) Peterson et al. (1994); (11) Thorpe (1982); (12) Baadsgaard et al. (1979); (13) Schiøtte et al. (1993); (14) Ashwal et al. (1986); (15) Scharer (1991); (16) Arcuri and Dickin (2018); (17) Sinha et al. (1996); (18) Kalsbeek and Taylor (1985); (19) Taylor and Upton (1993); (20) Moorbath et al. (1981); (21) Taylor et al. (1992); (22) Taylor et al. (1984); (23) Taylor et al. (1980); (24) Baadsgaard et al. (1986); (25) Kalsbeek et al. (1984); (26) Kalsbeek et al. (1988); (27) Kalsbeek et al. (1987); (28) Kalsbeek et al. (1993); (29) Hansen and Friderichsen (1989); (30) Thrane (2004); (31) Jensen (1994); (32) Ellam and Stuart (2000); (33) Andreasen et al. (2004); (34) Barker et al. (2006); (35) Hansen and Nielsen, (1999); (36) Farmer et al. (2003); (37) Saunders et al. (1999); (38) Holm (1988); (39) Jardine et al. (2021); (40) Aleinikoff et al. (2009).

Based on the available evidence, it therefore seems likely that changes in the provenance of Pb runoff could be responsible for at least a portion of the LGM-Holocene radiogenic trend in the Pb isotopic composition of the authigenic Fe-Mn oxyhydroxide fraction of Orphan Knoll sediments. By the same token, it is not clear, though, whether chemical weathering of the Abitibi Greenstone Belt alone could be solely responsible for the most radiogenic early Holocene Pb isotope values reported by Crocket et al. (2012) for our study site. This is because the drainage basins that sample this region of the SP (and host the Nottaway, Harricana, Moose and Albany rivers of Quebec and Ontario) are responsible for only ~22% of modern annual freshwater river discharge to Hudson Bay (Déry et al., 2011). Yet over 60% of river discharge into Hudson Bay comes from catchment areas that exclusively drain the SP (Déry et al., 2011). It is possible that SP runoff took a different route to the Labrador Sea during the last deglacial. SP runoff into Hudson Bay during T1 would have been restricted by the Hudson Bay Ice Saddle until ~8.4 ka (Dalton et al., 2020). Instead, isostatic rebound of North America during T1 could have altered geomorphologic gradients and re-routed SP runoff more directly eastwards into the Labrador Sea. A better appreciation of the magnitude of the role that changes in Pb provenance plays in setting the Pb isotope composition of bottom-waters bathing Orphan Knoll awaits the generation of whole-rock Pb isotope data from a wider region of the SP than is currently available, especially for its greenstone-granite belts with oceanic affinity and similar ore-deposit compositions to the Abitibi Subprovince. In the meanwhile, we consequently discuss the potential role of both Pb provenance and incongruent chemical weathering in driving any radiogenic trends in our datasets.

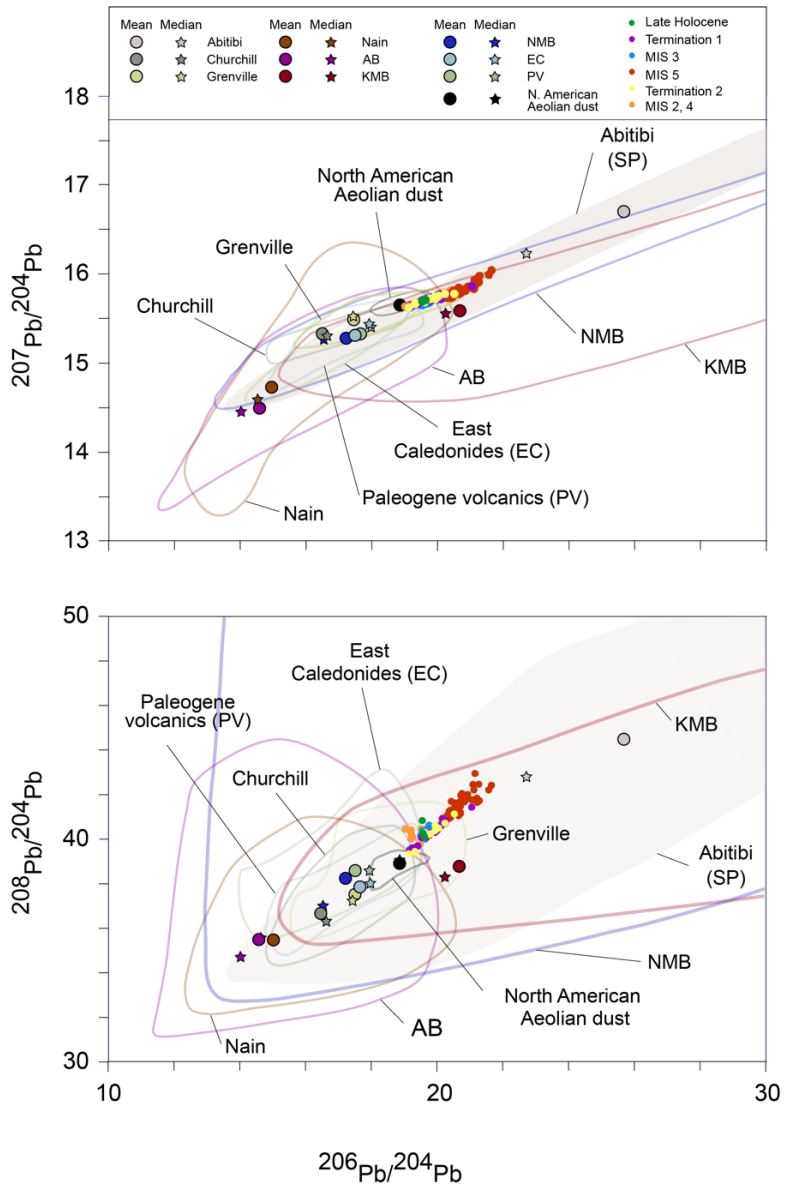

Figure 3.2: The Pb isotope composition of cratonic bedrock adjacent to Orphan Knoll Site U1302/3: **(A)** $^{206}Pb/^{204}Pb$ versus $^{207}Pb/^{204}Pb$ and **(B)** $^{206}Pb/^{204}Pb$ versus $^{207}Pb/^{204}Pb$. Based on a whole rock data compilation by Fagel et al. (2002) supplemented by additional datasets (see Tab. 1, Appendix A1 for data and their sources, A5-A17). The Pb isotopic composition of the authigenic Fe-Mn oxyhydroxide fraction of U1302/3 sediments is also shown for the late Holocene (green circles), Termination 1 (purple circles), MIS 3 (blue circles), MIS 5d-a (red circles), Termination 2 (yellow circles) and MIS 4, 2 (orange circles). See Figure 1 for craton locations. We defined the average weathering Pb isotope signal of each source following Innocent et al. (1997) and Fagel et al. (1999; 2002; 2004; 2011) by using the mean and median of the whole-rock data available for each craton. The degree of disparity between the mean and the median can be used as a first-order estimate of uncertainty in our understanding of each end-member's average Pb isotope composition.

3.3.3 Penultimate Glacial Maximum and Last Glacial Cycle ice sheet reconstructions of the Laurentide Ice Sheet

Global sea-level change is a primary indicator of global ice volume and is reasonably well constrained for the past ~130 kyr by data from fossil corals (e.g., Deschamps et al., 2012; Hibbert et al., 2016), submerged speleothems (e.g., Bard et al., 2002; Dorale et al., 2010; Antonioli et al., 2021), planktic foraminiferal $\delta^{18}O$ (e.g., Grant et al., 2014) and benthic foraminiferal $\delta^{18}O$ (e.g., Elderfield et al., 2012), albeit with well-known caveats (e.g., Skinner and Shackleton, 2005; Lisiecki and Raymo, 2009). The history of the individual continental ice-sheets that determines the changes in global sea-level that these records monitor is, however, much less well constrained.

The LIS was the largest continental ice-sheet in the northern hemisphere at the LGM. Its spatial extent at that time is widely documented by glaciomorphological evidence (e.g., Dyke et al., 2002) and inverse modelling (e.g., Lambeck et al., 2014). Our understanding of the evolution of its spatial extent prior to the LGM is, however, rudimentary (Ehlers et al., 2011). In this study, we focus on reconstructing LIS history prior to the LGM and as far back as MIS 6. Limited terrestrial glaciomorphological evidence exists for LIS extent for this time because any evidence would likely have been destroyed during its Last Glacial advance and what remains is challenging to date. Instead, most inferences of LIS evolution prior to the LGM are based on numerical models, underpinned, where available, by scant empirical data (e.g., Colleoni et al., 2016; Stokes et al., 2012). This combined approach forms the basis of a recent synthesis by Batchelor et al. (2019) that arguably provides our current best constraints on pre-LGM ice sheet configurations in terms of a ‘minimum’, ‘maximum’ and ‘best-estimate’ for LIS extents for all isotope stages. Here we test these estimates for the past ~130 kyr, alongside insights provided by selected subsequently published research (e.g., Dalton et al., 2019; Kerr et al., 2021) using our new Pb isotope data (Figs. 3.3 & 3.4). We focus on reconstructing chemical weathering and runoff flux of North American bedrock adjacent to Hudson Bay because they underly a key sector of the LIS that is home to the biggest ice-stream of the Last Glacial (the Hudson Bay Ice Stream) and freshwater runoff from these landmasses represents the dominant source today of dissolved Pb that is ultimately routed to our study site via the Labrador Current.

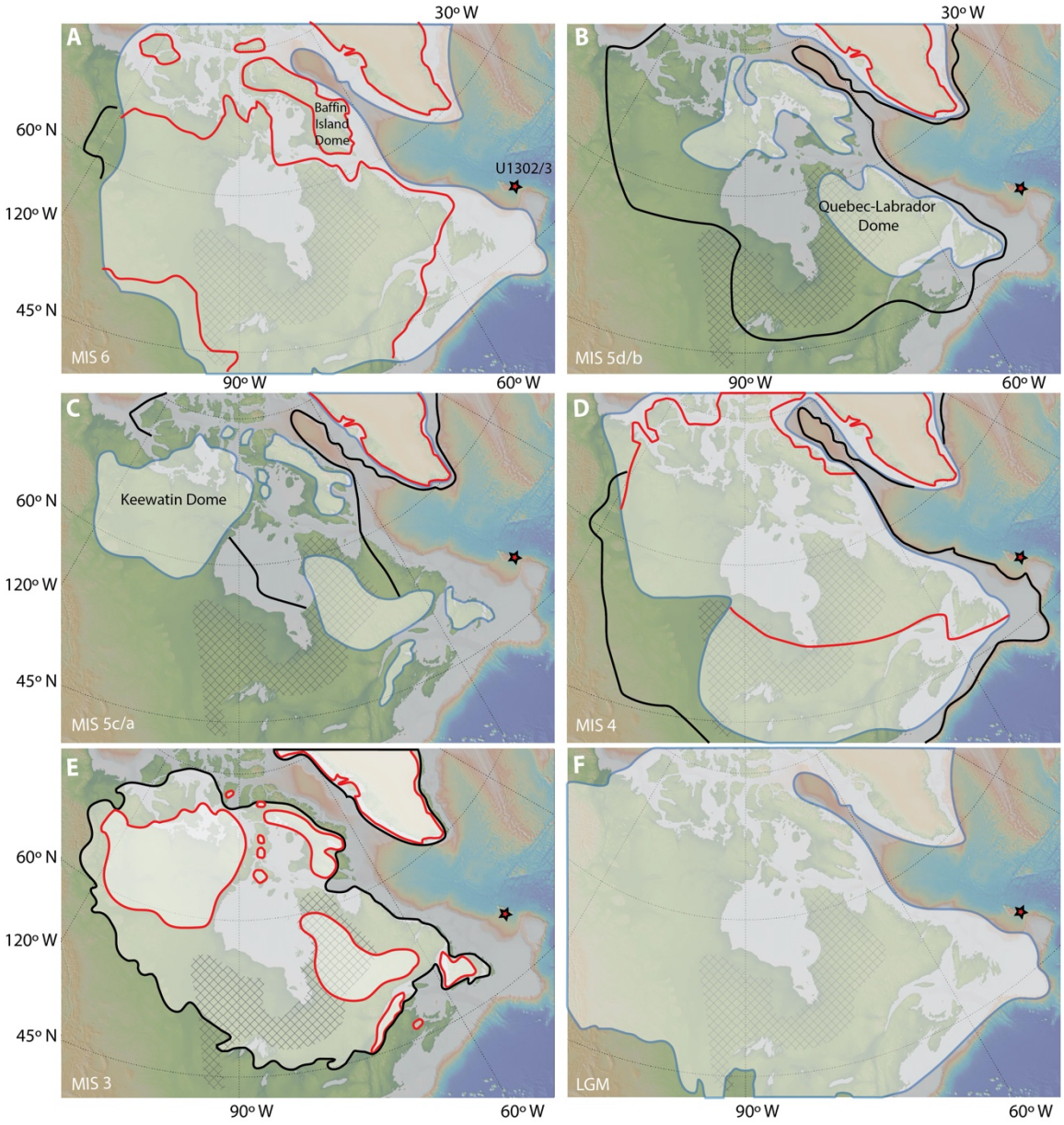

Figure 3.3: Reconstructions of Laurentide Ice Sheet and Greenland Ice Sheet extents following Batchelor et al. (2019). Maximum (black line), minimum (red line) and best-estimate (blue) ice-sheet extents for: **(A)** Marine Isotope Stage (MIS) 6 (132-140 ka); **(B)** MIS 5d/b (108-117; 86-92 ka, respectively); **(C)** MIS 5c/a (92-108; 72-86 ka), **(D)** MIS 4 (58-72 ka); **(E)** MIS 3 (29-57 ka) where minimum estimate is at peak warmth (40-45 ka; red line) and maximum estimate achieved following a period of LIS growth (30 ka; black line); **(F)** Last Glacial Maximum (26-19 ka). Black cross-hatched area denotes geographical extent of Superior Province craton (Montsion et al., 2018). Red stars highlight location of IODP Site U1302/3 on Orphan Knoll.

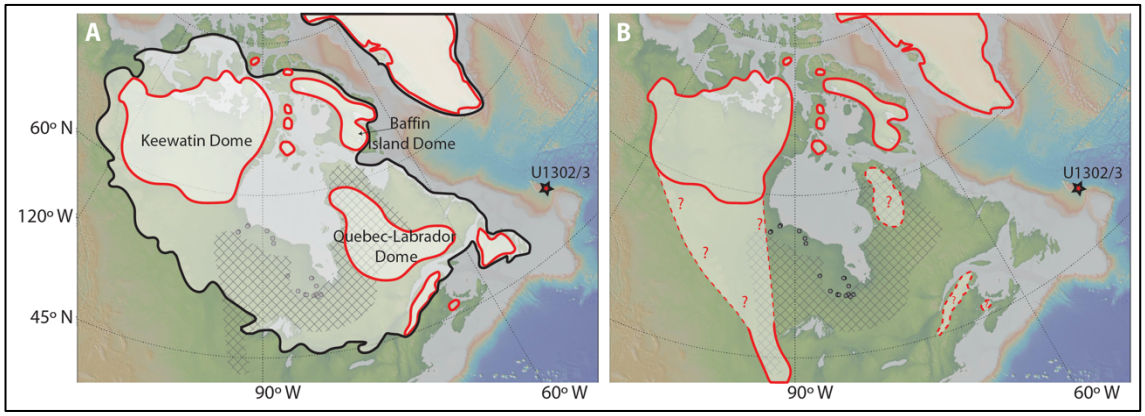

Figure 3.4: Reconstructions of Northern Hemisphere ice-sheet extents for Marine Isotope Stage (MIS) 3 (29-57 ka): **(A)** following Batchelor et al. (2019) where minimum estimate shown in (A) (red line) is at peak warmth (40-45 ka) and maximum estimate shown (black line) is during a subsequent period of LIS growth (30 ka); **(B)** peak warmth (40-45 ka) following Pico et al. (2017), Dalton et al. (2019) and Kerr et al. (2021) where dashed red line is inferred ice extent. Black cross-hatched area denotes geographical extent of Superior Province (Montsion et al., 2018). Grey circles (n = 35) represent locations of ^{14}C and optically stimulated luminescence geochronological dates of marine and fluvial strata from the Hudson Bay Lowlands used by Dalton et al. (2016; 2019) to infer a marine incursion into this area (and its deglaciation) between 52-42 ka.

3.4 Methods

3.4.1 Site description, sampling and age model

IODP Site U1302 (50° 10′N, 45° 38.3′W, water depth: 3560 m) and Site U1303 (50° 12.4′N, 45°41.2′W, water depth: 3520 m) are located on the SE flank of Orphan Knoll within the Labrador Sea, proximal to the coast of Newfoundland (Channell et al., 2006). They are positioned on a rise between two canyons that help to protect these sites from debrite and turbidite deposition by funnelling gravity flows down slope (Aksu and Hiscott, 1992). They are only ~3 nautical miles apart and have remarkably similar sedimentology (Expedition 303 Scientists, 2006). The similarity of strata between the two sites permitted the creation of a continuously spliced composite record using both sites based on correlation of physical property data down to 104 metres composite depth (mcd; Expedition 303 Scientists, 2006).

To extend the previously published record of the Pb isotopic composition of the Fe-Mn oxyhydroxide fraction of sediments deposited at Site U1302/3 spanning the last ~37 kyr (Crocket et al., 2012) back to ~130 ka (MIS 3-6), 5-cc samples were taken every 10-50 cm (83 in total) between 0.45-23.38 mcd. The same samples were also used to determine the elemental concentrations of the seawater derived Fe-Mn oxyhydroxide fraction. A subset of these samples (n =

18) were used to determine the Pb isotope composition and elemental composition of the detrital fraction. A further four samples were taken between 0.45-4.71 mcd to evaluate the reproducibility of our new data with those reported by Crocket et al. (2012). Highly radiogenic Pb isotope excursions in authigenic Fe-Mn oxyhydroxide data derived from detrital carbonate (Heinrich) layers deposited at Site U1302/3 are suggested to represent exceptionally high inputs of detrital particles containing a "pre-formed" coating sourced from Hudson Bay during destabilisation of the LIS (Crocket et al., 2012). Not all past episodes of enhanced detrital inputs to the Labrador Sea are expressed in the Site U1302/3 stratigraphy by clear sedimentological layers. Because we are only interested in the evolution of seawater Pb isotope compositions in the Labrador Sea over the past ~130 kyr, we therefore used the XRF-derived detrital-layer stratigraphy for Site U1302/3 (Channell et al., 2012) to minimise sampling the pre-formed signal of the detrital carbonate layers.

The age model for our record was generated by Channell et al. (2012), based on matching relative paleointensity (RPI) and $\delta^{18}O$ data from *Neogloboquadrina pachyderma* (*sin.*) to the PSIO-1500 RPI stack (Channell et al., 2009) and the LR04 benthic $\delta^{18}O$ stack (Lisiecki and Raymo, 2005). The detrital layer stratigraphy for our study site (Channell et al. 2012) also permits confident correlation of our datasets to those of other North Atlantic marine cores where Heinrich event iceberg rafting events have been identified.

3.4.2 Pb isotope analysis

All sample processing and laboratory analyses were conducted at the School of Ocean and Earth Science, University of Southampton. We extracted Pb from the authigenic Fe-Mn oxyhydroxide fraction in sediments of each sample closely following Blaser et al. (2016). Briefly, between 25-30 mg of dried, homogenised sediment was washed with ultra-pure water (18.2 MΩ) for 20 minutes on a vertical tube rotator, centrifuged at 3200 rpm for 7 minutes and decanted. The samples were then exposed to a leaching solution to extract only the seawater derived Fe-Mn oxyhydroxide fraction of sediment. The leaching solution (hereafter HH-leach) was a mixture of 3 mM Na-EDTA, 5 mM hydroxylamine-hydrochloride, 1.5 % vol/vol acetic acid and buffered to pH 4 using 0.04M NaOH. Following addition of 10 ml HH-leach, samples were resuspended using a vortex mixer, degassed to release any carbon dioxide from carbonate dissolution and placed on a vertical

tube rotator for 20 minutes to ensure all sediment was exposed to the reductive complexing solution. Samples were further centrifuged at 3200 rpm for 7 minutes and the solution pipetted into vials and prepared for analysis.

To ensure 200 ng of Pb was obtained for column chemistry, an aliquot of each leached solution was screened on a Thermo Scientific X-Series 2 ICP-MS. Based on the Pb concentration obtained through the above screening, an aliquot of leached solution was evaporated to dryness in Teflon pots, followed by the addition of 0.5 ml concentrated HNO_3 and left overnight on a hot plate at 130°C to react. The samples were left to evaporate to dryness followed by the addition of 0.5 ml 0.5M HBr and left on a hotplate at 130°C for at least one hour. The Pb fraction was separated from the matrix using Eichrom AG1-X8 200-400 mesh anion exchange resin (Strelow, 1978). The resultant aliquots were screened on a Thermo Scientific X-Series 2 ICP-MS to measure the Pb concentration to allow accurate spiking for isotope analysis.

To confirm that the above procedure was successful at extracting a seawater Pb signal, 30 of the same samples spanning the record were analysed for detrital (residual fraction) Pb isotopes. Samples were exposed to a second HH-leach with 10× solution strength for 24 hours on a vertical tube rotator to ensure complete removal of Fe-Mn oxyhydroxides following Gutjahr et al. (2007). The samples were then centrifuged, decanted, washed in Milli-Q water and decanted again. After drying, 100 mg of homogenised sediment was weighed into Teflon pots and subjected to 3 ml aqua regia overnight to remove organic compounds, evaporated to dryness and redissolved in concentrated HNO_3. The remaining silicates were digested in 2 ml of HF for 48 hours on a hotplate set at 130°C. Finally, $HClO_4$ was added and left overnight at 130°C. Once dried, a few drops of 6M HCl were added for 24 hours at 130°C, dried and repeated. Stock solutions comprised sample, ~10 ml 6M HCl and Milli-Q. These detrital fraction solutions were prepared for column chemistry following the same procedure as outlined above for the Fe-Mn oxyhydroxide fraction solutions.

Pb isotope ratios were measured using a Thermo Neptune MC-ICP-MS. samples were diluted with 3% HNO_3 to obtain ~20 ng/ml of Pb. A double spike run for each sample was used to correct for instrumental mass fractionation where the ^{207}Pb-^{204}Pb SBL74 spike (Taylor et al., 2015) was added such that $^{204}Pb_{sample}/^{204}Pb_{spike}$ was 0.09 ± 0.03. Procedural blanks for Fe-Mn oxyhydroxide and detrital fraction

samples averaged 0.028 ng (n = 14) and 0.001 ng Pb (n = 1), respectively with samples being blank-corrected. Blanks were treated in the same way as sediment samples to determine possible contamination from reagents and general handling. Authigenic Pb concentrations range from ~36-198 ng. Reproducibility of Pb isotope ratios was estimated based on 17 measurements of the standard SRM NBS 981 run from 2018-2020. This analytical period yielded average ratios and uncertainties at 2σ (relative to the values of Baker et al. (2004) as shown in parentheses): $^{206}Pb/^{204}Pb$ = 16.9424 ± 0.00044 (16.942 ± 0.00006), $^{207}Pb/^{204}Pb$ = 15.4982 ± 0.00097 (15.501 ± 0.00006) and $^{208}Pb/^{204}Pb$ =36.7182 ± 0.00276 (36.730 ± 0.00019). To monitor reproducibility of Pb isotope ratios further, an internal replicate was measured in every run (n = 5), producing average ratios of $^{206}Pb/^{204}Pb$ = 19.1946 ±0.000416 (2σ; range = 0.0057 ± 0.0008), $^{207}Pb/^{204}Pb$ = 15.6341 ±0.000859 (2σ; range = 0.0042 ±0.0001) and $^{208}Pb/^{204}Pb$ =3.5237 ±0.00205 (2σ; range = 0.000071 ±0.0008).

3.4.3 Rare and trace elements analysis

Trace element concentrations of the Fe-Mn oxyhydroxide fraction stock solutions were also used to evaluate the fidelity of our seawater Pb isotope data. To generate these data, 100 μl aliquots of the above mentioned stock solutions were dried in Teflon pots, then concentrated HNO_3 was added to remove HH-leach chemicals. The samples were dried and dissolved in 3% HNO_3 spiked with In (5 ppb), Re (5 ppb) and Be (20 ppb) to achieve a 100× dilution. Analyses were conducted on the Thermo Scientific X-Series 2 ICP-MS. Measurements were calibrated using a suite of international rock standards; JB-1a, JGB-1, BIR-1, BHVO-2, JB-3, JB-2, BCR-2, AGV-2 that were diluted with 3% HNO_3 spiked with In (5 ppb), Re (5 ppb) and Be (20 ppb) to achieve an ~4000× dilution for the trace elements. An additional set of standards were run with ~80000× dilution for Al and Fe. In-house reference materials BAS206 and BRR-1 and international reference material JA-2 were also run after the standards. Long term precision of JA-2 relative to the reference value (Jochum et al., 2016) is better than 5% except for Cu and Pb which are 6% and 7%, respectively.

Rare earth element (REE) concentrations of the samples were expressed relative to the REE profile of the Post-Archean Australian Shale (PAAS), which is a good approximation of the upper continental crust (Taylor and McLennan, 1985). To characterise REE patterns, ratios of PAAS-normalised concentrations were used

following Martin et al. (2010) and Blaser et al. (2016; 2019) and shown in equations 1–6:

Light REE: $LREE = La_n + Pr_n + Nd_n$ Eq. 1

Heavy REE: $HREE = Er_n + Yb_n + Lu_n$ Eq. 2

Middle REE: $MREE = Gd_n + Tb_n + Dy_n$ Eq. 3

REE slope: $HREE/LREE$ Eq. 4

REE bulge: $MREE/MREE* =$ Eq. 5

$$MREE/0.5(HREE + LREE)$$

where: $REE_n = REE_{sample}/REE_{PAAS}$ Eq. 6

3.5 Results and Discussion

3.5.1 New LGC Pb isotope data from Site U1302/3

In Figure 3.5 we integrate our new and published data to present the first high resolution LGC records of authigenic Fe-Mn oxyhydroxide-derived Pb isotopes from the subpolar North Atlantic that spans both the last (Termination 1) and penultimate (Termination 2) deglaciations. Comparable values, where overlap exists (for the LGM-Holocene), between our new data from Orphan Knoll Site U1302/3 and those previously published by Crocket et al. (2012) for this site, confirm the validity of splicing these two records together (Full dataset in Appendix A2).

The new longer record from Site U1302/3 confirms the suggestion of Crocket et al. (2012) that the U1302/3 authigenic signal of sediments deposited at our study site is characterised by short-lived highly radiogenic excursions during the deposition of Heinrich (H)-like layers in the Labrador Sea (see Pb data within green and light yellow vertical bars in Fig. 5c-e). However, on orbital timescales, Pb isotope ratios typically vary between ~19-21.5 ($^{206}Pb/^{204}Pb$), ~15.6-16 ($^{207}Pb/^{204}Pb$) and ~40.5-42 ($^{208}Pb/^{204}Pb$) with relatively radiogenic values occurring during warm stages MIS 5, 3 and 1, and the most unradiogenic values occurring during cold stages MIS 4 and 2 (Fig. 3.5c-e). While only the oldest datapoints in our Pb isotope records captures MIS 6, they hint that the Pb isotope composition of seawater bathing U1302/3 during this time were likely just as unradiogenic as during MIS 4 and 2 (Fig. 3.5c-e). The magnitude of change in Pb isotope ratios across Termination (T) 2 is comparable to its evolution across T1 (compare Pb isotope zones β & γ to θ & ι in Fig. 3.5c-e), but this pattern of change occurs more rapidly across T2 (~8 kyr) vs. T1 (~17 kyr). Strikingly, from MIS 5d to 5a, all Pb isotope ratios become progressively more radiogenic (from ~19.5-21.7 for $^{206}Pb/^{204}Pb$; ~15.7-16.0 for $^{207}Pb/^{204}Pb$; ~40.1-42.4 for $^{208}Pb/^{204}Pb$; Pb isotope zone δ in Fig. 3.5c-e; also see Fig. A3). LGM-like values are first recorded during the LGC in MIS 4 (Pb isotope zone ε in Fig. 3.5c-e) but return to ratios closest to late Holocene compositions (~19.6 $^{206}Pb/^{204}Pb$; ~15.7 $^{207}Pb/^{204}Pb$; ~40.0 $^{208}Pb/^{204}Pb$) during MIS 3 (Pb isotope zone ζ in Fig. 3.5c-e). By contrast, the detrital fraction Pb isotope record shows different absolute ratios (e.g., ~16-18 for $^{206}Pb/^{204}Pb$) and contrasting temporal trends to that recorded by the authigenic records (compare Fig. 3.5c-e to 3.5f-h; also see Appendix Fig. A4).

3.5.2 Fidelity of the authigenic Fe-Mn signal from Site U1302/3 as a record of Labrador Sea seawater Pb isotope composition

To assess the integrity of the seawater Pb isotope record extracted from the authigenic Fe-Mn oxyhydroxide sediment fraction, we employ a series of tests to check for the possible release of non-seawater-derived Pb from the detrital sediment fraction: (1) examination of detrital and authigenic Pb isotope trends for evidence of covariance, (2) evaluation of REE data to identify what material was leached (Haley et al., 2004; Martin et al., 2010) and, (3) comparison of Al/Nd, Al/Th and Al/Pb ratios of the authigenic and detrital fractions of our samples and abyssal ocean Fe-Mn crusts (Gutjahr et al., 2007).

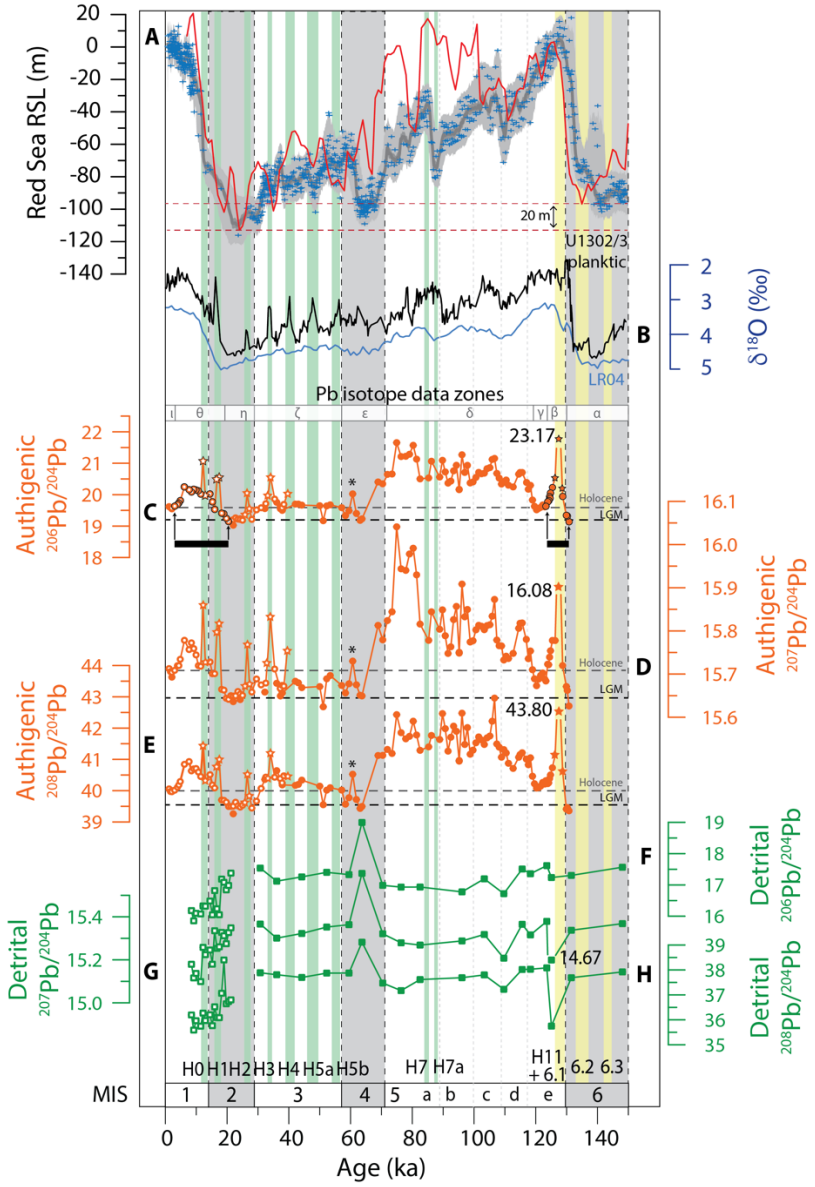

Figure 3.5: Pb isotope and $\delta^{18}O$ records from IODP Site U1302/3 spanning Marine Isotope Stage (MIS) 6-1: **(A)** Red Sea relative sea-level (RSL) record with data points (blue crosses), 95% probability interval for RSL data (dark grey envelope) and 95% probability interval for probability maximum (light grey envelope; Grant et al., 2012). Also shown is a benthic foraminiferal-derived RSL record from Ocean Drilling Program Site 1123 (red line; Elderfield et al. (2012); **(B)** U1302/3 planktic $\delta^{18}O$ (black line; Hillaire-Marcel et al., 2011) and the LR04 benthic $\delta^{18}O$ stack (blue line; Lisiecki & Raymo, 2005); Pb isotope ratios of authigenic Fe-Mn oxyhydroxides: **(C)** $^{206}Pb/^{204}Pb$; **(D)** $^{207}Pb/^{204}Pb$; **(E)** $^{208}Pb/^{204}Pb$; Pb isotope ratios of detrital sediment fraction: **(F)** $^{206}Pb/^{204}Pb$; **(G)** $^{207}Pb/^{204}Pb$; **(H)** $^{208}Pb/^{204}Pb$ ratios of Site U1302/3. "Detrital" refers to the full digestion of the authigenic-free fraction of marine sediment. Solid circles/stars = this study; open circle/stars = Crocket et al. (2012). MIS cold(warm) stages are shown by vertical light grey(white) bars. Heinrich (detrital) layers preserved in both the Labrador Sea (identified using scanning-derived XRF Ca/Sr ratios by Channell et al. (2012)) and subpolar North Atlantic sediments (Hemming, 2004; Hodell et al., 2008) are shown by labelled vertical light green bars. Vertical light-yellow bars highlight Heinrich-like detrital layers where deposition was restricted to the Labrador Sea (Channell et al., 2012; Hodell et al., 2008). Star-shaped symbols denote Pb isotope data from U1302/3 detrital layers. Horizontal dashed lines in (c) (d) and (e) highlight Pb isotopes values at U1302/3 during the late Holocene and Last Glacial Maximum. Horizontal black bars and arrows in (c) highlight intervals over which we infer enhanced supply of dissolved radiogenic weathered material from the Superior Province craton following Laurentide Ice Sheet retreat in the Hudson Bay region during Terminations 2 and 1 (data symbols in C-E with black outlines). Greek symbols α-ι labelled in (c) correspond to Pb isotope data zones referred to in main text. See Figure 1 for site locations.

The absence of any significant covariance between trends in the authigenic and detrital Pb isotope records (compare panels c-e to f-h in Fig. 3.5; Fig. A4) strongly suggests that detrital sediment leaching during sample processing does not control temporal variability in our leachate record. This is confirmed by the presence of a distinct PAAS-normalised mid-REE (MREE) enrichment in our leachate samples that is not characteristic of the distribution of REE in our detrital samples (Fig. 3.6; Piper, 1974). This MREE enrichment is somewhat different from water column REE concentration patterns (e.g., Patton et al., 2021) and considered characteristic of marine pore waters because particulate Fe^{3+} oxides are reduced and dissolved in pore waters to release REE scavenged in the water column (Haley et al., 2004). It has been shown that the REE signature of HH-extracted leachate seawater signals plots separately from that of the residual detrital fraction in cross plots of the REE slope (HREE/LREE) and MREE bulge (MREE/MREE*) (Haley et al., 2004; Martin et al., 2010). Most of the samples analysed in this study plot in this region (Fig. 3.7). Yet some of our MIS 5 authigenic data (n = 18 out of 83) encroach on the detrital field (red and yellow triangles in Fig. 3.7a-b), consistent with incomplete removal of oxides, partial leaching of the detrital component during sediment processing (Martin et al., 2010) or potentially by pore waters in the sediment pile (i.e., in situ chemical weathering at the seafloor after deposition; Blaser et al., 2020). The presence of positive Ce anomalies in some MIS 5 authigenic data may record contributions of detritally-sourced Ce to the leachate signal (Fig. 3.6). It may also reflect highly elevated early-deglacial trace-metal input into the Labrador Sea due to generally highly elevated chemical weathering rates following the PGM (compare with Vance et al., 2009).

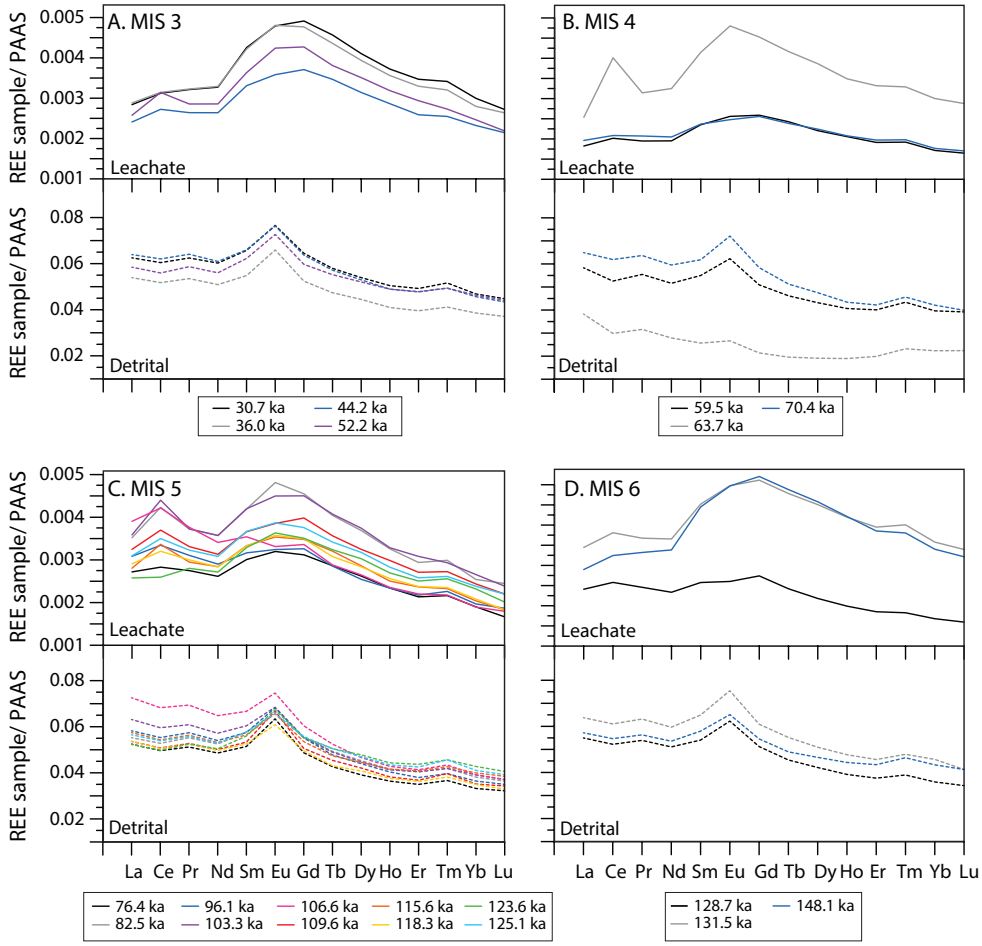

Figure 3.6: Post-Archean Australian Shale (PAAS) normalised rare earth element (REE) multi-element plots for paired authigenic Fe-Mn oxyhydroxide (solid lines) and detrital (dotted lines) samples deposited at IODP Site U1302/03 during **(A)** marine isotope stage (MIS) 3, **(B)** MIS 4, **(C)** MIS 5 and **(D)** MIS 6.

These MIS 5 data are characterised by some of the most radiogenic Pb isotope values in our records (of ~21.5 $^{206}Pb/^{204}Pb$; Fig. 3.5c-e). The general absence of detrital H-layer deposition at U1302/3 during this interval (green/light yellow bars in Fig. 3.5) rules out leaching of preformed radiogenic coatings from sediments sourced from Hudson Bay for the origin of this signal (Crocket et al., 2012). We cannot rule out the possibility that the detrital fraction itself was partially leached during the processing of our MIS 5 samples but consider it unlikely (see below). The relatively low MREE/MREE* ratios for many of these samples also suggest in-situ chemical weathering of sediments (i.e., they encroach on the detrital field; see red and yellow triangles in Figs. 3.7a-b & 3.8b). Blaser et al. (2020) observed that the Nd isotope composition of the authigenic fraction of U1302/3 sediments can be modified by sediment leaching in pore waters at times of enhanced supply of glacially-eroded materials from Hudson Bay to the Labrador Sea. While sand-sized IRD deposition on Orphan Knoll is negligible during MIS 5 (Fig. 3.8d-e),

XRF-scanning-derived Ca/Sr-ratios, indicative of Hudson Bay sourced-mud, are regularly high throughout MIS 5 (Fig. 3.8a). While we cannot rule out that in-situ weathering of seafloor sediments occurred at our study site during this time, we contend that the $^{206}Pb/^{204}Pb$ values of ~20.5-21.5 that characterise MIS 5d-a must reflect that the Pb isotope composition of seawater bathing our study site during this time was unusually radiogenic in the context of the past ~130 kyr. This is because the Pb isotope composition of the detrital fraction deposited at U1302/3 during MIS 5 is much more unradiogenic than the authigenic signal (by ~3-4 units), so its partial leaching through in-situ weathering would make seawater and authigenic Pb isotope compositions more unradiogenic. In-situ weathering would therefore act to mask a radiogenic seawater signal, not artificially imprint one. Given that Pb is much more particle-reactive than most REE, we also note that partial release of terrigenous REE during in-situ weathering at the seafloor does not necessarily result in the release of comparable quantities of Pb (Henderson and Maier-Reimer, 2002).

The IRD records from Orphan Knoll leave open the possibility that the onset of LGM-like unradiogenic authigenic Pb isotope ratios in our new data during MIS 4 was influenced by in-situ pore-water leaching of old (unradiogenic) cratonic materials delivered to our study site via iceberg rafting (Fig. 3.8d-e). While we cannot rule out that in-situ chemical weathering of IRD influenced the Pb isotope composition of seawater bathing our study site to some extent during the Last Glacial, we consider it unlikely that it is responsible for the major trends in our records, as the IRD and Pb isotope records do not co-vary. The highest deposition rates (and sediment concentrations) of IRD on Orphan Knoll occurred during MIS 2 (Fig. 3.8d-e; Zhou et al., 2021), meaning that if in-situ chemical weathering of IRD controlled the trends in our authigenic Pb isotope records the values we observe for MIS 4 should be more radiogenic than those reported for the LGM, but they are not (Fig. 3.8c). In any case, the Al/Nd, Al/Th and Al/Pb ratios of the authigenic fraction for all our samples are significantly lower than the Al/Nd, Al/Th and Al/Pb ratios of their detrital counterparts and are closest to those of deep ocean Fe-Mn crusts that represent a pristine seawater signal (Fig. 3.9). We therefore conclude that the major trends in U1302/3 authigenic Pb isotope

data are not dominated by release of Pb from sediments deposited in the Labrador Sea during the LGC.

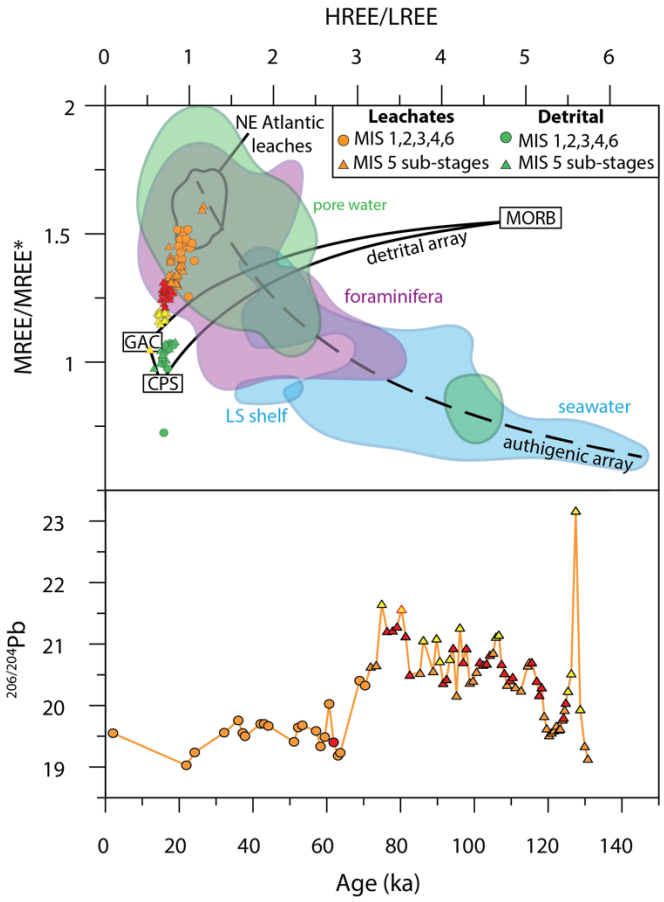

Figure 3.7: Comparison of PAAS normalised rare earth element (REE) slope (HREE/LREE) and mid-REE bulge (MREE/MREE*) of detrital sediment samples and their authigenic Fe-Mn oxyhydroxides coatings deposited at IODP Site U1302/3 during marine isotope stages (MIS) 6-1 (145-0 ka). Corresponding $^{206}Pb/^{204}Pb$ ratios are shown in the bottom panel. Seawater, pore fluids, foraminifera and authigenic phase fields shown are from Blaser et al. (2020): defined using foraminiferal REE data from core top to Last Glacial Caribbean, Northwest Atlantic and Equatorial Pacific sediments (purple, Osborne et al., 2017), seawater data from the eastern subpolar North Atlantic (Crocket et al., 2018), equatorial Atlantic (Zheng et al., 2016), and the Atlantic sector of the Southern Ocean (Hathorne et al., 2015), all blue), and pore water data of three sites from the Oregon margin (green, Abbott et al., 2015). Northeast Atlantic leaches comprise Holocene and LGM data from Blaser et al. (2019), generated with the same leach method used in this study. The curved dashed line defines a potential "authigenic array" following Du et al. (2016). It is defined by mixing of the most HREE enriched seawater included with the most MREE enriched diagenetic ferro-manganese Nodule reported by Bau et al. (2014) from Pacific Ocean Clarion-Clipperton Fracture Zone. The solid black curved lines define a detrital mixing array between Mid Ocean Ridge Basalts (MORB; Gale et al., 2013), Greenland Archaean Crust (GAC; Wedepohl et al., 1991), and Canadian Precambrian shield cratonic rocks (CPS; Shaw et al., 1986).

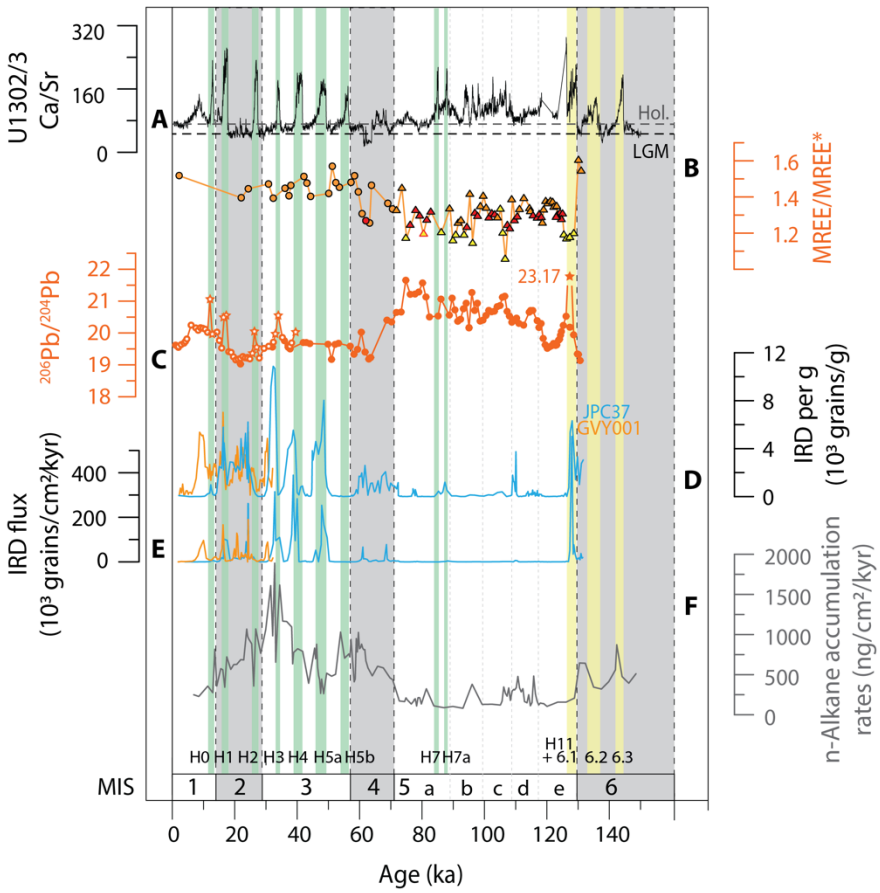

Figure 3.8: Palaeoclimate records spanning marine isotope stages (MIS) 6-1: **(A)** Orphan Knoll IODP Site U1302/03 XRF scanning Ca/Sr ratios (counts/counts; Channell et al., 2012) with late Holocene and LGM values highlighted by horizontal dashed lines; **(B)** MREE/MREE* elemental ratios of authigenic Fe-Mn oxyhydroxides fractions of Site U1302/3 sediments. Data symbols correspond to symbols plotted in Fig. 8; **(C)** Site U1302/3 authigenic Fe-Mn oxyhydroxides $^{206}Pb/^{204}Pb$ isotope ratios; **(D)** IRD concentrations (Zhou et al., 2021) and **(E)** IRD flux (Zhou et al., 2021) for Orphan Knoll sediment cores JPC37 (blue) and GVY001 (orange). **(F)** North American-sourced aeolian dust deposition at IODP Site U1313 (~40˚N) as tracked by n-alkane accumulation rates, the organic fraction of dust (Naafs et al., 2012). Trends in both $^{206}Pb/^{204}Pb$ and $^{208}Pb/^{204}Pb$ are consistent with the Pb isotopic composition of North American aeolian dust. Solid circles/stars = this study; open circles/stars = Crocket et al. (2012). MIS cold(warm) stages highlighted by vertical light grey(white) bars. Heinrich (detrital) layers preserved in both the Labrador Sea (identified using core-scanning-derived XRF Ca/Sr ratios by Channell et al. (2012) and subpolar North Atlantic sediments (Hemming, 2004; Hodell et al., 2008) are shown by labelled vertical light green bars. Labelled vertical light-yellow bars highlight Heinrich-like detrital layers where deposition was restricted to the Labrador Sea (Channell et al., 2012; Hodell et al., 2008). Star-shaped symbols denote Pb isotope data from U1302/3 Heinrich layers. See Figure 1 for site locations.

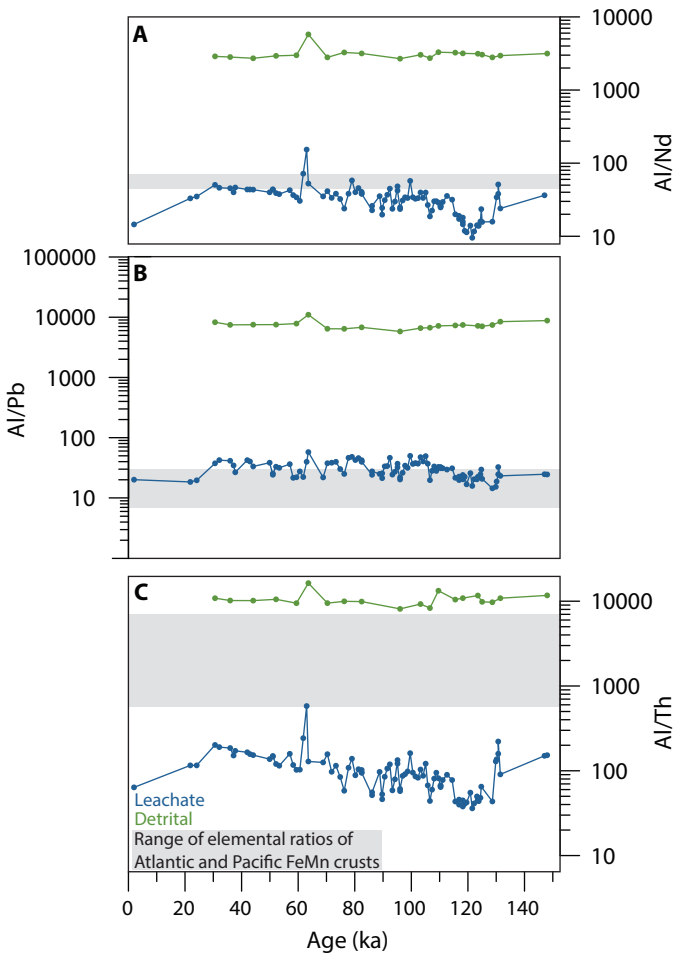

Figure 3.9: Elemental ratios of: **(A)** Al/Nd, **(B)** Al/Pb and (**C)** Al/Th of leachate (blue) and detrital sediment (green) fractions from IODP Site U1302/03. Note the log scale of y-axis. Grey boxes define the range of elemental ratios associated with Atlantic and Pacific Fe-Mn crusts (Hein et al., 1999).

3.5.3 What does the evolution of authigenic Pb isotopes at U1302/3 reveal about Laurentide Ice Sheet extent over the past ~130 kyr?

Both an increase in (i) physicochemical weathering intensity, (ii) incongruent weathering of highly reactive weakly-chemically altered glacial debris on North America (Crocket et al., 2012) and (iii) enhanced sourcing of weakly-weathered SP radiogenic material (Blaser et al., 2020) have been proposed to explain how the Pb isotope composition of bottom waters bathing U1302/3 can become more radiogenic following LIS retreat. Regardless of which of these mechanisms prevail, our new Pb isotope records from U1302/3 provide a way to shed new light on the evolution of the spatial extent of the LIS back to T2.

3.5.3.1 MIS 6 and Termination 2 LIS history

The Batchelor et al. (2019) reconstruction for MIS 6 suggests Hudson Bay was glaciated throughout the PGM, but no accurately dated empirical data exist that can be used to ground-truth this suggestion. While only the oldest datapoints in our Pb isotope records capture MIS 6 according to our RPI-based age model, they hint that the Pb isotope composition of seawater bathing U1302/3 just prior to T2 were just as unradiogenic as during the LGM at this site (compare Pb isotope zones α & η in Fig. 3.5c-e; Fig, 3.10). Our new data therefore suggest that the spatial foot-print of the LIS in Hudson Bay and the degree to which it suppressed the delivery of weathered Pb from interior of North America to Site U1302/3, at least immediately prior to the end of the PGM, were comparable to that of its LGM counterpart.

The radiogenic peak in the U1302/3 record during the last deglaciation is argued either to reflect incongruent weathering of highly reactive weakly-chemically altered glacial debris exposed following ice-sheet retreat (Crocket et al., 2012) or enhanced sourcing of weakly-weathered SP radiogenic material exposed following LIS retreat (Blaser et al., 2020). The overprint of H-layer deposition during Termination 2 (the 'so-called' H11) in our Pb isotope data partially masks the equivalent weathering and runoff signal for the MIS 6/5e transition (Pb isotope zone β in Fig. 3.5c-e; Fig. 3.10). There is, however, no evidence in our records that the radiogenic supply of Pb from the interior of North America survived younger than ~122 ka. This is because the Pb isotope values in all our authigenic records return to compositions observed during the late Holocene by this time (as recorded at the transition between Pb isotope zones β and γ in Fig. 3.5c). The restriction of H-layer deposition to the Labrador Sea during MIS 6 (Naafs et al., 2013a, b; Obrochta et al., 2014) points towards large differences in ice-mass distribution and ice-stream dynamics between the PGM and LGM LIS in the Hudson Bay area. The absence of detrital limestone-bearing H-layers in the central subpolar North Atlantic during MIS 6 has been attributed to a relatively thin (and therefore less voluminous) LIS that was cold-based and unable to generate H-events through surging of its Hudson Bay ice-stream (Obrochta et al., 2014). In this scenario, physical erosion of the SP terrane would have been reduced during the PGM relative to the LGM, leaving behind less weakly weathered radiogenic material that could be easily chemically weathered

following LIS retreat during T2. This may therefore explain the shorter time over which radiogenic values are a feature of our record during the MIS 6/5 transition (over no more than ~8 kyr) compared to the last deglaciation (~17 kyr) (compare width of horizontal black bars in Fig. 3.5c; Fig. 3.10).

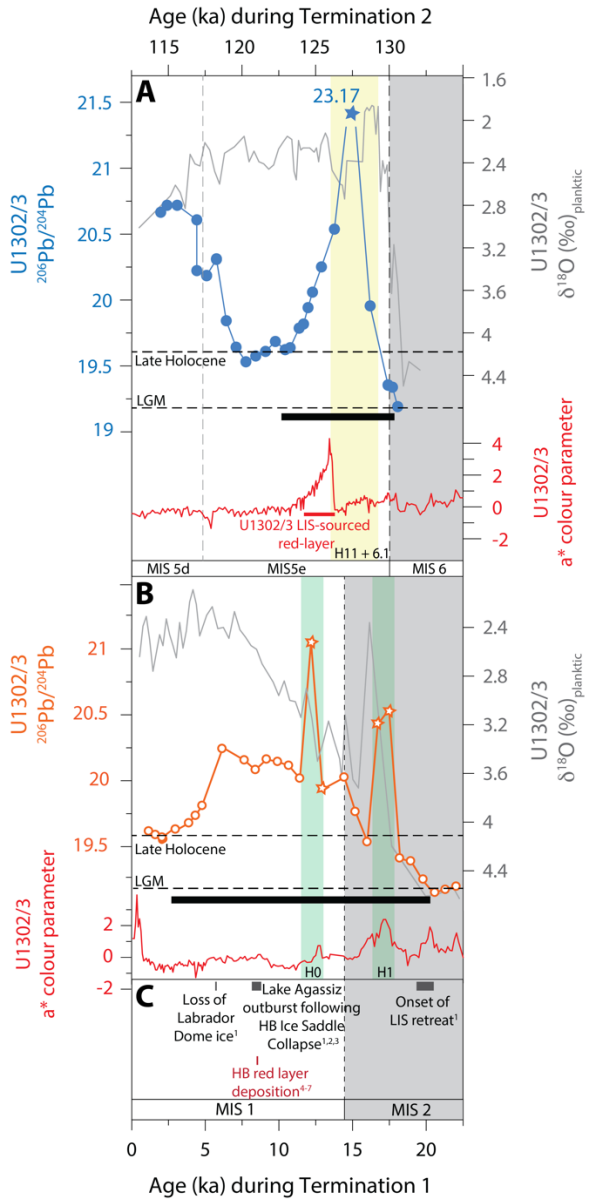

Figure 3.10: The evolution of the Pb isotope composition of authigenic Fe-Mn oxyhydroxides from IODP Site U1302/3 during **(A)** Termination 2 and **(B)** Termination 1. **(C)** Laurentide Ice Sheet dynamics. Horizontal black bars highlight the duration of enhanced supply of dissolved radiogenic weathered material from the Superior Province craton exposed following Laurentide Ice Sheet following the onset of each termination. Dark grey horizontal bars highlight major evolution of the Laurentide Ice Sheet, where 1= Dalton et al., 2020, 2 = Brouard et al., 2021, 3=Margold et al., 2018, 8= Dyke et al., 2002. Red layer depicted by red horizontal bar; 4= Barber et al., 1999, 5= Lajeunesse and St-Onge, 2008, 6= Jennings et al., 2015, 7= Lochte et al., 2019. Solid circles/stars = this study; open circle/stars = Crocket et al. (2012). MIS cold(warm) stages are shown by vertical light grey(white) bars. Heinrich (detrital) layers preserved in both the Labrador Sea (identified using U1302/3 core-scanning-derived XRF Ca/Sr ratios by Channell et al. (2012) and subpolar North Atlantic sediments (Hemming, 2004; Hodell et al., 2008) are shown by labelled vertical light green bars. Labelled vertical light-yellow bars highlight Heinrich-like detrital layers where deposition was restricted to the Labrador Sea (Channell et al., 2012; Hodell et al., 2008). Horizontal dashed lines in (a) and (b) highlight Pb isotopes values.

The relatively short time over which radiogenic values are a feature of authigenic Pb isotope records during T2 and T1 supports the idea that incongruent weathering did not play a leading role in changes in the Pb isotope composition of seawater bathing Orphan Knoll during LIS retreat. This is because it has been shown that any incongruent weathering signal should take tens of thousands of years to decay due to the half-life of ^{238}U, ^{235}U and ^{232}Th (Harlavan et al., 1998, Süfke et al., 2019), not ~3-5 kyr as we observe at U1302/3 (Fig. 3.5c-e). Leaching experiments on granitic rock from the Swiss Alps show that increases in the $^{208}Pb/^{204}Pb$ ratios of the solute products of incongruent weathering should also lag those in $^{207}Pb/^{204}Pb$ because the main source of radiogenic ^{208}Pb (Th-bearing minerals) is more resistant to dissolution than (U-bearing) mineral sources of ^{206}Pb and ^{207}Pb (Dausmann et al., 2019; Süfke et al., 2019). Yet, all three authigenic Pb isotope ratios from U1302/3 increase at the same time during both T2 and T1 (Fig 3.5c-e).

Independent reconstructions of LIS extent since the LGM highlight that while it began to retreat from ~20 ka (and seemingly first in Long Island Sound, Connecticut), a significant proportion of the SP was likely to have remained glaciated during T1 until ~12 ka (e.g., Dalton et al., 2020). If enhanced chemical weathering of SP craton was responsible for the radiogenic trends in U1302/3 authigenic Pb isotope data during T2 and T1, we might therefore expect these data to record only the more advanced stages of LIS retreat. Yet during T1, authigenic Pb isotope values at U1302/3 first began to increase ~20 ka (Fig. 3.5c-e). This disparity may highlight an important role for incongruent weathering in driving changes in the Pb isotope composition of bottom-waters bathing Orphan Knoll during the early stages of LIS retreat. Alternatively, the onset of radiogenic values at U1302/3 from ~20 ka and at ~130 ka during T2 may reflect an increase in microorganism-mediated chemical weathering of the SP beneath the LIS (cf. Wadnam et al., 2010) and its runoff as it shifted from a cold-based to warm-based ice sheet (cf. Gutjahr et al., 2014). We therefore infer that if there is an incongruent weathering influence on the Pb isotope composition of seawater bathing Orphan Knoll during LIS deglaciation, its role may have been subordinate to that of changes in Pb provenance.

The T2 radiogenic spikes in our authigenic Pb isotope records correlate with the deposition at our study site of a red detrital layer sourced from Hudson Bay during

a glacial outburst flood (Nicholl et al., 2012). This layer is argued to be the product of extensive deglaciation of the Hudson Bay region (Nicholl et al., 2012). We further note that the peak of radiogenic Pb supply to U1302/3 during the early Holocene is also broadly coincident with final outburst of glacial Lake Agassiz-Ojibway south of Hudson Bay that most recent estimates suggest to have occurred between ~8.7 (Dalton et al., 2020) and 8.15 ka (Brouard et al., 2021). While these radiogenic spikes in Pb runoff to our study site cannot provide us with a precise understanding of the regional history of LIS retreat during T1 and T2, their respective durations may actually therefore provide us with a stratigraphic marker for the timing of collapse of the Hudson Bay Ice Saddle (or at least a likely latest possible date for it), which is argued to have occurred faster following the PGM than it did following the LGM, and in response to greater boreal summer insolation forcing (Carlson, 2008).

3.5.3.2 MIS 5 LIS history

The sudden return to elevated radiogenic Pb isotope values between ~115-75 ka during MIS 5d-a following the start of the LGC is arguably the most notable feature of our new datasets (Pb isotope zone δ in Fig. 3.5c-e). If a change in Pb provenance is involved, it cannot be attributed to, e.g., an increase in chemical weathering of exposed Greenland bedrock (e.g., the Ketilidian Mobile Belt) due to a diminished Greenland Ice Sheet (Fig. 3.11). This is because the greenstone belts of the SP are the only circum-North Atlantic bedrock sufficiently radiogenic to explain these values (Fig. 3.2). Numerical ice-sheet modeling also shows that GIS regrowth following MIS 5e would have been relatively rapid (Kleman et al., 2013; Colleoni et al., 2014). Furthermore, it is challenging to explain the origin of this highly radiogenic interval by invoking continued chemical weathering (incongruent or otherwise) of weakly-chemically altered glacial debris on North America exposed following PGM LIS retreat because Pb isotope values recover to late Holocene-like values during the latter half of MIS 5e (by ~122 ka; compare Pb isotope zones γ & ι in Fig. 3.5c-e). This observation shows that the radiogenic weathering signal sourced from North America during Termination 2 had already been exhausted. Instead, we consider that two mechanisms acting in concert are likely responsible for the observed radiogenic increase: (1) MIS 5 Labrador Current invigoration and, (2) incipient LIS glaciation.

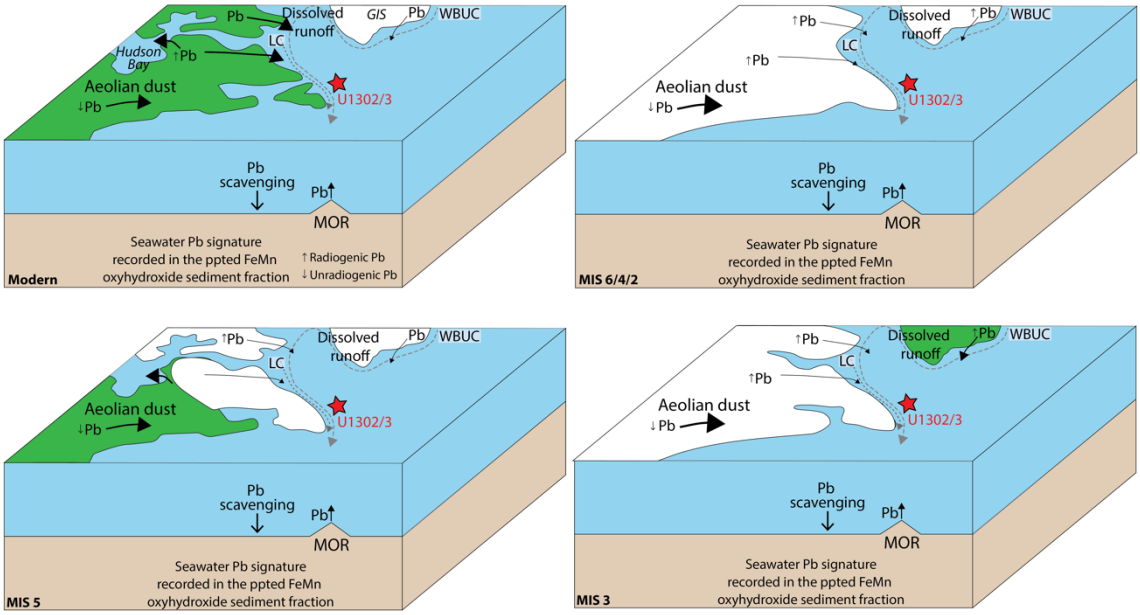

Figure 3.11: Schematic of North Atlantic highlighting Pb sources and geological processes during the Last Glacial Cycle that controls the Pb isotope signature recorded by IODP Site U1302/3 sediments, as discussed in text (where core site is denoted by red star). Arrows denote paths of key currents transporting dissolved Pb to the study site. LC = Labrador Current; WBUC = Western Boundary Undercurrent. (redrawn from Blake-Mizen et al., 2019). Weight of arrows corresponds to relative contribution of Pb source to the core site.

The Labrador Current contributes to the transport of dissolved Pb to U1302/3 and its flow was likely reinvigorated following MIS 5e (Mao et al., 2018). The elevated radiogenic Pb isotope signal that we observe between ~115-75 ka may therefore reflect a long-term increase in Labrador Current flow speed (Fig. 3.11). An increase in vigor would supply more radiogenic Pb from inner parts of the Labrador Sea that under less vigorous flow rates would not make it to U1302/3, given the particle-reactive nature and short seawater residence time of Pb. While our knowledge of Pb isotope compositions of the SP remains somewhat limited, the highly radiogenic signal preserved by our records for MIS 5d-a may itself provide indirect evidence that SP rocks are on average highly radiogenic. Numerical modelling by Batchelor et al. (2019) highlight the possibility that the high grounds of the SP terrane (the Quebec/Labrador region) were glaciated during this time. Renewed glaciation of the SP in this region would not have been extensive enough to prevent chemical weathering of their glacial outwash products and the dissolved transport of its signal to the Labrador Sea. The delivery of such radiogenic material to the Labrador Sea would have been facilitated by Labrador Current invigoration, but also by the fact that these early glacial ice-caps were wet-based (so were not frozen to the substrate), which may

have resulted in the highest delivery rates of dissolved SP materials to our study site over the past ~130 kyr. If this argument is correct, it implies that both retreating and progressing continental ice sheets are capable of facilitating elevated physicochemical weathering rates and associated runoff provided they coincide with relatively high precipitation rates as we might still expect during the relatively warm climate of MIS 5. We further note that this argument would only hold up if the resultant elevated freshwater runoff at this time did not weaken the Labrador Current to the extent that it reduced the overall supply of radiogenic Pb to Orphan Knoll.

3.5.3.3 MIS 4 LIS history

The pronounced decline in Pb isotope values across the MIS 5a/4 transition (e.g., from ~20.6 to ~19.3 $^{206}Pb/^{204}Pb$; Pb isotope zone ε in Fig. 3.5c-e) most likely reflects a decrease in Labrador Current vigour (Mao et al., 2018), an increase in deposition of North American-sourced aeolian dust (Fig. 3.8f), which has a relatively unradiogenic source signature (Fig. 3.11; Lang et al., 2014; Jardine et al., 2021; Fig. 3.2) and a significant reduction in the supply of weathered Pb from North America as the spatial footprint of the LIS increased notably for the first time during the LGC (Fig 3.11). This decline in Pb isotope ratios is also associated with the first sea-level lowstand of the LGC (compare panels a and c-e in Fig. 3.5), so likely documents a significant advance of the LIS across the SP and Hudson Bay. The 75 cm (~5.2 kyr) gap in our record spanning 10.05-10.80 mcd prevents us from establishing the exact timing of LIS advance during MIS 4. Regardless, the unradiogenic trends in our Pb isotope records at this time most likely reflects the westward advance of the Quebec-Labrador dome over Hudson Bay, inferred for this time from till fabrics and lineation swarms in the Hudson Bay Lowlands (Kleman et al., 2010; Gauthier et al., 2019). Using GIA modelling, Pico et al. (2017) conclude that relative high MIS 3 sea-level along the US mid-Atlantic is most consistent with a scenario where the eastern Labrador (Quebec) sector of the LIS is ice-free between ~80 and 44 ka (MIS 5a to MIS 3). Our data strongly imply, however, that the LIS expanded significantly across the MIS 5/4 transition and that their choice of ice-sheet configuration for MIS 4 in northeast North America is likely to be incorrect.

3.5.3.4 MIS 3 LIS history

The subsequent increase in U1302/3 Pb isotope ratios across the MIS 4/3 transition (e.g., of ~0.3 in $^{206}Pb/^{204}Pb$; Pb isotope zone ε in Fig. 3.5c-e) shows that the onset of MIS 3 is associated with increased delivery of radiogenic Pb to the Labrador Sea relative to MIS 4, perhaps enhanced by a strengthened Labrador Current (Fig. 3.11; Mao et al., 2018). Excluding H-events, the values in our $^{206}Pb/^{204}Pb$ and $^{208}Pb/^{204}Pb$ records are persistently late Holocene-like (e.g., ~19.5 in $^{206}Pb/^{204}Pb$ and ~40 in $^{208}Pb/^{204}Pb$) throughout MIS 3 (see Figs. 3.2 & 3.5) before decreasing towards LGM unradiogenic minima (e.g., of ~19.2 $^{206}Pb/^{204}Pb$ and ~39.5 $^{208}Pb/^{204}Pb$) over ~5 kyr from ~25 ka. These relatively radiogenic MIS 3 values were also recorded in the Crocket et al. (2012) Pb isotope records for Site U1302/3 between 25-37 ka, and have previously been interpreted by Blaser et al. (2020) to mean that Hudson Bay was ice-free during this time.

Widespread deglaciation of Hudson Bay, the Hudson Bay Lowlands and the eastern Quebec-Labrador sector of the LIS has also been hypothesized for MIS 3 by Dalton et al., (2019), based on their synthesis and re-interpretation of late Pleistocene geochronological data largely assembled by Dyke et al. (2002). If the spatial extent of the LIS was significantly reduced at this time, we might expect to see clear evidence of a large spike in radiogenic Pb runoff during the MIS 4/3 transition (i.e., as is recorded for T2 and 1 at U1302/3; Fig. 3.10) in response to an increase in chemical weathering rates inland on North America. A short-lived radiogenic spike is potentially evident in our Pb isotope records at ~61 ka (see black asterix in Fig. 3.5c-e), but it is much smaller than those associated with our study site for the last two deglaciations. This observation may reflect that the LIS retreated across MIS 4/3 during a failed termination of sorts (see also Schaefer et al., 2015), but the hydrological cycle remained largely sluggish resulting in a diminished chemical weathering response on North America, whether incongruent or otherwise. Yet, the corresponding $^{207}Pb/^{204}Pb$ isotope ratios of deep water bathing our study site during MIS 3, which are more unradiogenic than their late Holocene counterparts (by ~0.1, Fig. 3.5d), may highlight that a different explanation is required.

If the LIS did not retreat during MIS 3 markedly during the MIS 4/3 transition (as argued by, e.g., Miller and Andrews, 2019), the only non-American-based

regional source that could potentially explain the Pb isotope composition of the deep-waters bathing our study site during MIS 3 is the Ketilidian Mobile Belt of southern Greenland (Fig. 3.2; Fig. 3.11). West Greenland Ice Sheet retreat during MIS 3 has recently been inferred from a multi-proxy study of southern Davis Strait sediments (Seidenkrantz et al., 2019). Our data may therefore suggest that Greenland Ice Sheet retreat at this time could have also included the deglaciation and intensification in chemical weathering of the southern tip of this landmass.

3.6 Conclusions

We present new high-resolution records of authigenic Fe-Mn oxyhydroxide-derived Pb isotopes from Orphan Knoll IODP Site U1302/3 for the past ~130 kyr. We combine these new records with previously published Pb isotope data from this site spanning MIS 3-1 (Crocket et al., 2012) to track temporal variability in the input of Pb sourced from chemical weathering of the adjacent landmasses and its runoff to the Labrador Sea over the past ~130 kyr, which we argue predominantly varied as a function of Laurentide Ice Sheet extent in Hudson Bay.

We propose that the relatively short duration over which Fe-Mn authigenic Pb isotope compositions of bottom waters at U1302/3 during the MIS 6/5e transition are characterised by highly radiogenic values most likely reflects that Laurentide Ice Sheet retreat northwards across the Superior Province during T2 was relatively rapid compared to T1, and in response to greater boreal summer insolation forcing. The renewed existence and runoff of radiogenic Pb to the Labrador Sea during MIS 5d-a is recorded by the highest Pb isotope values in our data, which we argue most likely reflects invigoration of the Labrador Current and incipient glaciation and renewed glacial erosion of high grounds of the eastern Superior Province craton by wet-based localised ice-caps, most probably in the Quebec/Labrador region.

A subsequent large decrease in Pb isotope values towards unradiogenic LGM-like compositions between ~75–65 ka across the MIS 5/4 transition reflects an increase in North American glacial aeolian dust deposition, Labrador Current slow-down and a reduction in chemical weathering and runoff of Pb from North America due to a westward advance of the LIS westwards across Hudson Bay.

The relatively radiogenic Pb isotope composition of bottom-waters bathing our study site reported by Crocket et al. (2012) for MIS 3 has previously been argued to reflect that LIS extent in Hudson Bay was significantly reduced at this time compared to the LGM (Blaser et al., 2019). The relatively unradiogenic composition of authigenic $^{207}Pb/^{204}Pb$ ratios for our study site during MIS 3 (~0.1 lower) relative to the late Holocene highlights, however, that this interpretation may be incorrect. Instead, we propose that the LIS extent in Hudson Bay, and the Pb composition of runoff from this region of North America into the Labrador Sea, may not have changed significantly during MIS 3 compared to MIS 4 (cf. Miller and Andrews, 2019). Under this scenario, only southern Greenland Ice Sheet retreat, as recently inferred for this interval (Seidenkrantz et al., 2019), could explain the Pb isotope signature of seawater bathing U1302/3 during this time through increased chemical weathering of the Ketilidian Mobile Belt and Pb runoff from Greenland.

Chapter 4: Ice-sheet retreat on North America and southern Greenland during Termination 5: implications for the sea-level highstand during MIS 11

Chapter 4 is based on a manuscript prepared for submission to Earth and Planetary Letters. COVID restrictions (which stranded Rebecca L. Parker, R.L.P., in New Zealand from 2020) prevented the generation of authigenic Pb isotope records for the latest stages of MIS 11 (~410–395 ka) for this study and the construction a record of ice-rafted debris deposition at Orphan Knoll during MIS 12/11. R.L.P led this project with contributions as follows: Ian Bailey (I.B.) was responsible for project conception and supervised R.L.P. R.L.P acquired funding, performed Pb isotope and rare earth element analysis at the School of Ocean and Earth Science, University of Southampton, made the interpretations presented and co-wrote the manuscript with I.B. Paul A. Wilson (P.A.W) helped to finance the analyses. P.A.W., Gavin L. Foster and Marcus Gutjahr contributed to manuscript writing and the ideas presented. Matthew J. Cooper, Agnes Mitchelik and James A. Milton helped R.L.P to generate Pb isotope and rare earth element data, oversaw instrumentation and helped with analysis. Kate Littler and P.A.W. co-supervised R.L.P.

4.1 Abstract

Termination (T) 5, ~424 ka, was the most extreme deglaciation of the Quaternary. Global warming and ice-sheet retreat during this time led to an exceptionally long period of interglacial warmth known as Marine Isotope Stage (MIS) 11, ~424-395 ka, that is widely considered to provide the most recent palaeo-analogue for near-future changes in Earth's climate. It is estimated that global mean sea-level during the latter half of MIS 11 may have risen to ~6-13 m above present day. A detailed understanding of the decay history of continental ice-sheets across T5 is required, however, to disentangle regional contributions of ice-sheet retreat to this sea-level rise and to correct it for glacio-isostatic adjustments. Yet nothing is known about the timing and magnitude of retreat of the most volumetrically important continental ice-sheet in the Northern Hemisphere, the North American Laurentide Ice Sheet (LIS), during this time. To address this major unknown, we present new authigenic ferro-manganese (Fe-Mn) oxyhydroxide-derived high-resolution records of Pb isotope data and associated rare earth element profiles for samples spanning T5 from Labrador Sea IODP Site U1302/3. These records feature orbital-scale radiogenic Pb isotope excursions demonstrated to track increases in chemical weathering of North American bedrock and solute flux to the Labrador Sea associated with LIS retreat. They show that LIS retreat during T5 began ~432 ka and occurred over a similar timescale (~15 kyr) to that observed for T1 (~17 kyrs), but not as rapidly as during T2 (~7 kyr). They also show that Hudson Bay Ice Saddle collapse (and therefore LIS break-up) during T5 occurred ~427 ka, ~ 6 kyr earlier than previously published estimates of near-complete southern Greenland deglaciation during MIS 11. The deglacial history of southern Greenland during MIS 11 may also be reflected in our authigenic Pb isotope datasets with evidence for increased chemical weathering of the Ketilidian Mobile Belt from ~418 ka. Regardless, both LIS break-up and southern Greenland deglaciation appear to pre-date the onset of the second of the two weak precessional-paced cycles in insolation associated with MIS 11. We therefore conclude that the sea-level highstand associated with the later half of this interglacial is likely to reflect additional ice-mass loss from the Antarctic ice sheets, and that sea-level rise during this time is likely to sit at the upper-end of published estimates.

4.2 Introduction

Marine Isotope Stage (MIS) 11, ~424-395 ka, is the longest and warmest interglacial of the last ~500 kyr (Loutre and Berger, 2003; Rohling et al., 2010). It is argued by some, from the perspective of astronomically-driven insolation, that it also represents the most recent analogue in the geological past for near-future changes in Earth's climate (Droxler and Farrell, 2000; Loutre and Berger, 2000, 2003; McManus et al., 2003; Masson-Delmotte et al., 2006; Dickson et al., 2009) although others disagree (e.g., Rohling et al., 2010). Best estimates of global mean sea-level for MIS 11 lie somewhere between ~+1 m (Rohling et al., 2010) and ~+6 to +13 m (Bowen, 2010; Raymo and Mitrovica, 2012; Dutton et al., 2015) relative to modern. MIS 11 may therefore feature significant reductions in the volume of both the Greenland (de Vernal and Hillaire-Marcell, 2008; Reyes et al., 2014; Hatfield et al., 2016) and Antarctic (Wilson et al., 2018) ice sheets relative to today. The preceding glacial maximum during MIS 12 featured a mean global sea-level that was ~-115 m below present (Grant et al., 2014) and thus potentially represents the largest northern hemisphere glaciation of the Cenozoic. The MIS 12/11 climate transition, otherwise known as Termination (T) 5 (hereinafter T5), is therefore viewed as the most extreme deglaciation in the Quaternary (Barker et al., 2021).

Termination 5 has also recently been labelled as a 'protracted deglaciation' (Barker et al., 2019) since the full glacial-interglacial transition in mean global sea-level between MIS 12 to 11 (Rohling et al., 2010; Raymo and Mitrovica, 2012) was seemingly not reached until the second of two weak precessional-paced maxima in insolation associated with MIS 11 was crossed (at ~410 ka). Palaeoclimate data for this time seemingly record a brief (but commonly mild) relapse to more glacial-style conditions during the intervening insolation minima at ~ 418 ka (Loulergue et al., 2008; Dickson et al., 2009; Tzedakis et al, 2009). Global mean sea-level also plateaued at this time before subsequent slow ice-volume reductions led to the MIS 11 sea-level highstand during the second insolation maximum (Rohling et al., 2010).

A detailed understanding of the history of the growth and decay of continental ice-sheets across T5 is required to disentangle regional contributions of ice-sheet retreat to this sea-level history. It is also required to correct estimates of MIS 11 sea-level rise accurately for glacial-isostatic adjustment (GIA), so for the

deformational, gravitational and rotational impacts on sea level driven by cryospheric loading and unloading of the land and ocean (e.g., Raymo and Mitrovica, 2012; Dendy et al., 2017). It has been shown, for instance, that GIA corrections for global mean sea-level rise during the Last Interglacial (the Eemian) are highly sensitive to the choice of ice-sheet configuration during the preceding glaciation, the Penultimate Glacial Maximum (PGM), for the largest ice-mass in the northern hemisphere, the North American Laurentide Ice Sheet (LIS; Dendy et al., 2017; Dyer et al., 2021).

Our knowledge of LIS extent during MIS 12 is rudimentary compared to what is known about its Last Glacial Maximum (LGM) counterpart (e.g., Dyke et al., 2002; Carlson et al., 2007; 2008; Dalton et al., 2020). To date, reconstructions of the LIS during MIS 12 have either adopted the aerial extent assumed for this ice-sheet during the PGM (e.g., Batchelor et al., 2019) or its known configuration for the LGM (e.g., Raymo and Mitrovica, 2012). Yet a recently published stratigraphic reinterpretation of the age of Pre-Illinoian (so pre-MIS 6) glacial tills from northern Missouri, USA, concluded that the middle of three till deposits (the Columbia Till Member) that forms the middle Pleistocene McCredie Formation was most likely emplaced at ~38˚N, during MIS 12 (Rovey and Siemens, 2021). This new stratigraphic framework thus highlights that the LIS may have had a larger footprint in the mid-continent of the US during this cold stage than its LGM counterpart. Nothing is known, however, about its footprint in other sectors of North America. While strong evidence exists to show that near-complete deglaciation of southern Greenland occurred during MIS 11 by ~418 ka (e.g., De Vernal and Hillaire-Marcel, 2008; Reyes et al., 2014; Hatfield et al., 2016), nothing is known about the timing and magnitude of LIS retreat during T5.

To help address these unknowns, we present new high resolution ferro-manganese (Fe-Mn) oxyhydroxide-derived Pb isotope ratios and rare earth element (REE) profiles of 37 samples from Integrated Ocean Drilling Program (IODP) Site U1302/3 in the northwest North Atlantic on Orphan Knoll that span MIS 12/11 (Fig. 4.1). The Pb isotope composition of the oxyhydroxide fraction of marine sediments deposited at this site tracks the runoff signal of chemical weathering on North America and Greenland (Crocket et al., 2012; Chapter 3), and has previously been used successfully to track LIS extent in Hudson Bay over the past ~130 kyr (Parker et al., in revision; Chapter 3). We find that both

LIS break-up (~427 ka) and southern Greenland deglaciation (from ~418 ka) pre-date the onset of second of two weak precessional-paced cycles in insolation associated with MIS 11, and we discuss the implications of this observation for the likely magnitude of sea-level rise associated with this interglacial.

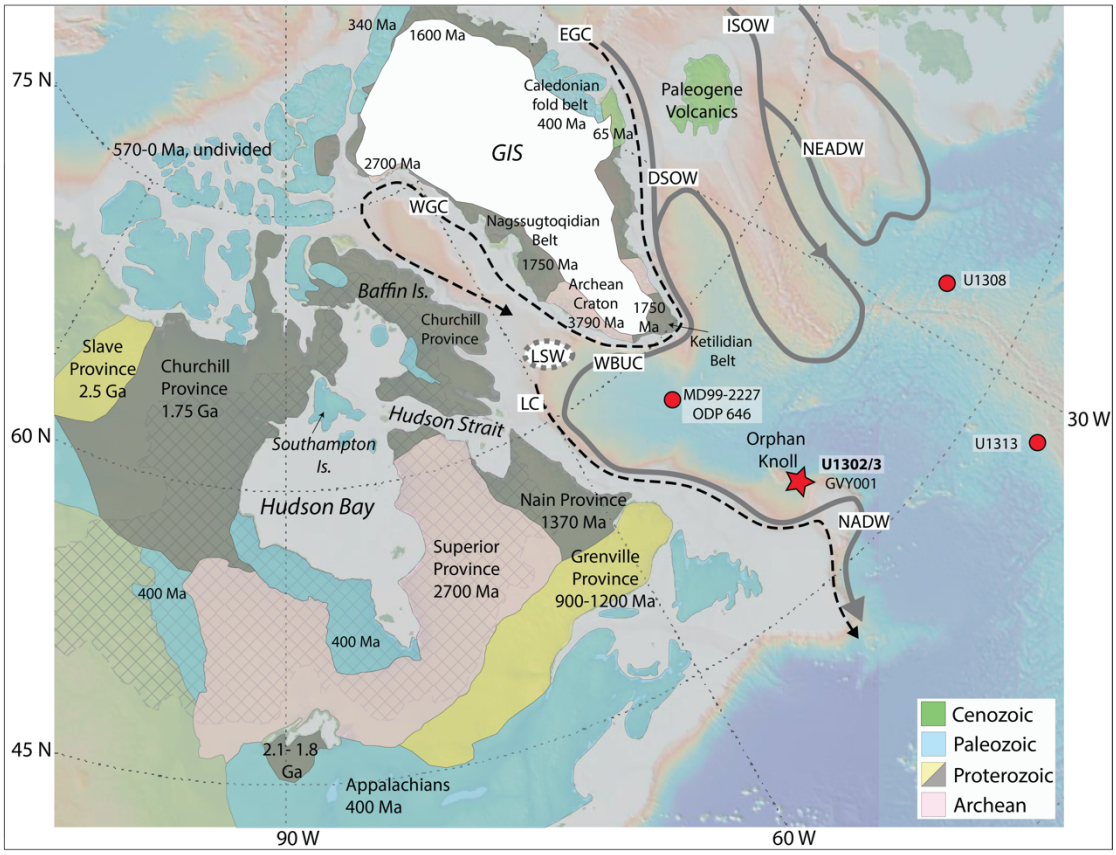

Figure 4.1: Map showing location of IODP Site U1302/3, other sites discussed in the text and relevant surrounding cratonic (bedrock) geology. Geology of North America and Greenland redrawn from Reed et al. (2005) and White et al. (2016). Grey hatched region denotes modern area of watershed drainage into Hudson Bay and its straits (Natural Resources Canada, 2006). Arrows denote paths of key modern deep (solid grey) and surface (dashed grey) ocean currents relevant to this study (redrawn from Blake-Mizen et al., 2019). GIS = Greenland Ice Sheet. ISOW = Iceland-Scotland Overflow Water. DSOW = Denmark-Scotland Overflow Water. NEADW = Northeast Atlantic Deep Water. WBUC = Western Boundary Undercurrent. LSW = Labrador Sea Water. NADW = North Atlantic Deep Water. WGC = West Greenland Current. EGC = East Greenland Current.

4.2.1 How are changes in Fe-Mn oxyhydroxide-derived Pb isotope ratios from Site U1302/3 related to changes in ice-sheet extent on North America?

The evolution of the Pb isotope composition of seawater bathing Orphan Knoll over the past ~130 kyr is argued to reflect changes in the magnitude of chemical weathering and solute runoff associated with LIS extent in the Hudson Bay region

of North America (Crocket et al., 2012; Chapter 3). This evolution can be tracked by analysing the Pb isotope composition of the Fe-Mn oxyhydroxide fraction of marine sediments deposited at IODP Site U1302/3.

The unradiogenic Pb isotope signature of seawater bathing Orphan Knoll during the LGM (Fig. 4.2a) is argued to reflect a reduction in North American chemical weathering and runoff under a spatially extensive LIS, and a dominance of a North American aeolian dust and Mid-Atlantic Ridge Pb isotope signal (Crocket et al., 2012; Chapter 3). It is also suggested to reflect a sluggish Labrador Current, which, given the particle-reactive nature and short seawater residence time of Pb, would have reduced the supply of radiogenic Pb to U1302/3 from inner parts of the Labrador Sea during this time (Chapter 3).

Highly radiogenic millennial-scale excursions in Site U1302/3 authigenic Pb isotope data occur during Last Glacial Heinrich events (Fig. 4.2a) and are thought to represent exceptionally high inputs of detrital particles to Orphan Knoll with 'pre-formed' coatings sourced from Hudson Bay (Crocket et al., 2012). Site U1302/3 authigenic Pb isotope data spanning the past ~130 kyr also feature longer-term orbital-scale radiogenic excursions during T2 (from ~130 ka, Fig. 4.2b; Chapter 3) and T1 (from ~20 ka, Fig. 4.2a; Crocket et al., 2012). Two main processes have been proposed to explain these deglacial trends: 1) incongruent weathering of highly reactive weakly-chemically altered glacial debris, exposed following LIS retreat (Crocket et al., 2012) and/or, 2) changes in Pb provenance through enhanced sourcing and congruent weathering of weakly-weathered radiogenic Superior Province (SP) material (Fig. 4.3; Blaser et al., 2020; Chapter 3). The relative importance of these two processes in controlling the Pb isotope composition of solute flux is debated (e.g., Crocket et al., 2012; Dausmann et al., 2019; Süfke et al., 2019). Their relative roles in controlling changes in authigenic Pb isotope records from U1302/3 have recently been discussed extensively in Section 3.3.1 of Chapter 3 where it was concluded that if incongruent weathering influences the Pb isotope composition of seawater bathing Orphan Knoll during LIS deglaciation its role is likely to have been subordinate to that of changes in Pb provenance. Regardless of the mechanisms involved, the radiogenic deglacial signals recorded in authigenic Pb isotope data from U1302/3 appear to provide important insights into the pace of LIS retreat during T2 and T1.

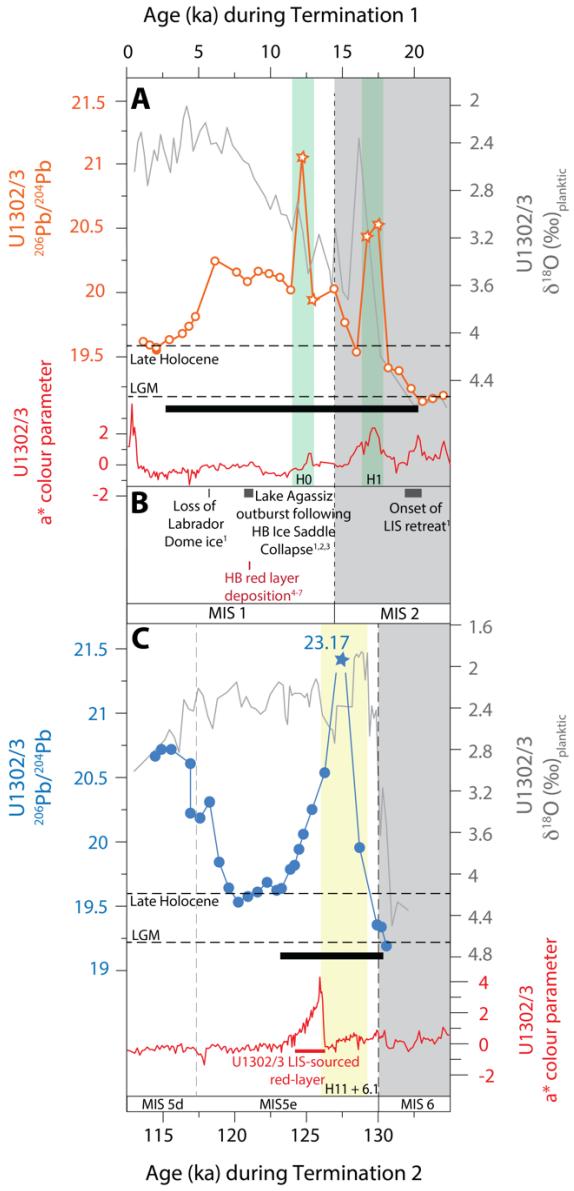

Figure 4.2: The evolution of the Pb isotope composition of authigenic Fe-Mn oxyhydroxides from IODP Site U1302/3 during **(A)** Termination 1 associated with **(B)** major events of Laurentide Ice Sheet retreat and **(C)** Termination 2. Horizontal black bars highlight the inferred duration of enhanced supply of dissolved radiogenic weathered material from the Superior Province craton exposed following Laurentide Ice Sheet retreat during each termination. Dark grey horizontal bars and associated superscript numbers in (**B**) highlight timing of major events that characterise Laurentide Ice Sheet retreat during Termination 1, whereby 1 = Dalton et al., 2020, 2 = Brouard et al., 2021, 3 = Margold et al., 2018, 8 = Dyke et al., 2002. Also shown is timing of the deposition of a red layer in Hudson Bay (HB) during T1 (4 = Barber et al., 1999, 5 = Lajeunesse and St-Onge, 2008, 6 = Jennings et al., 2015, 7 = Lochte et al., 2019), argued to be the product of extensive deglaciation of the Hudson Bay region following the collapse of the Hudson Bay (HB) Ice Saddle and the final outburst of glacial Lake Agassiz-Ojibway (Carlson et al., 2008). A similar red layer was also deposited in the Labrador Sea during Termination 2 (see red horizontal bar associated with peak in a* sediment colour in (C) and is argued to document a large glacial outburst flood from a precursor to glacial Lake Agassiz-Ojibway (Nicholl et al., 2012). Solid circles/stars = Parker et al., in revision; Chapter 3; open circle/stars = Crocket et al. (2012). MIS cold(warm) stages are shown by vertical light grey(white) bars. Heinrich (detrital) layers preserved in both the Labrador Sea (identified using U1302/3 core-scanning-derived XRF Ca/Sr ratios by Channell et al. (2012)) and subpolar North Atlantic sediments (Hemming, 2004; Hodell et al., 2008) are shown by labelled vertical light green bars. Labelled vertical light-yellow bars highlight Heinrich-like detrital layers where deposition was restricted to the Labrador Sea (Channell et al., 2012; Hodell et al., 2008). Horizontal dashed lines in (a) and (c) highlight average Pb isotopes values for the LGM and late Holocene.

The deglacial sequence of LIS retreat during T1 has been mapped out in great detail using a combination of geomorphology, stratigraphy and radiocarbon dating (e.g., Dyke et al., 2002; Dalton et al., 2020). This evidence shows that the onset of the orbital-scale increase in radiogenic values in U1302/3 Pb isotope records at ~20 ka coincides with the earliest stages of LIS retreat on North America (in Long Island Sound, Connecticut; Dalton et al., 2020). It also shows that peak radiogenic Pb values in the Orphan Knoll record for T1 were reached ~2 kyr following the collapse of the Hudson Bay Ice Saddle between the Keewatin and Labrador domes (~8.7–8.15 ka; Dalton et al., 2020; Brouard et al., 2021). It also shows that the decay towards late Holocene unradiogenic authigenic Pb isotope values (e.g., ~19.6 $^{206}Pb/^{204}Pb$) was complete (by ~3 ka) not long after the loss of the Labrador Dome ~5.7 ka (Fig. 4.2a, b; Dalton et al., 2020). Glaciation in northeast North America after this time was largely restricted to the Canadian Arctic Archipelago (Dalton et al., 2020). The collapse of the Hudson Bay Ice Saddle caused the final outburst of glacial Lake Agassiz-Ojibway south of Hudson Bay (Brouard et al., 2021) and the deposition of a red detrital marker bed in Hudson Straits sediments (Fig. 4.2a, b; Kerwin, 1996; Barber et al., 1999; Lajeunesse and St-Onge, 2008; Jennings et al., 2015). A similar red (hematite-rich) detrital layer has been found in sediments deposited at Site U1302/3 during T2 (Fig. 4.2c; Nicholl et al., 2012), which correlates with peak radiogenic values in the authigenic Pb isotope record from this site ~126 ka (Fig. 4.2c; Section 3.5.3.1 of Chapter 3). This detrital red layer is associated with increased values in an a* colour reflectance record of U1302/3 sediments (Fig. 4.2c), argued to be the product of extensive deglaciation of the Hudson Bay region following a last deglacial-like collapse of the Hudson Bay Ice Saddle and a subsequent Lake Agassiz-like glacial outburst flood (Nicholl et al., 2012).

The amount of summer insolation received at high northern latitudes plays a major role in determining the timing and duration of northern hemisphere deglaciation (Carlson et al., 2008; Past Interglacials Working Group of PAGES, 2016; Tzedakis et al., 2017; Chapter 3). The LIS is, for instance, argued to have retreated faster during T2 than it did during T1, and as a result of greater boreal summer insolation forcing (Carlson et al., 2008); a fact consistent with the evolution of orbital-scale changes in radiogenic authigenic values in U1302/3 Pb isotope data (Fig. 4.2 & 4.4c, d). Insolation forcing during T5 across the MIS 12/11 transition is weaker (by ~20 and 40 W/m^2) than during T1 and T2, respectively

(compare June 21st insolation time series in Fig. 4.4c). Maximum values in insolation were also not reached until the second of two weak precessional-paced maxima associated with MIS 11 (Fig. 4.4c), 17 to 14-kyr later than maximum values in insolation were reached during MIS 5e and the Holocene, respectively. In this study, we use a new high-resolution authigenic Pb isotope record from Site U1302/3 to track LIS retreat during T5 with respect to this insolation history. In doing so we address the following questions: 1) When did LIS retreat begin during T5? 2) What is the relationship between the timing of Hudson Bay Ice Saddle collapse and the two weak precessional-paced maxima in insolation associated with MIS 11? 3) Is there any evidence for LIS regrowth during the intervening insolation minima? 4) By what likely time was LIS deglaciation complete during MIS 11.

4.3 Methods

4.3.1 Site Description, sampling and age model

IODP Site U1302 (50° 10′N, 45° 38.3′W, water depth: 3560 m) and Site U1303 (50° 12.4′N, 45°41.2′W, water depth: 3520 m) are located just ~3 nautical miles apart on the southeastern flank of Orphan Knoll within the Labrador Sea, proximal to the coast of Newfoundland (Fig, 4.1; Channell et al., 2006). The Pb isotope composition of bottom waters bathing these sites is therefore strongly influenced by changes in weathering intensity and solute flux associated with the glacial history of the LIS in the Hudson Bay region (Crocket et al., 2012; Chapter 3). The similarity of strata between the two sites has been used to create continuously spliced composite records of changes in bottom-water Pb isotope compositions over the past ~130 kyr (Crocket et al., 2012; Chapter 3).

To reconstruct the Pb isotope composition of bottom waters bathing Site U1302/3 during T5, we determined the authigenic Fe-Mn oxyhydroxide fraction of 5-cc samples (n = 37) taken every 10-20 cm between 59.25-63.51 metres composite depth, mcd (Expedition 303 Scientists, 2006). These samples were also used to determine the elemental concentrations of the seawater derived Fe-Mn oxyhydroxide fraction. The age model for our record is the same as that presented in Chapter 3, which was generated by Channell et al. (2012), based on matching relative paleointensity (RPI) and $\delta^{18}O$ composition of the planktic

foraminifera *Neogloboquadrina pachyderma* (*sin.*) to the PSIO-1500 RPI stack (Channell et al., 2009) and the LR04 benthic $\delta^{18}O$ stack (Lisiecki and Raymo, 2005).

4.3.2 Pb isotope analysis

We generated new authigenic Pb isotope and REE data for the MIS 12/11 transition during T5 (~440–410 ka), following the procedures outlined in Chapter 3. All sample processing and laboratory analyses were conducted at the School of Ocean and Earth Science, University of Southampton. Briefly, Pb was extracted from the authigenic Fe-Mn oxyhydroxide fraction of sediments from each sample closely following Blaser et al. (2016). Dried, homogenised sediment samples were exposed to a leaching solution (mixture of 3 mM Na-EDTA, 5 mM hydroxylamine-hydrochloride, 1.5% acetic acid and buffered to pH 4 using 0.04M NaOH) to extract their authigenic coating. The leached solution was then screened on a Thermo Scientific X-Series 2 ICP-MS to ensure adequate quantities of Pb were extracted for column chemistry, before being separated from the matrix using Eichrom AG1-X8 200-400 mesh anion exchange resin (Strelow, 1978). A set of 8 detrital (residual fraction) samples were also prepared for Pb isotope analysis. All samples were analyzed in the same run used to generate the Pb isotope data presented in Chapter 3. The procedural blanks, standards and internal replicate values used in the generation of the new MIS 12/11 data presented here are therefore the same and are reported for monitoring contamination, drift and reproducibility reported in Chapter 3 (for the analytical period of 2018-2020).

4.3.3 Rare and trace elements analysis

Trace element concentrations of the Fe-Mn oxyhydroxide fraction stock solutions were determined following the methods described in Chapter 3 and were used to evaluate the fidelity of our MIS 12/11 seawater Pb isotope data. Briefly, aliquots were prepared for analysis on a Thermo Scientific X-Series 2 ICP-MS at the School of Ocean and Earth Science, University of Southampton. Measurements were calibrated using the same suite of international rock standards and in-house and international reference materials outlined in Chapter 3. REE concentrations of samples were normalised relative to the REE profile of the Post-Archean Australian Shale (PAAS; Taylor and McLennan, 1985) and a number of ratios of

PAAS-normalised concentrations were calculated following Martin et al. (2010) and Blaser et al. (2016; 2019; see Section 3.4.3 of Chapter 3).

4.4 Results and Discussion

4.4.1 New MIS 12/11 Pb isotope data from Site U1302/3

In Figure 4.4 we present the first high-resolution records of authigenic Fe-Mn oxyhydroxide-derived Pb isotope ratios from Site U1302/3 that span the transition between MIS 12/11 during T5, in comparison to MIS 6 to 5e (T2) and MIS 2 to 1 (T1; see Appendix A1 for full dataset). The Pb isotope zones for MIS 6/5e and MIS 2/1 shown in Fig. 4.4 (and labelled with Greek letters α–δ and η–ι) are the same as those used by Parker et al. (Chapter 3) to highlight important features in the evolution of the Pb isotope composition of Orphan Knoll seawater during these times. Here we extend these Pb isotope zones back to MIS 12 (κ-μ) to aid comparison of the deglacial trends in these U1302/3 authigenic datasets across T5, T2 and T1.

Our new MIS 12/11 records show that detrital carbonate layers (Heinrich; (H)-like events) deposited at our study site during MIS 12 (12.3 and 12.2) and T5 (12.1) are associated with millennial-scale highly radiogenic excursions comparable to those observed for detrital layers deposited in the Labrador Sea during Heinrich events of Last Glacial (see Pb data within green bars in Fig. 4.4d-f; Chapter 3; Crocket et al., 2012). At the orbital scale, these records also demonstrate that the general evolution of authigenic Pb isotope data from U1302/3 during T5 was similar to that observed for T2 and T1 – all three Pb isotope ratios ($^{206}Pb/^{204}Pb$, $^{207}Pb/^{204}Pb$ and $^{208}Pb/^{204}Pb$) are most unradiogenic during MIS 12 (Pb isotope zone μ in Fig. 3d-f) and most radiogenic during T5 and the early stages of MIS 11 (Pb isotope zone λ in Fig. 4.3d-f) before decaying to values intermediate to these from ~424 ka. Prior to ~433 ka, MIS 12 is characterized by LGM-like Pb isotope values, but only intermittently and vary between ~19-19.4 for $^{206}Pb/^{204}Pb$, ~15.63-15.67 for $^{207}Pb/^{204}Pb$ and ~39.5-40.1 for $^{208}Pb/^{204}Pb$ on suborbital timescales (Pb isotope zone μ in Fig. 4.4d-f). All Pb isotope ratios become progressively more radiogenic from ~433 ka during T5 (and shift from ~19.0 to 20.9 for $^{206}Pb/^{204}Pb$, ~15.6 to 15.8 for $^{207}Pb/^{204}Pb$ and ~39.2 to 41.6 for

$^{208}Pb/^{204}Pb$; Pb isotope zone λ in Fig. 4.4d-f). Excluding H-events, the magnitude of change in these records during this time is comparable to the evolution the authigenic Pb isotope data from our study site during T2 and T1 (compare Pb isotope zones μ–κ for MIS 12/11 with those for MIS 6/5e (α–γ) and MIS 2/1 (η–ι) in Fig. 4.4d-f). The duration over which authigenic Pb isotope data from U1302/3 during T5 are characterised by highly radiogenic values (~15 kyr), is highly comparable to T1 (~17 kyr) but not to T2 (~7 kyr; compare Pb isotope zones λ, β and θ in Fig. 4.4d). Late Holocene-like Pb isotope compositions (~19.6 $^{206}Pb/^{204}Pb$; ~15.7 $^{207}Pb/^{204}Pb$; ~40.0 $^{208}Pb/^{204}Pb$) indicative of full deglaciation of the LIS are not recorded in all three authigenic Pb isotope ratios at the same time; they are, for example, first recorded in $^{207}Pb/^{204}Pb$ from ~424 ka, in $^{206}Pb/^{204}Pb$ from ~421 ka and finally in $^{208}Pb/^{204}Pb$ from ~416 ka (Fig 4.4d-f). While $^{206}Pb/^{204}Pb$ and $^{208}Pb/^{204}Pb$ ratios remain late Holocene-like for the rest of our MIS 11 records, $^{207}Pb/^{204}Pb$ ratios decrease again at ~418 ka from ~15.7 to ~15.66 (Fig. 4.4e). By contrast, our detrital fraction Pb isotope records show different absolute ratios (e.g. ~17–18 for $^{206}Pb/^{204}Pb$) and contrasting temporal trends across MIS 12 and 11 to those recorded by our authigenic records (compare Fig 4.4g-i to d-f).

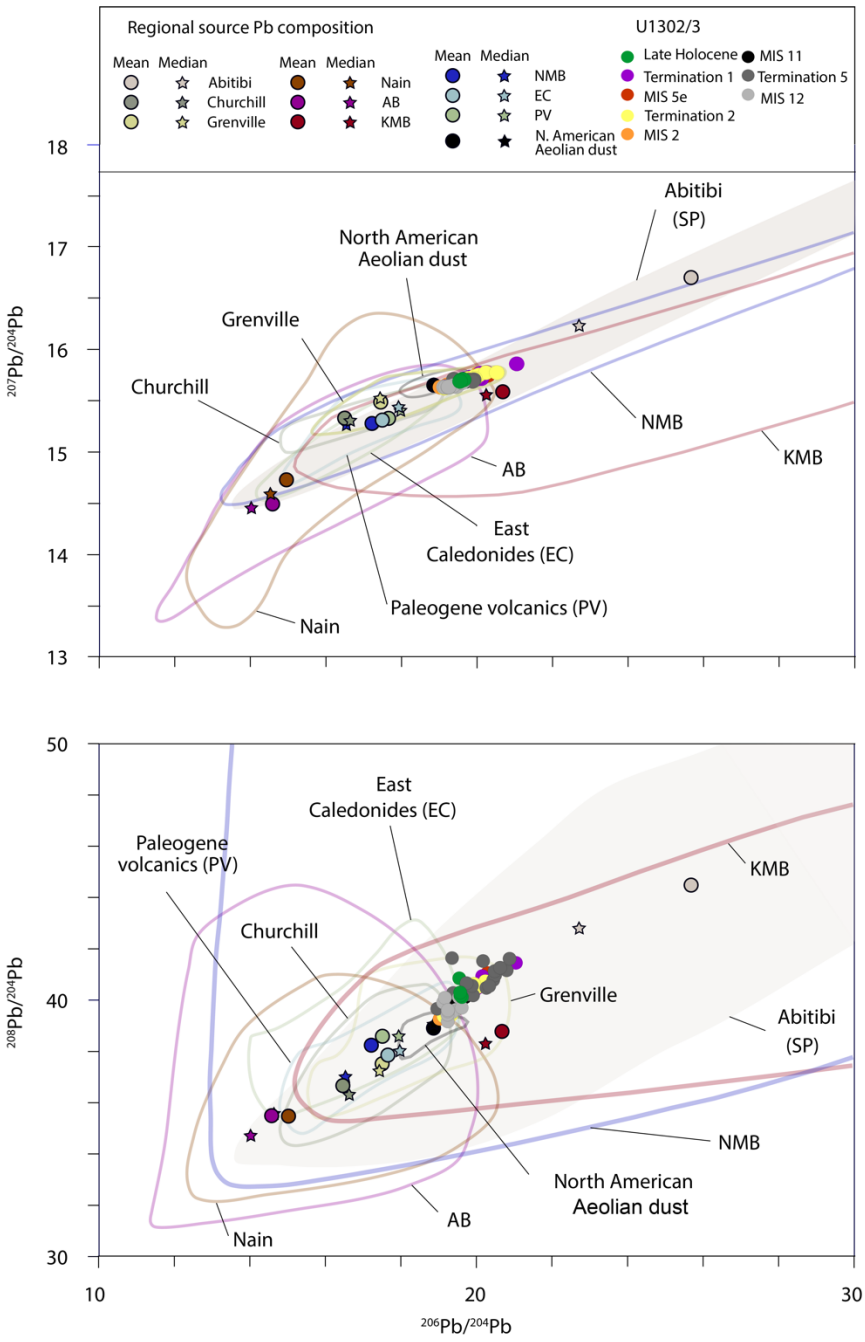

Figure 4.3: The Pb isotope composition of cratonic bedrock adjacent to Orphan Knoll Site U1302/3: **(A)** $^{206}Pb/^{204}Pb$ versus $^{207}Pb/^{204}Pb$ and **(B)** $^{206}Pb/^{204}Pb$ versus $^{207}Pb/^{204}Pb$. Redrawn from Parker et al. (in revision; Chapter 3), which in turn was based on a whole rock data compilation by Fagel et al. (2002) supplemented by additional datasets. The Pb isotopic composition of the authigenic Fe-Mn oxyhydroxide fraction of U1302/3 sediments is also shown for the late Holocene (green circles), Termination 1 (purple circles), MIS 5e (red circles), Termination 2 (yellow circles) and MIS 2 (orange circles). See Figure 1 for craton locations. We defined the average weathering Pb isotope signal of each source following Innocent et al. (1997) and Fagel et al. (1999; 2002; 2004; 2011) by using the mean and median of the whole-rock data available for each craton. The degree of disparity between the mean and the median can be used as a first-order estimate of uncertainty in our understanding of each end-member's average Pb isotope composition.

4.4.2 Fidelity of the authigenic Fe-Mn signal from Site U1302/3 as a record of Labrador Sea seawater Pb isotope composition

To determine the fidelity of our new seawater Pb isotope records extracted from the authigenic Fe-Mn oxyhydroxide fraction of sediments deposited at U1302/3 during MIS 12 and 11, we checked for the possible release of non-seawater-derived Pb from the detrital sediment fraction. We did this by employing the same series of tests used previously (and outlined in Chapter 3, Section 3.5.2) to prove the high fidelity of authigenic Pb isotope data generated from our study site for the past ~130 kyr. These tests are: 1) examination of detrital and authigenic Pb isotope trends for evidence of covariance, 2) evaluation of REE data to identify what material was leached (Haley et al., 2004; Martin et al., 2010) and, 3) comparison of Al/Nd, Al/Th and Al/Pb ratios of the authigenic and detrital fractions of our samples and abyssal ocean Fe-Mn crusts (Gutjahr et al., 2007).

Figure 4.4: Comparison of palaeoceanographic and palaeoclimate records during Termination (T) 5, T2 and T1: **(A)** Red Sea relative sea-level (RSL) record with 95% probability interval for the RSL data (dark grey envelope) and 95% probability interval for the probability maximum (light grey envelope; Grant et al., 2012). Also shown is a benthic foraminiferal-derived seawater-$\delta^{18}O$-based RSL record from Ocean Drilling Program Site 1123 (red line; Elderfield et al. (2012); **(B)** Site U1302/3 planktic $\delta^{18}O$ (black line; Hillaire-Marcel et al., 2011) and the LR04 benthic $\delta^{18}O$ stack (blue line; Lisiecki & Raymo, 2004); **(C)** Insolation forcing at 21st June 65°N (W/m^2; Laskar et al., 2004); Pb isotope ratios of authigenic Fe-Mn oxyhydroxides from U1302/3: **(D)** $^{206}Pb/^{204}Pb$; **(E)** $^{207}Pb/^{204}Pb$; **(F)** $^{208}Pb/^{204}Pb$ (T1 and T2, Parker et al., Chapter 3; T5, this study); Pb isotope ratios of detrital sediment fraction: **(H)** $^{206}Pb/^{204}Pb$; **(I)** $^{207}Pb/^{204}Pb$; **(J)** $^{208}Pb/^{204}Pb$ ratios of Site U1302/3 (T1 and T2, Parker et al., Chapter 3; T5, this study). "Detrital" refers to the full digestion of the authigenic-free fraction of marine sediment **(J)** a* colour reflectance parameter highlighting red detrital sediment layers; **(K)** XRF Ca/Sr ratios (counts/counts) from U1302/3 (Channell et al., 2012). MIS cold(warm) stages are shown by vertical light grey(white) bars. Heinrich-like (detrital carbonate) layers preserved in both the Labrador Sea (identified using core-scanning-derived XRF Ca/Sr ratios by Channell et al., 2012) and subpolar North Atlantic sediments (Hemming, 2004; Hodell et al., 2008) are shown by labelled vertical light green bars. Horizontal dashed lines in (D) (E) and (F) highlight average Pb isotopes values at U1302/3 for the late Holocene and Last Glacial Maximum (LGM). Horizontal black bars and associated arrows in (d) highlight intervals over which we infer enhanced supply of dissolved radiogenic weathered material from the Superior Province craton following Laurentide Ice Sheet (LIS) retreat in the Hudson Bay region during T5, 2 and 1. Blue arrows highlight inferred timings of LIS break-up (Hudson Bay Ice Saddle collapse) during T1 (1 = Carlson et al., 2008; 2 = Dalton et al., 2020; 3 = Brouard et al., 2021), T2 (4 = Nicholl et al., 2012; 5 = Parker et al., Chapter 3) and T5 (this study). Green arrows highlight inferred culmination of southern Greenland Ice Sheet retreat during T1 (7 = Hatfield et al., 2016; 8 = Colville et al., 2011), T2 (8 – Colville et al., 2011). The GRiS experienced near-complete deglaciation during T5, from ~418 ka (9 = Reyes et al., 2014; 7 = Hatfield et al., 2016). Greek symbols θ-ι labelled in (d) correspond to Pb isotope data zones referred to in main text.

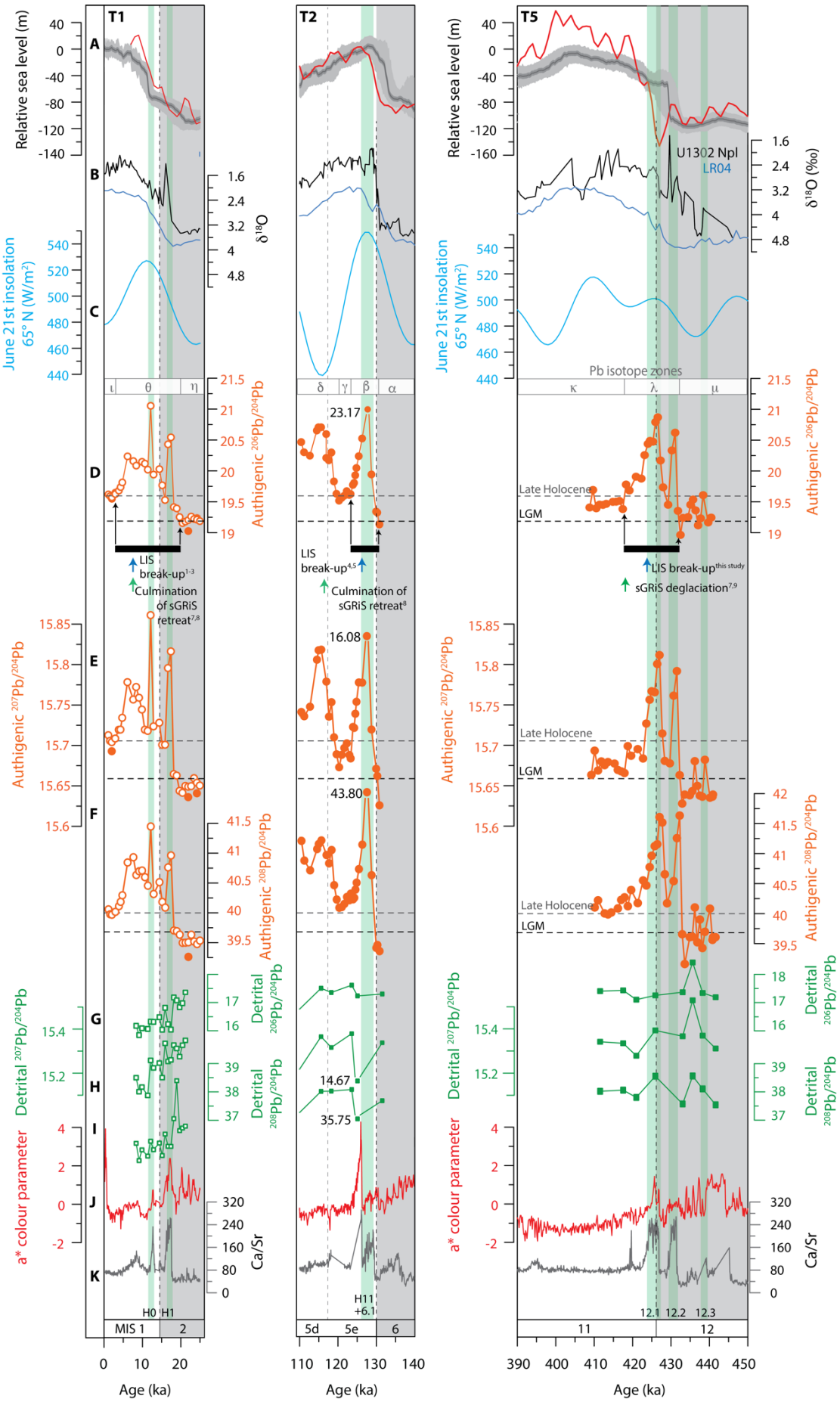

Caption opposite

The absence of strong covariance between our authigenic and detrital Pb isotope records strongly suggests that leaching of the detrital sediment fraction, either via in-situ chemical weathering at the seafloor and/or during sample processing, does not control temporal variability in our authigenic records spanning MIS 12 and 11 (Fig. 4.5). This is supported by the presence of a distinct PAAS-normalised mid-REE (MREE) enrichment in our leachate samples that is not observed in the distribution of REE in our detrital samples (Fig. 4.6; Piper, 1974). Excluding detrital carbonate layers, the REE signature of most of our MIS 12 and 11 samples (n = 20 out of 29) overlap with that of HH-extracted leachate seawater signals in a cross plot of the REE slope (HREE/LREE) and MREE bulge (MREE/MREE*; Fig. 4.7). Some of our authigenic data (n = 9 out of 29) encroach on the REE signature of residual detrital sediment fractions (blue triangles and blue circles with black outlines in Fig. 4.7a, b), consistent with incomplete removal of oxides, partial leaching of the detrital component during sediment processing (Martin et al., 2010) or potentially by pore waters in the sediment pile (Blaser et al., 2020). We cannot rule out that the detrital fraction was partially leached during the processing of these samples, but we consider this possibility unlikely given the 'light touch' nature of our Pb extraction approach (cf. Blaser et al., 2016). We also cannot rule out that in-situ weathering of seafloor sediments influenced the authigenic Pb isotope composition of these samples. Although we note that the particle-reactive nature of Pb means that partial release of terrigenous REE during in-situ weathering at the seafloor does not necessarily result in the release of comparable quantities of Pb (Henderson and Maier-Reimer, 2002).

Chemical weathering at the seafloor could not be responsible for the existence of the orbital-scale radiogenic trend in our authigenic Pb isotope record across the MIS 12/11 transition. This is because the Pb isotope compositions of the detrital fraction deposited at U1302/3 during MIS 12 and 11 is much more unradiogenic than the authigenic signal (by ~2-4 units; compare Fig. 4.4g-i with 4.3d-f), so its partial leaching during sample processing and/or through in-situ weathering would act to mask a radiogenic seawater signal, not artificially imprint one across T5. Most of the nine samples with a REE signature that encroaches on that of our detrital sediment fractions correspond to the tail-end of the decay of the authigenic Pb isotope radiogenic signal associated with this transition (see blue circles with black outlines in Fig. 4.7a that correspond to the authigenic Pb isotope data spanning ~416-423 ka in panel b). This leaves open the possibility that the

duration of this radiogenic signal may, however, be influenced by in-situ weathering of seafloor sediments, and we discuss the significance of this possibility for our inferences of LIS history during this interglacial.

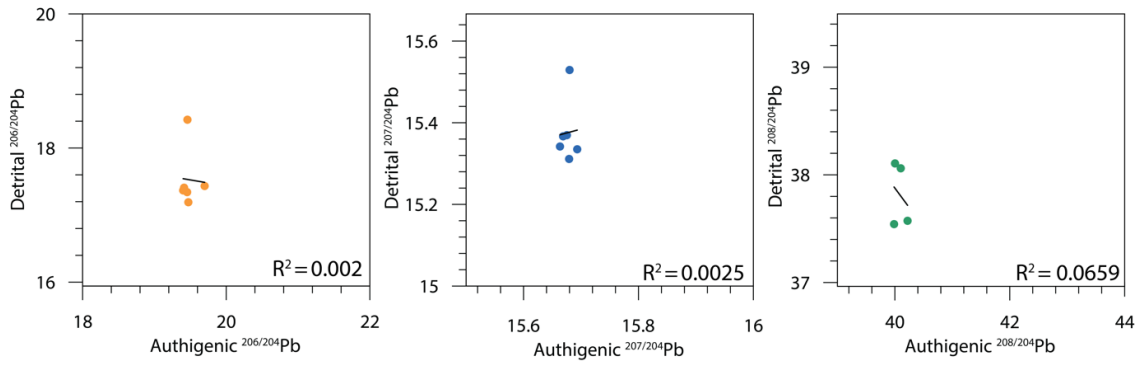

Figure 4.5: Cross plots of paired authigenic and detrital Fe-Mn oxyhydroxide-derived Pb isotope data from IODP Site U1302/3 with regression analysis.

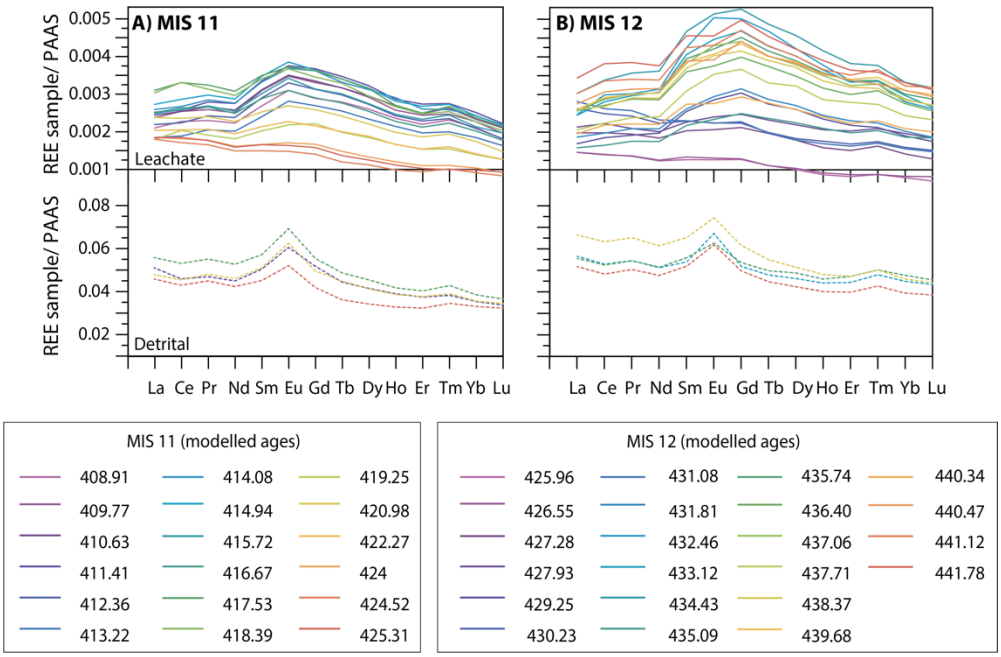

Figure 4.6: Post-Archean Australian Shale (PAAS) normalised rare earth element (REE) multi-element plots for paired authigenic Fe-Mn oxyhydroxide (solid lines) and detrital (dotted lines) samples deposited at IODP Site U1302/3 during **(A)** Marine Isotope Stage (MIS) 11, **(B)** MIS 12.

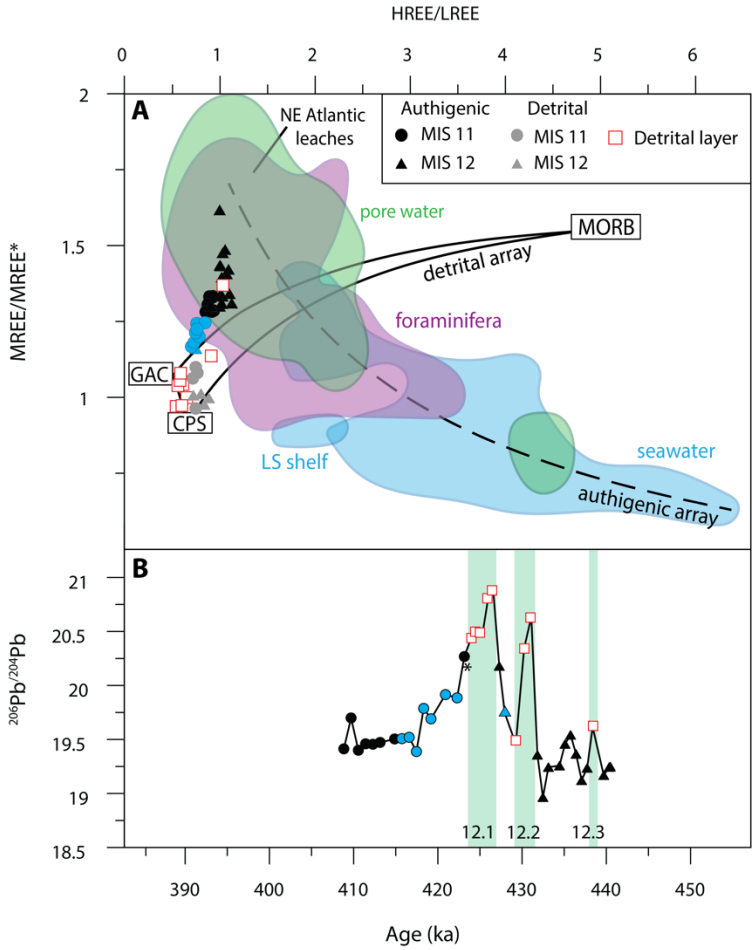

Figure 4.7: (A) Comparison of PAAS normalised rare earth element (REE) slope (HREE/LREE) and mid-REE bulge (MREE/MREE*) of detrital sediment samples and their authigenic Fe-Mn oxyhydroxides coatings deposited at IODP Site U1302/3 during marine isotope stages (MIS) 12/11 (450-400 ka). **(B)** Corresponding $^{206}Pb/^{204}Pb$ ratios with same symbols. Seawater, pore fluids, foraminifera and authigenic phase fields shown are from Blaser et al. (2020), defined using foraminiferal REE data from core top to Last Glacial Caribbean, Northwest Atlantic and Equatorial Pacific sediments (purple, Osborne et al., 2017), seawater data (blue) from the eastern subpolar North Atlantic (Crocket et al., 2018), equatorial Atlantic (Zheng et al., 2016), and the Atlantic sector of the Southern Ocean (Hathorne et al., 2015) and pore water data of three sites from the Oregon margin (green, Abbott et al., 2015). Northeast Atlantic leaches comprise Holocene and LGM data from Blaser et al. (2019), generated with the same leach method used in this study. The curved dashed line defines a potential **"**authigenic array" following Du et al. (2016). It is defined by mixing of the most HREE enriched seawater included with the most MREE enriched diagenetic ferro-manganese Nodule reported by Bau et al. (2014) from Pacific Ocean Clarion-Clipperton Fracture Zone. The solid black curved lines define a detrital mixing array between Mid Ocean Ridge Basalts (MORB; Gale et al., 2013), Greenland Archean Crust (GAC; Wedepohl et al., 1991), and Canadian Precambrian shield cratonic rocks (CPS; Shaw et al., 1986). Sample with no corresponding REE data is denoted by an asterix (*).

In-situ pore-water leaching of old cratonic materials delivered to our study site via iceberg rafting may have also influenced some of the authigenic Pb isotope values that we report for MIS 12. Although our detrital Pb isotope records are lower resolution than our authigenic datasets, their apparent relationship during this cold stage may, for example, highlight that in-situ weathering of seafloor sediments was responsible for the suborbital-scale variations in authigenic Pb isotopes that we report for this time (Fig. 4.4d-f). We consider it unlikely, however, that in-situ sediment leaching of ice-rafted materials is responsible for the major orbital-scale trends in our authigenic Pb isotope records for MIS 12/11. No iceberg rafted debris (IRD) records exist for U1302/3 spanning our study interval. Yet we can infer major IRD inputs to our study site occurred until ~423 ka as tracked by the deposition of detrital carbonate layer 12.1 (Fig. 4.4k), so ~9 kyr after the onset of the trend towards radiogenic values is recorded in our records from ~432 ka. In any case, the Al/Nd, Al/Th and Al/Pb ratio compositions of the authigenic fraction for all our samples are significantly lower than the Al/Nd, Al/Th and Al/Pb ratios of their detrital counterparts and are closest to those of deep ocean Fe-Mn crusts that represent a pristine seawater signal (Fig. 4.8). We therefore conclude that the major orbital-scale trends in U1302/3 authigenic Pb isotope data across T5 are not dominated by release of Pb from sediments deposited in the Labrador Sea during this time.

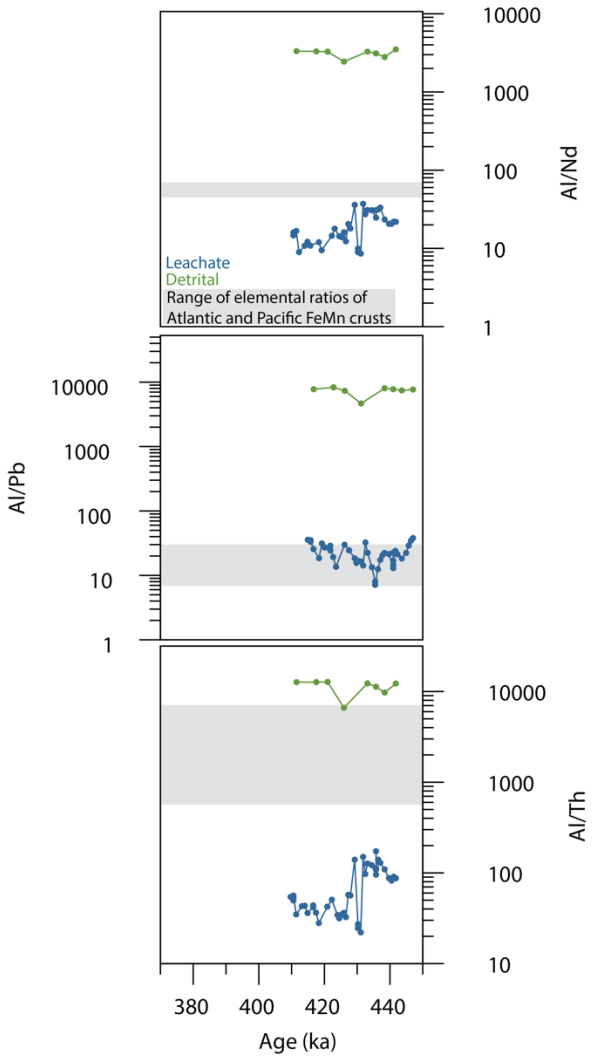

Figure 4.8: Elemental ratios of: **(A)** Al/Nd, **(B)** Al/Pb and **(C)** Al/Pb of leachate (blue) and detrital sediment (green) fractions for MIS 12-11 from IODP Site U1302/03. Note the log scale of y-axis. Grey boxes define the range of elemental ratios associated with Atlantic and Pacific Fe-Mn crusts (Hein et al., 1999).

4.4.3 What do trends in authigenic Pb isotope records from U1302/3 reveal about Laurentide Ice Sheet extent during MIS 12 and its retreat during Termination 5?

MIS 12 is considered to be the most severe glaciation of the Quaternary (e.g., Shackleton, 1987; Raymo, 1997; Poli et al., 2000; Rohling et al., 2014) with global ice-volume during full glacial conditions of this cold stage ~15% greater than during the LGM, and sea-level estimated to have been between ~120–130 m below present (Fig. 4.9a; Elderfield et al., 2012; Rohling et al., 2014; Grant et al., 2014). European ice sheets were at their largest size during this time (Toucanne et al., 2009) having featured the first Quaternary coalescence of the Fennoscandian and British ice-sheets in the North Sea basin (Donner, 1995). It

has also recently been argued that the Columbia Till of the late Middle Pleistocene till sequence in northern Missouri may have been emplaced during the full glacial conditions of MIS 12 and therefore that the LIS may have reached the Missouri River (~39°N) during this cold stage (Rovey and Siemens, 2021). The existence of a large LIS during MIS 12 is consistent with evidence for the occurrence of Heinrich(-like) Event 12.1 during the latest-most stage of this glacial (Hodell et al., 2008; Naafs et al., 2014). It is also consistent with our new U1302/3 authigenic Pb isotope data for MIS 12 (Fig. 4.9d-f).

The relatively unradiogenic values of authigenic Pb isotope data at U1302/3 during MIS 12 (e.g., ~19.6 $^{206}Pb/^{204}Pb$; Fig. 4.9d-f) reflect LIS suppression of chemical weathering on North America, increased deposition of relatively unradiogenic North American-sourced aeolian dust and a reduction in Labrador Current vigour (Fig. 4.9j). The LGM-like nature of most of these values (n = 7 out of 11) therefore shows that the Hudson Bay region of North America was occupied by a thick ice sheet during this time (Fig. 4.3d-f). The more radiogenic (sometimes Holocene-like) subset of authigenic Pb isotope values that we report for MIS 12 (n = 4 out of 11) may reflect increases in microorganism-mediated chemical weathering of the SP beneath the LIS (Wadnam et al., 2010) and Pb runoff as it shifted from a cold-based to warm-based ice sheet during minor suborbital-scale reductions in its volume/spatial extent (cf. Gutjahr et al., 2014). They are more likely, however, to reflect in-situ seafloor sediment leaching of the U1302/3 terrigenous fraction (see discussion above in Section 4.4.2). Regardless, the orbital-scale trend towards more radiogenic values from ~432 ka records an increase in chemical weathering of North American bedrock due to the onset of LIS retreat during T5. Hudson Bay-sourced detrital carbonate layers are much more common in the U1302/3 stratigraphy for MIS 12 than they are in equivalent-aged central North Atlantic sediments (compare Fig. 4.9c). Rather than reflecting classic Hudson Bay-sourced Last Glacial-like Heinrich events, detrital layers 12.3 and 12.2 at U1302/3 therefore likely owe their origin to debris-flows initiated by LIS drainage events. The second of these layers (12.2) is seemingly the sedimentological expression of the onset of LIS retreat during T5 in Labrador Sea sediments.

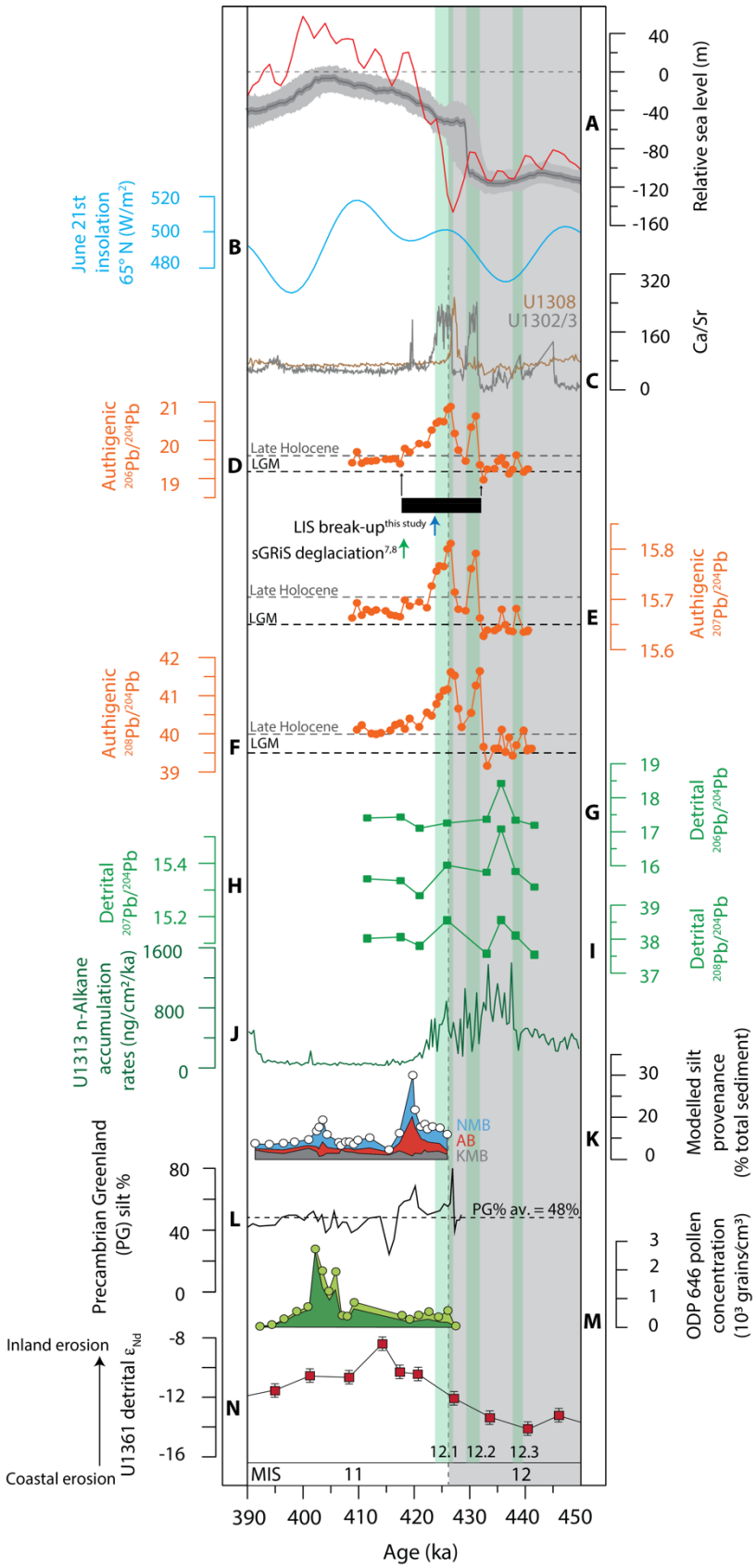

Caption overleaf

The collapse of the Hudson Bay Ice Saddle during MIS 11 is not documented in U1302/3 sediments by a red detrital layer (*sense stricto*) as it was during MIS 5e (Fig. 4.4j). In the absence of a layer of this nature, a latest possible age for its collapse can instead be inferred from the time at which the most radiogenic values were recorded in deglacial authigenic Pb isotope data from our study site (Fig. 4.3d; also see Chapter 3). In the case of MIS 11, these peak values are, however, masked by the deposition of Heinrich-event layer 12.1, ~427 ka (Fig. 4.9). We therefore propose that this Heinrich event itself represents the final collapse of the Hudson Bay Ice Saddle and thus of the LIS during T5. These observations demonstrate that LIS collapse occurred on North America during the first of the two precessional-paced maxima in insolation associated with MIS 11 (Fig. 4.9b).

Figure 4.9: Palaeoclimate data spanning MIS 12/11 and Termination 5: **(A)** Red Sea relative sea-level (RSL) record with 95% probability interval for the RSL data (dark grey envelope) and 95% probability interval for the probability maximum (light grey envelope; Grant et al., 2012). Also shown is a benthic foraminiferal-derived seawater-δ^{18}O-based relative sea-level (RSL) record from Ocean Drilling Program Site 1123 (red line; Elderfield et al. (2012); **(B)** Insolation forcing at 21st June 65°N (W/m^2; Laskar et al., 2004); **(C)** Orphan Knoll IODP Site U1302/03 and central subpolar North Atlantic IODP Site U1308 (grey and brown, respectively) XRF scanning Ca/Sr ratios (Channell et al., 2012). The misalignment in time of the Ca/Sr ratio expression of Heinrich detrital layer 12.1 from these two sites is due to age model discrepancies; Pb isotope ratios of authigenic Fe-Mn oxyhydroxides: **(D)** ^{206}Pb/^{204}Pb; **(E)** ^{207}Pb/^{204}Pb; **(F)** ^{208}Pb/^{204}Pb (T1 and T2, Parker et al., in revision; Chapter 3; T5, this study); Pb isotope ratios of detrital sediment fraction: **(G)** ^{206}Pb/^{204}Pb; **(H)** ^{207}Pb/^{204}Pb; **(I)** ^{208}Pb/^{204}Pb ratios of Site U1302/3 (T1 and T2, Parker et al., in revision; Chapter 3; T5, this study). "Detrital" refers to the full digestion of the authigenic-free fraction of marine sediment. Late Holocene and LGM values highlighted by horizontal dashed lines; **(J)** Site U1313 n-alkane non-reworked (ng/g) record (Naafs et al., 2012); **(K)** Median inferred provenance of silt deposited at Site MD99-2227 on North Atlantic Eirik Drift - estimated an Sr-Nd-Pb isotope mixing model expressed as percent of total sediment derived from the Ketilidian Mobile Belt (KMB; grey), Archean Basement (AB; red) and Nagssugtoqidian Mobile Belt (NMB; blue) terranes. Provenance estimates do not sum to 100% because they do not include clay or sand size fractions (Reyes et al., 2014). **(L)** Modeled contribution of Precambrian Greenland (PG) % silt to sediments deposited at Site MD99-2227 based on a (Mrs/Ms) unmixing model, whereby the ratio of saturation remanence (Mrs) to saturation magnetization (Ms) is used as a proxy for ferrimagnetic grain size with PG silt-sized sediments being magnetically coarser ((Mrs/Ms range 0.03–0.1; Hatfield et al., 2016). The average PG mixing of 48% is shown by a dashed line; **(M)** Labrador Sea ODP Site 646 pollen data (de Vernal and Hillaire-Marcel, 2008), showing Picea (dark green) and total (minus Pinus; light green) pollen concentrations. Site 646 data plotted on the MD99-2227 age model following Reyes et al. (2014); (N) IODP Site U1361 detrital sediment Nd isotopes offshore East Antarctic Wilkes Subglacial Basin. Arrows indicate coastal erosion of Lower Paleozoic granitoids versus inland erosion of FLIP/Beacon lithologies (error bars are 2 s.d. external reproducibility; Wilson et al., 2018). Horizontal black bars (D) highlight intervals over which we infer enhanced supply of dissolved radiogenic weathered material from the Superior Province craton exposed following Laurentide Ice Sheet retreat in the Hudson Bay region during Termination 5. Blue arrow highlights inferred timing of LIS break up (so Hudson Bay Ice Saddle collapse; this study). Horizontal green arrow highlights inferred timing of near-complete deglaciation of southern Greenland Ice Sheet (7 = Hatfield et al., 2016; 8 = Reyes et al., 2014).

The time from which authigenic Pb isotope data from Orphan Knoll first become late Holocene-like (e.g., ~19.6 $^{206}Pb/^{204}Pb$) provides a subsequent marker for the total loss of the LIS during deglaciation (so from when glaciation of northeast North America was mainly restricted to the Canadian Arctic Archipelago). Unlike during MIS 5e and 1, the onset of late Holocene-like values in our U1302/3 authigenic Pb isotope records is, however, diachronous during MIS 11 and occurs between ~424 and ~418 ka during MIS 11 (Fig. 4.9d-f). Given the detrital-like REE signature of the samples that define this transition (Fig. 4.7), its diachronous nature most likely reflects that its precise timing in our records may be influenced by in-situ sea-floor weathering (see Section 4.4.2). Regardless, the latest likely age for this transition (of ~418 ka), which seemingly occurred during the middle of the precessional-paced insolation minima during MIS 11, implies that any relapse to more glacial-style conditions proposed for this time (by, e.g., Loulergue et al., 2008; Dickson et al., 2009; Tzedakis et al., 2009) did not lead to any substantial LIS regrowth. We therefore conclude that it is highly likely that LIS deglaciation was completed prior to the onset of the second weak precessional-paced cycle in insolation during MIS 11.

According to our authigenic Pb isotope records, LIS retreat during T5 occurred over ~15-kyr (Fig. 4.9d-f). This duration is highly comparable to its history of break-up during the last deglaciation (which occurred over ~17-kyr; Chapter 3). These observations strongly suggest that the apparently protracted nature of deglaciation during T5 (Rohling et al., 2010; Barker et al., 2019) is therefore unlikely to have been dictated by the pace of LIS retreat. According to the available records, global sea-level increased by at least a further +20 m following LIS deglaciation during MIS 11 (Fig. 4.9a), which our new authigenic Pb isotope records indicate must have been due to melting of the Fennoscandinavian, Greenland and/or Antarctic ice-sheets.

Precambrian-aged silt is discharged from glaciated regions of Greenland into the Western Boundary Undercurrent and deposited at Eirik Drift south of Greenland (Colville et al., 2011). The proportion of Precambrian Greenland (PG)-sourced silt in Eirik Drift sediments is thought to be highest during intervals of Greenland Ice-Sheet retreat and lowest when Greenland is unglaciated (Colville et al., 2011). PG-silt discharge to Eirik Drift sediments over the past ~430 kyr has been tracked successfully using their magnetic properties (Hatfield et al., 2016) and

Sr-Nd-Pb isotope compositions (Colville et al., 2011; Hatfield et al., 2016; Reyes et al., 2014). A large reduction in PG-silt in sediments deposited on Eirik Drift from ~417 ka (Fig. 4.9k–l) is interpreted to record the timing of near complete deglaciation of southern Greenland during MIS 11 (Reyes et al., 2014; Hatfield et al., 2016). Southern Greenland deglaciation from this time is reflected in the high abundance of pollen in sediments deposited on Eirik Ridge at Ocean Drilling Program Site 646 (de Vernal and Hillaire-Marcel, 2008; Fig. 4.9m). It is also seemingly recorded in the Pb isotope composition of seawater bathing U1302/3 from ~418 ka. While $^{206}Pb/^{204}Pb$ and $^{208}Pb/^{204}Pb$ ratios of our authigenic data remain unchanged from this time, $^{207}Pb/^{204}Pb$ ratios shift to more unradiogenic values by ~0.4 units (Fig. 4.9e). Although the REE signature of our MIS 11 samples highlights that the precise timing of this shift may be influenced by in-situ sea-floor weathering (see Fig. 4.7 and Section 4.4.2), the persistence of depleted $^{207}Pb/^{204}Pb$ ratios throughout the remainder of our record highlights that this signal is real. In a modern-day-like setting (so one where glaciation is restricted to Greenland), only increased chemical weathering of the Ketilidian Mobile Belt of southern Greenland could explain this change in the Pb isotope composition of the deep-waters bathing U1302/3 from this time. This is because while the average $^{206}Pb/^{204}Pb$ and $^{208}Pb/^{204}Pb$ compositions of the Ketilidian Mobile Belt are similar to those of seawater bathing U1302/3 during the modern, it is the only radiogenic regional source that is also relatively depleted in $^{207}Pb/^{204}Pb$ (compare U1302/3 ‘late Holocene’ and Ketilidian Mobile Belt mean and median Pb isotope compositions in Fig. 4.3). Our new authigenic Pb isotope records spanning MIS 11 may therefore also be consistent with the idea that southern Greenland was deglaciated by ~418 ka during this interglacial. We note that southern Greenland Ice Sheet retreat during the Eemian (e.g., Colville et al., 2011), may also be evident in a similar, but shorter-lived, signal for enhanced chemical weathering of the Ketilidian Mobile Belt in U1302/3 authigenic data spanning MIS 5e between ~124–119 ka (see Fig. 4.4e).

During the Holocene, LIS Hudson Bay Ice Saddle collapse (Carlson, 2008; Dalton et al., 2020; Parker et al., Chapter 3) and southern Greenland Ice Sheet retreat (Colville et al., 2011; Hatfield et al., 2016) culminated at the same time (~8.4 ka; Fig. 4.4f). During MIS 5e, southern Greenland Ice Sheet retreat continued, however, for ~10 kyr (Hatfield et al., 2016) after LIS Hudson Bay Ice Saddle collapse (Fig. 4.4). During MIS 11, southern Greenland Ice Sheet collapse (from

~418 ka; Reyes et al., 2014; Hatfield et al., 2016) also appears to have lagged LIS collapse (from ~424 ka; this study), but according to our records only by ~6 kyr. These new observations provide important new constraints on the deglacial histories of Northern Hemisphere ice-sheets for those that seek to correct MIS 11 sea-level records for GIA (e.g., Raymo and Mitrovica, 2012).

If both LIS and southern Greenland Ice Sheet deglaciation occurred prior to ~418 ka, and with no known records of Fennoscandinavian Ice Sheet retreat during this time, the sea-level highstand associated with the second peak in precessional-paced insolation during the latter half of MIS 11, may well reflect additional ice-mass loss from the Antarctic ice sheets. This scenario is supported by recently published evidence (from radiogenic-isotope-based provenance study of IODP Site U1631 sediments) for significant ice margin retreat and/or thinning in the vicinity of the Wilkes Subglacial Basin of East Antarctica by the late stages of MIS 11 (Fig. 4.9n; Wilson et al., 2018). Collectively, these observations highlight that the sea-level rise reported for the second half of MIS 11 by Raymo and Mitrovica (2012) of ~+6–13 m relative to present is likely to be a more realistic prediction than that which can be inferred from the Red Sea sea-level record for this time (of ~+1 m, Fig. 4.9a; Rohling et al., 2010).

4.5 Conclusions

We present new high-resolution records of authigenic Fe-Mn oxyhydroxide-derived Pb isotopes from Orphan Knoll IODP Site U1302/3 for MIS 12 and 11 (~440-410 ka) that record what is arguably the largest Northern Hemisphere deglaciation of the Quaternary, Termination (T) 5, ~424 ka. While the history of ice-sheet retreat on Greenland is well documented for this glacial termination (by, e.g., de Vernal and Hillaire-Marcel, 2008; Reyes et al., 2014; Hatfield et al., 2016), nothing is known about the deglacial history of the most volumetrically important continental ice sheet in the Northern Hemisphere, the North American Laurentide Ice Sheet (LIS) during this time. To address this gap in our knowledge, we compare the evolution of orbital-scale radiogenic excursions evident in our new MIS 12/11 records of T5 and previously published authigenic Pb isotope datasets from our study site spanning T2, ~130 ka (Parker et al., Chapter 3) and T1, ~14 ka (Crocket et al., 2012), which we argue record differences in the pace of LIS retreat in the Hudson Bay region of North America during these glacial terminations.

The radiogenic excursions recorded by U1302/3 Pb authigenic Pb isotope records for T5, T2 and T1 reflect increases in chemical weathering of North American bedrock and solute flux to Orphan Knoll associated with LIS retreat (Crocket et al., 2012; Chapter 3). According to these records, LIS retreat during T5 began ~432 ka and occurred over a similar timescale (~15 kyr) to that observed for T1 (~17 kyrs), but not as rapidly as during T2 (~7 kyr). It has been shown (in Chapter 3) that the collapse of the Hudson Bay Ice Saddle during T2 and T1 is tracked by peak radiogenic values in deglacial U1302/3 authigenic Pb isotope data. Using this marker, we infer from our new MIS 12/11 datasets that LIS break-up during T5 (and therefore the collapse of the Hudson Bay Ice Saddle) was caused by Heinrich event 12.1 ~424 ka. A subsequent decrease in the $^{207}Pb/^{204}Pb$ of seawater bathing our study site from ~418 ka most likely tracks increased chemical weathering of the Ketilidian Mobile Belt of southern Greenland, which records from Eirik Drift (e.g., Reyes et al., 2014; Hatfield et al., 2016) show was probably caused by near-full deglaciation of the southern Greenland Ice Sheet during MIS 11. We therefore conclude that southern Greenland deglaciation lagged LIS break-up during this interglacial by ~6 kyr.

T5 is known as a ‘protracted deglaciation’ because the full interglacial-glacial transition in mean global sea-level between MIS 12 to 11 was seemingly not reached until the second of two weak precessional-paced maxima in insolation associated with MIS 11 was crossed (at ~410 ka; Rohling et al., 2010). It has also been proposed that MIS 11 was characterized by a brief relapse to more glacial-style conditions during the intervening insolation minima (Loulergue et al., 2008). Our new records show, however, that any cooling during this time did not lead to LIS regrowth. Most importantly, our new records demonstrate that LIS break-up and southern Greenland deglaciation during MIS 11 occurred prior to the start of the second of the two precessional-paced maxima in insolation associated with this interglacial. This observation may therefore highlight that the ‘protracted' nature of T5 and sea-level highstand associated with the second peak in precessional-paced insolation during the latter half of MIS 11 reflect additional ice-mass loss from the Antarctic ice sheets. Sea-level rise during the second half of MIS 11 is most likely to sit at the upper-end of estimates (i.e., +6–13 m by, e.g., Raymo and Mitrovica (2012)).

Chapter 5: The Nd isotope composition of the deep western North Atlantic during the Last Glacial Cycle: implications for the evolution of the preformed composition of northern sourced waters and Plio-Pleistocene climate

Chapter 5 represents the foundations for a manuscript that will be prepared for submission to Paleoceanography and Paleoclimatology. It is based on low-resolution fish-debris Nd isotope data generated from IODP Site U1313 for the Last Glacial Cycle (~130–45 ka) by David C. Lang (D.C.L.) at the School of Ocean and Earth Science, University of Southampton. Covid restrictions (which stranded Rebecca L. Parker, R.L.P., in New Zealand from 2020) prevented R.L.P. from planned efforts to increase the resolution of this LGC fish debris dataset, to generate an equivalent LGC detrital sediment ε_{Nd} record from this site, and to generate fish debris-based ε_{Nd} data from IODP Site U1313 prior to the

LGC that would have complimented the low resolution Quaternary record presented by Kim et al. (2021) for DSDP Site 607. R.L.P led this project with contributions as follows: Ian Bailey (I.B.) was responsible for project conception and supervised R.L.P. R.L.P acquired funding, made the interpretations presented and co-wrote the manuscript with I.B. Paul. A. Wilson (P.A.W.) paid for the analyses. Tom B. Chalk generated the compiled LGC Nd isotope record for IODP Site U1313 and V30-97. Matthew J. Cooper and James A. Milton helped D.C.L to generate Nd isotope data, oversaw instrumentation and helped with analysis. Kate Littler and P.A.W. co-supervised R.L.P.

5.1 Abstract

The neodymium isotopic composition of seawater (ε_{Nd}) has been an important proxy in the palaeoceanographer's toolkit for reconstructing deep water-mass mixing in the geological past. Its use has traditionally relied on the assumption that the ε_{Nd} of northern sourced waters (NSW) has been constant through time. Recently published records from the shallow North Atlantic demonstrate, however, that NSW ε_{Nd} may have been up to ~4 epsilon units more radiogenic during the Last Glacial Maximum (LGM) than it is today. Our understanding of the evolution of NSW for older times remain uncertain, as do the mechanisms responsible for driving these changes. To this end, we present the first fish debris-based ε_{Nd} record from IODP Site U1313 spanning the entire Last Glacial Cycle (LGC). We combined this record with recently published datasets from the same site and others nearby to create the first fully error-propagated record of LGC changes in NSW ε_{Nd} bathing the deep mid-latitude western North Atlantic, which we infer tracks the evolution of the composition of this water-mass end-member over the past ~130 kyr. Our new record shows that while NSW ε_{Nd} during the last interglacial and the Holocene was highly comparable, it was up to ~1 epsilon unit more radiogenic during MIS 5d and 5b, ~2 epsilon units more radiogenic during MIS 4, and ~3 epsilon units more radiogenic during the LGM. We propose that reductions in the entrainment of unradiogenic Labrador Sea Water and Subpolar Mode Waters into radiogenic deep-water formed in the Nordic Seas were responsible for setting NSW ε_{Nd} during MIS 5 to MIS 3, as were contemporaneous

glacial-erosion-driven changes in the end-member composition of these NSW-constituent water masses. Yet we contend that only a shift in the location of NSW formation from an ice-covered Nordic Seas to south of Iceland during MIS 2 and partial dissolution of radiogenic basaltic volcanic phases deposited in the Iceland Basin following a slowdown in Atlantic Meridional Overturning Circulation (AMOC) can explain the full LGM-Holocene difference in NSW ε_{Nd}. Further-still, we argue that this LGC framework can be applied to North Atlantic Plio-Pleistocene ε_{Nd} records to hind-cast the oceanographic conditions of this region in deeper time. This exercise shows that interglacial trends in NSW ε_{Nd} over the past ~3.3 Ma were most likely controlled by the baseline warm-stage extent of northern hemisphere glaciation (NHG). It also demonstrates that while extensive Nordic Seas sea ice, LGM-magnitude AMOC slowdowns and NSW formation in the Iceland Basin likely occurred during the most prominent cold stages since the onset of the Quaternary, ~2.6 Ma, they were not persistent features of cold stages until the onset of the Mid Pleistocene Transition, ~1 Ma.

5.2 Introduction

One prominent theory proposed to help explain a drop of ~90 ppm in the atmospheric concentration of CO_2 during the Last Glacial Cycle (LGC) involves enhanced oceanic carbon storage via deep-water stratification due to a "two-cell" circulation structure in the Atlantic Ocean (e.g., Sigman et al., 2010). It is suggested that this theory is supported by benthic foraminiferal carbon isotope ($\delta^{13}C$ and $\Delta^{14}C$) and B/Ca-based reconstructions of water-mass provenance which are traditionally argued to show that, unlike for the modern, old, carbon-rich and nutrient-depleted southern-sourced waters (SSW) occupied depths greater than ~2500 m in both the western and eastern North Atlantic during the Last Glacial Maximum (LGM) ~21 ka (e.g., Curry and Oppo, 2005; Yu et al., 2008; Chalk et al., 2019).

Studies of the Nd isotope (ε_{Nd}) composition of bottom waters bathing the deep Atlantic during the LGM have also reported evidence for northward penetration and shoaling of SSW, but the magnitude of SSW expansion at this time inferred from ε_{Nd} data is generally less than that based on $\delta^{13}C$ data (e.g., Böhm et al.,

2015; Howe et al., 2016). The ε_{Nd} of deep-waters is widely considered to behave more conservatively than its $\delta^{13}C$ composition since it is not affected by changes in the carbon cycle (van de Flierdt et al., 2016; Ravelo and Hillaire-Marcel, 2007). The perceived quasi-conservative nature of ε_{Nd} has led to the suggestion that the larger signal of SSW incursion based on North Atlantic $\delta^{13}C$ records reflects greater remineralisation of carbon in deep-waters (Howe et al., 2016) under a more sluggish glacial deep Atlantic circulation (Böhm et al., 2015; Ng et al., 2018). It remains unclear, though, how much of the disparity between conclusions drawn on Atlantic water-mass provenance for the LGM based on ε_{Nd} and benthic $\delta^{13}C$ data can also be attributed to our understanding of watermass end-member compositions, which for ε_{Nd} remain the most uncertain.

Traditionally, it has been assumed that end-member ε_{Nd} compositions of northern sourced waters (NSW; today –12.4 ± 0.4; Lambelet et al., 2016) and SSW (–9.0 ± 0.4; Stichel et al., 2012) did not change appreciably on glacial-interglacial timescales (e.g., Foster et al., 2007; Piotrowski et al., 2005; Böhm et al., 2015; Howe et al., 2016). Yet it has recently been argued that the distribution of Nd in the LGM Atlantic Ocean is better explained by a change in the preformed NSW ε_{Nd} signature (Du et al., 2020; Abbott et al., 2022). Indeed, a variety of recently generated high-resolution ε_{Nd} records highlight the possibility that NSW ε_{Nd} may have been ~4 epsilon units higher during the LGM compared to today (e.g., Wilson et al., 2014; Zhao et al., 2019; Pöppelmeier et al., 2021) while SSW ε_{Nd} may have been ~3.5 epsilon units higher (Piotrowski et al., 2012; Huang et al., 2020).

Today, the NSW that bathes the deep northwest North Atlantic (Lower NADW, LNADW) is dominated by radiogenic Denmark Straits Overflow Water (DSOW, ε_{Nd} = ~–8.4; Lacan and Jeandel, 2004a). It acquires its relatively unradiogenic ε_{Nd} composition, though, through entrainment of Labrador Seawater (LSW, ε_{Nd} = ~–14.2 ± 0.3; Lambelet et al., 2016) and North Atlantic Current (NAC)-sourced Subpolar Mode Waters (SPMW, ε_{Nd} = –14.8; Lacan and Jeandel, 2004a) as it overflows the Denmark Strait, and through additional mixing with western Lower Deep Water (LDW) at ~50˚N (modified Antarctic Bottom Water, ε_{Nd} = –12.2 ± 1.0; Lambelet et al., 2016). It is proposed (hereinafter known as the 'top-down' hypothesis) that NSW ε_{Nd} was higher during the LGM than today because extensive northern hemisphere ice-sheets at this time reduced chemical

weathering of old unradiogenic cratonic rocks on Canada and Greenland making Labrador Seawater (LSW) more radiogenic (Zhao et al, 2019; Pöppelmeier et al., 2020). An alternative interpretation is that the higher values of NSW ε_{Nd} existed during the LGM because LSW formation did not occur at this time (Hillaire-Marcel et al., 2001a; 2011) and the location and mode of NSW formation shifted south of Iceland, due to sea-ice expansion in the Nordic Seas (Duplessy et al., 1988; Sarnthein et al., 1994). Here, its preformed composition was made more positive in the Iceland Basin by 'bottom-up' conservative processes (i.e., partial dissolution of radiogenic authigenic volcanic phases), enhanced by a more sluggish glacial circulation (hereinafter known as the 'bottom-up' hypothesis; Du et al., 2020). The more zonal (i.e., E-W) flow direction and southerly (~37-43 N˚) location of the NAC during the LGM (Calvo et al., 2001) may also have led to a change in the preformed ε_{Nd} composition of NSW because a southward expansion of the polar front of this magnitude would have prevented SPMW from being entrained into NSW (Crocker et al., 2016), regardless of whether it formed north or south of Iceland at this time. Putting the mechanisms involved aside, the idea that NSW ε_{Nd} can change appreciably on orbital timescales has been used to argue that more radiogenic ε_{Nd} values reported for the deep Northwest Atlantic during the LGM reflect changes in the ε_{Nd} of watermass end-members and that, contrary to the conclusions drawn based on $\delta^{13}C$, the deep North Atlantic has remained bathed in NSW since the LGM (Pöppelmeier et al., 2020; 2021; Kim et al., 2021).

In this study, we build on the consequences of these ideas as presented in Pöppelmeier et al. (2020; 2021) and Du et al. (2020). We do this by reporting the first fish debris ε_{Nd} record from a single core in the deep mid-latitude western North Atlantic spanning the entire LGC. To generate this record, we have studied Integrated Ocean Drilling Program (IODP) Site U1313 (~41˚N, 3427m water depth; Fig. 5.1). Site U1313 (Lang et al., 2016) and its predecessor Deep Sea Drilling Project (DSDP) Site 607 (Raymo et al., 1990) have been benchmark sites for monitoring the water-mass structure of the deep Plio-Pleistocene North Atlantic. Our new record compliments recently published ε_{Nd} datasets from DSDP Site 607 and near-by V30-97 (that span the past 1.5 Myr; Kim et al., 2021) and IODP Site U1313 (that spans 25-90 ka; Pöppelmeier et al., 2021). Today these sites are situated in the core of modern LNADW and lie in a region predicted by

Pöppelmeier et al. (2020; 2021) and Du et al. (2020) to have been bathed entirely by NSW during the LGM.

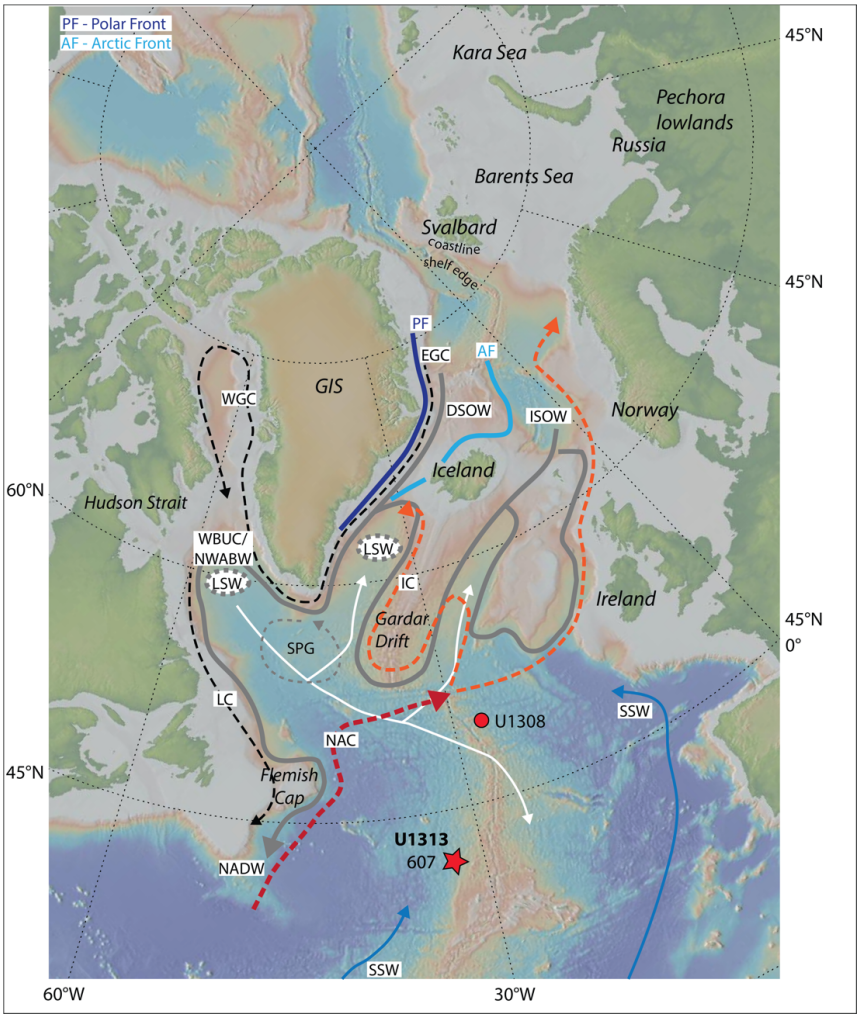

Figure 5.1: Location of IODP Site U1313 (red star) and Site U1308 (red circle). Also shown is a schematic of modern pathways of deep (solid lines) and surface (dashed lines) waters relevant to this study and two proposed locations of LSW production (Duplessy et al., 1988; Sarnthein et al., 1994); SPG = Subpolar Gyre. ISOW = Iceland-Scotland Overflow Water. DSOW = Denmark-Scotland Overflow Water. WBUC = Western Boundary Undercurrent. NWABW = Northwest Atlantic Bottom Water. SSW = Southern Source Water. LSW = Labrador Sea Water. LC = Labrador Current. NADW = North Atlantic Deep Water. WGC = West Greenland Current. EGC = East Greenland Current. NAC = North Atlantic Current. IC = Irminger Current. PF = Polar Front. AF = Arctic Front. Ocean current pathways redrawn from Blake-Mizen et al. (2019). Front locations redrawn from Mokeddem and McManus (2016).

Herein we proceed assuming that if the northwest Atlantic was bathed entirely by NSW during the cold-climate extreme of the LGM then it was throughout the LGC. By doing so, we address the following questions: 1) How does NSW ε_{Nd} evolve during the LGC at Site U1313? 2) What North Atlantic oceanographic and climatic factors are responsible for controlling the preformed composition of NSW that is recorded in this ε_{Nd} record? We examine in turn the contribution that the 'top-

down' hypothesis (chemical weathering; Section 5.4.3.1), Labrador Sea Water (LSW) production (Section 5.4.3.2), southward migration of the polar front (Section 5.4.3.3) and the 'bottom-up' hypothesis (Section 5.4.3.4) may have played in explaining the trends in this new record. By assuming deep northwest North Atlantic was also continuously bathed by NSW throughout the Plio-Pleistocene, we then use these observations to infer changes in North Atlantic oceanography and climate during important intervals since ~3.3 Ma using previously published ε_{Nd} datasets from Site U1313 (Lang et al., 2016; Kirby et al., 2020; Pöppelmeier et al., 2021) and Site 607 (Kim et al., 2021).

5.3 Methods

5.3.1 Study site, sampling and chronology

IODP Site U1313 (41˚N, 32.4˚W) is located at the base of the upper western flank of the Mid-Atlantic Ridge at a water depth of 3426 m (Fig. 5.1). Today, Site U1313 is bathed in LNADW (–12.4 ± 0.4; Lambelet et al., 2016). In the subpolar North Atlantic, LNADW is composed mostly (50%) of relatively radiogenic DSOW (–8.4 ± 1.4; Lacan and Jeandel, 2004a), which entrains some unradiogenic LSW (–13.7 ± 0.9; Lambelet et al., 2016) and SPMW (–14.8; Lacan and Jeandel, 2004b) as it overflows the Denmark Strait sill at ~600 m. To extend a previously published last glacial-Holocene fish-debris based Nd isotope record for Site U1313 spanning 0-34 ka (Lang et al., 2016) to characterise all of the LGC, we analysed 20 additional samples from 'out-of-splice' cores from Holes A and D every 12 to 42 cm (~24 cm on average) from 2.50-6.50 meters composite depth (mcd). Composite depths were assigned to these samples by correlating the stratigraphies of these holes to the Site U1313 primary splice using shipboard-derived volume-specific magnetic susceptibility data (Chalk et al., 2019). The published age model we use for our LGC record (Naafs et al., 2013b) is based on correlation of Heinrich (H-) layers in the Site U1313 stratigraphy (tracked by X-ray diffraction dolomite/calcite ratio data) to X-ray fluorescence-based Ca/Sr elemental data that track the position of H-layers in the stratigraphy of northeast North Atlantic Ocean IODP Site U1308 (~50˚N), which has a high resolution benthic $\delta^{18}O$ stratigraphy on LR04 ages (Hodell et al., 2008). When placed on

this age model, our LGC record for Site U1313 has an average temporal resolution of ~2.9 kyr. We compare our new composite fish-based Nd isotope LGC record to previously published bulk-sediment authigenic ε_{Nd} records from Site U1313 spanning the past ~90 kyr (Lippold et al., 2016; Pöppelmeier et al., 2021) and low resolution foraminiferal coating-based Nd isotope record from Site V30-97 at the same location (41˚N, 32.6˚W, 3371 m water depth; Kim et al., 2021).

5.3.2 Nd-isotope preparation and analysis

Nd was extracted from fish debris (n = 20) following the protocol of Lang et al. (2016). The Nd isotopic compositions were measured on a Neptune multicollector–inductively coupled plasma–mass spectrometer at National Oceanography Centre Southampton. Instrumental mass fractionation was corrected by normalising $^{146}Nd/^{144}Nd$ to 0.7219 and a secondary normalisation to $^{142}Nd/^{144}Nd$ = 1.141876 (Vance and Thirwall, 2002). Total procedural blanks averaged 35 pg for the fish debris. The samples were also bracketed by the JNdi-1 standard reference solution normalized to the accepted value of $^{143}Nd/^{144}Nd$ = 0.512115 (Tanaka et al., 2000). External reproducibility of the JNdi standards was ± 0.000006 (2 s.d.), corresponding to an external error of ± 0.13 ε_{Nd} (2 s.d.).

5.4 Results and discussion

5.4.1 Evolution of fish debris ε_{Nd} at Site U1313 during the LGC

A new record of Site U1313 fish debris ε_{Nd} for the LGC is shown in Figure 5.2 (full dataset in Appendix B1) alongside previously published fish debris-based (Lang et al., 2016) and bulk sediment authigenic-based (Lippold et al., 2016; Pöppelmeier et al., 2021) ε_{Nd} data from this site, as well as foraminiferal coating-based ε_{Nd} data from Site V30-97 (Kim et al., 2021). The strong correspondence in ε_{Nd} values between these records demonstrates that each of these archives faithfully tracks the Nd isotope composition of bottom waters bathing this region of the deep northwest North Atlantic during the LGC. The ε_{Nd} of waters bathing this region during the last interglacial MIS 5e, ~130 ka, and interstadials MIS 5c, ~100 ka and MIS 5a, 82 ka, (~–13.30 ± 0.13 to –14.00 ± 0.13) is highly

comparable to the range of Holocene values previously reported for Site U1313 (~–13.20 ± 0.13 to –14.60 ± 0.13; Lang et al., 2016; Lippold et al., 2016). Bottom water ε_{Nd} varied by ~1.5 epsilon units on interstadial-stadial timescales throughout MIS 5 with more radiogenic values (~–12.5) associated with cold stages MIS 5d and 5b. The transition between MIS 5/4 is associated with an increase in ε_{Nd} of +1. The maximum ε_{Nd} values obtained during MIS 4 (~–12.0) are not LGM-like (i.e., ~–10.8), a feature of our record that is maintained at Site U1313 throughout MIS 3.

5.4.2 Evaluating the fidelity of using U1313 authigenic ε_{Nd} as a regional record of NSW

It is shown that ε_{Nd} records generated on cores recovered from within the centre North Atlantic ice-rafted debris (IRD) belt (~43-55˚N; Ruddiman, 1977) may not always reflect a regional seawater signal because they can bear an overprint of local detrital inputs (e.g., Lang et al., 2016; Blaser et al., 2019; Du et al., 2020; Abbott et al., 2022). This is probably true of Site U1313 even though it lies south of the southernmost fringe of the IRD belt. It has been argued, for instance, that increased inputs of detrital carbonate sourced from the Canadian Shield (Hudson Bay) to Site U1313 during Heinrich event (HE) 1 is responsible for a millennial-scale unradiogenic excursion in authigenic ε_{Nd} at this site (Lang et al., 2016; Du et al., 2020). The overprint is so significant during HE-1 that it may have masked the ε_{Nd} trend of global ocean circulation associated with Termination (T) 1 in the deep northwest North Atlantic at U1313 by causing ε_{Nd} values from this site to recover to unradiogenic interglacial-like values ~3 kyr earlier than at other deep North Atlantic sites (e.g., Böhm et al., 2015). Clear short-term unradiogenic spikes are also evident in U1313 ε_{Nd} spanning HE-5, HE-4 and HE-2 (Fig. 5.2a-c; Lang et al., 2016; Pöppelmeier et al., 2021; Kim et al., 2021).

Recently, it has been argued that a detrital impact on North Atlantic authigenic ε_{Nd} records is not restricted to times of HE IRD deposition, just that the detrital impact from HE IRD represents the most pronounced example of such overprint signals (Abbott et al., 2022). The strong correspondence between values of bulk detrital sediment and authigenic ε_{Nd} records from the centre of the Last Glacial sub-polar North Atlantic IRD belt at IODP Site U1308 (~50˚N) and far south of it

at, e.g., Ocean Drilling Program (ODP) Site 1063 (~30˚N) during the Last Glacial (Abbott et al., 2022) highlights the important role that remobilisation of detrital sediment Nd may play in setting bottom water ε_{Nd} in this region via benthic flux or directly in the sediment column during early diagenesis, especially during times of reduced AMOC vigour (Du et al., 2020). Although no detrital ε_{Nd} records exist for Site U1313 spanning the LGC, outside of HEs we do not, however, anticipate a dominant role of such non-conservative processes in setting authigenic ε_{Nd} at this site.

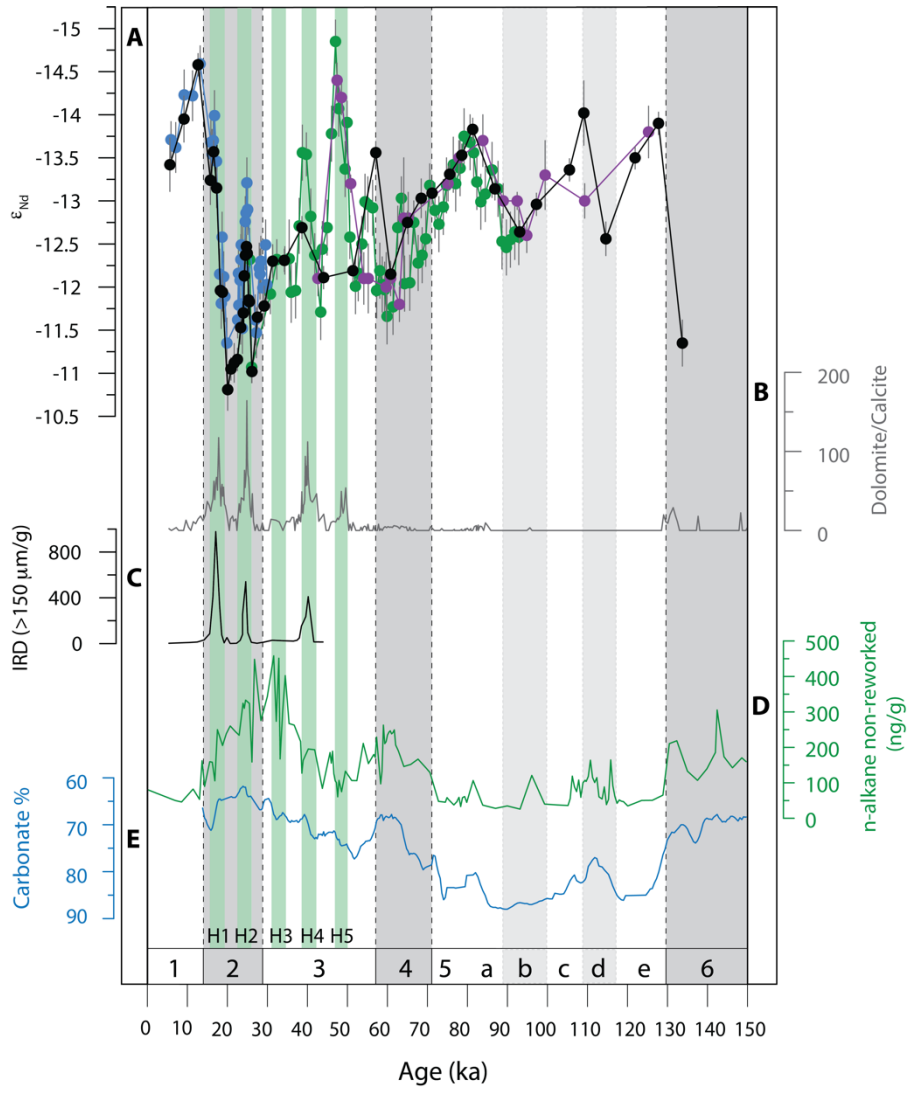

Figure 5.2: ε_{Nd} records from IODP Site U1313 and V30-97 spanning marine isotope stage (MIS) 6-1: **(A)** ε_{Nd} records derived from fish debris (this study and Lang et al., 2016; black circles), authigenic bulk sediment (Lippold et al., 2016; blue circles; Pöppelmeier et al., 2021; green circles) and foraminifera (from Site V30-97; Kim et al., 2021; purple circles) with 2 s.d. **(B)** U1313 dolomite/calcite ratios whereby peaks are associated with detrital carbonate input by ice-berg rafting during Heinrich events (Naafs et al., 2013b). **(C)** U1313 IRD concentration (Lang et al., 2016). **(D)** U1313 n-alkane non-reworked (ng/g) record (Naafs et al., 2012). **(E)** U1313 calcium carbonate percentage (Lang et al., 2014).

The notion that non-conservative processes are unlikely to control the evolution of U1313 fish debris ε_{Nd} we report is supported by three key observations: 1) sedimentation at this site is dominated by pelagic rain from above (Lang et al., 2014) and, unlike ODP Site 1063, is not strongly influenced by lateral advection of sortable silt of potentially varying provenance (and ε_{Nd}). The difference in oceanographic setting between these two sites is reflected by the order of magnitude lower sedimentation rates experienced at U1313 during the Last Glacial (~4-6 cm ka^{-1}; Naafs et al., 2012) compared to Site 1063 (~40-70 cm ka^{-1}; Channell et al., 2012); 2) The terrigenous fraction of U1313 glacial sediments is an admixture of three components, but is dominated by unradiogenic (ε_{Nd} = –14 to –16; pers. comm. Paul A. Wilson; Lang et al., 2014) North American-sourced aeolian dust (Naafs et al., 2012; Lang et al., 2014). It also contains some IRD and volcanic glass (Lang et al., 2016), but outside of HE-layers they constitute minor components (Lang et al., 2016). Because U1313 was located on the southernmost fringe of the North Atlantic IRD belt in cold stages of the past ~2.6 Ma, the terrigenous fraction deposited at this site has instead been dominated by aeolian dust throughout the Quaternary (Lang et al., 2014; Bolton et al., 2018; Kirby et al., 2020); 3) The terrigenous sediment component deposited at U1313 during the onset of Quaternary northern hemisphere glaciation is relatively unradiogenic (ε_{Nd} typically ~–14 to –16; Lang et al., 2014) and is weakly correlated with changes in fish debris ε_{Nd} (Lang et al., 2016).

The concentration of aeolian dust is highest in U1313 sediments deposited during the Last Glacial between ~13–75 ka (MIS 4-2, Fig. 5.2d; Naafs et al., 2012). If circulation in the deep Atlantic was reduced during this time (e.g., Böhm et al., 2015), the resultant longer benthic exposure would have led to the ε_{Nd} of deep-waters bathing U1313 and fish debris preserved at this site converging toward the unradiogenic Nd isotope composition of this dust. Non-conservative processes would therefore have acted to retard, and not amplify, the radiogenic trends recorded by fish debris ε_{Nd} data from U1313 during MIS 4 to 2. We therefore conclude that outside of HEs, the trends in ε_{Nd} data from our study site are a good approximation of the relative changes in the regional watermass signal of NSW in the deep western North Atlantic during LGC ambient climate conditions.

The suggestion that ε_{Nd} data from Site U1313 reflect the evolution of the end-member composition of NSW during the LGC is also supported by the similarity of their values to those from nearby but shallower (by 1 km) Site SU90-03 (~40˚N; Fig. 5.2a). Our U1313 record shows that NSW was at least ~3 epsilon units more radiogenic during the LGM than the Holocene (Fig. 5.2a). This magnitude of change is approximately three-quarters of that inferred for NSW between the LGM-Holocene based on the ε_{Nd} of bottom waters bathing a composite of cores from the northwest North Atlantic New England Slope ('KNR198 '40˚N, ~1.8 km depth; Zhao et al., 2019). Terrigenous sediment deposited on the New England Slope during the LGM is ~3 epsilon units more radiogenic than its Holocene counterparts (see Fig. 2c in Zhao et al., 2019). The difference in the amplitude of LGM-Holocene ε_{Nd} change between U1313 and KNR198 (~3 vs 4 epsilon units) may therefore either reflect that pore-water dissolution of unradiogenic terrigenous materials deposited at U1313 during the LGM acted to decrease the ε_{Nd} of NSW bathing this site during this time and/or that the amplitude of contemporaneous change in records from the New England Slope was inflated through the remobilisation of relatively radiogenic Nd of terrigenous sediments deposited in this region during the LGM.

5.4.3 New insights on NSW ε_{Nd} evolution during the LGC

In Figure 5.3, we present a fully error-propagated record of LGC changes in ε_{Nd} at U1313, its predecessor 607 and nearby V30-97, constructed using all the available Nd isotope records from these sites. In assuming that these sites were continuously bathed in NSW during the LGC, we argue that variations in ε_{Nd} in this record track the relative evolution of the pre-formed NSW end-member during the LGC. We examine in turn the contribution that the 'top-down' hypothesis (chemical weathering; Section 5.4.3.1), Labrador Sea Water (LSW) production (Section 5.4.3.2), southward migration of the polar front (Section 5.4.3.3) and the 'bottom-up' hypothesis (Section 5.4.3.4) may have played in explaining the trends in this new record. To facilitate this analysis, we use reconstructed histories of North American chemical weathering (Batchelor et al., 2019; Parker et al.; Chapter 3), LSW formation (Hillaire-Marcel et al., 2001a, b; 2011), Polar Front latitudinal migration (Sarnthein et al., 1994; Mokeddem et al., 2014;) and AMOC (Böhm et al., 2015) alongside a simple mass balance exercise that explores the

sensitivity of NSW ε_{Nd} to changes in mixing and preformed composition of constituent end-member water masses that make up NSW (see Appendix B2).

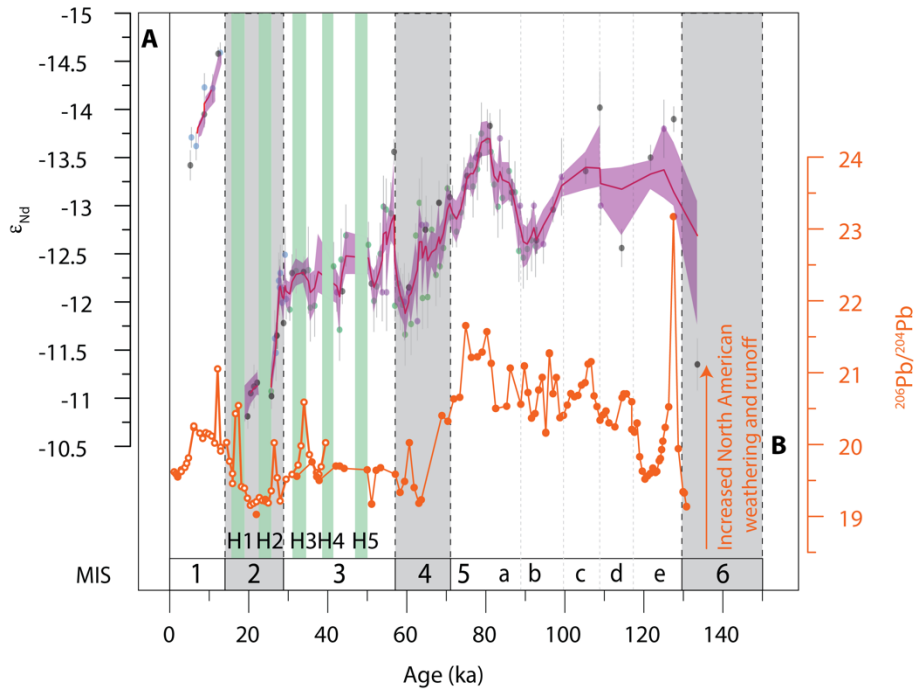

Figure 5.3: Compiled ε_{Nd} records from IODP Site U1313 and Site V30-97 spanning Marine Isotope Stage (MIS) 6-1 compared to 'top down' continental weathering. **(A)** Compiled ε_{Nd} record for U1313 generated using a gaussian distribution with monte carlo error propagation; by splicing the U1313 and V30-97 records together (including uncertainties) with a matrix of uncertainties for each age, which are randomly assigned within the 2 s.d. of the data in a normal distribution around the central value. The record is split at ~90 ka to smooth the high (0-90 ka) and low (90-130 ka) resolution intervals separately. For each interval, 1000 smoothed records are generated by sampling within the uncertainty with the smoother for each using parameters drawn from a random selection of the 8 and 6 closest data points for the high and low resolution intervals, respectively. Their importance is weighted by the distance in kyr away from the part being smoothed, The mean of all smoothed records is line of best fit (red line) with 95% confidence interval (purple shading). H-layer data is excluded as it does not represent seawater ε_{Nd} values **(B)** IODP Site U1302/3 authigenic Fe-Mn oxyhydroxide Pb isotopes isotopes (Parker et al., Chapter 3).

5.4.3.1 Evaluating the role of the 'top-down' hypothesis in controlling the evolution of NSW ε_{Nd} during the LGC.

One hypothesis proposed to explain how the preformed ε_{Nd} of NSW could have been more radiogenic during the LGM relative to today invokes a substantial reduction in chemical weathering of the unradiogenic Canadian Shield and its solute flux via runoff to the Labrador Sea due to the expansion of the Laurentide Ice Sheet (LIS; Zhao et al., 2019; Pöppelmeier et al., 2020). It is theoretically plausible that chemical weathering modulated by the waxing and waning of ice sheets could have an important influence on NSW ε_{Nd} (as it may have had for the isotope composition of multiple elements, e.g., U, Pb, Hf) during the Quaternary

(Gutjahr et al., 2014; Chen et al., 2016; Blaser et al., 2020; Parker et al., Chapter 3). The plausibility of the 'chemical weathering' hypothesis can be questioned, however, on three main fronts: 1) It is incompatible with the long-term unradiogenic trend in the ε_{Nd} of North Atlantic crust records (Burton et al., 1999; Vance and Burton, 1999; Reynolds et al., 1999); 2) Changes in continental chemical weathering flux cannot explain the observed LGM-Holocene change in Atlantic ε_{Nd} (= +2 epsilon units) from a tracer budget perspective (Du et al., 2020); 3) It is also inconsistent with LGC reconstructions of the spatial extent of North American glaciation (Batchelor et al., 2019; Parker et al., Chapter 3).

The notion that the extent of chemical weathering on North America controls the ε_{Nd} of NSW is challenged by North Atlantic crust records because they demonstrate that as ice-sheet coverage of high northern latitude Archean and Proterozoic cratons increased over the past ~3.3 Myr, the long-term Nd isotope composition of NSW became more unradiogenic (Burton et al., 1999; Vance and Burton, 1999; Reynolds et al., 1999). In the modern, sediment fluxes dominate external sources of Nd to the ocean (Du et al., 2020). The long-term unradiogenic trend in North Atlantic crust ε_{Nd} is therefore best attributed to an increase in glacial erosion of old unradiogenic cratonic terranes in the circum-North Atlantic over the past 3 Ma (Burton et al., 1999; Vance and Burton, 1999; Reynolds et al., 1999).

A role for chemical weathering in changing NSW ε_{Nd} is rejected by Du et al. (2020) on the basis that even if the Canadian Shield is ignored, the circum-Atlantic landmass cannot provide a sufficiently radiogenic LGM riverine weathering flux (of +14 epsilon units higher compared to the modern) to explain the average change in Atlantic ε_{Nd} between the LGM and the Holocene (of +2 epsilon units). These authors also highlight that LGM-Holocene differences in North Atlantic bottom water ε_{Nd} increase with depth, which is inconsistent with a 'top-down' control of continental chemical weathering flux on NSW.

Finally, if the magnitude of chemical weathering on North America controls NSW ε_{Nd}, the relatively unradiogenic values that we report from U1313 prior to MIS 2 are not consistent with independent reconstructions of LIS spatial extent. This is because multiple lines of independent evidence demonstrate that the spatial extent of the LIS during MIS 4 was comparable to MIS 2 in regions of Canada that drain into the Labrador Sea (Batchelor et al., 2019; Parker et al.; Chapter 3; Fig. 5.3b).

5.4.3.2 Evaluating the role of changes in LSW production in controlling the evolution of NSW ε_{Nd} during the LGC.

Changes to LSW production is likely to impact the evolution of the NSW ε_{Nd} end-member signature recorded at Site U1313. Today, LSW is formed by winter convection in the Labrador Sea (Gascard and Clarke, 1983) and is exported from this region northeastwards within the subpolar gyre and Irminger Sea (Lavender et al., 2000; Pickart et al., 2003) and subsequently as part of LNADW in the deep WBUC (>2000 m depth, Dickson and Brown, 1994; Cuny et al., 2002). Since LSW is relatively unradiogenic (ε_{Nd} = –13.7; Lambelet et al., 2016) and is incorporated into what will eventually become LNADW at the Denmark Sill where it mixes at ~600 m with relatively radiogenic DSOW, a reduction or cessation of its formation should increase the ε_{Nd} of deep waters bathing U1313.

Although LSW is an important component of LNADW today, its formation is considered to be a feature specific to the present interglacial (Hilliare-Marcel et al., 2001a). Based on paleo-density estimates of the vertical structure of the water-column at Orphan Knoll, it has been inferred that continuous deep convection of LSW during the LGC was in fact limited to the last ~7 ka (Fig 5.4a; Hillaire-Marcel et al., 2001a, b). Holocene-like MIS 5e ε_{Nd} values at U1313 (Fig. 5.4g) make it unlikely that LSW was not a feature of the last interglacial, but the apparent lack of evidence for its continuous production throughout the LGC may hint at how sensitive its formation is to modest increases in meltwater input to the Labrador Sea relative to the present. It is therefore plausible that a reduction, or cessation, of LSW formation during MIS 5d/5b could have contributed to the ~1 epsilon unit increase in NSW ε_{Nd} recorded at U1313 during these relatively cold stadials (Fig. 5.4g). Similarly, a more permanent loss of LSW formation from MIS 4 onwards could have contributed to the permanent transition towards more radiogenic values for NSW recorded at our study site across the MIS5/4 transition (Fig 5.5). These radiogenic trends in NSW ε_{Nd} cannot be the product of changes in the preformed compositions of DSOW or LSW because glacial erosion of the circum-Nordic and Labrador Sea landmass following incipient glaciations could only drive the ε_{Nd} composition of these water masses toward more unradiogenic values (e.g., Struve et al., 2019; Blaser et al., 2020). Simple mass balance considerations, which show that LNADW today would only become ~0.3 epsilon

units more radiogenic if LSW formation stopped (Appendix B2), highlight, though, that forcing factors other than changes in LSW formation must be involved.

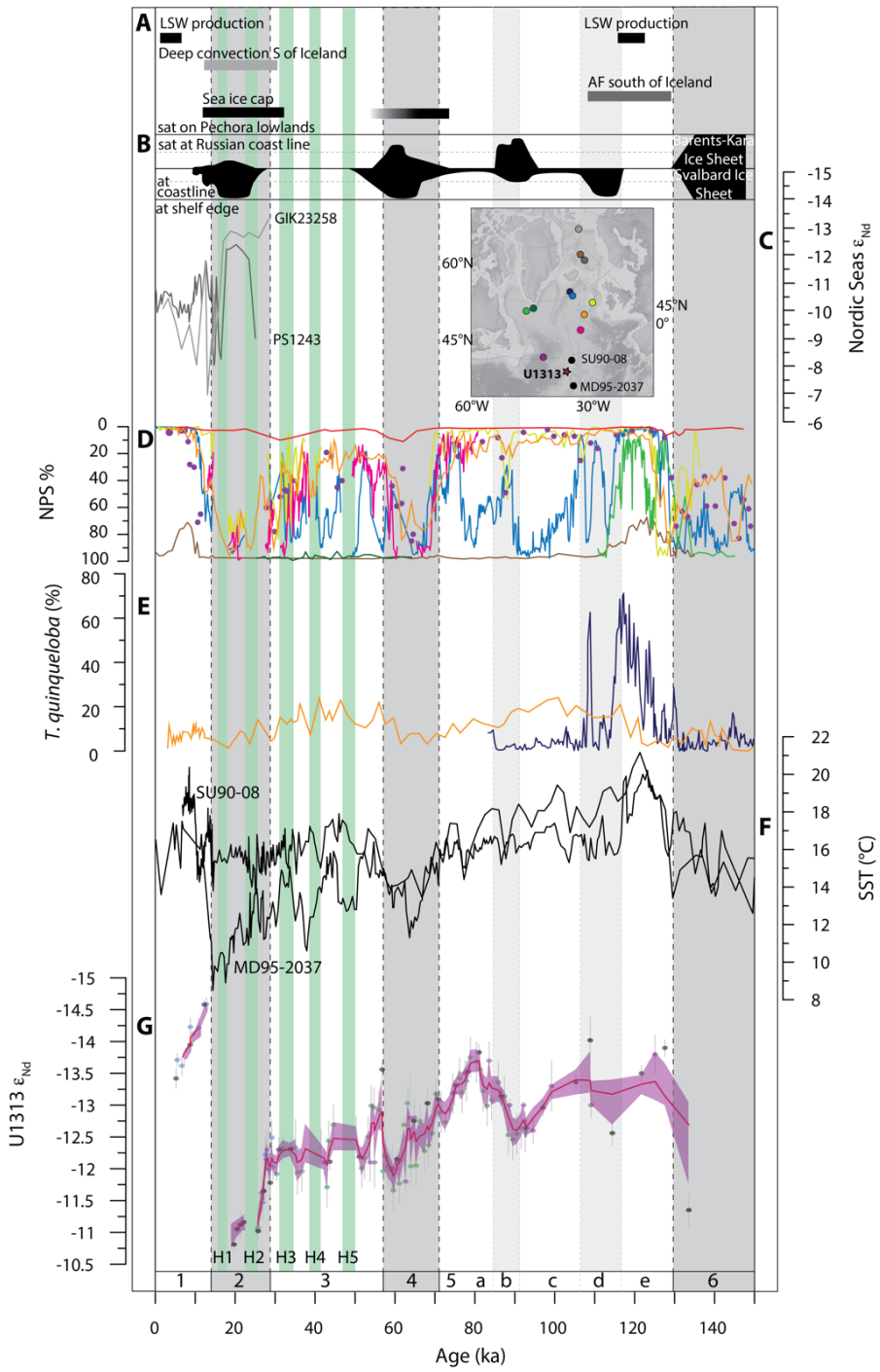

Figure 5.4: Proxy records highlighting frontal migration in the subpolar North Atlantic. **(A)** Summary of inferred histories of major oceanographic processes. **(B)** Time-distance diagram showing advances of the Svalbard and Barents-Kara Ice Sheets modified from Svendsen et al. (2004b). The location of ice sheet margins are shown in Fig 5.1. **(C)** Nordic Seas ε_{Nd} records; GIK23258 (light grey, Struve et al., 2019), PS1243 (dark grey, Struve et al., 2019). **(D)** Percentage *N. pachyderma* (s.), where records correspond to same colour circle on inset site map (north to south); brown (HM 71-19 (brown; Fronval & Jansen 1997), Site 983 (light blue; Barker et al., 2015), GS16-204-2-2CC-A (dark green; Griem et al., 2019), MD03-2664 (light green; Irvali et al., 2012), Site 980 (yellow; McManus et al., 1999), M23414 (orange; Kandiano and Bauch, 2007); ODP Site 609 (pink; Bond et al., 1992), HU90-08 (purple; Rashid et al., 2021), SU90-08 (black; Labeyrie et al., 1995), MD95-2037(black; Calvo et al., 2001 **(E)** Percentage *T. quinqueloba,* records correspond to same colour circle on inset site map; Site 984 (dark blue; Mokeddem et al., 2014), M23414 (orange; Bashirova et al., 2014). **(F)** uk_{37}-derived SST records (north to south); SU90-08 (black; Labeyrie et al., 1995), MD95-2037 (black; Calvo et al., 2001). **(G)** Compiled U1313/607 ε_{Nd} record (see Fig. 5.3 caption for details).

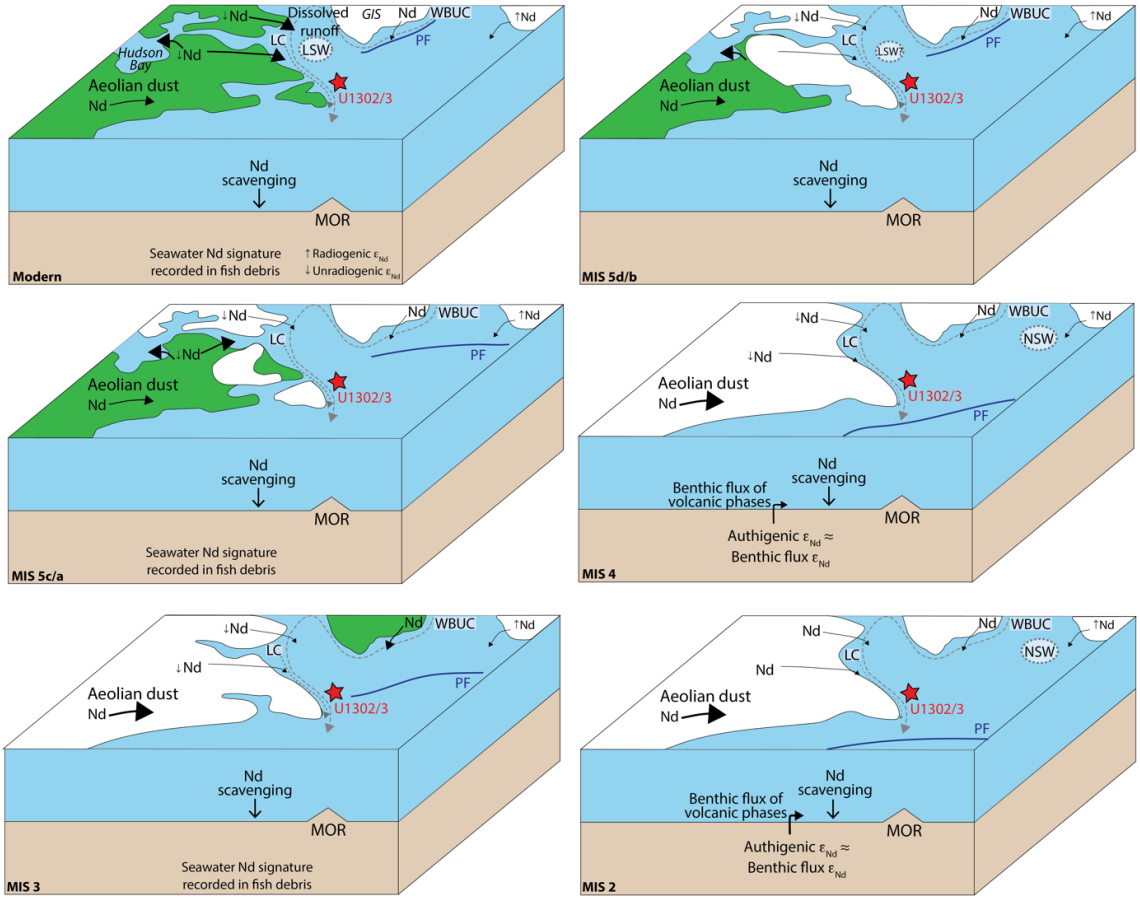

Figure 5.5: Schematic of North Atlantic highlighting Nd sources and geological processes during the Last Glacial Cycle that controls the Nd isotope signature recorded by IODP Site U1302/3 sediments, as discussed in text (where core site is denoted by red star).Arrows denote paths of key currents transporting dissolved Nd to the study site. LC = Labrador Current; WBUC = Western Boundary Undercurrent. (redrawn from Blake-Mizen et al., 2019). Blue solid line denotes location of Polar Front (PF). Dashed line circles denote sites of deep water formation: LSW: Labrador Sea Water and NSW: North Sourced Water. Weight of arrows corresponds to relative contribution of Nd source to the core site.

5.4.3.3 Evaluating the role of equatorward migrations in the polar front in controlling the evolution of NSW ε_{Nd} during the LGC.

The equatorward migration of the polar front in the North Atlantic during the LGC should also have somewhat controlled changes in NSW ε_{Nd}. This is because once it was located south of Iceland unradiogenic SPMW would not have been entrained into DSOW as it spilled over the Denmark sill. We estimate that this process alone is also capable of modifying modern-day NSW ε_{Nd} by ~0.3 epsilon units (see Appendix B2). The existence of a strong SST gradient (~6-7˚C; Fig. 5.4f) in the subtropical North Atlantic during the LGM has been used to infer that the polar front lay far south of its modern-day location (along the east Greenland margin and north of Iceland) at this time (Fig. 5.4a, 5.5 & 5.6; CLIMAP, 1976;

Calvo et al., 2001; Pflaumann et al., 2003). The evolution of the polar front prior to the LGM during the LGC is, however, less clear. This is because efforts to map polar front evolution prior to this time have focused either on its most extreme southerly position in the subtropical gyre (along the western Iberian margin) during MIS 3 H-events (e.g., Eynaud et al., 2009) or in its migration across the sub-polar northeast North Atlantic during the last interglacial (e.g., Bauch et al., 2012; Bashirova et al., 2014) and the onset of the LGC (e.g., Mokeddem et al., 2014; Mokeddem and McManus, 2016).

One common feature of these studies is that they have sought to map polar-front migration during these intervals using planktic foraminiferal assemblage data. Two species of planktic foraminifera, in particular, provide important information about North Atlantic-surface frontal systems: 1) abundances of ~>90% of *Neogloboquadrina pachyderma* (sinistral coiling (s.), Nps) in planktic foraminiferal populations are associated with polar waters in the Arctic and Nordic Seas in the modern (Bé, 1960; Pflaumann et al., 1996), but are absent in surface waters south of the Arctic front (Eynaud et al., 2009); 2) Highest abundances of the planktic foraminifera *Turbortalia quinqueloba* are strongly associated with the modern-day Arctic front, but decrease dramatically in abundance in waters poleward and equatorward of this location (Bé, 1960). Dramatic suborbital-scale changes in %Nps in sediments deposited ~60˚N in the Iceland Basin at Site 983 between ~118–72 ka imply that both the Arctic and polar fronts migrated meridionally and repeatedly across this latitude on stadial-interstadial timescales during MIS 5d-a. Small increases in %Nps and *T. quinqueloba* abundance in sediments deposited further south in the northeast North Atlantic at sites M23414 (~53˚N) and 980 (~55˚N) during this time confirm that these fronts occupied a more southerly location than modern, but they also highlight that they remained north of ~55˚N throughout MIS 5d-a (Fig. 5.4d, e & 5.6). Where our U1313 ε_{Nd} record is resolved highly enough, some aspects of the history of polar front migration during MIS 5c-a (as tracked most clearly by the Site 983 %Nps record; Fig. 5.4d, 5.5 & 5.6) seem to covary with changes in the NSW ε_{Nd} end-member (i.e., U1313 ε_{Nd} is most radiogenic when %Nps is highest at 983 during the MIS 5c/b transition). A lack of one-to-one correspondence between these two records throughout MIS 5d-a may, however, highlight that the most southerly advances of the polar front during this time were not always sufficient to prevent SPMW from being entrained into DSOW.

A ~1 epsilon unit shift is highly resolved in U1313 ε_{Nd} for NSW between MIS 5b and MIS 5a (Fig. 5.4g). We estimate that a change of this magnitude cannot be explained by the entire loss of either LSW formation or SPMW entrainment into DSOW, since in isolation they are only capable of increasing modern day NSW ε_{Nd} by ~0.3 epsilon units. Yet, their combined loss has a far more profound impact, leaving the ε_{Nd} of NSW to be effectively controlled by the Nd isotopic composition of DSOW, which today is –8.4 ± 1.4 by the time it spills over the Denmark Strait (Lacan and Jeandel, 2004a; see Appendix B2). Norwegian Sea Overflow Water (NSOW) was ~2 epsilon units more unradiogenic during the LGM relative to the modern because of glacial erosion of unradiogenic bedrock on Scandinavia and Svalbard by the Scandinavian and Svalbard–Barents Ice Sheets (Struve et al., 2019). We contend that a similar process was likely to be in operation during the cold stadials of MIS 5 in response to incipient glaciation of these landmasses (Svendsen et al., 2004a, b; Fig 5.4b). While no records of NSDW exist prior to ~30 ka (Struve et al., 2019), from a simple mass balance perspective, a ~1 epsilon unit change in NSW from the modern could be achieved on a sliding scale of scenarios with the following end-members: 1) a combined loss of LSW formation and SMPW entrainment into NSW if DSOW ε_{Nd} was LGM-like (so ~ 2 epsilon units more unradiogenic than it is today) or, 2) a ~40% reduction in the contribution of LSW and SPMW to DSOW ε_{Nd} at the Denmark Strait (from ~50% today to ~30%) while DSOW remained more or less as radiogenic as it is today (see Appendix B2).

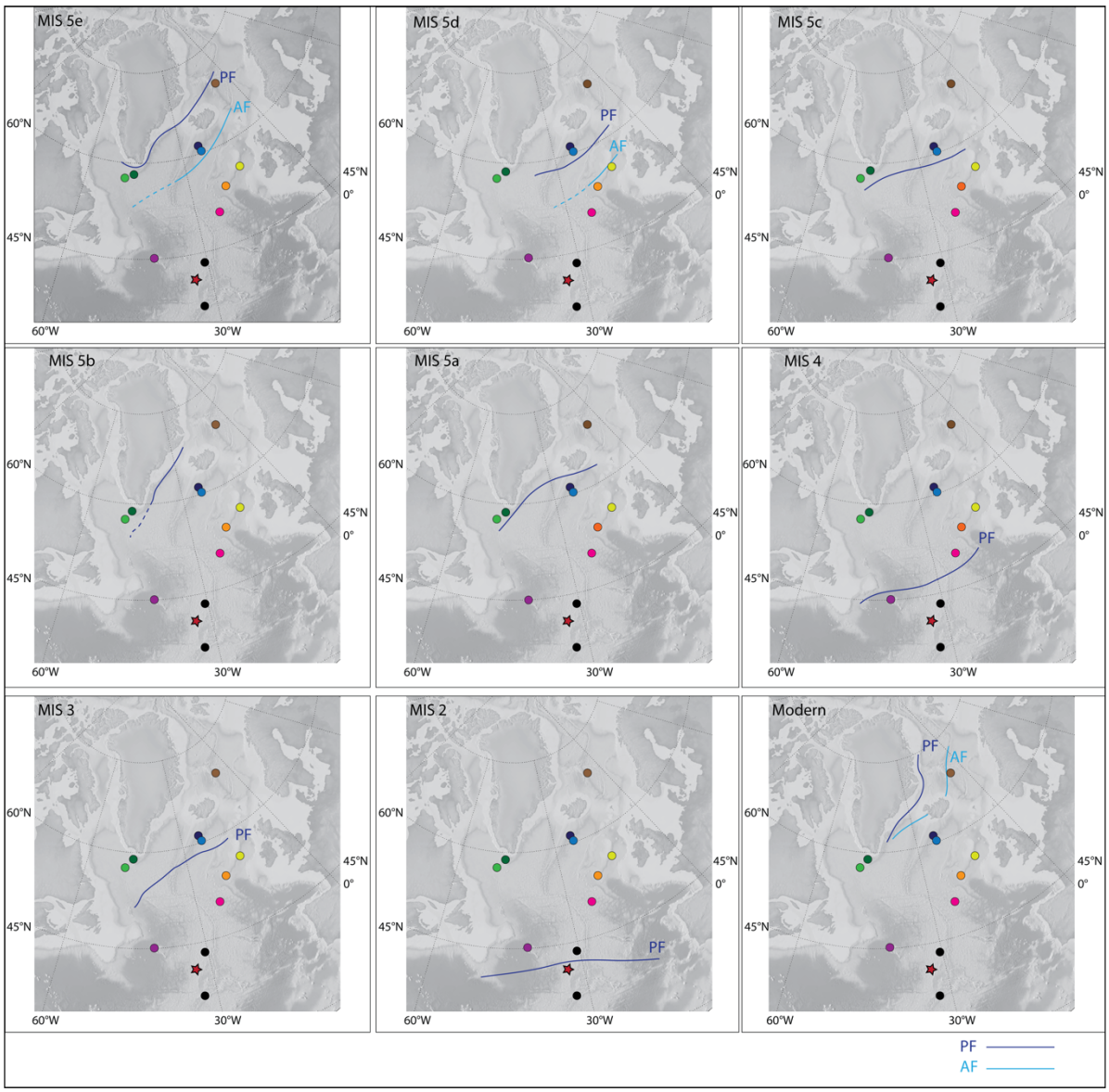

Figure 5.6: Study setting in the subpolar North Atlantic, highlighting the migration of the polar (PF; dark blue line) and Arctic (AF; light blue) fronts during the LGC. Star indicates Site U1313. Circles denote core sites (north to south); HM 71-19 (brown; Fronval & Jansen 1997), Site 984 (dark blue; Mokeddem et al., 2014), Site 983 (light blue; Barker et al., 2015), GS16-204-2-2CC-A (dark green; Griem et al., 2019), MD03-2664 (light green; Irvali et al., 2012), Site 980 (yellow; McManus et al., 1999), M23414 (orange; Bashirova et al., 2014; Kandiano and Bauch, 2007), ODP Site 609 (pink; Bond et al., 1992), HU90-08 (purple; Rashid et al., 2021), SU90-08 (black; Labeyrie et al., 1995), MD95-2037(black; Calvo et al., 2001).

According to our U1313 record, during the MIS 5a/4 transition (by ~60 ka), NSW ε_{Nd} increased by ~+2 epsilon units relative to the modern, and whilst it decreased by ~0.5 epsilon units during MIS 3, it never returned to modern-like values again until the Holocene (Fig. 5.4g). The distribution of %Nps in subpolar North Atlantic sediments deposited between ~70–15 ka highlights that the polar front was situated far south of Iceland during MIS 4 and MIS 2, and occupied a more southerly position during MIS 3 relative to MIS 5 (Fig. 5.6). The history of

glaciation in the Barents-Kara Sea region during this time also highlights that DSOW was likely to have permanently become more unradiogenic than present from MIS 4 onwards, due to glacial erosion of relatively unradiogenic bedrock (Fig. 5.4b, c). If overflow waters continued to be formed in the Nordic Seas until near the end of MIS 3 (e.g., Sarnthein et al., 1994; Thornalley et al., 2015), our mass balance investigations show that, provided DSOW ε_{Nd} was LGM-like throughout this time (i.e., ε_{Nd} = -10.5) these trends can only be explained by a complete loss of LSW and SPMW entrainment into DSOW by MIS 4 and a recovery to MIS 5-like conditions during MIS 3. In this scenario, LSW and SPMW must still have been actively contributing to the make-up of NSW ε_{Nd} throughout MIS 5.

5.4.3.4 Evaluating the role of the 'bottom-up' hypothesis in controlling the evolution of NSW ε_{Nd} during MIS 4-2

The 'bottom-up' hypothesis proposed to explain how the preformed ε_{Nd} of NSW could have been more radiogenic during the LGM relative to modern invokes partial dissolution of radiogenic volcanic phases deposited in the Iceland Basin following a shift in the location of NSW formation from an ice-covered Nordic Seas to south of Iceland (Du et al., 2020). Under this scenario, a sluggish AMOC amplified relabelling of NSW because it increased benthic exposure time in the Iceland Basin, encouraging seawater and authigenic ε_{Nd} to converge toward detrital sediment ε_{Nd} (Du et al., 2020; Abbott et al., 2022).

Numerical simulations of the LGM show that NSW formed south of Iceland during this time because the Nordic Sea was capped by extensive sea-ice (Fig 5.5; Otto-Bliesner et al., 2007). This mode of deep water formation is supported by IP25-based reconstructions of Nordic Seas sea-ice (Hoff et al., 2016) and benthic $\delta^{13}C$-based reconstructions of northeast North Atlantic circulation (Sarnthein et al., 1994), which are argued to show that the main site of North Atlantic deep water formation switched from the Nordic Seas to the Iceland Basin near the end of MIS 3 (Fig 5.7a). An incomplete picture exists of the history of deep water formation and sea-ice extent in the Nordic Seas prior to this time. Emerging sea-ice proxy data highlight the possibility, though, that Nordic Seas sea-ice may have also expanded significantly during MIS 4 (Fig. 5.6a, b; Hoff et al., 2016; Maffezzoli et al., 2019) and consequently that NSW formation may have temporarily

switched from the Nordic Seas to the Iceland Basin during this earlier cold stage as well. IRD and basalt concentrations first become high in sediments deposited in the Iceland Basin during the LGC during MIS 4 (Fig. 5.7e-g; Grützner and Higgins, 2010; Barker et al., 2015). Basalt remains an important, but variable, component of Iceland Basin sediments throughout MIS 3, and exhibit their highest abundances in sediments deposited in this region of the North Atlantic during the LGM (Fig. 5.7f, g).

The only North Atlantic $^{231}Pa/^{230}Th$ record spanning the past ~140 kyr also suggests that AMOC suppression during the LGC may have been a feature of ambient glacial climate conditions from MIS M4 onwards (Fig. 5.7h). AMOC suppression during MIS 4 may also be recorded by LGM-like $\delta^{13}C$ values in deep North Atlantic records during this cold stage (Chalk et al., 2019; Fig. 5.7c) if these values reflect greater remineralisation of carbon in deep-waters under a more sluggish glacial deep Atlantic circulation (e.g., Howe et al., 2016; Du et al., 2020). We infer from our U1313 record that NSW ε_{Nd} was ~1 epsilon unit more radiogenic during the LGM relative to MIS 4 (Fig. 5.7d). The bottom-up hypothesis could help to explain this difference in NSW ε_{Nd} if AMOC suppression was greater during the LGM than during MIS 4 because the extent to which seawater and authigenic ε_{Nd} will converge towards volcanic-rich detrital sediment ε_{Nd} under this scenario will be related to benthic exposure time in the Iceland Basin. Any NSW relabelling in this region would also have been magnified during the LGM relative to MIS 4 by the apparently higher concentration of basaltic materials in Iceland Basin sediments deposited during this time (Fig. 5.7f, g).

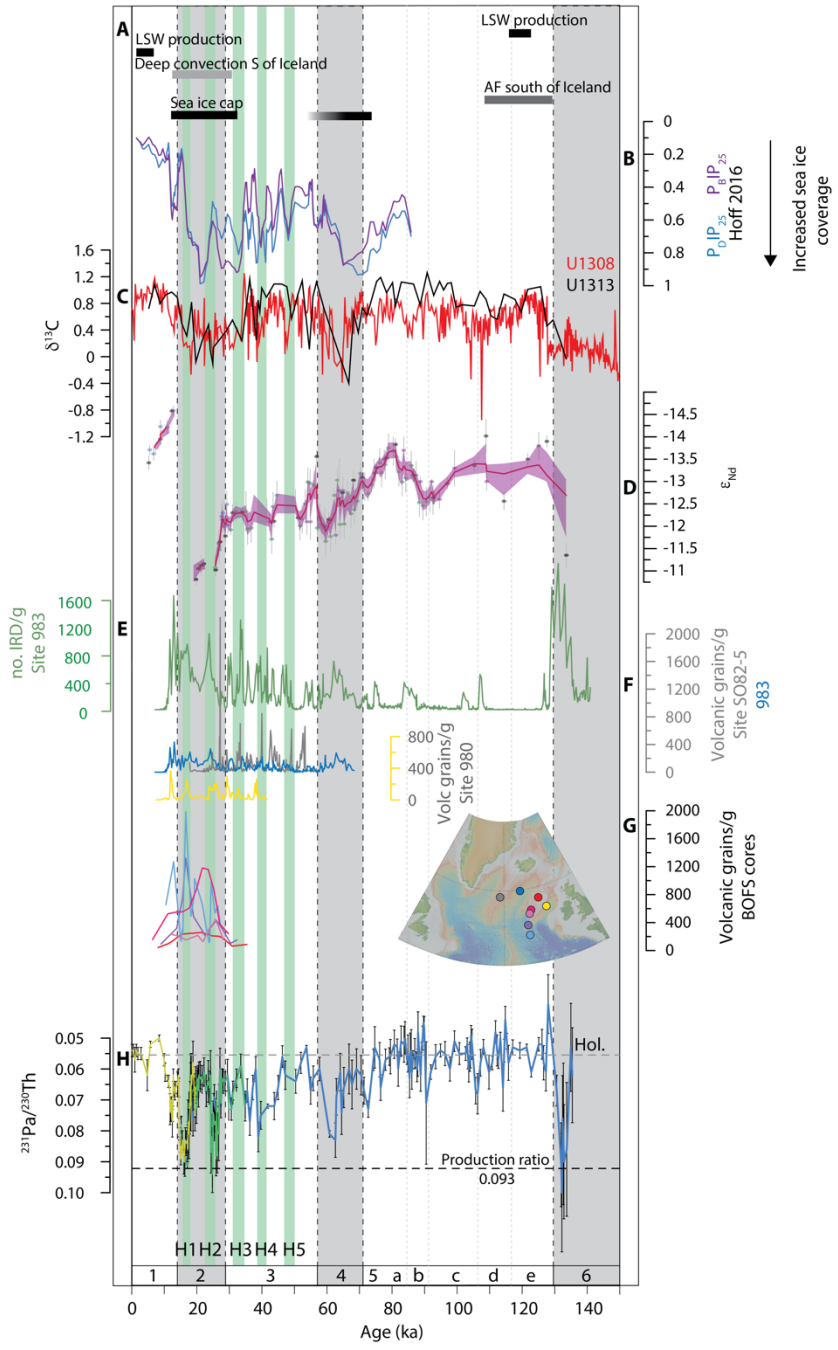

Figure 5.7: Oceanographic processes operating in the northeastern North Atlantic during the LGC: **(A)** Summary of inferred histories of major oceanographic processes. **(B)** Nordic Sea sea ice extent based on P_DIP_{25}, P_BIP_{25} (Hoff et al., 2016). **(C)** Benthic $\delta^{13}C$ of Site U1308 (red line; Chalk et al., 2019) and U1313 (black line; Bolton et al., 2010). **(D)** Fully-propagated ε_{Nd} record for Site U1313, predecessor 607 and nearby V30-97 (see Fig. 5.3 caption for details). **(E)** IRD/g bulk sediment at Site 983 (Barker et al., 2015). **(F)** Volcanic >150 μm/g dry sediment for Site SO82-5 (grey, van Kreveld et al., 2000), 983 (blue; Barker et al., 2015), 980 (yellow, Crocket et al., 2011). **(G)** Volcanic >150 μm/g dry sediment for BOFS 17K (red; 1150 m), BOFS 11K (orange; 2004 m), BOFS 10K (yellow; 2777 m), BOFS 5K (purple; 3547 m) and BOFS 8K (green; 4045m). **(H)** Bermuda Rise $^{231}Pa/^{230}Th$ data (axis reversed; error bars, 2 s.d.) for Sites 1063 (Böhm et al., 2015; Lippold et al., 2009) and GGC5 (McManus et al., 2004) where a low production ratio provides evidence for persistent export of ^{231}Pa as a consequence of an active deep Atlantic Meridional Overturning Circulation. MIS cold(warm) stages highlighted by vertical light grey(white) bars. Heinrich (detrital) layers preserved in sediments at Site U1313 are shown by labelled vertical light green bars, identified using dolomite/calcite ratios (Naafs et al., 2013b) and IRD concentrations (Lang et al., 2016) whereby peaks are associated with input by iceberg rafting during Heinrich events. Inset North Atlantic map highlights core sites with IRD and volcanic grains datasets in panels E-G, where circle colours correspond to each respective dataset.

In order to understand fully the temporal history and magnitude of change in NSW ε_{Nd} during the LGC, we propose, that it may also be necessary to understand the provenance of Iceland Basin volcanic debris. The spatial distribution of volcanic IRD in last glacial North Atlantic sediments strongly implicates Iceland as a major source. Iceland is, however, not the only major source of basaltic IRD deposited in this region during the last glacial. The Geikie Plateau in East Greenland is composed of Paleogene basalts. It is the dominant source of ice-rafted lithics deposited in the modern in the nearby Kangerlussuaq trough (Andrews et al., 2014; White et al., 2016) and was also a likely contributor of volcanic IRD deposition in the Iceland Basin during the last glacial (Knutz et al., 2001; Hagen and Hald, 2002; Andrews, 2008). This fact may have important implications for the 'bottom-up' hypothesis because the average ε_{Nd} isotope composition of basalt ice-rafted from Iceland may be more radiogenic by ~2-5 epsilon units than that incorporated into East Greenland icebergs (e.g. Peate and Stecher, 2003).

Greenlandic basalt can be more unradiogenic than Icelandic basalt because its isotope composition can be contaminated by assimilation of unradiogenic Archean quartzo-feldspathic gneisses and a thin veneer of Cretaceous-Cenozoic clastic sediments (Peate and Stecher, 2003). A large part of Iceland's crust is composed of Pleistocene and Miocene basalts. The ε_{Nd} of these basalts are more negative than post-glacially formed volcanic rocks on Iceland (Hemend et al., 1993). This is because they have interacted with meteoric waters at elevated temperatures over time (Hemend et al., 1993), although secular variations due to corresponding variations in the isotopic mantle source regions cannot be ruled out (O'Nions and Pankhurst, 1973; Cohen and O'Nions, 1982). The available data show, however, that Pleistocene to Miocene basalts from Iceland, including those formed during the last glacial, are highly radiogenic (+5 to +8 ε_{Nd}; Cohen and O'Nions, 1982; Peate et al., 2009). A provenance study of volcanic IRD deposited in the Denmark Strait (the passage of water between Greenland and Iceland) over the past ~30 kyr indicates that Icelandic sources of basaltic IRD deposited in this region became more prominent between 18-25 ka (Andrews, 2008). The Icelandic Ice Sheet (IIS) is also considered by some to be an important source of basaltic IRD in the North Atlantic during MIS 3 (Bond and Lotti, 1995). Yet, evidence exists that the IIS was reduced in size during MIS 3 compared to its LGM extent (Andrews, 2005; Principato et al., 2005) and that Iceland's coastal areas were ice-free at this time (Norðdahl and Pétursson,

2005). We propose that basaltic IRD deposition in the Iceland Basin prior to ~25 ka was dominated by east Greenland sources. If the bottom-up hypothesis can be invoked to explain the evolution of NSW ε_{Nd} from MIS 4 onwards, the absence of large abundances of Icelandic-sourced basaltic IRD in the Iceland Basin sediments prior to MIS 2 may help to explain why LGM-like radiogenic values evident in the deep western North Atlantic are not a feature of our Site U1313 record prior to this time.

5.4.4 What do changes in U1313 ε_{Nd} tell us about climate evolution in the high-latitude North Atlantic since ~3.3 Ma?

Site U1313 (Lang et al., 2016; Lippold et al., 2016; Kirby et al., 2020; Pöppelmeier et al., 2021), its predecessor Site 607 (Kim et al., 2021; Yehudai et al., 2021) and nearby Site V30-97 (Kim et al., 2021) currently provide us with our most complete picture of orbital-scale changes in the ε_{Nd} of bottom-waters bathing the deep mid-latitude western North Atlantic over the past ~3.3 Ma (Fig. 5.8 & 5.9). This picture is not complete, but spans two climate transitions critical to our understanding of Quaternary northern hemisphere glaciation (NHG): 1) the Plio-Pleistocene transition, ~3.3-2.4 Ma during which significant NHG first occurred during the Cenozoic on ~41-kyr timescales (Fig. 5.8) and 2) the past 1.5 Myr, including the Mid-Pleistocene Transition (MPT) and the emergence of large and ~100-kyr-long (inter)glacial cycles (Fig. 5.9).

The most positive ε_{Nd} values over this time are traditionally interpreted to reflect that major SSW incursions into the deep western North Atlantic have been a feature of the largest glaciations of the past ~2.5 Ma (Lang et al., 2016; Lippold et al., 2016; Kirby et al., 2020; Kim et al., 2021; Yehudai et al., 2021). In this section, and informed by the discussion of oceanographic and climatic controls in Section 5.4.3, we explore what the consequence of the alternative explanation – that the evolution of bottom-water ε_{Nd} at U1313/607 over the past 3.3 Ma reflects changes in the pre-formed composition of NSW – has for our understanding of climate change in the high-latitude North Atlantic over this time.

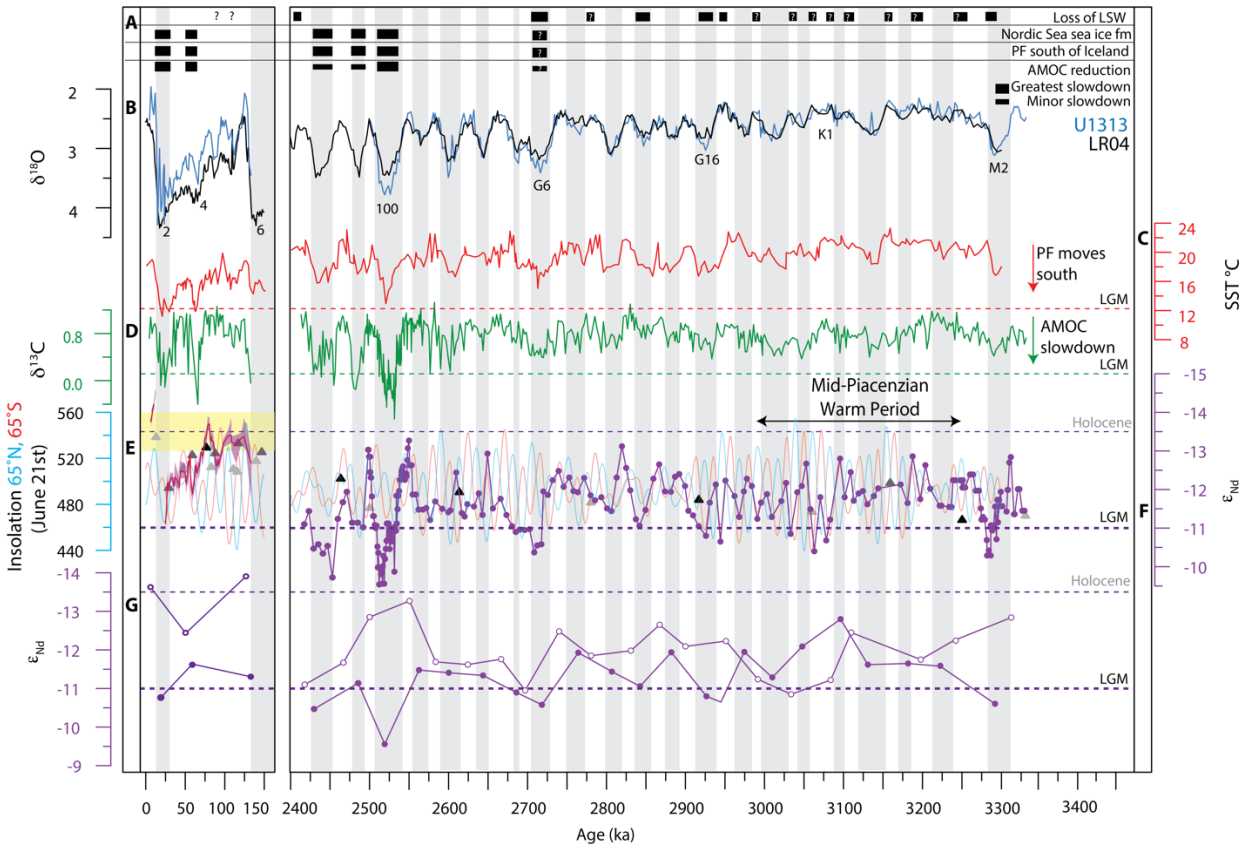

Figure 5.8: Last Glacial Cycle and Late Pliocene-earliest Pleistocene climate evolution: **(A)** Summary of inferred histories of major oceanographic processes. **(B)** Benthic $\delta^{18}O$; LR04 (black; Lisiecki and Raymo, 2004) and U1313 (blue; Pliocene record from Bolton et al., 2010 and LGC from Chalk et al., 2019) **(C)** Alkenone-derived sea surface temperature (SST °C; Naafs et al., 2012). **(D)** U1313 $\delta^{13}C$ (LGC; Chalk et al., 2019, Pliocene; Lang et al., 2016, Kirby et al., 2020). **(E)** Insolation at 65°N (blue line) and 65°S (red line). **(F)** U1313/607 ε_{Nd} record (LGC; compiled record from Fig. 5.3; Pliocene; Lang et al., 2016; Kirby et al., 2020). Fe-Mn crusts records precipitated in the shallow North Atlantic; TR079-D14 (dark grey triangles; 2000 water depth; 0-0.04 Ma from Foster et al., 2007, 2.4-3.4 Ma from Reynolds et al., 1999), BM1969.05 (light grey triangles; 0-0.04 Ma from Foster et al., 2007, 2.4-3.4 Ma from Burton et al., 1999 on chronology of O'Nions et al., 1998), ALV539 2-1 (black triangles; 2.4-3.4 Ma from Burton et al., 1999 on chronology of O'Nions et al., 1998). **(G)** Glacial (filled purple circles) and interglacial (open purple circles) maxima ε_{Nd} for 607, based on timing of LR04 benthic $\delta^{18}O$ peak glacial and interglacials (Kim et al., 2021; Yehudai et al., 2021). Horizontal dashed lines are labelled to show LGM and late Holocene averages of each record. MIS cold(warm) stages highlighted by vertical light grey(white) bars.

5.4.4.1 The climate of interglacials in the high northern latitudes over the past ~3.3 Ma

A long-term unradiogenic trend exists in low-resolution North Atlantic ε_{Nd} crust records over the past ~3 Ma. The higher resolution marine-core ε_{Nd} records from U1313/607 provide additional insights into the evolution of this trend (Figs. 5.7 & 5.8). Fish debris ε_{Nd} data from U1313 between ~3.3 and 2.6 Ma (Lang et al., 2016; Kirby et al., 2020) show that interglacial values of NSW ε_{Nd} are variable,

but are typically more positive by ~2 epsilon units compared to the late Holocene (Fig. 5.8f). These data also show that NSW ε_{Nd} first approaches modern-like values during the earliest Pleistocene interglacials MIS 101 and MIS 99 (Fig. 5.8f, g), following the onset of major northern hemisphere glaciation ~2.6 Ma (Bailey et al., 2013; Bolton et al., 2018). While no ε_{Nd} records exist from U1313/607 between ~1.5 and 2.4 Ma, relatively low resolution ε_{Nd} data from Site 607 for the past ~1.5 Ma hints at the fact that prior to MIS 25 (~900 ka) interglacial NSW ε_{Nd} values may have been either late Holocene-like or more unradiogenic by ~1 epsilon unit, but may have become persistently late Holocene-like thereafter (Fig. 5.9f). We propose that this evolution in warm-stage NSW ε_{Nd} can be attributed to a combination of two factors: 1) a loss of LSW formation during warmer than present times; 2) the volume of residual ice present on continents in the high-northern latitudes (e.g., on Svalbard, Baffin Island and Greenland) during interglacials, and therefore the extent to which the end-member ε_{Nd} of LSW and NSOW at these times was relabelled by glacial erosion of the old unradiogenic bedrock adjacent to both the Labrador Sea and Nordic Seas.

Given the apparent sensitivity of LSW production to changes in climate relative to the modern (Hillaire-Marcel et al., 2001a, b) it is plausible that a part, if not all, of the relatively radiogenic composition of the NSW end-member during late Pliocene interglacials could be attributable to a loss of deep water formation in the Labrador Sea (Fig. 5.8a). A detailed understanding of NHG in space and time over the past ~3.3 Ma currently remains elusive. Several fundamental observations, nevertheless, also support the notion that the evolution of NSW ε_{Nd} during interglacials over this time may have been controlled significantly by the baseline warm-stage extent of NHG: 1) according to the late Pliocene U1313 ε_{Nd} record, the NSW end-member was typically most radiogenic, and at times least variable, during the mid Piacenzian warm period (Fig. 5.8f), an interval during which global mean sea-level is widely considered to range from +10 to +40 m above present (Raymo et al., 2011; 2018; Miller et al., 2012; 2020; Dumitru et al., 2019; Grant et al., 2019; Hearty et al, 2020), implying complete loss of Greenland Ice Sheet at this time; 2) a deconstruction of benthic $\delta^{18}O$ (a first-order, but imperfect, proxy for glaciation) for interglacial and glacial periods over the past ~3.3 Myr hints at the fact that NHG extent during warm stages over this time was likely to have been at its lowest prior to ~2.5 Ma, at its greatest between 2-1.5

Ma, and most analogous to the late Holocene over the past ~1 Ma (Fig. 5.10). Confirmation of this suggestion awaits independent reconstructions of Greenland Ice Sheet extent over this time. In the meanwhile, we speculate that the late-Holocene-like NSW ε_{Nd} values at U1313 during MIS 101 (~2.54 Ma) and MIS 99 (~2.5 Ma) reflect the first interglacials during the Plio-Pleistocene transition in which significant volumes of continental ice survived in the high northern latitudes following deglacial warming (cf. Lawrence et al., 2009).

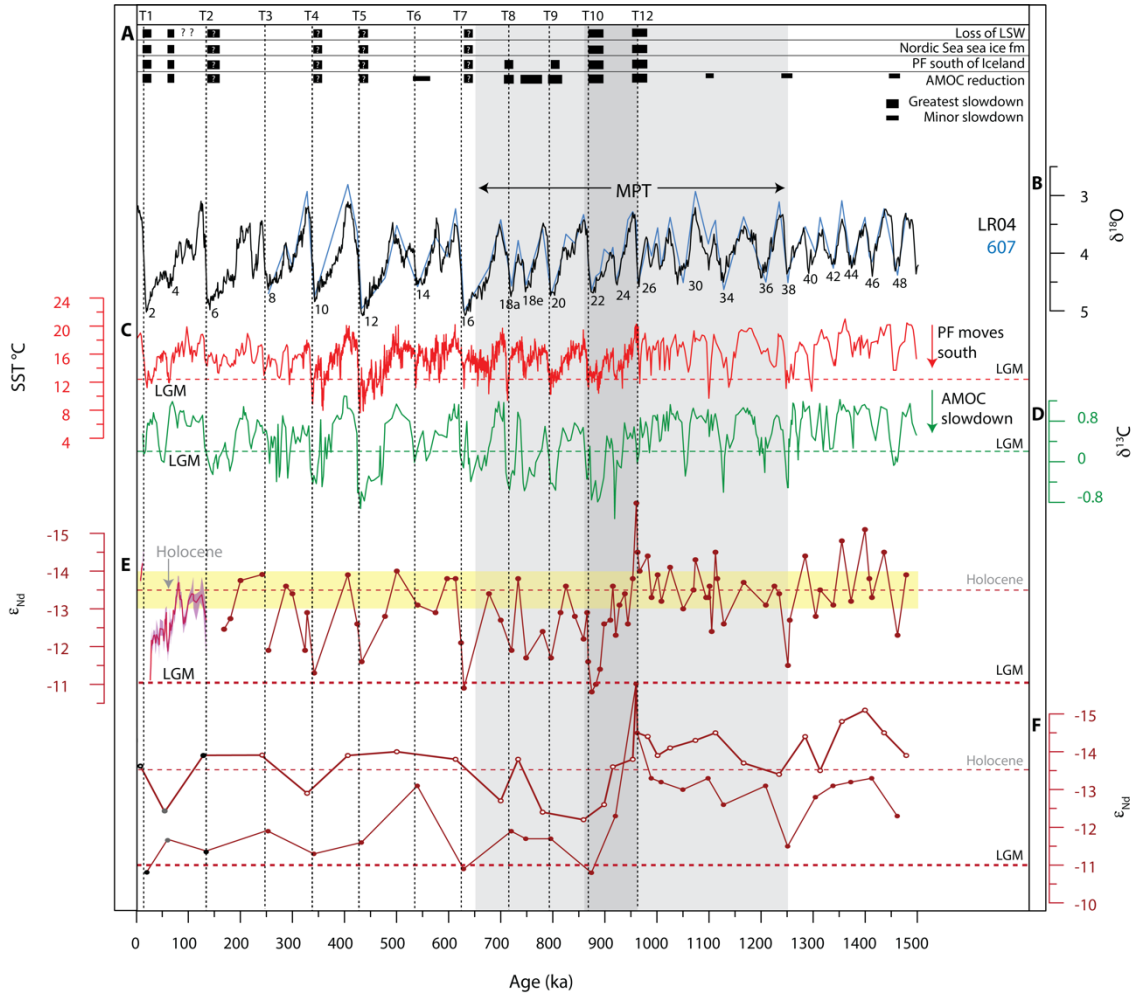

Figure 5.9: History of North Atlantic climate evolution over the last 1.5 Myr: **(A)** Summary of inferred histories of major oceanographic processes. **(B)** Benthic $\delta^{18}O$; LR04 (blue; Lisiecki and Raymo, 2005) and Site 607 (blue; Kim et al., 2021). **(C)** Alkenone-derived sea surface temperature (SST °C; Naafs et al., 2012). **(D)** Site 607 $\delta^{13}C$ (LGC; Raymo et al., 2004). **(E)** U1313/607 ε_{Nd} record (LGC; compiled record from Fig. 5.3; ~150-1500 ka; Site 607 from Kim et al., 2021; Yehudai et al., 2021). Yellow horizontal bar represents the range of present-day NADW ε_{Nd} values. The shaded light grey vertical bar highlights the MPT and dark grey vertical bar highlights the 'AMOC-crisis' as defined by Kim et al., 2021. **(F)** Glacial (filled red circles) and interglacial (open red circles) maxima ε_{Nd} for 607, based on timing of LR04 benthic $\delta^{18}O$ peak glacial and interglacials (Kim et al., 2021; Yehudai et al., 2021). Horizontal dashed lines are labelled to show LGM and late Holocene averages of each record. Vertical dashed lines show Terminations 12 to 1 from the onset of the 100-kyr world, as defined by Barker et al. (2021). MIS cold(warm) stages highlighted by vertical light grey(white) bars.

Compared to interglacials, glacial ε_{Nd} values show greater variability over the past 3.3 Ma. Fish debris ε_{Nd} data from U1313 between 3.3 and 2.4 Ma (Lang et al., 2016; Kirby et al., 2020) show that glacial values in the NSW end-member were more radiogenic than the LGM during cold stages MIS M2, G16, G6, 100, 98 and 96 (Fig. 5.8). Lower resolution data from Site 607 for the last ~1.5 Ma hints that prior to MIS 25, glacial NSW ε_{Nd} was more unradiogenic by ~2 epsilon units than during the LGM and often similar in composition to NSW values during contemporary interglacials, but approached LGM-like from MIS 22 (~950 ka) onwards (e.g., during MIS 22, 16 and 12, 10 and 6; Fig. 5.9).

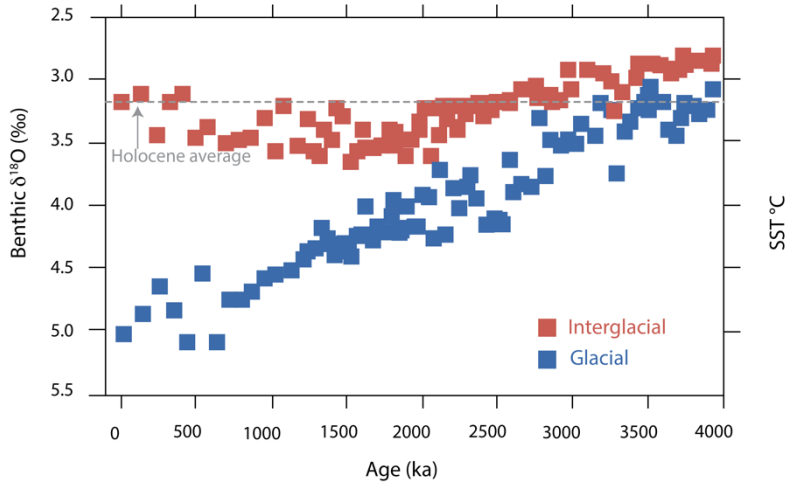

Figure 5.10: Evolution of benthic $\delta^{18}O$ for glacial and interglacial periods over the past 4 Myr. Grey horizontal dashed line represents the late Holocene average of interglacial $\delta^{18}O$ values. Redrawn from Herbert et al. (2010).

The climate of glacial maxima in the late Pliocene and earliest Pleistocene

The LGM-Holocene-like amplitude of change in ε_{Nd} recorded at U1313 across MIS 101–99 has previously been interpreted to record either: 1) major incursion of SSW into the deep western North Atlantic during MIS 100 (Lang et al., 2016; Kirby et al., 2020) or, 2) by analogy to the LGC (see Section 5.4.3), a loss of unradiogenic Labrador Seawater formation, a southward shift of the polar front and relabelling of NSW ε_{Nd} via partial dissolution of radiogenic volcanic phases under a relatively sluggish AMOC, following a shift in the location of the main site of NSW formation from a sea-ice-covered Nordic Sea to south of Iceland (Kirby et al., 2020). The apparent more radiogenic than LGM values of NSW ε_{Nd} during

MIS 100 could reflect that AMOC during this earliest Pleistocene cold stage was less vigorous than it was during the LGM, resulting in greater convergence of authigenic and seawater ε_{Nd} to detrital ε_{Nd} values in the Iceland Basin (as the residence time of bottom-waters increased). Alternatively, it could reflect that sediments deposited in the Iceland Basin during MIS 100 was more volcanic debris-rich than their LGM counterparts because icebergs shed from east Greenland and Iceland during the earliest Pleistocene contained relatively high abundances of IRD sourced from debris-rich pre-glacially weathered landscapes. Regardless, we invoke the same mechanisms (i.e., loss of LSW production, southward polar front migration, sea-ice expansion and a reduction in AMOC vigour), to explain the changes in NSW ε_{Nd} that we infer for MIS G6, 98 and 96 (Fig. 5.8a). We propose, however, that the less radiogenic values that characterize these cold stages most likely reflects that AMOC vigour during these glaciations was not as diminished as it was during MIS 100 (Fig. 5.8c). Evidence to support this suggestion comes in the form of North Atlantic benthic $\delta^{13}C$ records (Fig. 5.8d). The large negative excursion recorded in North Atlantic benthic $\delta^{13}C$ data during the LGM is proposed to reflect enhanced remineralisation of carbon in deep-waters (Howe et al., 2016) under a more sluggish AMOC relative to modern (Du et al., 2020). The only glacial during the late Pliocene and earliest Pleistocene to exhibit an LGM-Holocene magnitude negative excursion in U1313 benthic $\delta^{13}C$ is MIS 100 (Fig. 5.8d).

The times prior to 2.52 Ma when the ε_{Nd} of NSW bathing U1313 approached its LGM composition at our study site (e.g., during MIS M2, K1, G16, and G12; Fig. 5.8f) are harder to explain. The amplitude of the ε_{Nd} cycles associated with these radiogenic values (Fig. 5.8f), imply that NSW ε_{Nd} varied long before continental glaciation became a significant feature of the high northern latitudes. Site U1313 benthic $\delta^{13}C$ values demonstrate that these times are unlikely to have been associated with any significant reduction in AMOC vigour (Fig. 5.8d). Unlike during the LGC, the U1313 ε_{Nd} record hints at the possibility that the Nd isotope composition of the NSW end-member varied in phase with precessionally-paced southern hemisphere insolation prior to ~2.7 Ma (compare LGC and late Pliocene ε_{Nd} data to the insolation curves in Fig. 5.8e), and hence the most radiogenic NSW values at this time coincided with enhanced northern hemisphere insolation forcing. Under this scenario the most radiogenic NSW ε_{Nd} values prior to 2.7 Ma

are more likely to reflect times when LSW was not formed in the Labrador Sea leaving NSW that was still forming in a relatively sea-ice-free Nordic Seas at this time to be dominated by radiogenic NSOW.

The climate of glacial maxima over the past ~1.5 Myr

We can infer from U1313 ε_{Nd} data spanning the late Pliocene to earliest Pleistocene that the most prominent cold stages since the onset of the Quaternary (e.g., from MIS 100 onward, <2.52 Ma) were likely characterized by extensive Nordic Sea sea-ice and significant declines in AMOC vigour. Yet, the available early and mid Pleistocene ε_{Nd} data from Site 607 spanning the past ~1.5 Myr highlight that these conditions were unlikely to have been a persistent feature of Quaternary glaciations of the ~41 kyr (inter)glacial world and were not so until the onset of the MPT, ~1 Ma (Fig. 5.9e).

The MPT featured the development of larger and longer lasting (~100 kyr-long) northern hemisphere glaciations that were characteristically saw-tooth in shape (e.g., Clark et al., 2006; McClymont et al., 2013). Their saw-tooth nature was a product of relatively rapid transitions between full glacial and full interglacial climates otherwise known as terminations (Denton et al., 2010). The seemingly diachronous nature of the transition between the ~41-kyr and 100-kyr (inter)glacial worlds across our planet makes it challenging to define a start date for the MPT (Barker et al., 2021). The first ~100-kyr-paced glaciation may, however, have emerged ~1.17 Ma during MIS 30 and ended following MIS 26 during what is known as Termination 12 (Fig. 5.9b; Barker et al., 2021). The ε_{Nd} of bottom-waters bathing Site 607 during MIS 26 may have been unusually unradiogenic (ε_{Nd} = –16; Kim et al., 2021; Fig. 5.9e). This unradiogenic signal is attributed to the first time that crystalline bedrock on North America was exposed to glacial erosion following long-term removal by ~41-kyr-paced glaciations of a thick deformable pre-glacial regolith developed on this landmass during the warm Pliocene (Yehudai et al., 2021). The existence of LGM-like radiogenic deep-waters at Site 607 during subsequent glaciations is argued to reflect that cold-stage incursions of SSW over-whelmed any unradiogenic weathering signal resulting from a large LIS being in direct contact with crystalline basement during the 100-kyr world (Yehudai et al., 2021). Multiple issues exist, however, with this interpretation.

Our understanding of the history of water-mass mixing at Site 607 between ~1.5 and 0.125 Ma is based on just one or two data points per glacial and interglacial (Fig. 5.9e, f; Kim et al., 2021). High resolution ε_{Nd} data from U1313 demonstrate that using maxima and minima in benthic $\delta^{18}O$ stratigraphies to guide sampling plans that seek to capture the full orbital-scale change in ε_{Nd} can provide a false impression of the amplitude of interglacial-glacial change on such timescales (e.g., MIS M2, MIS 100, Fig. 5.9b, e). The significance of the small hand-full of unradiogenic ε_{Nd} values reported for MIS 26 from Site 607 therefore remains unclear. Multiple lines of evidence support the notion that the first Quaternary advances of a slippery and thin LIS ~2.5 to 2.4 Ma (so during the cold stages MIS 100, 98 and 96) were glaciologically anomalous due to the presence of a deformable preglacial regolith (Balco and Rovey, 2010; Bailey et al., 2010; Shakun et al., 2016). Yet, the history of LIS advance into the mid-continent of the United States inferred from terrestrial tills between ~2.4 and 1.3 Ma suggests it is unlikely that any such regolith persisted on North America until the MPT (Balco and Rovey, 2010). Finally, if the unradiogenic ε_{Nd}-weathering signature of North American bedrock was masked in deep waters bathing the deep western North Atlantic during glacials by major SSW incursions from MIS 24 onwards, that unradiogenic signature should still be preserved in ε_{Nd} records from western North Atlantic sites persistently bathed in NSW at depths shallower than Site 607 (<3400 m). LGM ε_{Nd} values from near-by Site SU90-03 (at ~2480 m) are, however, as radiogenic as the deepwater bathing Site U1313/607 at this time (Pöppelmeier et al., 2021).

The radiogenic excursion between ~950–860 ka that culminates in LGM-like values during MIS 22 (so the ~100-kyr glacial cycle ended by Termination 10; Fig. 9e) is interpreted by Kim et al. (2021) and others (e.g., Pena and Goldstein, 2014; Yehudai et al., 2021) as a major incursion of SSW into the deep North Atlantic due to a slow-down in AMOC. We interpret this interval in a similar fashion, but instead attribute the LGM-like values during MIS 22 to the same oceanographic factors proposed to modify the end-member ε_{Nd} of NSW during the LGM (Fig 5.8a, c-d; i.e., AMOC decline, no LSW production and the polar front sat far south of its present day location). We therefore consider MIS 24-22 to be the first ~100 kyr glacial during which sea-ice formation in the Nordic Seas was extensive enough to cause the site of NSW formation to switch to the Iceland

Basin (Fig 5.9a). The relatively low resolution of the available Site 607 ε_{Nd} data limits our ability to evaluate how frequently LGM-like conditions like these characterized the full glacial climate of the glacial cycles that followed. It seems likely, though, that a higher resolution ε_{Nd} dataset from this site would reveal that the large glacials MIS 16, 12, 10 and 6 were probably characterized by LGM-like oceanographic conditions that we infer for MIS 22.

5.5 Conclusions

We present the first fish debris-based ε_{Nd} record from IODP Site U1313 spanning the entire Last Glacial Cycle (LGC). We combined this record with recently published ε_{Nd} datasets from the same site and others nearby (DSDP Site 607 and V30-97), to create the first fully error-propagated record of LGC changes in ε_{Nd} bathing the deep mid-latitude western North Atlantic Ocean, which we infer tracks the evolution of the Nd isotope composition of the Northern Sourced Water (NSW) end-member in the deep Atlantic Ocean over this time. This new record shows that NSW ε_{Nd} during the last interglacial and the Holocene was highly comparable (~–13.5), but that it was up to ~1 epsilon unit more radiogenic during MIS 5d and 5b, ~2 epsilon units more radiogenic during MIS 4, and ~ 3 epsilon units more radiogenic during the Last Glacial Maximum (LGM).

Through testing North Atlantic oceanographic and climatic controls on bottom water ε_{Nd} at Site U1313, we rule out a substantial reduction in chemical weathering of the unradiogenic Canadian Shield due to the expansion of the Laurentide Ice Sheet (LIS; the 'top-down' hypothesis) as a viable mechanism for driving these changes. Instead, a simple mass balance exercise shows that the evolution of NSW ε_{Nd} that we report for the LGC was most likely driven by: 1) reductions in unradiogenic Labrador Sea Water (LSW) production and entrainment of Subpolar Mode Waters (SPMW) into relatively radiogenic Denmark Strait Overflow Waters (DSOW) due to southward migration of the polar front, and a simultaneous increase in glacial erosion of unradiogenic circum-Nordic and Labrador Sea landmass following their incipient glaciations during MIS 5d and 5b; 2) a total loss of LSW formation during the MIS 5a/4 transition and the fact that the polar front lay far south of its modern-day location (at ~60˚N)

from this time; 3) partial dissolution of radiogenic basaltic volcanic phases deposited in the Iceland Basin following a shift in the location of NSW formation from an ice-covered Nordic Seas to south of Iceland during MIS 2 (the 'bottom-up' hypothesis). A sluggish AMOC is thought to have amplified relabelling of NSW during the LGM by increasing benthic exposure time of bottom waters in the Iceland Basin, which would have encouraged seawater and authigenic ε_{Nd} to converge toward detrital sediment ε_{Nd}. We propose, though, that to understand fully the LGM-Holocene difference in NSW ε_{Nd}, it may also be necessary to consider that the provenance of ice-rafted basalt deposited in the Iceland Basin during the LGC was most likely dominated by relatively unradiogenic east Greenland sources during MIS 3 and only by more radiogenic Icelandic sources during MIS 2.

Armed with this interpretive framework and previously published orbital-scale Site U1313 and Site 607 ε_{Nd} records spanning the past ~3.3 Ma, we infer interglacial trends in NSW ε_{Nd} over this time were most likely significantly controlled by the baseline warm-stage extent of northern hemisphere glaciation and that MIS 101, ~2.54 Ma, may represent the first time during the Plio-Pleistocene transition that significant volumes of continental ice survived in the high northern latitudes following deglacial warming. We also infer that while extensive sea-ice expansion in the Nordic Seas likely occurred during the most prominent glaciations of the northern hemisphere since the onset of the Quaternary, ~2.6 Ma, this aspect of the high northern latitude cryosphere was not a persistent feature of cold stage climates until the onset of the Mid Pleistocene Transition ~1 Ma.

Chapter 6: Conclusions

This chapter summarises a two-pronged approach used to investigate two major aspects of Earth's climate during the Plio-Pleistocene using two marine records recovered during Integrated Ocean Drilling Program (IODP) Expeditions 303 and 306:

1) the mid to late Pleistocene evolution of the North American Laurentide Ice Sheet (LIS) using authigenic Pb isotope records from IODP sites U1302/3 from Orphan Knoll, specifically during the most extreme termination of the Quaternary, Termination (T) 5 (~430 ka), T2 (~130 ka) and the Last Glacial Cycle (LGC; 124–0 ka)

2) Changes in high-latitude climate over the past ~3.3 Myr using North Atlantic ε_{Nd} data from deep northwest North Atlantic Site U1313, with a focus on the late Pliocene-earliest Pleistocene intensification of Northern Hemisphere glaciation (iNHG, ~3.5–2.4 Ma), the mid-Pleistocene Transition (MPT, ~1.2–0.8 Ma) and the LGC.

6.1 Summary of main findings

Little is known about the deglacial history of the most volumetrically important continental ice sheet in the Northern Hemisphere, the North American LIS prior to the Last Glacial Maximum. Chapter 3 successfully presents the history of LIS extent for the past ~130 kyr. High-resolution records of authigenic ferro-manganese (Fe-Mn) oxyhydroxide-derived Pb isotopes from IODP sites U1302/3 from Orphan Knoll ($^{206}Pb/^{204}Pb$, $^{207}Pb/^{204}Pb$ and $^{208}Pb/^{204}Pb$) are used to track temporal variability in the input of Pb sourced from chemical weathering of the

adjacent landmasses and its runoff to the Labrador Sea, which predominantly varied as a function of LIS extent in the Hudson Bay region of North America. These new records show that bottom-waters bathing Orphan Knoll over the past ~130 kyr were characterised by relatively high (radiogenic) values during warm marine isotope stages (MIS) 5, 3 and 1 and relatively unradiogenic values occurred during cold stages MIS 6, 4 and 2. They demonstrate that LIS break-up during T2 was relatively rapid (~7 kyr) compared to T1 (~17 kyr). They also show that, contrary to previous suggestions (e.g., Pico et al., 2017), Hudson Bay was not ice free during MIS 4 (~71-57 ka). The Pb isotope composition of bottom-waters bathing sites U1302/3 during MIS 3 (~57-29 ka) does not support the notion that Hudson Bay was ice-free during this time, but may support the recent suggestion that southern Greenland was partially deglaciated during this interstadial (Seidenkrantz et al., 2019).

New U1302/3 authigenic Pb isotope records spanning MIS 12/11 (~440-410 ka) are presented in Chapter 4. These new data document the Pb isotope composition of bottom waters bathing Orphan Knoll during what is arguably the largest Northern Hemisphere deglaciation of the Quaternary, T5, ~424 ka. They show that LIS retreat during T5 began ~432 ka and occurred over a similar timescale (~15 kyr) to that observed for T1 (~17 kyrs), but not as rapidly as during T2 (~7 kyr). These new records also show that LIS break-up (~427 ka) occurred ~6 ka before southern Greenland deglaciation during MIS 11. MIS 11 may be an analogy for future changes in Earth's climate. This interglacial features two precessional cycles in insolation and during the second of these, the sea-level is estimated to have risen between +1 m (Rohling et al., 2010) and +6–13 m (Raymo and Mitrovica, 2012). According to our age-model, LIS break-up and southern Greenland deglaciation pre-date the onset of the second of the two weak precessional-paced cycles in insolation associated with MIS 11. We therefore conclude that the sea-level highstand associated with the latter half of this interglacial is likely to reflect additional ice-mass loss from the Antarctic ice sheets and that sea-level rise during MIS 11 is likely to sit at the upper-end of published estimates (+6–13 m).

Chapter 5 presents the first fish debris-based ε_{Nd} record from IODP Site U1313 spanning the entire Last Glacial Cycle and explores the ε_{Nd} evolution in terms of changes to the NSW ε_{Nd} end-member, rather than changes in water-mass mixing.

This chapter invokes a reduction in the entrainment of unradiogenic Labrador Sea Water and Subpolar Mode Waters into radiogenic deep water formed in the Nordic Seas that sets NSW ε_{Nd} during MIS 5 to MIS 3, with contemporaneous glacial-erosion-driven changes in the end-member composition of these NSW-constituent water masses. Only a shift in the location of NSW formation from an ice-covered Nordic Seas to south of Iceland during MIS 2 and partial dissolution of radiogenic basaltic volcanic phases deposited in the Iceland Basin following a slowdown in Atlantic Meridional Overturning Circulation (AMOC) can explain the full LGM-Holocene difference in NSW ε_{Nd}. The LGC interpretive framework is applied to North Atlantic Plio-Pleistocene ε_{Nd} records to hind-cast the oceanographic conditions of this region in deeper time. This exercise shows that interglacial trends in NSW ε_{Nd} over the past ~3.3 Ma were most likely controlled by the baseline warm-stage extent of northern hemisphere glaciation (NHG). It also demonstrates that while extensive Nordic Seas sea ice, LGM-magnitude AMOC slowdowns and NSW formation in the Iceland Basin likely occurred during the most prominent cold stages since the onset of the Quaternary, ~2.6 Ma, they were not persistent features of cold stages until the onset of the Mid Pleistocene Transition, ~1 Ma.

6.2 Future perspectives

6.2.1 Laurentide Ice Sheet extent during the Mid Pleistocene Transition and Pleistocene terminations

One of the most exciting outcomes of this thesis has been the demonstration that authigenic Pb isotope records from Orphan Knoll can be used to gain important insights into LIS history prior to the LGM. One explanation for the transition from the ~41-kyr to ~100-kyr (inter)glacial world, ~1200-800 ka, is that it was caused by a change from a soft-bedded to a hard-bedded LIS through glacial erosion of a thick chemically weathered regolith that developed on North America prior to iNHG that allowed ice-sheets to build up for longer (Clark and Pollard, 1998; 2006; Yehudai et al., 2021). This theory could be tested by extending authigenic Pb isotope records from Orphan Knoll back through the MPT. A thick intensely chemically weathered regolith should be characterized by a highly unradiogenic Pb isotope composition. If the LIS grew on this substrate during the 41-kyr

(inter)glacial world, we might therefore expect the Pb isotope composition of bottom waters bathing Orphan Knoll during the early Pleistocene to be relatively unradiogenic in comparison to the mid to late Pleistocene. Pre-MPT sediments have yet to be recovered from Orphan Knoll (Channell et al., 2012). Future IODP drilling of this region of the North Atlantic is thus required.

6.2.2 Late Pleistocene sea-level reconstructions

Glacio-isostatic adjustment-based corrections of Late Pleistocene interglacial sea-level highstands would benefit from knowledge of LIS deglaciation history during all terminations, of the past ~1 Ma (through the MPT), when large amplitude 100-kyr glacial-interglacial cycles emerged. An extension of the Site U1302/3 Pb isotope record presented in Chapter 3 and 5 would therefore aid in refining sea-level estimates for past Late Pleistocene interglacials.

6.2.3 Fidelity of the Last Glacial Cycle IODP Site U1313 ε_{Nd} record

Chapter 5 would benefit from either of two additional records, that was not produced due to Covid restrictions: 1) the generation of a detrital ε_{Nd} record from IODP Site U1313 during the LGC is crucial to confirm the fidelity of the fish-debris ε_{Nd} record, or 2) the ε_{Nd} signal recorded by fish debris can be modified by partial dissolution of fresh radiogenic basaltic volcanic glass by sediment pore waters post deposition (Du et al., 2016). Therefore, a volcanic glass record could be produced for this site during the LGC to confirm whether there is any potential relabelling of the ε_{Nd} signal.

6.2.4 Testing different climate scenarios that influence NSW end-member ε_{Nd} compositions

Chapter 5 highlights that the interpretations of proxies for palaeo-reconstructions are constantly being improved, which in turn can revise our understanding of the climate system and highlight new applications of established proxies. In this case, Chapter 5 builds upon new ε_{Nd} records from the deep North Atlantic (Du et al., 2020; Zhao et al., 2019; Pöppelmeier et al., 2021; Abbott et al., 2022) that suggest there was no SSW incursion during the LGM, and that relatively negative $\delta^{13}C$ compositions reflect increased remineralisation under a sluggish Atlantic Meridional Ocean Circulation. One outcome of Chapter 5 is that more than one high latitude climate evolution may explain the LGC trend in the NSW ε_{Nd} record

from IODP Site U1313. Future work could therefore include simple box modelling of NSW ε_{Nd} during the LGC, taking into account uncertainties in, e.g., water-mass end member compositions and their Nd concentrations. This could be used to generate synthetic records of NSW ε_{Nd} for each scenario that could be compared to the U1313 ε_{Nd} record to identify the scenarios most likely to explain the trends shown in Chapter 5.

6.2.5 High-resolution extension of the ε_{Nd} dataset across the Mid Pleistocene Transition

Chapter 5 could benefit from producing the high-resolution ε_{Nd} record from Site U1313 up to and through the MPT (~1200-800 ka), complementing the low resolution record presented by Kim et al. (2021). By doing so, this new ε_{Nd} record combined with a Pb isotope record (suggested in Section 6.2.1) for the same interval tracking LIS extent, will likely provide insight into climate processes operating during the MPT.

References

Abbott, A.N., Haley, B.A., McManus, J., Reimers, C.E., 2015. The sedimentary flux of dissolved rare earth elements to the ocean. Geochim. Cosmochim. Acta 154, 186–200.

Abbott, A.N., Haley, B.A., McManus, J. 2016. The impact of sedimentary coatings on the diagenetic Nd flux. Earth Planet. Sci. Lett.449, 217–227.

Abbott, A.N., Löhr, S.C., Payne, A., Kumar, H., Du, J. 2022. Widespread lithogenic control of marine authigenic neodymium isotope records? Implications for paleoceanographic reconstructions, Geochim. Cosmochim. Acta.

Abe-Ouchi, A., Saito, F., Kawamura, K., Raymo, M.E., Okuno, J.I., Takahashi, K., Blatter, H., 2013. Insolation-driven 100,000-year glacial cycles and hysteresis of ice-sheet volume. Nature, 500, 190–193.

Aksu, A.E., Hiscott, R.N., 1992. Shingled Quaternary debris flow lenses on the northeast Newfoundland Slope. Sedimentology. 39 (2), 193–206.

Aleinikoff, J.N., Muhs, D.R., Bettis, E.A. III, Johnson, W.C., Fanning, C.M., Benton, R., 2009. Isotopic evidence for the diversity of late Quaternary loess in Nebraska: Glaciogenic and nonglaciogenic sources. Geological Society of America Bulletin 120 (11/12).

Andreasen, R,., Peate, D.W., Brooks, C.K., 2004. Magma plumbing systems in large igneous provinces; inferences from cyclical variations in Paleocene east Greenland basalts. Contrib. Mineral. Petrol. 147, 438–452.

Andrews, J.T., 2005. Late Quaternary marine sediment studies of the Iceland shelf, Paleoceanography and land/ice sheet/ocean interactions. In Iceland: Modern Processes and Past Environments, Caseldine, C., Ruseell, A., Hardardottir, J., Knudsen, O. (eds.). Elsevier: London, 5–24.

Andrews, J.T., 2008. The role of the Iceland Ice Sheet in the North Atlantic during the late Quaternary: a review an evidence from Denmark Strait. Journal of Quaternary Science 23(1), 3–20.

Andrews, J.T., Bigg, G.R., Wilton, D.J., 2014. Holocene ice-rafting and sediment transport from the glaciated margin of East Greenland (67–70°N) to the N Iceland shelves: detecting and modelling changing sediment sources. Quat. Sci. Rev. 91, 204–217.

Antonioli, F., Furlani, S., Montagna, P., Stocchi, P., 2021. The Use of Submerged Speleothems for Sea Level Studies in the Mediterranean Sea: A New Perspective Using Glacial Isostatic Adjustment (GIA). Geosciences 11, no. 2: 77.

Arcuri, G.A., Dickin, A.P., 2018. Pb Isotope Mapping of Paleoproterozoic Gneisses in the SW Grenville Province: Evidence for a Cryptic Continental Suture. Geosciences 8, 247.

Ashwal, L.D., Wooden, J.L., Emslie, R.F., 1986. Sr, Nd and Pb isotopes in Proterozoic instrusives astride the Grenville Front in Labrador: Implications for crustal contamination and basement mapping. Geochim. Cosmochim. Acta 50, 2571-2585.

Baadsgaard, H., Collerson, K.D., Bridgwater D., 1979. The Archaean gneiss complex of northern Labrador. 1. Preliminary U–Th–Pb geochronology. Can J Earth Sci 16(4), 951–961.

Baadsgaard, H., Nutman, A.P., Bridgwater, D. Geochronology and isotope geochemistry of the early Archaean Amîtsoq gneisses of the Isukasia area, southern West Greenland. Geochim. Cosmochim. Acta, 50 (1986), pp. 2173-2183.

Bailey, I., Bolton, C.T., DeConto, R.M., Pollard, D., Schiebel, R., & Wilson, P.A., 2010. A low threshold for North Atlantic ice rafting from “low-slung slippery” late Pliocene ice sheets, Paleoceanography, 25, PA1212.

Bailey, I., Hole, G.M., Foster, G.L., Wilson, P.A., Storey, C.D., Trueman, C.N., Raymo, M.E., 2013. An alternative suggestion for the Pliocene onset of major northern hemisphere glaciation based the geochemical provenance of North Atlantic Ocean ice-rafted debris. Quat. Sci. Rev. 75, 181–194.

Bajo, P., Drysdale, R.N., Woodhead, J.D., et al. 2020. Persistent influence of obliquity on ice age terminations since the Middle Pleistocene transition. Science 367, 1235–1239.

Baker, J,M Peate, D., Waight, T., Meyzen, C., 2004. Pb isotopic analysis of standards and samples using a ^{207}Pb–^{204}Pb double spike and thallium to correct for mass bias with a double-focusing MC-ICP-MS. Chemical Geology 211 (3-4), 275–303.

Balco, G., and Rovey, C. W., 2010, Absolute chronology for major Pleistocene advances of the Laurentide Ice Sheet, Geology, 38(9), 795–798.

Barber, D. C., Dyke, A., Hillaire-Marcel, C., Jennings, A.E., Andrews, J.T.A. Kerwin, M., Bilodeau, W.G., McNeely, R., Southon, J., Morehead, M.D., Gagnon, J.-M. 1999. Forcing of the cold event 8,200 years ago by catastrophic drainage of Laurentide lakes, Nature, 400, 344–348.

Bard, E., Antonioli, F., Silenzi, S., 2002. Sea-level during the penultimate interglacial period based on a submerged stalagmite from Argentarola Cave (Italy). Earth. Planet. Sco/ Lett. 196, 135–146.

Barker, A.K., Baker, J.A., Peate, D.W., 2006. Interaction of the rifting East Greenland margin with a zoned ancestral Iceland plume. Geology 34(6), 481–484.

Barker, S., Chen, J., Gong, X., Jonkers, L., Knorr, G., & Thornalley, D. 2015. Icebergs not the trigger for North Atlantic cold events. Nature, 520(7547), 333–336.

Barker, S., Knorr, G., Conn, S., Lordsmith, S., Newman, D., & Thornalley, D. 2019. Early interglacial legacy of deglacial climate instability. Paleoceanography and Paleoclimatology, 34, 1455–1475.

Barker, S., Zhang, X., Jonkers, L., Lordsmith, S., Conn, S., & Knorr, G., 2021. Strengthening Atlantic inflow across the mid-Pleistocene transition. Paleoceanog. and Paleoclimatol., 36, e2020PA004200.

Bashirova, L.D., Kandiano, E.S., Sivkov, V.V., Bauch, H.A., 2014. Migrations of the North Atlantic Polar front during the last 300 ka: Evidence from planktic foraminiferal data. Oceanology 54 (6), 798–807.

Batchelor, C.L., Margold, M., Krapp, M., Murton, D.K, Dalton, A.S., Gibbard, P.L., Stokes, C.R., Murton, J.B., Manica, A., 2019. The configuration of Northern Hemisphere ice sheets through the Quaternary. Nat. Commun. 10(10), 3713.

Bau, M., Schmidt, K., Koschinsky, A., Hein, J., Kuhn, T., Usui, A., 2014. Discriminating between different genetic types of marine ferro-manganese crusts and nodules based on rare earth elements and yttrium. Chem. Geol. 381, 1–9.

Bauch, H.A., Kandiano, E.S., and Helmke, J.P., 2012. Contrasting ocean changes between the subpolar and polar North Atlantic during the past 135 ka. Geophys. Res. Lett. 39 (11604), 1–7.

Bayon, G., German, C.R., Boella, R.M., Milton, J.A., Taylor, R.N., Nesbitt, R.W., 2002. An improved method for extracting marine sediment fractions and its application to Sr and Nd isotopic analysis. Geochim. Cosmochim. Acta 187, 170–199.

Bé, A. W. H., 1960. Some Observations on Arctic Planktonic Foraminifera. Contributions from the Cushman Foundation for Foraminiferal Research 11: 64-68.

Bea, F. 1996. Residence of REE, Y, Th and U in granites and crustal protoliths; implications for the chemistry of crustal melts. J. Petrol., 37, 521-552.

Bereiter, B., Eggleston, S., Schmitt, J., Nehrbass-Ahles, C., Stocker, T.F., Fischer, H., Kipfstuhl, S., Chappellaz, J. 2015. Revision of the EPICA Dome C CO_2 record from 800 to 600 kyr before present. Geophys. Res. Lett. 42 (2), 542-549.

Blake-Mizen, K.R., Hatfield, R.G., Stoner, J.S., Carlson, A.E., Xuan C, Walczak, M.H., Lawrence, K.T., Channell, J.E.T., Bailey, I., 2019. Southern Greenland glaciation and western boundary undercurrent evolution recorded on Eirik Drift during the late Pliocene intensification of Northern Hemisphere glaciation. Quat Sci Rev (209), 40–51.

Blaser P., Lippold J., Gutjahr M., Frank N., Link J.M. and Frank M., 2016. Extracting foraminiferal seawater Nd isotope signatures from bulk deep sea sediment by chemical leaching. Chemical Geology. 439, 189–204.

Blaser, P., Pöppelmeier, F., Schulz, H., Gutjahr, M., Frank, M., Lippold, J., Heinrich, H., Link, J.M., Hoffmann, J., Szidat, S., Frank, N., 2019. The resilience and sensitivity of Northeast Atlantic deep water ε_{Nd} to overprinting by detrital fluxes over the past 30,000 years. Geochim. Cosmochim. Acta, 245, 79–97.

Blaser, P., Gutjahr, M., Pöppelmeier, F., Frank, M., Kaboth-Bahr, S., Lippold, J., 2020. Labrador Sea bottom water provenance and REE exchange during the past 35,000 years. Earth. Plant. Sci. Lett. 542, 116299.

Böhm, E., Lippold, J., Gutjahr, M., Frank, M., Blaser, P., Antz, B., Fohlmeister, J., Frank, N., Andersen, M.B., Deininger, M., 2015. Strong and deep Atlantic meridional overturning circulation during the last glacial cycle. Nature 517, 73–76.

Bolton, C.T., Bailey, I., Friedrich, O. et al., 2018. North Atlantic Midlatitude Surface-Circulation Changes Through the Plio-Pleistocene Intensification of Northern Hemisphere Glaciation. Paleoceanogr. and Paleoclimatol. 33, 1186–1205.

Bolton, C.T., Wilson, P.A., Bailey, I., Friedrich, O., Beer, C.J., Becker, J., Baranwal, S., Schiebel, R. 2010. Millennial-scale climate variability in the subpolar North Atlantic Ocean during the late Pliocene. Paleoceaography, 25, PA4218.

Bond, G., Heinrich, H., Broecker, W.S., Labeyrie, L., McManus, J., Andrews, J.T., Huon, S., Jantschik, R., Clasen, S., Simet, C., Tedesco, K., Klas, M., Bonani, G., Ivy, S., 1992. Evidence for massive discharges of icebergs into the glacial Northern Atlantic. Nature 360, 245–249.

Bond, G.C., Lotti, R.L., 1995. Iceberg Discharges into the North Atlantic on Millennial Time Scales During the Last Glaciation. Science 267, 1005–1010.

Bond, G.C., Showers, W., Elliot, M., Evans, M., Lotti, R., Hajdas, I., Bonani, G., Johnson, S. 1999. The North Atlantic's 1–2~kyr climate rhythm: relation to Heinrich events, Dansgaard–Oeschger events, and the Little Ice Age. Geophys. Monogr. Ser., 112, 35-58.

Bowen, D.Q., 2010. Sea level, 400000 years ago (MIS 11): analogue for present and future sea-level? Clim. Past 6, 19–29.

Broecker, W. S. & van Donk, J., 1970. Insolation changes, ice volumes and the ^{18}O in deep-sea cores. Rev. Geophys. Space Phys. 8, 169–198.

Broecker, W. S., 1982. Glacial to interglacial changes in ocean chemistry. Prog. Oceanogr. 11, 151–197.

Broecker, W.S., and Peng, T.H. 1982. Tracers in the Sea. Lamont-Doherty Geological Observatory, Columbia University, Palisades, NY, 243 pp.

Brouard, E., Roy, M., Godbout, P-M, Veillette, J.J., 2021. A framework for the timing of the final meltwater outburts from glacial Lake Agassiz-Ojibway. Quat. Scr. Rev. 274, 107269.

Burton, K. W., Lee, D.-C., Christensen, J. N., Halliday, A. N. & Hein, J. R. 1999. Actual timing of neodymium isotopic variations recorded by FeMn crusts in the western North Atlantic. Earth Planet. Sci. Lett 171, 149–156.

Calvo, E., Villanueva, J., Grimalt, J.O., Boelaert, A., Labeyrie, L. 2001. New insights into the glacial latitudinal temperature gradients in the North Atlantic. Results from UK'37 sea surface temperatures and terrigenous inputs. Earth Planet. Sci. Rev. 188(3-4), 509-519.

Carlson, A.E., Clark, P.U., Raisbeck, G.M., Brook, E.J. 2007. Rapid Holocene deglaciation of the Labrador sector of the Laurentide ice sheet J. Clim., 20.

Carlson, A.E., Stoner, J.S., Donnelly, J.P., Hillaire-Marcel, C., 2008. Response of the southern Greenland Ice Sheet during the last two deglaciations. Geology 36, 359-362.

Chalk, T.B., Hain, M.P., Foster, G.L. et al., 2017. Causes of ice age intensification across the Mid-Pleistocene Transition. Proc. Natl Acad. Sci. USA 114, 13114–13119.

Chalk, T.B., Foster, G.L., Wilson, P.A., 2019. Dynamic storage of glacial CO_2 in the Atlantic Ocean revealed by boron [CO_3^{2-}] and pH records. Earth Planet. Sci. Lett. 510(15), 1–11.

Champion, D.C. 2013. Neodymium depleted mantle model age map of Australia: explanatory notes and user guide. Record 2013/44. Geoscience Australia: Canberra.

Channell, J.E.T., Kanarnatsu, T., Sato, T., Stein, R., Alvarez Zarikian, C.A., Malone, M.J., 2006. Sites U1302 and U1303. In: Proceedings of the IODP, Volume 303/306, College Station TX (Integrated Ocean Drilling Program Management).

Channell, J. E. T., Hodell, D. A., Romero, O., Hillaire-Marcel, C., de Vernal, A., Stoner, J. S., et al., 2012. A 750-kyr detrital-layer stratigraphy for the North Atlantic (IODP Sites U1302-U1303, Orphan Knoll, Labrador Sea). Earth Planet. Sci. Lett., 317–318, 218–230.

Channell, J.E.T., Xuan, C., Hodell, D.A., 2009. Stacking paleointensity and oxygen isotope data for the last 1.5 Myrs (PISO-1500). Earth Planet. Sci. Lett. 283, 14–23.

Chen, T. et al., 2016. Ocean mixing and ice-sheet control of seawater $^{234}U/^{238}U$ during the last deglaciation. Science 354, 626–629.

Clark, P.U. & Pollard, D. 1998. Origin of the middle Pleistocene transition by ice sheet erosion of regolith. Paleoceanography 13, 1–9.

Clark, P. U., & Mix, A. C., 2002. Ice sheets and sea level of the Last Glacial Maximum. Quaternary Science Reviews, 21(1-3), 1–7.

Clark, P.U., Archer, D., Pollard, D., Blum, J.D., Rial, J.A., Brovkin, V., Mix, A.C., Pisias, N. G., & Roy, M., 2006. The middle Pleistocene transition: Characteristics, mechanisms, and implications for long-term changes in atmospheric pCO_2, Quat. Sci. Rev., 25(23-24), 3150–3184.

Clark, P. U., Dyke, A. S., Shakun, J. D., Carlson, A. E., Clark, J., Wohlfarth, B., et al., 2009. The Last Glacial Maximum. Science, 325(5941), 710–714.

CLIMAP, 1976. The surface of the ice age Earth. Science, 191, 1131–1137.

Cohen, R.S., O'Nions, R.K., 1982. The Lead, Neodymium and Strontium Isotopic Structure of Ocean Ridge Basalts. Journal of Petrology 23, 299–324.

Colleoni, F., Liakka, J., Krinner, G., Jakobsson, M., Masina, S., Peyaud, V., 2011. The sensitivity of the Late Saalian (140 ka) and LGM (21 ka) Eurasian ice sheets to sea surface conditions. Clim. Dyn. 37, 531–553.

Colleoni, F., Masina, S., Cherchi, A., Iovino, D., 2014. Impact of orbital parameters and greenhouse gas on the climate of MIS 7 and MIS 5 glacial inceptions. J. Clim. 27, 8918–8933.

Colleoni, F., Wekerle, C., Neaslund, J.-O., Brandefelt, J., Masina, S., 2016. Constraint on the penultimate glacial maximum Northern Hemisphere ice topography (~140 kyrs BP). Quat. Sci. Rev. 137, 97–112.

Colville, E.J., Carlson, A.E., Beard, B.J., Hatfield, R.G., Stone, J.S., Reyes, A.V., Ullman, D.J., 2011. Sr-Nd-Pb Isotope Evidence for Ice-Sheet Presence on Southern Greenland During the Last Interglacial. Science 333, 620.

Connelly, T.N. 2001. Constraining the Timing of Metamorphism: U-Pb and Sm/Nd Ages from a Transect across the Northern Torngat Orogen, Labrador, Canada. The Journal of Geology, 109(1), 57-77.

Crocker, A.J., Chalk, T.B., Bailey, I., Spencer, M.R., Gutjahr, M., Foster, G.L., Wilson, P.A. 2016. Geochemical response of the mid-depth Northeast Atlantic Ocean to freshwater input during Heinrich events 1 to 4. Quat. Sci. Rev. 151, 236-254.

Crocket, K.C. Vance, D., Gutjahr, M., Foster, G.L.Richards, D.A. 2011. Persistent Nordic see-water overflow to the glacial North Atlantic. Geology, 39(6) 515–518.

Crocket, K.C., Vance, D., Foster, G.L., Richards, D.A., Tranter, M., 2012. Continental weathering fluxes during the last glacial/interglacial cycle: insights from the marine sedimentary Pb isotope record at Orphan Knoll, NW Atlantic. Quat. Sci. Rev. 30, 89–99.

Crocket, K.C., Hill, E., Abell, R.E., Johnson, C., Gary, S.F., Brand, T., Hathorne, E.C., 2018. Rare Earth element distribution in the NE Atlantic: evidence for benthic sources, longevity of the seawater signal, and biogeochemical cycling. Front. Mar. Sci.5.

Cuny, J., Rhines, P.B., Niiler, P.P. and Bacon, S., 2002: Labrador Sea boundary currents and the fate of Irminger Sea water. J. Phys. Oceanogr., 32 , 627–647.
Curry, W.B., Oppo, D.W., 2005. Glacial water mass geometry and the distribution of $\delta^{13}C$ of ΣCO_2 in the western Atlantic Ocean: Paleoceanography 20, PA1017.
Dalton, A.S., Finkelstein, S.A., Barnett, P.J., Forman, S.L., 2016. Constraining the late Pleistocene history of the Laurentide ice sheet by dating the Missinaibi Formation, Hudson bay lowlands, Canada. Quat. Sci. Rev. 146, 288–299.
Dalton, A.S., Finkelstein, S.A., Forman, S.L., Barnett, P.J., Pico, T., Mitrovica, J.X., 2019. Was the Laurentide ice sheet significantly reduced during marine Isotope stage 3? Geology 47, 111–114.
Dalton, A.S., Margold, M., Stokes, C.R., Tarasov, L., Dyke, A.S., Adams, R.S, et al., 2020. An updated radiocarbon-based ice margin chronology for the last deglaciation of the North American Ice Sheet Complex. Quat Sci Rev, 234.
Dausmann, V., Gutjahr, M., Frank, M., Kouzmanov, K., Schaltegger, U., 2019. Experimental evidence for mineral-controlled release of radiogenic Nd, Hf and Pb isotopes from granitic rocks during progressive chemical weathering. Chem. Geol. 507, 64–84.
de Boer, B., Lourens, L., van de Wal, R.S., 2014. Persistent 400,000-year variability of Antarctic ice volume and the carbon cycle is revealed throughout the Plio-Pleistocene. Nat. Commun. 5, 2999.
de la Vega, E., Chalk, T.B., Wilson, P.A. et al. 2020. Atmospheric CO_2 during the Mid-Piacenzian Warm Period and the M2 glaciation. Sci Rep 10, 11002.
De Paolo, D.J., and Wasserburg, G.J. 1976. Nd isotopic variations and petrogenic models. Geophys. Res. Lett. 3, 249-252.
de Vernal, A., Hillaire-Marcel, C., Peltier, W.R., Weaver, A.J., 2002. Structure of the upper water column in the northwest North Atlantic: Modern versus Last Glacial Maximum conditions, Paleoceanography 17(4), 1050.
de Vernal, A., and Hilliare-Marcel, C. 2008. Natural Variability of Greenland Climate, Vegetation, and Ice Volume During the Past Million Years. Science, 320, 1622-1625.
Deaney, E. L., Barker, S., & Van De Flierdt, T. 2017. Timing and nature of AMOC recovery across Termination 2 and magnitude of deglacial CO_2 change. Nature Communications, 8(14),595.
Dendy, S., Austermann, J., Creveling, J.R., Mitrovica, J.X., 2017. Sensitivity of Last Interglacial sea-level high stands to ice sheet configuration during Marine Isotope Stage 6. Quat. Sci. Rev. 171, 234–244.
Denton, G.H., Anderson, R.F., Toggweiler, J.R., Edwards, R.L., Schaefer, J.M. and Putnam, A.E., 2010. The Last Glacial Termination. Science. 328:1652-1656.
Déry, S.J., Mlynowski, T.J., Hernandex-Henriquez, M.A., Straneo, F., 2011. Interannual variability and interdecadal trends in Hudson Bay streamflow. Journal of Marine Systems 88, 341–351.
Deschamps, P., Durand, N., Bard, E., Hamelin, B., Camoin, G., Thomas, A.L., Henderson, G.M., Okuno, J., Yokoyama, Y., 2012. Ice-sheet collapse and sea-level rise at the Bølling warming 14,600 years ago. Nature 483(7391), 559–64.
Dickson, R.R., and Brown, J., 1994. The production of North Atlantic Deep Water: Sources, rates and pathways. J. Geophys. Res., 99 , 12319–12341.
Dickson, A.J., Beer, C.J., Dempsey, C., Maslin M.A., Bendle, J.A., McClymont, E.L., Pancost, R.D., 2009. Oceanic forcing of the Marine Isotope Stage 11 interglacial. Nature Geoscience, 2, 428-433.
Doe, B.R., Delevaux, M.H., 1980. Lead-isotope investigations in the Minnesota River Valley– Late-tectonic and post tectonic granites. Geological Society of America Special Paper 182, 105–112.
Donner, J., 1995. The Quaternary History of Scandinavia. Cambridge University Press, Cambridge. 200 pp.
Dorale, J.A., Onac, B.P., Fornós, J.J., Ginés, J., Ginés, A., Tuccimei, P., Peate, D.W., 2010. Sea-Level Highstand 81,000 Years Ago in Mallorca. Science 327, 5967, 860–863.

Droxler, A.W., Farrell, J.W., 2000. Marine isotope stage 11 (MIS 11): new insights for a warm future. Glob. Planet. Change 24, 1–5.
Du, J., Haley, B.A., Mix, A.C., 2016. Neodymium isotopes in authigenic phases, bottom waters and detrital sediments in the Gulf of Alaska and their implications for paleo-circulation reconstruction. Geochim. Cosmochim. Acta 193, 14–35.
Du J., Haley B.A., and Mix A.C., 2020. Evolution of the Global Overturning Circulation since the Last Glacial Maximum based on marine authigenic neodymium isotopes, Quat. Sci. Rev. 241, 106396.
Dumitru, O.A., Austermann, J., Polyak, V.J. et al., 2019. Constraints on global mean sea level during Pliocene warmth. Nature 574, 233–236.
Duplessy, J.C., Shackleton, N.J., Fairbanks, R.G., Labeyrie, L., Oppo. D., Kallel, N. 1988. Deepwater source variations during the last climatic cycle and their impact on the global deep water circulation. Paleoceanography 3(3), 343–360.
Dutton, A, Carlson, A.E., Long, A.J., Milne, G.A., Clark, P.U., DeConto, R., Horton, B.P., Rahmstorf, S., Raymo, M.E. 2015. Sea-level rise due to polar ice-sheet mass loss during past warm periods. Science, 349.
Dwyer, B., Austermann, J., D'Andrea, W.J., Crell, R.C., Sandstrom, M.R., Cashman, M., Rovere, A., Raymo, M.E., 2021. Sea-level trends across The Bahamas constrain peak last interglacial ice melt. PNAS 118 (33), e202689118.
Dyer, B., Austermann, J., D'Andrea, W.J., Crell, R.C., Sandstrom, M.R., Cashman, M., Rovere, A., Raymo, M.E., 2021. Sea-level trends across The Bahamas constrain peak last interglacial ice melt. PNAS 118 (33), e202689118.
Dyez, K.A., Hönisch, B. & Schmidt, G.A., 2018. Early Pleistocene obliquity-scale pCO_2 variability at ~1.5 Million Years Ago. Paleoceanogr. Paleoclimatol. 33, 1270–1291.
Dyke, A.S., Andrews, J.T., Clark, P.U., England, J.H., Miller, G.H., Shaw, J., Veillette, J.J., 2002. The Laurentide and Innuitian ice sheets during the last glacial maximum. Quat. Sci. Rev. 21, 9–31.
Ehlers, J., Gibbard, P. L. & Hughes, P. D. (eds). Quaternary Glaciation Extent and Chronology: a Closer Look. Developments in Quaternary Science 15 (Elsevier, Amsterdam, 2011).
Elderfield, H., Ferretti, P., Greaves, M., Crowhurst, S., McCave, I.N., Hodell, D., Piotrowski, A.M., 2012. Evolution of ocean temperature and ice volume through the Mid-Pleistocene Climate Transition. Science 337, 704–709.
Elmore, A.C., Piotrowski, A.M., Wright, J.D., Scrivner, A.E., 2011. Testing the extraction of past seawater Nd isotope composition from North Atlantic deep sea sediments and foraminifera. Geochem. Geophys. Geosyst., 12, Q09008.
Erel, Y.G., Harlavan, Y., Blum, J.D., 1994. Lead-isotope systematics of granitoid weathering. Geochim. Cosmochim. Acta. 58(23), 5299-5306.
Expedition 303 Scientists, 2006. Site U1308. In: North Atlantic Climate. Channell, J.E.T. et al. (Eds.) Proc. Integr. Ocean Drill. Program, 303.
Eynaud, F., De Abreu, L., Voelker, A., Schonfeld, J., Salgueiro, E., Turon, J.-L., et al., 2009. Position of the Polar Front along the western Iberian margin during key cold episodes of the last 45 ka. Geochemistry, Geophysics, Geosystems, 10(7).
Fagel, N., Innocent, C., Gariepy, C., Hillaire-Marcel, C., 2002. Sources of Labrador Sea sediments since the last glacial maximum inferred from Nd-Pb isotopes. Geochim. et Cosmochim. Acta 66(14), 2569–2581.
Fagel, N., Innocent, C., Stevenson, R.K., Hillaire-Marcel, C. 1999. Deep circulation changes in the Labrador Sea since the Last GlacialMaximum: New constraints from Sm-Nd data on sediments, Paleoceanography, 14, 777–788.
Fagel, N., Hillaire-Marcel, C., Humblet, M., Brasseur, R., Weis, D. and Stevenson, R. 2004. Nd and Pb isotope signatures of the clay-size fraction of Labrador Sea sediments during the Holocene: Implications for the inception of the modern deep circulation pattern. Paleoceanography, 19, PA3002.
Fagel, N., and Mattielli, N. 2011. Holocene evolution of deep circulation in the northern North Atlantic traced by Sm, Nd and Pb isotopes and bulk sediment mineralogy. Paleoceanography, 26(4), PA4220.

Farmer, G.L., Barber, D., Andrews, J.T., 2003. Provenance of Late Quaternary ice-proximal sediments in the North Atlantic: Nd, Sr and Pb isotopic evidence. Earth Planet. Sci. Lett. 209, 227–243.

Fowland, S.G., 1982. Geochemistry, geochronology and origin of an Archean greenstone-granite terrain Wabigoon Subprovince northwestern Ontario. Graduate Student Theses. Dissertations, & Professional Papers. 7500.

Forsström, L. & Punkari, M., 1997. Initiation of the last glaciation in northern Europe. Quat. Sci. Rev. 16, 1197–1215.

Foster, G.L., Vance, D., 2006. Negligible glacial–interglacial variation in continental chemical weathering rates. Nature 444, 918–921

Foster, G.L., Vance, D. & Prytulak, J., 2007. No change in the neodymium isotope composition of deep water exported from the North Atlantic on glacial-interglacial time scales. Geology 35, 37–40.

Frank, M., 2002. Radiogenic isotopes: tracers of past ocean circulation and erosional input. Rev. Geophys. 40, 1001.

Fronval, T., Jansen, E. 1997. Eemian and early Weichselian (140-60 ka) paleoceanography and paleoclimate in the Nordic Seas with comparisons to Holocene conditions. Paleoceanography 12, 443-462.

Gale, A., Dalton, C.A., Langmuir, C.H., Su, Y., Schilling, J.-G., 2013. The mean composition of ocean ridge basalts. Geochem. Geophys. Geosyst.14, 489–518.

Gariepy, C. and Allegre, C.J. 1985. The lead isotope geochemistry and geochronology of late-kinematic intrusives from the Abitibi greenstone belt, and the implications for late Archean crustal evolution. Geochim. Cosmochim. Acta 49, 237 1–2383.

Gascard, J-C, Clarke, R.A., 1983. The Formation of Labrador Sea Water. Part II. Mesoscale and Smaller-Scale Processes. Journal of Physical Oceanography, 13 (10). 1779-1797.

Gauthier, M.S., Hoer, T.J., Ross, M, Kelley, S.E., Rochester, A., McCausland, P., 2019. The subglacial mosaic of the Laurentide Ice Sheet; a study of the interior region of southwestern Hudson Bay. Quat. Sci. Rev. 214, 1–27.

Goldstein, S.L., Hemming, S.R., 2003. Long-lived isotopic tracers in oceanography, paleoceanography, and ice-sheet dynamics. In: Holland, H.D., Turekian, K.K. (Eds.), Treatise on Geochemistry. Pergamon, Oxford, pp. 453-489.

Gowan, E.J., Zhang, X., Khosravi, S. et al., 2021. A new global ice sheet reconstruction for the past 80 000 years. Nat Commun 12, 1199.

Grant, K. M., Rohling, E.J., Bar-Matthews, M., Ayalon, A., Medina-Elizalde, M., Ramsey, C.B., Satow, C., and Roberts, A.P. 2012. Rapid coupling between ice volume and polar temperature over the past 150,000 years, Nature, 491, 744–747.

Grant, K.M., Rohling, E.J., Ramsey, C.B., Cheng, H., Edwards, R.L., Florindo, F., Heslop, D., Marra, F., Roberts, A.P., Tamisiea, M.E., Williams, F., 2014. Sea-level variability over five glacial cycles. Nat. Commun. 5, 5076.

Grant, G.R., Naish, T.R., Dunbar, G.B., Stocchi, P., Kominz, M.A., Kamp, P.J.J., Tapia, C.A., McKay, R.M., Levy, R.H., Patterson, M.O. 2019. The amplitude and origin of sea-level variability during the Pliocene epoch. Nature, 574, 237–241.

Gregory, J.M., Griffies, S.M., Hughes, C.W. et al., 2019. Concepts and Terminology for Sea Level: Mean, Variability and Change, Both Local and Global. Surv Geophys 40, 1251–1289.

Griem, L., Voelker, A. H. L., Berben, S.M. P., Dokken, T. M., & Jansen, E. 2019. Insolation and glacial meltwater influence on sea-ice and circulation variability in the northeastern Labrador Sea during the last Glacial period. Paleoceanography and Paleoclimatology, 34, 1689–1709.

Grützner, J., & Higgins, S. M., 2010. Threshold behavior of millennial scale variability in deep water hydrography inferred from a 1.1 Ma long record of sediment provenance at the southern Gardar Drift. Paleoceanography, 25, PA4204.

Gutjahr, M., Frank, M., Stirling, C.H., Klemm, V., van de Flierdt, T., Halliday, A.N., 2007. Reliable extraction of a deepwater trace metal isotope signal from Fe-Mn oxyhydroxide coatings of marine sediments. Chemical Geology, 242 (3-4), 351-370.

Gutjahr, M., Frank, M., Halliday, A.N., Keigwin, L.D., 2009. Retreat of the Laurentide ice sheet tracked by the isotopic composition of Pb in western North Atlantic seawater during termination 1. Earth Planet. Sci. Lett. 286, 546–555.

Gutjahr, M., Frank, M., Lippold, J., Halliday, A.N., 2014. Peak Last Glacial weathering intensity on the North American continent recorded by the authigenic Hf isotope composition of North Atlantic deep-sea sediments. Quat. Sci. Rev. 99, 97–111.

Hagen, S., Hald, M., 2002. Variation in surface and deep water circulation in the Denmark Strait, North Atlantic, during marine isotope stages 3 and 2. Paleoceanography 17(4), 1061.

Haley, B. A., Frank, M., Hathorne, E., and Pisias, N., 2014. Biogeochemical implications from dissolved rare earth element and Nd isotope distributions in the Gulf of Alaska. Geochim. Cosmochim. Acta 126, 455–474.

Haley, B.A., Du, J., Abbott, A.N., McManus, J., 2017. The impact of benthic processes on rare earth element and neodymium isotope distributions in the oceans. Front. Mar. Sci. 4.

Haley, B.A., Klinkhammer, G.P., McManus, J., 2004. Rare earth elements in pore waters of marine sediments. Geochim. Cosmochim. Acta 68, 1265–1279.

Hansen, B.T. and Friderichsen, J.D. 1989. The influence of recent lead loss on the interpretation of disturbed U-Pb systems in zircons from igneous rocks in East Greenland. Lithos. 209–223.

Hansen, H., Nielsen, T.F.D, 1999. Crustal contamination in Paleogene East Greenland flood basalts: plumbing system evolution during continental rifting, Chem. Geol. 157, 89–188.

Harlavan, Y., Erel, Y. & Blum, J.D., 1998. Systematic changes in lead isotopic composition with soil age in glacial granitic terrains. Geochim. Cosmochim. Acta 62, 33–46.

Hatfield, R. G., Reyes, A. V., Stoner, J. S., Carlson, A. E., Bard, B. L., Winsor, K., & Welke, B. 2016. Interglacial responses of the Southern Greenland ice sheet over the last 430,000 years determined using particle-size specific magnetic and isotopic tracers. Earth and Planet. Sci. Lett., 454, 225–236.

Hathorne, E.C., Stichel, T., Brück, B., Frank, M., 2015. Rare Earth element distribution in the Atlantic sector of the Southern Ocean: the balance between particle scavenging and vertical supply. Mar. Chem. 177, 157–171.

Hays, J. D., Imbrie, J. & Shackleton, N. J., 1976. Variations in the Earth's orbit: Pacemaker of the Ice Ages. Science 194, 1121–1132.

Haywood, A.M., Valdes, P.J., Aze, T. et al., 2019. What can Palaeoclimate Modelling do for you?. Earth Syst Environ. 3, 1–18.

Hearty, P.J., Rovere, A., Sandstrom, M.R., O'Leary, M.J., Roberts, D., & Raymo, M.E., 2020. Pliocene-Pleistocene stratigraphy and sea-level estimates, Republic of South Africa with implications for a 400 ppmv CO_2 world. Paleoceanogr. Paleoclimatol. 35, e2019PA003835.

Hefter, J., Naafs, B.D.A., Zhang, S., 2017. Tracing the source of ancient reworked organic matter delivered to the North Atlantic Ocean during Heinrich Events. Geochem. et Cosmochim. Acta 205, 211–255.

Hein, J.R., Koschinsky, A., Bau, M., Manheim, F.T., Kang, J.-K., Roberts, L., 1999. Cobalt-rich ferromanganese crusts in the Pacific. In: Cronan, D.S. (Ed.), Handbook of Marine Mineral Deposits. CRC Press, 239–279.

Hemend, C., Arndt, N.T., Lichtenstein, U., Hofmann, A.W., 1993. The Heterogeneous Iceland Plume: Nd-Sr-O Isotopes and Trace Element Constraints. Journal of Geophysical Research 98, No. B9, 15,833-15,850.

Hemming, S.R. 2004. Heinrich events: Massive late Pleistocene detritus layers of the North Atlantic and their global climate imprint. Reviews of Geophysics. 42(1).

Henderson, G.M., Maier-Reimer, E., 2002. Advection and removal of 210Pb and stable Pb isotopes in the oceans: a general circulation model study. Geochim. Cosmochim. Acta 66, 257–272.

Herbert, T.D., Lawrence, K.T., Jiu, Z. 2010. Tropical Ocean Temperatures of the past 3.5 Million Years. Science, 328, 1530.

Hermann, J. 2002. Allanite: thorium and light rare earth element carrier in subducted crust. Chem. Geol., 192, 289-306.
Hibbert, F.D., Rohling, E.J., Dutton, A., Williams, F.H., Chutcharavan, P.M., Zhao, C., Tamisiea, M.E., 2016. Corals as indicators of past sea-level change: a global repository of U-series dated benchmarks. Quat. Sci. Rev. 145, 1–56.
Hillaire-Marcel, C., de Vernal, A., Bilodeau, G., Weaver, A.J., 2001a. Absence of deep-water formation in the Labrador Sea during the last interglacial period. Nature 410, 1073–1077.
Hillaire-Marcel, C., De Vernal, A., Candon, L., Bilodeau, G. and Stoner, J., 2001b. Changes of Potential Density Gradients in the Northwestern North Atlantic During the Last Climatic Cycle Based on a Multiproxy Approach. In The Oceans and Rapid Climate Change (eds. D. Seidov, B.J. Haupt and M. Maslin).
Hillaire-Marcel, C., de Vernal, A., McKay, J., 2011. Foraminifer isotope study of the Pleistocene Labrador Sea, northwest North Atlantic (IODP Sites 1302/03 and 1305), with emphasis on paleoceanographical differences between its “inner” and “outer” basins. Mar. Geol. 279, 188–198.
Hodell, D.A., Channell, J.E.T., Curtis, J., Romero, O., Rohl, U., 2008. Onset of “Hudson Strait” Heinrich events in the eastern north Atlantic at the end of the middle Pleistocene transition (~640 ka)? Paleoceanography 23.
Hoff, U., Rasmussen, T., Stein, R., Ezart, M.M., Fahl. K. 2016. Sea ice and millennial-scale climate variability in the Nordic seas 90 kyr ago to present. Nat Commun 7, 12247.
Holm, P.M., 1988. Nd, Sr and Pb isotope geochemistry of the Lower Lavas, E Greenland Tertiary Igneous Province. In Morton, A.C., Parson, L.M. (eds), Early Tertiary Volcanism and the Opening of the NE Atlantic, Geological Society Special Publications 39, 181–195.
Hönisch, B., Hemming, N.G., Archer, D., Siddall, M. & McManus, J.F., 2009. Atmospheric carbon dioxide concentration across the Mid-Pleistocene transition. Science 324, 1551–1554.
Howe, J.N.W., Piotrowski, A.M., Noble, T.L., Mulitza, S., Chiessi, C.M., Bayon, G., 2016. North Atlantic Deep Water Production during the Last Glacial Maximum. Nature Communications 7, 11765.
Huang, H., Gutjahr, M., Eisenhauer, A., & Kuhn, G. 2020. No detectable Weddell Sea Antarctic bottom water export during the last and penultimate glacial maximum. Nature Communications, 11, 424.
Huck, C. E., van de Flierdt, T., Jiménez-Espejo, F. J., Bohaty, S. M., Röhl, U., & Hammond, S. J. (2016). Robustness of fossil fish teeth for seawater neodymium isotope reconstructions under variable redox conditions in an ancient shallow marine setting. Geochemistry, Geophysics, Geosystems.
Huybers, P., 2011. Combined obliquity and precession pacing of late Pleistocene deglaciations. Nature 480, 229–232.
Imbrie, J., Boyle, E.A., Clemens, S.C., Duffy, A., Howard, W.R., Kukla, G., Kutzbach, J., Martinson, D.G., McIntyre, A., Mix, A.C., 1992. On the structure and origin of major glaciation cycles 1. Linear responses to Milankovitch forcing. Paleoceanography, 7(6),701-738.
Innocent, C., Fagel, N., Stevenson, K., Hillaire-Marcel, C., 1997. Sm-Nd signature of modern and late Quaternary sediments from the northwest North Atlantic: Implications for deep current changes since the Last Glacial Maximum. Earth. Planet. Sci. Lett. 146 (3-4), 607-625.
Irvalı, N., Ninnemann, U.S., Galaasen, E.V., Rosenthal, Y., Kroon, D., Oppo, D.W., Kleiven, H.F., Darling, K.F., Kissel, C. 2012. Rapid switches in subpolar North Atlantic hydrography and climate during the Last Interglacial (MIS 5e). Paleoceanography, 27, PA2207.
Jackson, L. P. & Jevrejeva, S. A., 2016. Probabilistic approach to 21st century regional sea-level projections using RCP and High-end scenarios. Glob. Planet. Change 146, 179–189.

Jacobsen, S.B., Wasserburg, G.J., 1980. Sm-Nd isotopic evolution of chondrites. Earth Planet Sci. Lett. 50, 139-155.
Jardine, G.E., Crocker, A.J., Bailey, I., Cooper, M.J., Milton, J.A., Wilson, P.A., 2021. The imprint of windblown dust from the North American Southwest on the California Channel Islands and Pacific Ocean sediments. Quat. Sci. Rev. 261.
Jeandel, C., Arsouze, T., Lacan, F., T´echin´e, P., Dutay, J.C. 2007. Isotopic Nd compositions and concentrations of the lithogenic inputs into the ocean: a compilation, with an emphasis on the margins. Chem. Geol. 239, 156–164.
Jennings, A., Andrews, J., Pearce, C., Wilson, L., Ólfasdótttird, S., 2015. Detrital carbonate peaks on the Labrador shelf, a 13-7ka template for freshwater forcing from the Hudson Strait outlet of the Laurentide Ice Sheet into the subpolar gyre. Quat. Sci. Rev. 107(1), 62-80).
Jensen, S.M., 1994. Lead isotope signatures of mineralized rocks in the Caledonian fold belt of North-East Greenland. App. Grønlands. Geol. Under. 162, 169–176.
Jochum, K.P., Weis, U., Schwager, B., Stoll, B., Wilson, S.A., Haug, G.H., Andreae, M.O., Enzweiler, J. 2016. Reference values following ISO guidelines for frequently requested rock reference materials. Geostandards and Geoanalytical Research. 40(3), 333–350.
Jouzel, J., Masson-Delmotte, V., Cattani, O., Dreyfus, G., Falourd, S., Hoffmann, G. et al., 2007. Orbital and millennial Antarctic climate variability over the past 800,000 years. Science, 317(5839), 793–796.
Kalsbeek, F., Pidgeon, R.T., Taylor, P.N., 1987. Nagssugtoqidian mobile belt of West Greenland: a cryptic 1850 Ma suture between two Archaean continents–chemical and isotopic evidence. Earth Planet. Sci. Lett. 85, 365–385.
Kalsbeek, F., Taylor, P.N. & Pidgeon, R.T. 1988. Unreworked Archaean basement and Proterozoic supracrustal rocks from northeastern Disko Bugt, West Greenland: implications for the nature of Proterozoic mobile belts in Greenland. Canadian Journal of Earth Sciences 25, 773–782.
Kalsbeek, F., Taylor, P.N. & Henriksen, N. 1984. Age of rocks, structures, and metamorphism in the Nagssugtoqidian mobile belt, West Greenland – field and Pb-isotopic evidence. Canadian Journal of Earth Sciences 21, 1126–1131.
Kalsbeek, F and Taylor, P.N 1985. Isotopic and chemical variation in granites across a Proterozic continental margin – the Ketilidian mobile belt of south Greenland. Earth Planet. Sci. Lett. 73, 65–80.
Kalsbeek, F., Austrheim, H., Bridgwater, D., Hansen, B.T., Pedersen, S., Taylor, P.N., 1993. Geochronology of Archaean and Proterozoic events in the Ammassalik area, South-East Greenland, and comparisons with the lewis ian of Scotland and the Nagssugtoqidian of West Greenland. Precambrian Research 62, 239–270.
Kandiano, E.S., Bauch, H.A. 2007. Phase relationship and surface water mass change in the North East Atlantic during Marine Isotope stage 11 (MIS 11). Quaternary Research 68, 445–455.
Kerr, P.J., Tassier-Surine, S.A., Kilgore, S.M., Bettis III, E.A., Dorale, J.A., Cramer, D. B. et al., 2021. Timing, provenance, and implications of two MIS 3 advances of the Laurentide Ice Sheet into the Upper Mississippi River Basin, USA. Quat. Sci. Rev. 261, 106926.
Kerwin, M.W., 1996. A regional stratigraphic isochron (ca. 8000 ^{14}C yr B.P.) from final deglaciation of Hudson Strait, Quat. Res., 46, 89–98.
Kim, J., Goldstein, S.L., Pena, L.D., Jaume-Segu, M., Knudson, K.P. Yehudai, M., Bolge, L. 2021. North Atlantic deep water during Pleistocene interglacials and glacials. Quat. Sci. Rev. 269, 107146.
Kirby, K., Bailey, I., Lang, D.C., Brombacher, A., Chalk, T.B., Parker, R.L., Crocker, A.J. Taylor, V.E., Milton, J.A., Foster, G.L., Raymo, M.E., Kroon, D., Bell, D.B., Wilson, P.A. 2020. On climate and abyssal circulation in the Atlantic Ocean during late Pliocene marine isotope stage M2, ~3.3 million years ago. Quat. Sci. Rev. 250.

Kleiven, H.F., Jansen, E., Fronval, T., Smith, T.M., 2002. Intensification of Northern Hemisphere glaciations in the circum Atlantic region (3.5-2.4 Ma) - ice-rafted detritus evidence. Palaeogeogr. Palaeoclimatol. Palaeoecol., 184, 213-223.

Kleman, J., Jansson, K., De Angelis, H., Stroeven, A.P., Hättestrand, C., Alm, G., and Glasser, N., 2010, North American Ice Sheet build-up during the last glacial cycle, 115–21 kyr: Quat. Sci. Rev. 29, 2036–2051.

Kleman, J., Fastook, J., Ebert, K., Nilsson, J., Caballero, R., 2013. Pre-LGM Northern Hemisphere ice sheet topography. Clim. Past. 9, 2365–2378.

Klemm, V., Reynold, B., Frank, M., Pettke, T., Halliday, A.N. 2007. Cenozoic changes in atmospheric lead recorded in Central Pacific ferromanganese crusts. Earth Planet. Sci. Lett. 253(1-2), 57-66.

Knutz, P.C., Austin, W.E.N., Jones, E.J.W., 2001. Millennial-scale depositional cycles related to British Ice Sheet variability and North Atlantic paleocirculation since 45 kyr B.O., Barra Fan, U.K. margin. Paleoceanography 16(1), 53–64.

Kopp, R.E., Simons, F.J., Mitrovica, J.X., Maloof, A.C., Oppenheimer, M.A., 2013. A probabilistic assessment of sea level variations within the last interglacial stage, Geophysical Journal International 193(2), 711–716.

Kopp, R.E., Horton, R.M., and Little, C.M. et al., 2014. Probabilistic 21st and 22nd century sea-level projections at a global network of tide-gauge sites. Earth's. Future 2, 383–406.

Kulp, S.A., & Strauss, B.H. 2019. New elevation data triple estimates of global vulnerability to sea-level rise and coastal flooding. Nat Commun. 10, 4844.

Kurzweil, F., Gutjahr, M., Vance, D., Keigwin, L., 2010. Authigenic Pb isotopes from the Laurentian Fan: changes in chemical weathering and patterns of North American freshwater runoff during the last deglaciation. Earth Planet. Sci. Lett. 299, 458–465.

Labeyrie, L., Vidal, L., Cortijo, E., Paterne, M., Arnold, M., Duplessy, J. C., Vautravers, M., Labracherie, M., Duprat, J., Turon, J. L., Grousset, F., van Weering, T., 1995. Surface and deep hydrology of the Northern Atlantic Ocean during the past 150,000 years. Philosophical Transactions Royal Society London, B 348, 255 264.

Lacan, F and Jeandel, C., 2004a. Denmark Strait water circulation traced by heterogeneity in neodymium isotopic compositions. Deep-Sea Research I, 51, 71-82.

Lacan, F and Jeandel, C. 2004b. Subpolar Mode Water formation traced by neodymium isotope composition. Geophysical Research Letters, American Geophysical Union, 2004, 31, L14306.

Lajeunesse, P., St-Onge, G., 2008. The subglacial origin of the Lake Agassiz-Ojibway final outburst flood. Nat. Geosci. 1, 184-188.

Lambeck, K. Purcell, A., Funder, S., Kjaer, K., Larsen, E., Möller, P., 2006. Constraints on the Late Saalian to early Middle Weichselian ice sheet of Eurasia from field data and rebound modelling. Boreas 35, 539–575.

Lambeck, K., Purcell, A., Zhao, J., Svensson, N.O., 2010. The Scandinavian Ice Sheet: from MIS 4 to the end of the last glacial maximum. Boreas 39, 410–435.

Lambeck, K., Rouby, H., Purcell, A., Sun, Y., Sambridge, M. 2014. Sea level and global ice volumes from the last glacial maximum to the Holocene. Proc. Natl. Acad. Sci. Unit. States Am. 111, 15296-15303.

Lambeck, K., Purcell, A., Zhao, S., 2017. The North American Late Wisconsin ice sheet andmantle viscosity from glacial rebound analyses. Quat. Sci. Rev. 158, 172–210.

Lambelet, M., van de Flierdt, T., Crocket, K., Rehkämper, M., Kreissig, K., Coles, B., Rijkenberg, M.J.A., Gerringa, L.J.A., de Baar, H.J.W., Steinfeldt, R., 2016. Neodymium isotopic composition and concentration in the western North Atlantic Ocean: Results from the GEOTRACES GA02 section. Geochimica et Cosmochimica Acta 177, 1–29.

Larsen, B. S., Jr., Keevil, N. B., and Harrison, H. O., 1952. Method for determining the age of igneous rocks using the accessory minerals: Geol. Soc. America Bull. 63,1045-1052.

Lang, D.C., Bailey, I., Wilson, P.A., Beer, C., Bolton, C.T., Newsam, C., Spencer, M.R., Friedrich, O., Gutjahr, M., Foster, G.L., Cooper, C.J., Milton, A., 2014. The transition on North America from the warm humid Pliocene to the glaciated Quaternary traced by eolian dust deposition at a benchmark North Atlantic Ocean drill site. Quat. Sci. Rev. 93C, 125-141.

Lang, D.C., Bailey, I., et al., 2016. Incursions of southern-sourced water into the deep North Atlantic during late Pliocene glacial intensification. Nature Geoscience 9, 375–379.

Laskar, J., Fienga, A., Gastineau, M., Manche, H., 2011. La2010: a new orbital solution for the long-term motion of the Earth. Astronomy Astrophys. 532, A89.

Lavender K., Davis R., Owens W., 2000. Mid-depth recirculation observed in the interior Labrador and Irminger seas by direct velocity measurements. Nature, 407(6800), 66-69.

Lawrence, K.T., Herbert, T.D., Brown, C.M., Raymo, M.E., and Haywood, A.M., 2009. High-amplitude variations in North Atlantic sea surface temperature during the early Pliocene warm period, Paleoceanography, 24, PA2218.

Lear, C.H., Billups, K., Rickaby, R.E.M., Diester-Haass, L., Mawbey, E.M., Sosdian, S.M. 2016. Breathing more deeply: Deep ocean carbon storage during the mid Pleistocene climate transition. Geology 44, 1035–1038.

Lear, C.H., Anand, P., Blenkinsop, T., Foster, G.L., Gagen, M., Hoogakker, B., Larter, R.D., Lunt, D.J., McCave, I.N., McClymont, E., Pancost, R.D., Rickaby, R.E.M., Schultz, D.M., Summerhayes, C., Williams, C.J.R., Zalasiewicz, J., 2021. Geological Society of London Scientific Statement: what the geological record tells us about our present and future climate, Journal of the Geological Society, 178, jgs2020-239.

Lenton, T. M., Rockström, J., Gaffney, O., Rahmstorf, S., Richardson, K., Steffen, W., & Schellnhuber, H. J., 2019. Climate tipping points—too risky to bet against. Nature, 575(7784), 592–595.

Lippold, J., Grützner, J., Winter, D., Lahaye,Y., Mangini, A., Christl, M., 2009. Does sedimentary $^{231}Pa/^{230}Th$ from the Bermuda Rise monitor past Atlantic meridional overturning circulation? Geophys. Res. Lett. 36, L12601.

Lippold, J., Gutjahr, M., Blaser, P., Christner, E., de Carvalho, M.L., Mulitza, S., Christl, M., Wombacher, F., Böhm, E., Antz, B., Cartapanis, O., Vogel, H., Jaccard, S.L, 2016. Deep water provenance and dynamics of the (de)glacial Atlantic meridional overturning circulation. Earth and Planetary Science Letters 445, 68-78.

Lisiecki, L. E., & Raymo, M. E., 2005. A Pliocene-Pleistocene stack of 57 globally distributed benthic $\delta^{18}O$ records. Paleoceanography, 20(1), 1–17.

Lisiecki, L. E., & Raymo, M.E., 2009. Diachronous benthic $\delta^{18}O$ responses during late Pleistocene terminations. Paleoceanography 24, PA3210.

Lochte, A.A., Repschläger, J., Kienast, M. 2019. Labrador Sea freshening at 8.5 ka BP caused by Hudson Bay ice saddle collapse. Nat. Commun. 10, 586.

Loulergue, L., Schilt, A., Spahni, R., Masson-Delmotte, V., Blunier, T., Lemieux, B., Chappellaz, J. (2008). Orbital and millennial-scale features of atmospheric CH_4 over the past 800,000 years. Nature, 453, 383–386.

Loutre, M.F., Berger, A., 2000. Future climatic changes: are we entering an exceptionally Long interglacial? Clim. Change 46, 61–90.

Loutre, M.F., Berger, A., 2003. Marine Isotope Stage 11 as an analogue for the present interglacial. Glob. Planet. Change 36, 209–217.

Lynch-Stieglitz, J. et al., 2007. Atlantic meridional overturning circulation during the Last Glacial Maximum. Science 316, 66–69.

Maffezzoli, N., Vallelonga, P., Edwards, R., Saiz-Lopez, A., Turetta, C., Kjaer, H.A., Barbante, C., Vinther, B., Spolaor, A., 2019. A 120,000-year record of sea ice in the North Atlantic? Clim. Past 15, 2031-2051.

Mao, L., Piper, D.J.W., Saint-Ange, F., Andrews, J.T., 2018. Labrador current fluctuation during the last glacial cycle. Mar. Geol. 395, 234–246.
Margold, M., Stokes, C.R., Clark, C.D. 2018. Reconciling records of ice streaming and ice margin retreat to produce a palaeogeographic reconstruction of the deglaciation of the Laurentide Ice Sheet. Quat. Sci. Rev. 189, 1-30.
Martin, E. E., Blair, S. W., Kamenov, G. D., Scher, H. D., Bourbon, E., Basak, C., and Newkirk, D. N., 2010. Extraction of Nd isotopes from bulk deep sea sediments for paleoceanographic studies on Cenozoic time scales. Chem. Geol. (269), 414-43.
Martínez-Botí, M., Foster, G., Chalk, T. et al., 2015. Plio-Pleistocene climate sensitivity evaluated using high-resolution CO_2 records. Nature 518**,** 49–54.
Maslin, M., Seidov. D., Lowe, J. 2001. Synthesis of the Nature and Causes of Rapid Climate Transitions During the Quaternary. The Oceans and Rapid Climate Change: Past, Present, and Future, AGU Geophysical Monograph, vol. 126, 9-52.
Masson-Delmotte, V., Deyfus, G., Braconnot, P., Johnsen, S., Jouzel, J., Kageyama, M., Landais, A., Loutre, M.-F., Nouet, J., Parrenin, F., Raynaud, D., Stenni, B., Tuenter, E., 2006. Past temperature reconstructions from deep ice cores: relevance for future climate change. Clim. Past 2, 145–165.
Mathieu, L., Crepon, A., Kontak, D.J., 2020. Tonalite-Dominated Magmatism in the Abitibi Subprovince, Canada, and Significance for Cu-Au Magmatic-Hydrothermal Systems. Minerals, 10, 242.
McClymont, E.L., Sosdian, S., Rosell-Mele, A., & Rosenthal, Y. 2013. Pleistocene sea-surface temperature evolution: Early cooling, delayed glacial intensification, and implications for the mid-Pleistocene climate transition, Earth Sci. Rev., 123.
McManus, J.F., Oppo, D.W., Cullen, J.L. 1999. A 0.5-million-year record of millennial-scale climate variability in the North Atlantic. Science 283, 971–975.
McManus, J., Oppo, D., Cullen, J., & Healey, S. 2003. Marine isotope stage 11 (MIS 11): Analog for Holocene and future Climate? In Geophysical Monograph Series (Vol. 137, pp. 69–85). Washington, DC: American Geophysical Union.
McManus, J.F., Francois, R., Gherardi, J.-M., Keigwin, L.D, Brown-Leger, S., 2004. Collapse and rapid resumption of Atlantic meridional circulation linked to deglacial climate changes. Nature 428, 834–837.
Miller, G.H., Andrews, J.T., 2019. Hudson Bay was not deglaciated during MIS-3. Quat. Sci. Rev. 225, 105944.
Miller, K.G., Browning, J.V., Schmelz, W.J., Kopp, R.E., Mountain, G.S., Wright, J.D., 2020. Cenozic sea-level and cryospheric evolution from deep-sea geochemical and continental margin records. Sci. Adv. 6, eaaz1346.
Miller, K.G., Wright, J.D., Browning, J.V., Kulpecz, A., Kominz, M., Naish, T.R., Cramer, B.S. Rosenthal, Y., Peltier, W.R., Sosdian, S. 2012. High tide of the warm Pliocene: Implications of global sea level for Antarctic deglaciation. Geology, 40, 407–410.
Mitrovica, J., Tamisiea, M., Davis, J., Milne, G.A.2001. Recent mass balance of polar ice sheets inferred from patterns of global sea-level change. Nature 409, 1026–1029.
Mitrovica, J. X., Gomez, N., Morrow, E., Hay, C., Latychev, K., & Tamisiea, M. E., 2011. On the robustness of predictions of sea level fingerprints. Geophysical Journal International, 187(2), 729–742.
Mokeddem, Z., and McManus, J. F., 2016, Persistent climatic and oceanographic oscillations in the subpolar North Atlantic during the MIS 6 glaciation and MIS 5 interglacial Paleoceanography, 31, 758–778, doi:10.1002/2015PA002813.
Mokeddem, Z., McManus, J. F. and Oppo, D. W. 2014. Oceanographic dynamics and the end of the last interglacial in the subpolar North Atlantic, Proc. Natl. Acad. Sci. U. S. A., 111(31), 11, 263–11,268.
Montsion, R.M. , Thurston, P. , Ayer, J., 2018. 1:2 000 000 Scale Geological Compilation of the Superior Craton - Version 1: Mineral Exploration Research Centre, Harquail School of Earth Sciences, Laurentian University Document Number MERC-ME-2018-017.

Mudelsee, M., & Raymo, M.E., 2005. Slow dynamics of the Northern Hemisphere glaciation, Paleoceanography, 20(4), PA4022

Naafs, B.D.A, Hefter, J., Stein, R., 2013a. Millennial-scale ice rafting events and Hudson Strait Heinrich(-like) Events during the late Pliocene and Pleistocene: a review. Quat. Sci. Rev. 80, 1–28.

Naafs, B.D.A., Hefter, J., Grutzner, J., Stein, R., 2013b. Warming of surface waters in the mid- latitude North Atlantic during Heinrich events. Paleoceanography 28, 153–163.

Naafs, B.D.A., Hefter, J., Acton, G., Haug, G.H., Martínez-Garcia, A., Pancost, R., Stein, R., 2012. Strengthening of North American dust sources during the late Pliocene (2.7 Ma). Earth Planet. Sci. Lett. 317–318, 8–19.

Naafs, B.D.A., Hefter, J., Stein, R., 2014. Dansgaard-Oeschger forcing of sea surface temperature variability in the midlatitude North Atlantic between 500 and 400 ka (MIS 12). Paleoceanography, 29 (11), 1024-1030.

Naafs, B.D.A., Voelker, A.H.L., Karas, C., Andersen, N., Sierro, F.J. 2020. Repeated near-collapse of the Pliocene sea surface temperature gradient in the North Atlantic. Paleoceanograph. Paleoclimatol. 35 (5) PA003905.

Natural Resources Canada, 2006. Atlas of Canada Watershed Framework. https://www.nrcan.gc.ca/maps-tools-publications/tools/geodetic-reference-systems/water/16888 (Accessed 10 June 2021).

Nicholl, J.A.L., Hodell, D.A., Naafs, B.D.A, Hillaire-Marcel, C., Channell, J.E.T., Romero,O.E., 2012. A Laurentide outburst flooding event dur-ing the last interglacial period. Nat. Geosci. 5, 901-904.

Ng, H.C., Robindson, L.F., McManus, J.F., Mohamed, K.J., Jacobel, A.W., Ivanovic, R.F., Gregoire, L.J., and Chen, T., 2018. Coherent deglacial changes in western Atlantic Ocean circulation: Nature Communications 9, p. 2947.

Norðdahl, H., Pétursson, H.G., 2005. Relative sea-level changes in Iceland, new aspects of the Weichselian deglaciation of Iceland. C. Caseldine, A. Russell, J. Harðardóttir, O. Knudsen (Eds.), Iceland, Modern Processes and Past Environments, Elsevier, Amsterdam, 25-78.

O'Nions, R.K., Pankhurst, R.J., 1973. Secular variation in the Sr-isotope composition of Icelandic Volcanic rocks. Earth Planet Sci. Lett. 21, 13–21.

O'Nions, R. K., Frank, M., von Blanckenburg, F. & Ling, H. F. 1998. Secular variation of Nd and Pb isotopes in ferromanganese crusts from the Atlantic, Indian and Pacific Oceans. Earth Planet Sci. Lett. 155, 15–28.

Obrochta, S.P., Crowley, T.J., Channell, J.E.T., Hodell, D.A., Baker, P.A., Seki, A., Yokoyama, Y., 2014. Climate variability and ice-sheet dynamics during the last three glaciations. Earth Planet. Sci. Lett. 406, 198–212.

Oppenheimer et al., 2019. Sea Level Rise and Implications for Low Lying Islands, Coasts and Communities, Chapter 4 in IPCC 235 Special Report on the Ocean and Cryosphere in a Changing Climate. H.-O. Pörtner, D.C. Roberts, V. Masson-Delmotte, P. Zhai, M. Tignor, E. Poloczanska, K. Mintenbeck, M. Nicolai, A. Okem, J. Petzold, B. Rama, N. Weyer (eds.).

Osborne, A.H., Hathorne, E.C., Schijf, J., Plancherel, Y., Böning, P., Frank, M., 2017. The potential of sedimentary foraminiferal rare earth element patterns to trace water masses in the past. Geochem. Geophys. Geosyst. 18, 1550–1568.

Otto-Bliesner, B.L., Hewitt, C.D., Marchitto, T.M., Brady, E., Abe-Ouchi, A., Crucifix, M., Murakami, S., Weber, S.L., 2007. Last Glacial Maximum ocean thermohaline circulation: PMIP2 model intercomparisons and data constraints. Geophysical Research Letters 34(12).

Parish, R.R. 2001. The response of mineral chronometers to metamorphism and deformation in orogenic belts. In: Miller, J.A., Holdsworth, R.E., Buick, I.S., Hand, M. (Eds.), Continental Reactivation and Reworking, 184, Geological Society Special Publication, London, 289-301.

Patton, G.M., Francois, R., Weis, D., Hathorne, E., Gutjahr, M., Frank, M., Gordon, K., 2021. An experimental investigation of the acquisition of Nd by authigenic phases of marine sediments. Geochem. et Cosmochim. Acta 301, 1–29.

Pearce, C.R., Jones, M.T., Oelkers, E.H., Pradoux, C., Jeandel, C., 2013. The effect of particulate dissolution on the neodymium (Nd) isotope and Rare Earth Element (REE) composition of seawater. Earth Planet. Sci. Lett. 369–370, 138–147.

Peate, D.W. and Stecher, O., 2003. Pb isotope evidence for contributions from different Iceland mantle components to Palaeogene East Greenland flood basalts. Lithos, 67, 39-52.

Peate, D.W., Baker, J.A., Jakobsson, S.P., Waight, T.E., Kent, A.J.R., Grassineau, N.V., Skovgaard, A.C., 2009. Historic magmatism on the Reykjanes Peninsula, Iceland; a snap-shot of melt generation at a ridge segment. Contrib. Mineral Petrol. 157, 359–382.

Pena, L.D., Goldstein, S.L., 2014. Thermohaline circulation crisis and impacts during the mid-Pleistocene transition. Science 345 (80), 318–322.

Percival, J.A., 2007, Geology and metallogeny of the Superior Province, Canada, in Goodfellow, W.D., ed., Mineral Deposits of Canada: A Synthesis of Major Deposit-Types, District Metallogeny, the Evolution of Geological Provinces, and Exploration Methods: Geological Association of Canada, Mineral Deposits Division, Special Publication.

Percival, J.A., Skulski, T., Sanborn-Barrie, M., Stott, G.M., Leclair, A.D., Corkery, M.T., and Boily, M. 2012. Geology and tectonic evolution of the Superior Province, Canada. Chapter 6 In Tectonic Styles in Canada: The LITHOPROBE Perspective. Edited by J.A. Percival, F.A. Cook, and R.M. Clowes. Geological Association of Canada, Special Paper 49, 321–378.

Peterson, T.D., Esperanca, S., LeCheminant, A.N. 1994. Geochemistry and origin of the Proterozoic ultrapotassic rocks of the Churchill Province, Canada. Mineralogy and Petrology. 51, 251-276.

Pflaumann, U., Sarnthein, M., Chapman, M., D'Abreu, L., Funnell, B., Huels, M., Kiefer, T., Maslin, M., Schulz, H., Swallow, J., van Kreveld, S., Vautravers, M., Vogelsang, E., and Weinelt, M. 2003. Glacial North Atlantic: Sea-surface conditions 61 reconstructed by GLAMAP 2000, Paleoceanography, 18.

Pflaumann, U., Duprat, J., Pujol, C, Labeyrie, L.D., 1996. SIMMAX: a modern analog technique to deduce Atlantic Sea surface temperatures from planktonic foraminifera in deep-sea sediments. Paleoceanography, 11(1), 15-35.

Pickart, R.S., Straneo, F., Moore, G. 2003. Is Labrador Sea Water formed in the Irminger basin? Deep Sea Res. Part I, 50(1) 23-52.

Pico, T., Creveling, J.R., and Mitrovica, J.X., 2017. Sea-level records from the U.S. mid-Atlantic constrain Laurentide Ice Sheet extent during Marine Isotope Stage 3: Nature Communications, 8, 15612.

Piotrowski, A.M., Goldstein, S.L., Hemming, S.H., Fairbanks, R.G., 2004. Intensification and variability of ocean thermohaline circulation through the last deglaciation. Earth Planet. Sci. Lett. 225, 205–220.

Piotrowski, A.M., Goldstein, S.L., Hemming S.R., Fairbanks, R.G., 2005. Temporal Relationships of Carbon Cycling and Ocean Circulation at Glacial Boundaries. Science 307, 1933–1938.

Piotrowski, A.M., Goldstein, S.L., Hemming, S.H., Fairbanks, R.G., Zylberberg, D.R., 2008. Oscillating glacial nothern and southern deep water formation from combined neodymium and carbon isotopes. Earth Planet. Sci. Lett. 272, 394–405.

Piotrowski, A.M., Galy, A., Nicholl, J.A.L., Roberts, N., Wilson, D.J., Clegg, J.A., Yu, J., 2012. Reconstructing deglacial North and South Atlantic deep water sourcing using foraminiferal Nd isotopes. Earth Planet. Sci. Lett. 357–358, 289–297.

Piper D. Z.,1974. Rare earth elements in the sedimentary cycle: A summary. Chem. Geol. 14, 285–304.

Poli, M.S., Thunnel, R.C., Rio, D., 2000. Millennial-scale changes in North Atlantic deep water circulation during Marine Isotope Stages 11 and 12: linkage to Antarctic climate. Geology 28, 807-810.

Pöppelmeier, F., Blaser, P., Gutjahr, M., Jaccadr, S.L., Frank, M., Max, L., Lippold, J., 2020. Northern-sourced water dominated the Atlantic Ocean during the Last Glacial Maximum. Geology 48(8), 826–829.

Pöppelmeier, F., Gutjahr, M., Blaser, P., Schulz, H., Süfke, F., & Lippold, J. 2021. Stable Atlantic deep water mass sourcing on glacial-interglacial timescales. Geophysical Research Letters, 48, e2021GL092722.

Potter, E.K., Lambeck, K., 2003. Reconciliation of sea-level observations in the Western North Atlantic during the last glacial cycle. Earth Planet. Sci. Lett. 217, 171–181.

Principato, S.M., Jennings, A.E., Kristjánsdóttir, G.B., Andrews, J.T., 2005. Glacial-Marine or Subglacial Origin of Diamicton Units from the Southwest and North Iceland Shelf: Implications for the Glacial History of Iceland. Journal of Sedimentary Research 75, 968–983.

Quinn, C., Sieber, J., von der Heydt, A.S., Lenton, T.M. 2018. The Mid-Pleistocene Transition induced by delayed feedback and bistability, *Dynamics and Statistics of the Climate System,* 3(1), dzy005.

Rabineau, M., Berné, S., Olivet, J.L., Aslanian, D., Guillocheau, F., Joseph, P., 2006. Paleo sea levels reconsidered from direct observation of paleoshoreline position during Glacial Maxima (for the last 500,000 yr). Earth Planet. Sci. Lett. 252, 119–137.

Rashid, H., Lu, Q.Q., Zeng, M., Wang, Y., Zhang, Z.W. 2021. Sea-Surface Characteristics of the Newfoundland Basin of the Northwest Atlantic Ocean during the Last 145,000 Years: A Study Based on the Sedimentological and Paleontological Proxies. Appl. Sci. 11, 3343.

Raymo, M.E., Ruddiman, W.F., Shackleton, N.J., 1990. Evolution of Atlantic-Pacific $d^{13}C$ gradients over the last 2.5 m.y. Earth Planet. Sci. Lett. 97, 353–368.

Raymo, M.E., 1997. The timing of major climate terminations. Paleoceanography, 12, 577-585.

Raymo, M.E., Oppo, D.W., Flower, B.P. Hodell, D.A., McManus, J., Venz, K.A., Kleiven, K.F., and McIntyre, K. 2004. Stability of North Atlantic water masses in face of pronounced climate variability during the Pleistocene, *Paleoceanography*, 19, PA2008.

Raymo, M. E., Mitrovica, J. X., O'Leary, M. J., DeConto, R. M., & Hearty, P. J., 2011. Departures from eustasy in Pliocene sea-level records. Nature Geoscience, 4, 328–332.

Raymo, M.E., Mitrovica, J.X., 2012. Collapse of polar ice sheets during the stage 11 interglacial. Nature 483, 453–456.

Raymo, M.E., Kozdon, R., Evans, D., Lisiecki, L., Ford, H.L., 2018. The accuracy of mid-Pliocene $\delta^{18}O$-based ice volume and sea-level reconstructions. Earth Sci. Rev., 177, 291-302.

Reed, J.C., Wheeler, J.O., Tucholke, B.E., Card, K.D., Davidson, A., Hoffman, P.F., Okulitch, A.V., Palmer, A.R., Sanford, B.V., Williams, G.K., Williams, H., Dixon, J., Embry, A.F., Holcombe, T.L., Laine, E.P., Mountain, G.S., Popenoe, P., and Wiley, T., 2005, Geologic map of North America. Geological Society of America, Continent-Scale Map 001, scale 1:5,000,000.

Reyes, A., Carlson, A., Beard, B., Hatfield, R.G., Stoner, J.S., Winsor, K., Welke, B., Ullman, D.J., 2014. South Greenland ice-sheet collapse during Marine Isotope Stage 11. Nature 510, 525–528.

Reynolds, B., Frank, M. & O'Nions, R. 1999. Nd-and Pb-isotope time series from Atlantic ferromanganese crusts: implications for changes in provenance and paleocirculation over the last 8 Myr. Earth Planet Sci. Lett. 173, 381-396.

Richardson, A.J., Hollings, P. and Franklin, J.M. 2005. Geochemistry and radiogenic isotope characteristics of the sills of the Nipigon Embayment: Lake Nipigon Region Geoscience Initiative; Ontario Geological Survey, Open File Report 6175, 88p.

Ridgwell, A.J., Watson, A.J., and Raymo, M.E., 1999. Is the spectral signature of the 100 kyr glacial cycle consistent with a Milankovitch origin? Paleoceanography, 14(4), 437–440, 1999

Roberts, N.L., Piotrowski, A.M., 2015. Radiogenic Nd isotope labeling of the northern NE Atlantic during MIS 2. Earth Planet. Sci. Lett. 423, 125–133.

Robinson, S., Ivanovic, R., van de Flierdt, T., Blanchet, C.L., Tachikawa, K., Martin, E.E., Cook, C.P., Williams, T., Gregoire, L., Plancherel, Y., Jeandel, C., Arsouze, T. 2021. Global continental and marine detrital εNd: an updated compilation for use in understanding marine Nd cycling. Chem. Geol. 567, 12011.

Rohling, E.J., Braun, K., Grant, K., Kucera, M., Roberts, A.P., Siddall, M., Trommer, G., 2010. Comparison between Holocene and Marine Isotope Stage-11 sea-level histories. Earth Planet. Sci. Lett. 291, 97–105.

Rohling, E.J., Foster, G.L., Grant, K.M., Marino, G., Roberts, A.P., Tamisiea, M.E., Williams, F., 2014. Sea-level and deep-sea-temperature variability over the past 5.3 million years. Nature 508, 477-482.

Rohling, E.J., Hibbert, F. D., Williams, F.H., Grant, K.M., Marino, G., Foster, G.L., Hennekam, R., de Lange, G.J., Roberts, A.P., Yu, J., Webster, J.M., Yokoyama, Y., 2017. Differences between the last two glacial maxima and implications for ice-sheet, $d^{18}O$, and sea-level reconstructions. Quaternary Science Reviews 178, 1–28.

Rovey II, C.W., Siemens, M., 2021. Age constraints of the Middle Pleistocene till and loess sequence in northeast Missouri, USA, based on pedostratigraphy within a polygenetic paleosol. Catena 203.

Rovey, C.W., McLouth, T., 2015. A near synthesis of pre-Illinoian till stratigraphy in the central United States: Iowa, Nebraska and Missouri. Quat. Sci. Rev. 126, 96–111.

Ruddiman, W.F., 1977. Late Quaternary deposition of ice-rafted sand in the subpolar North Atlantic (lat 40-65 N). Geol. Soc. Am. Bull. 88, 1813-1827.

Rutberg, R.L., Hemming, S.H., Goldstein, S.L., 2000. Reduced North Atlantic Deep Water flux to the glacial Southern Ocean inferred from neodymium isotope ratios. Nature 405, 935–938.

Sarnthein, M., Winn, K., Jung, S.J.A., Duplessy, J.-C., Labeyrie, L., Erlenkeuser, H., Ganssen G. 1994. Changes in east Atlantic deepwater circulation over the last 30,000 years: Eight time slice reconstructions. Paleoceanography 9(2), 209–267.

Saunders, A.D., Kempton, P.D., Fitton, J.G., Larsen, L.M., 1999. Sr, Nd, and Pb isotopes and trace element geochemistry of basalts from the Southeast Greenland margin, Proc. Ocean Drilling Prog., Sci. Results 163, 77–93.

Schaefer, J.M. et al., 2015. The Southern Glacial Maximum 65,000 years ago and its Unfinished Termination. Quat. Sci. Rev. 114, 52–60.

Scharer, U., 1991. Rapid continental crust formation at 1.7 Ga from a reservoir with chondritic isotope signatures, eastern Labrador. Earth Planet. Sci.Lett. 102, 110-133.

Schiøtte, L., Hansen, B.T., Shirey, S.B., Bridgwater, D., 1993. Petrological and whole rock isotopic characteristics of tectonically juxtaposed Archaean gneisses in the Okay area of the Main Province, Labrador: relevance for terrane models. Precambrian Research 63, 293–323.

Seidenkrantz, M-S., Kuijpers, A., Olsen, J., Pearce, C., Lindblom, S., Ploug, J., Przybylo, P., Snowball, I, 2019. Southwest Greenland shelf glaciation during MIS 4 more extensive than during the Last Glacial Maximum. Scientific Reports 9, 15617.

Shackleton, N.J., 1987. Oxygenic isotopes, ice volume and sea level. Quat. Sci. Rev. 6(3–4), 183–190.

Shakun, J.D., Raymo, M. E. & Lea, D.W., 2016. An early Pleistocene Mg/Ca-$\delta^{18}O$ record from the Gulf of Mexico: Evaluating ice sheet size and pacing in the 41-kyr world, Paleoceanography, 31, 1011–1027.

Shaw, D.M., Cramer, J.J., Higgins, M.D., Truscott, M.G., 1986. Composition of the Canadian Precambrian shield and the continental crust of the Earth. Geol. Soc. Lond. Spec. Publ.24, 275–282.

Siddall, M., Khatiwala, S., van de Flierdt, T., Jones, K., Goldstein, S.L., Hemming, S., Anderson, R.F., 2008. Towards explaining the Nd paradox using reversible scavenging in an ocean general circulation model. Earth Planet Sci. Lett. 274, 448-461.

Sigman, D.M., Hain, M.P., Haug, G.H., 2010. The polar ocean and glacial cycles in atmospheric CO_2 concentration. Nature, 466, 47–55.

Sinha, A.K., Hogan, J.P., Parks, J., 1996. Lead Isotope Mapping of Crustal Reservoirs Within the Grenville Superterrane: I. Central and Southern Appalachians, in Earth Processes: Reading the Isotopic Code, edited by A. H. Basu, and R. Stanley, pp. 293– 305, AGU, Washington, D. C.

Skinner, L.C., Shackleton, N. J., 2005. An Atlantic lead over Pacific deep-water change across Termination I: implications for the application of the marine isotope stage stratigraphy. Quat. Sci. Rev. 24, 571–580.

Smith, P.E., 1988. U-Th-Pb Geochronology of Archean rocks of the Eastern Superior Province and application of initial Pb and Hf isotope ratios to greenstone belt evolution; unpublished PhD thesis, University of Toronto, Toronto, Ontario, 125p.

Steiger, R.H. and Jager, E. 1977. Subcommision on geochronology: Convention on the use of decay constants in geo and cosmochronology. Earth Planet. Sci. Lett. 36, 359-362

Stevenson, R., Henry, P., Gariepy, C., 1999. Assimilation-fractional crystallization origin of Archean Sanukitoid Suites: Western Superior Province, Canada. Precambrian Research 96, 83–99.

Stichel, T., Frank, M., Rickli, J., and Haley, B.A., 2012. The hafnium and neodymium isotope composition of seawater in the Atlantic sector of the Southern Ocean. Earth Planet. Sci. Lett , 317–318, 282–294.

Stocker, T. et al. Climate Change 2013: The Physical Science basis. Contribution of Working Group I to the Fifth Assessment Report of the Intergovernmental Panel on Climate Change (Cambridge University Press, Cambridge, New York, 2013)

Stokes, C.R., Tarasov, L., Dyke, A.S., 2012. Dynamics of the North American Ice Sheet complex during its inception and build-up to the Last Glacial Maximum. Quat. Sci. Rev. 50, 86–104.

Strelow, F.W.E., 1978. Distribution Coefficients and Anion-Exchange Behavior of Some Elements in Hydrobromic Nitric Acid Mixtures. Analytical Chemistry 50 (9), 1359-1361.

Struve, T., Roberts, N.L., Frank, M., Piotrowski, A.M., Spielhagen, R.F., Gutjahr, M., Teschner, C., Bauch, H.A., 2019. Ice-sheet driven weathering input and water mass mixing in the Nordic Seas during the last 25,000 years Earth Planet Sci. Lett., 514, 108-118.

Süfke, F., Gutjahr, M., Gilli, A., Anselmetti, F.S., Glur, L., Eisenhauer, A., 2019. Early stage weathering systematics of Pb and Nd isotopes derived from a high-Alpine Holocene lake sediment record. Chem. Geol. 507, 42–53.

Süfke, F., Gutjahr, M., Keigwin, L.D., Reilly, B., Giosan, L., Lippold, J, 2022. Arctic drainage of Laurentide Ice Sheet meltwater throughout the past 14,700 years.Commun. Earth Environ. 3 (98), 1-11.

Svendsen, J.I., Alexanderson, H., Astakhov, V.I., Demidov, I., Dowdeswell, J.A., Funder, S., Gataullin, V., Henriksen, M., Hjort, C., Houmark-Nielsen, M., Hubberten, H.W., 2004a. Late Quaternary ice sheet history of northern Eurasia. Quat. Sci. Rev. 23, 1229–1271.

Svendsen, J.I., Gataullin, V., Mangerud, J. and Polyak, L., 2004b. The glacial history of the Barents and Kara Sea region; Quaternary Glaciations – Extent and Chronology 1 369–378.

Tachikawa, K., Jeandel, C., Roy-Barman, M., 1999. A new approach to the Nd residence time in the ocean: the role of atmospheric inputs. Earth Planet. Sci. Lett. 170, 433-446.

Tachikawa, K., Arsouze, T., Bayon, G., Bory, A., Colin, C., Dutay, J.-C., Frank, N., Giraud, X., Gourlan, A.T., Jeandel, C., Lacan, F., Meynadier, L., Montagna, P., Piotrowski, A.M., Plancherel, Y., Pucéat, E., Roy-Barman, M., Waelbroeck, C.,

2017. The large-scale evolution of neodymium isotopic composition in the global modern and Holocene ocean revealed from seawater and archive data. Chem. Geol. 457, 131–148.
Tanaka, T., et al., 2000. JNdi-1: A neodymium isotopic reference in consistency with La Jolla neodymium: Chemical Geology 168, 279–281.
Taylor, P.N., Jones, N.W. Moorbath, S., 1984. Iso- topic assessment of relative contributions from crust and mantle sources to the magma genesis of Precambrian granitoid rocks. Philos. Trans. R. Soc. London, Ser. A 310, 605–625.
Taylor, P.N., Moorbath, S., Goodwin, R., Petrykowski, A.C. 1980. Crustal contamination as an indicator of the extent of early Archaean crust: Pb isotopic evidence from the late Archaean gneisses of West Greenland. Geochim. Cosmochim. Acta. 44, 1437–1453.
Taylor, P.N., Kalsbeek F., Bridgwater, D., 1992. Discrepancies between neodymium, lead and strontium model ages from the Precambrian of southern East Greenland: Evidence for a Proterozoic granulite-facies event affecting archaean gneisses. Chem. Geol. 94, 281–291.
Taylor, P.N., Upton, B.G.J., 1993. Contrasting Pb isotopic compositions in two intrusive complexes of the Gardar Magmatic Province of South Greenland. Chemical Geology. 104, 261–268.
Taylor, R.N., Ishizuka, O., Michalik, A., Milton, J.A., Croudace, I.W. 2015. Evaluating the precision of Pb isotope measurement by mass spectrometry. Journal of Analytical. Atomic Spectrometry 30, 198–213.
Taylor, S.R., and McLennan, S.M., 1985. The continental crust: Its composition and evolution. Oxford: Blackwell, 312 pp.
Thornalley, D. J. R., Bauch, H. A., Gebbie, G., Guo, W., Ziegler, M., Bernasconi, S. M., Barker, S., Skinner, L.C., Yu, J., 2015. A warm and poorly ventilated deep Arctic Mediterranean during the last glacial period. Science, 349(6249), 706–710.
Thorpe, R.I., 1982. Lead Isotope Evidence Regarding Archean and Proterozoic Metallogeny in Canada. Revista Brasileira de Geosciencias. 12(1–2), 510–521.
Thorpe, R.I., 2008. Release of lead isotope data in 4 databases: Canadian, Western Superior, foreign, and whole rock and feldspar. GSC Open file 5664.
Thrane, K., 2004. Palaeoproterozoic age of a basement gneiss complex in the Charcot Land tectonic window, East Greenland Caledonides. In: Higgins, A.K., Kalsbeek, F. (eds.), East Greenland Caledonides: stratigraphy, structure and geochronology. Geological Survey of Denmark and Greenland Bulletin 6.
Thurston, P.C., Williams, H.R., Sutcliffe, R.H., Stott, G.M. (eds.), 1991. Geology of Ontario. Ontario Geological Survey Special, Vol. 4.
Toucanne, S., Zaragosi, S., Bourillet, J.F., Gibbard, P.L., Eynaud, F., Giraudeau, J., Turon, J.L., Cremer, M., Cortijo, E., Martinez, P., Rossignol, L., 2009. A 1.2 Ma record of glaciation and fluvial discharge from the West European Atlantic margin. Quat. Sci. Rev. 28(25-26), 2974-2981.
Tzedakis, P.C., Raynaud, D., McManus, J.F., Berger, A., Brovkin, V., Kiefer. 2009. Interglacial diversity, Nature Geoscience, 2, 751-755.
Tzedakis, P.C., Crucifix, M., Mitsui, T. & Wolff, E. W., 2017. A simple rule to determine which insolation cycles lead to interglacials. Nature 542, 427–432.
van de Flierdt, T., Griffiths, A.M., Lambelet, M., Little, S.H., Stichel, T., and Wilson, D.J., 2016. Neodymium in the oceans: A global database, a regional comparison and implications for palaeoceanographic research: Philosophical Transactions, ser. A 374, 2015029,
Van Nieuwenhove, N., Hillaire-Marcel, C., Bauch, H. A., de Vernal, A., 2016. Sea surface density gradients in the Nordic Seas during the Holocene as revealed by paired microfossil and isotope proxies, Paleoceanography 31, 380–398.
Vance, D., Burton, K., 1999. Neodymium isotopes in planktonic foraminifera: a record of the response of continental weathering and ocean circulation rates to climate change. Earth Planet. Sci. Lett. 173, 365-379.

Vance, D., and Thirlwall, M.F., 2002. An assessment of mass discrimination in MC-ICPMS using Nd isotopes, Chem. Geol., 185, 227–240.
Vance, D., Teagle, D.A.H., Foster, G.L., 2009. Variable Quaternary chemical weathering fluxes and imbalances in marine geochemical budgets. Nature 458, 493–496.
Vervoort, J.D., White, W.M., Thorpe, R.I., Franklin, J.M. 1993. Postmagmatic thermal activity in the Abitibi Greenstone Belt, Noranda and Matagami districts: evidence from whole-rock Pb isotope data. Econ. Geol. 88, 1598–1614.
Vincent, J., and Prest, V.K., 1987. The early Wisconinan history of the Laurentide Ice Sheet: Geographis physique et Quaternaire, 41(2), 199–213.
Von Blanckenburg, F. 1999. Tracing past ocean circulation? Science 286, 1862-1863.
Wainer, K.A.I., Rowe, M.P., Thomas, A.L., Mason, A.J., Williams, B., Tamisiea, M.E., Williams, F.H., Düsterhus, A., Henderson, G.M., 2017. Speleothem evidence for MIS 5c and 5a sea level above modern level at Bermuda. Earth Planet. Sci. Lett. 457, 325–334.
Wedepohl, K.H., Heinrichs, H., Bridgwater, D., 1991. Chemical characteristics and genesis of the quartz-feldspathic rocks in the Archean crust of Greenland. Contrib. Mineral. Petrol.107, 163–179.
White, L.E., Bailey, I., Foster, G.L., Georgina, A., Kelley, S.P., Andrews, J.T., Hogan, K., Dowdeswell, J.A., Storey, C.D., 2016. Tracking the provenance of Greenland-sourced, Holocene aged individual sand-sized ice-rafted debris using the Pb-isotope composition of feldspars and $^{40}Ar/^{39}Ar$ ages of hornblendes. Earth. Planet. Sci. Lett. 433, 192-203.
Williams, M.L., Jercinovic, M.J., Terry, M.P. 1999. Age mapping and dating of monazite on the electron microprobe: deconvoluting multistage tectonic histories. Geology, 27, 1023-1026.
Wilson, D.J., Crocket K.C., van de Flierdt T., Robinson L.F., Adkins J. F., 2014. Dynamic intermediate ocean circulation in the North Atlantic during Heinrich Stadial 1: a radiocarbon and neodymium isotope perspective. Paleoceanography 29, 1072–1093.
Wilson, D. J., Bertram, R. A., Needham, E. F., van de Flierdt, T., Welsh, K. J., McKay, R. M., Mazumder, A., Riesselman, C. R., Jimenez-Espejo, F. J., and Escutia, C. 2018. Ice loss from the East Antarctic Ice Sheet during late Pleistocene interglacials, Nature, 561, 383–386.
Wright J., Seymour R. S., and Shaw H. F. 1984. REE and Nd isotopes in conodont apatite. Variations with geological age and depositional environment. In Conodont Biofacies and Provincialism (ed. D. L. Clark), Geol. Soc. Amer. Spec. Pap., 196, 325–340.
Wu, T., Polat, A., Frei, R., Fryer, B.J., Yang, K.-G., Kusty, T., 2016. Geochemistry, Nd, Pb and Sr isotope systematics, and U-Pb zircon ages of the Neoarchean Bad Vermillion Lake greenstone belt and spatially associated granitic rocks, western Superior Province, Canada. Precambrian Research 282, 21–51.
Yehudai, M., Kim, J., Pena, L.D., Jaume-Seguí, M., Knudson, K.P., Bolge, L.L., Malinverno, A., Bickert, T., & Goldstein, S.L., 2021. Evidence for a Northern Hemispheric trigger of the 100,000-y glacial cyclicity. Proceedings of the National Academy of Sciences, 118.
Yu, J., Elderfield, H., Piotrowski, A.M., 2008. Seawater carbonate ion-$\delta^{13}C$ systematics and application to glacial-interglacial North Atlantic ocean circulation. Earth Planet. Sci. Lett. 271, 209–220.
Zachos, J.C. et al., 2008. An early Cenozoic perspective on greenhouse warming and carbon-cycle dynamics. Nature, 451(7176), 279-283.
Zartman, R.E. 1974. Lead isotopic provinces in the Cordillera of the western United States and their geologic significance. Econ. Geol., 69, 792-805.
Zartman, R.E., Wasserburg, G.J. 1969. The isotopic composition of lead in potassium feldspars from some 1.0-b.y. old North American igneous rocks. Geochim. Cosmochim. Acta. 33, 901-942.

Zhao, N., Oppo, D.W., Huang, K.-F., Howe, J.N.W., Blusztajn, J., and Keigwin, L.D., 2019. Glacial- interglacial Nd isotope variability of North Atlantic Deep Water modulated by North American ice sheet: Nature Communications 10, 5773.

Zheng, X.-Y., Plancherel, Y., Saito, M.A., Scott, P.M., Henderson, G.M., 2016. Rare Earth elements (REEs) in the tropical South Atlantic and quantitative deconvolution of their non-conservative behavior. Geochim. Cosmochim. Acta177, 217–237.

Zhou, Y., McManus, J.F., Jacobel, A.W., Costa, K.M., Wang, S., Caraveo, B.A., 2021. Enhanced iceberg discharge in the western North Atlantic during all Heinrich events of the last glaciation. Earth Planet. Sci. Lett. 564, 116910.

Appendices

Appendix A: Chapter 3 & 4 – Additional Pb isotope datasets

A1: Compiled whole rock regional source Pb isotope data for the circum-Atlantic Ocean – see spreadsheet 'A1'.

A2: Pb isotope and rare earth element data for Sites U1302/3 – see spreadsheet 'A2'.

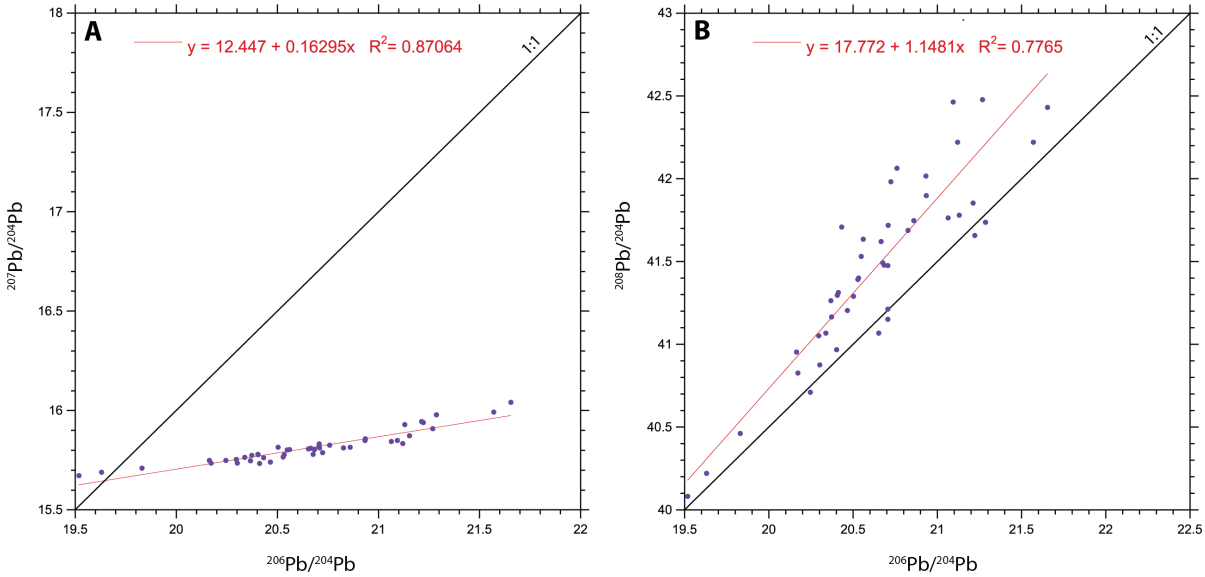

Figure A3: Cross plot of MIS 5d-a authigenic Fe-Mn oxyhydroxide-derived Pb isotopes from marine sediment at Site U1302/3 with regression analysis. **(A)** $^{206}Pb/^{204}Pb$ vs. $^{207}Pb/^{204}Pb$, **(B)** $^{206}Pb/^{204}Pb$ vs. $^{208}Pb/^{204}Pb$.

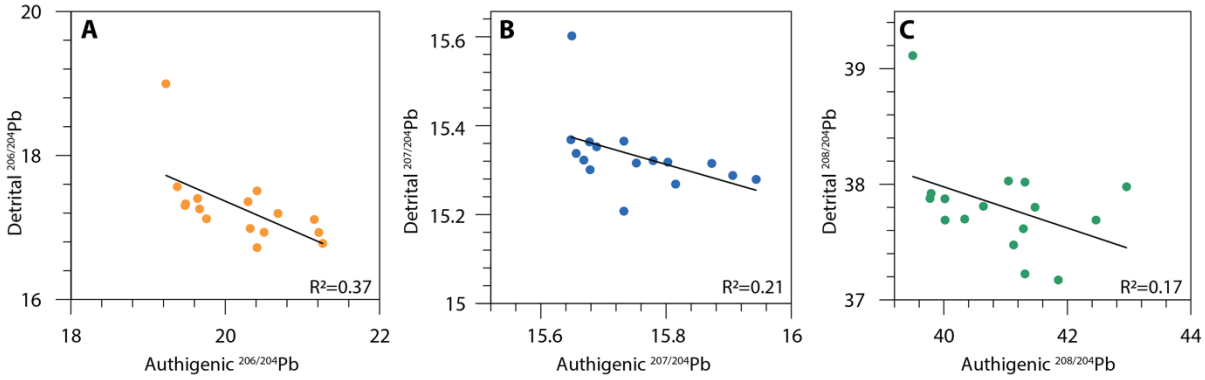

Figure A4: Cross plot of paired authigenic and detrital Fe-Mn oxyhydroxide-derived Pb isotopes from marine sediment at Site U1302/3 with regression analysis. **(A)** $^{206}Pb/^{204}Pb$ isotope ratios, **(B)** $^{207}Pb/^{204}Pb$ isotope ratios, **(C)** $^{208}Pb/^{204}Pb$ isotope ratios

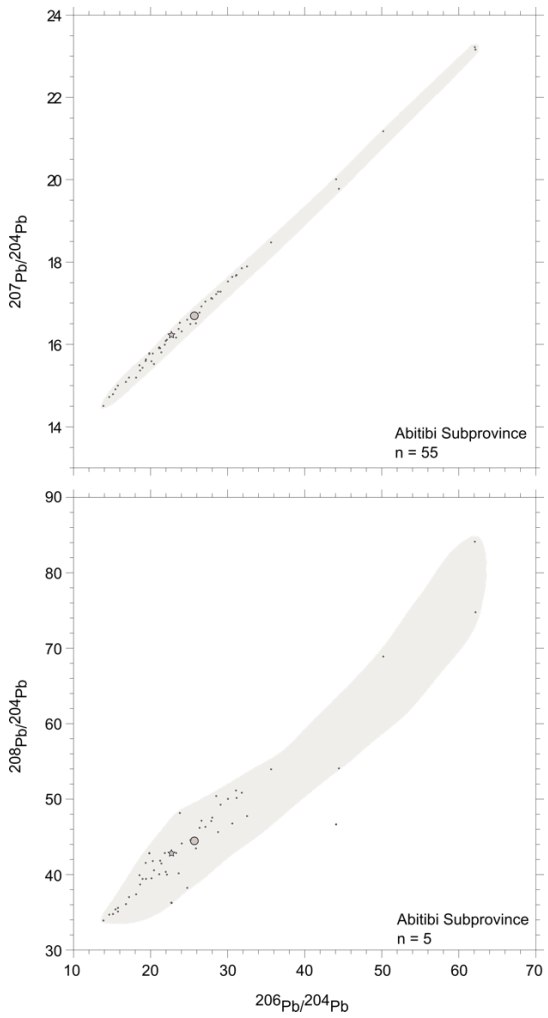

Figure A5: Whole-rock Pb isotope composition of the Abitibi subprovince. Top panel = $^{206}Pb/^{204}Pb$ vs. $^{207}Pb/^{204}Pb$, bottom panel = $^{206}Pb/^{204}Pb$ vs. $^{208}Pb/^{204}Pb$. Mean = circle and median = star. Envelope highlights range of Pb compositions that characterises the subprovince.

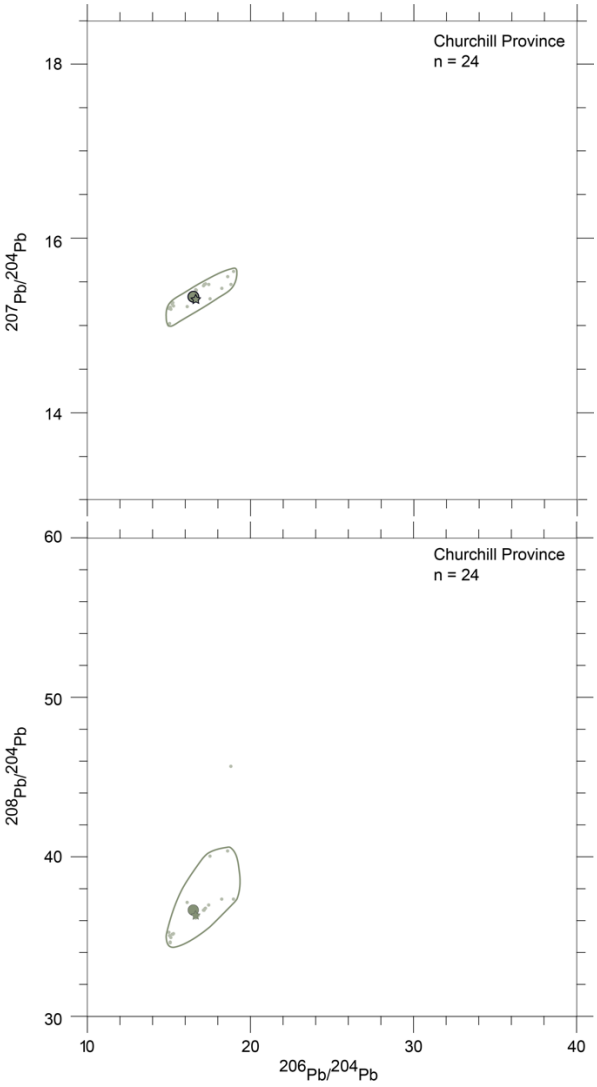

Figure A6: Whole-rock Pb isotope composition of the Churchill Province. Top panel = $^{206}Pb/^{204}Pb$ vs. $^{207}Pb/^{204}Pb$, bottom panel = $^{206}Pb/^{204}Pb$ vs. $^{208}Pb/^{204}Pb$. Mean = circle and median = star. Envelope highlights range of Pb compositions that characterises the province.

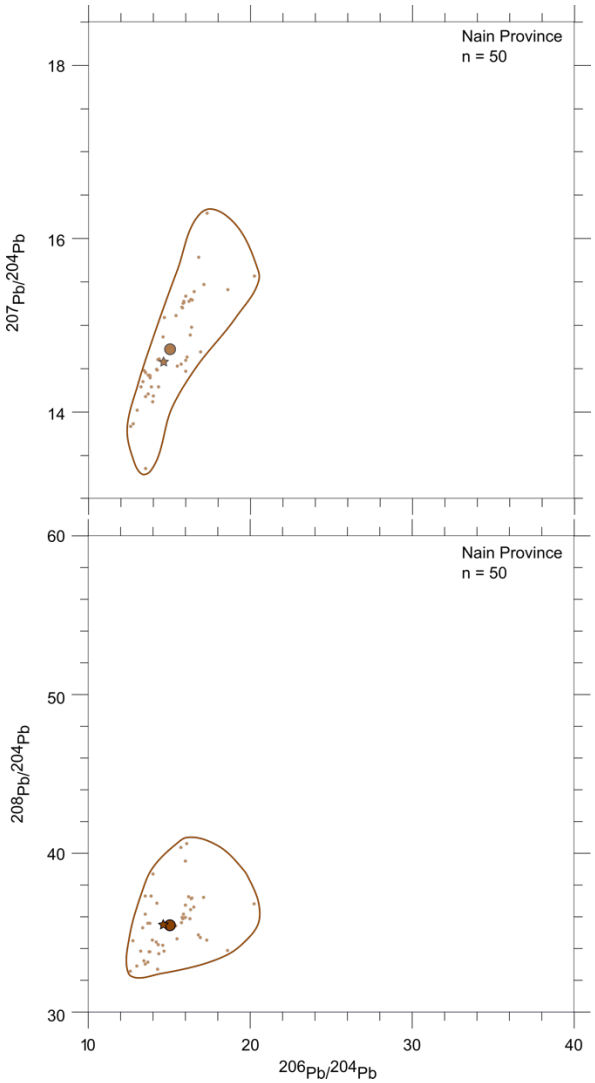

Figure A7: Whole-rock Pb isotope composition of the Nain Province. Top panel = $^{206}Pb/^{204}Pb$ vs. $^{207}Pb/^{204}Pb$, bottom panel = $^{206}Pb/^{204}Pb$ vs. $^{208}Pb/^{204}Pb$. Mean = circle and median = star. Envelope highlights range of Pb compositions that characterises the province.

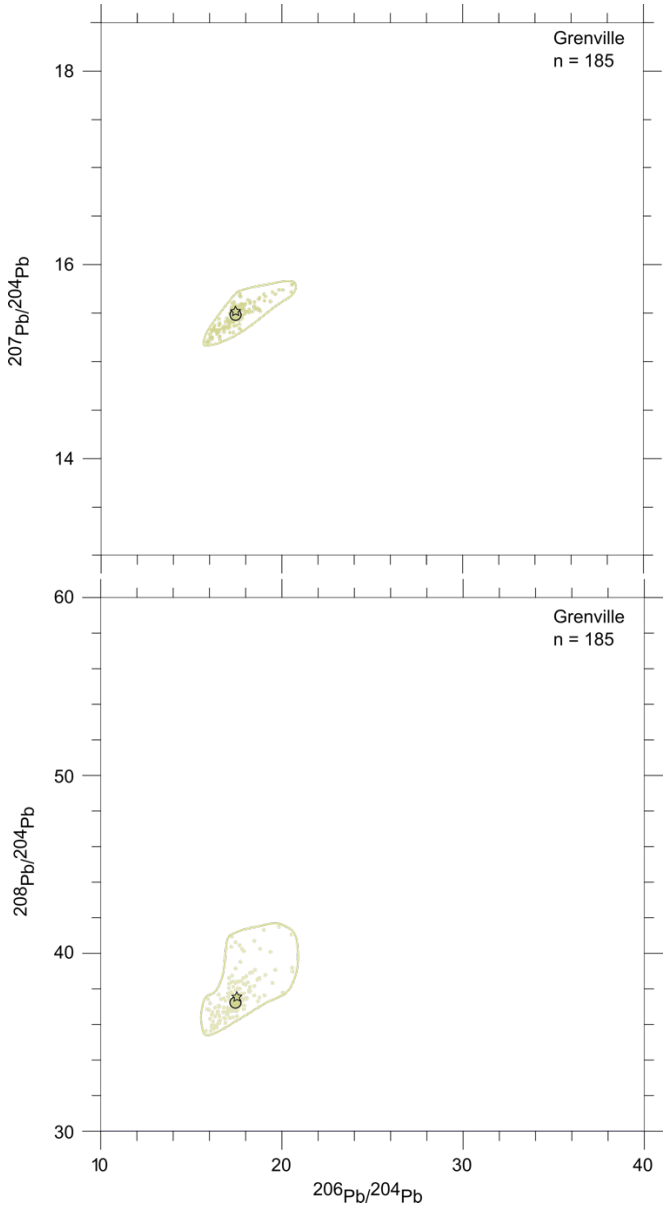

Figure A8: Whole-rock Pb isotope composition of the Grenville Province. Top panel = $^{206}Pb/^{204}Pb$ vs. $^{207}Pb/^{204}Pb$, bottom panel = $^{206}Pb/^{204}Pb$ vs. $^{208}Pb/^{204}Pb$. Mean = circle and median = star. Envelope highlights range of Pb compositions that characterises the province.

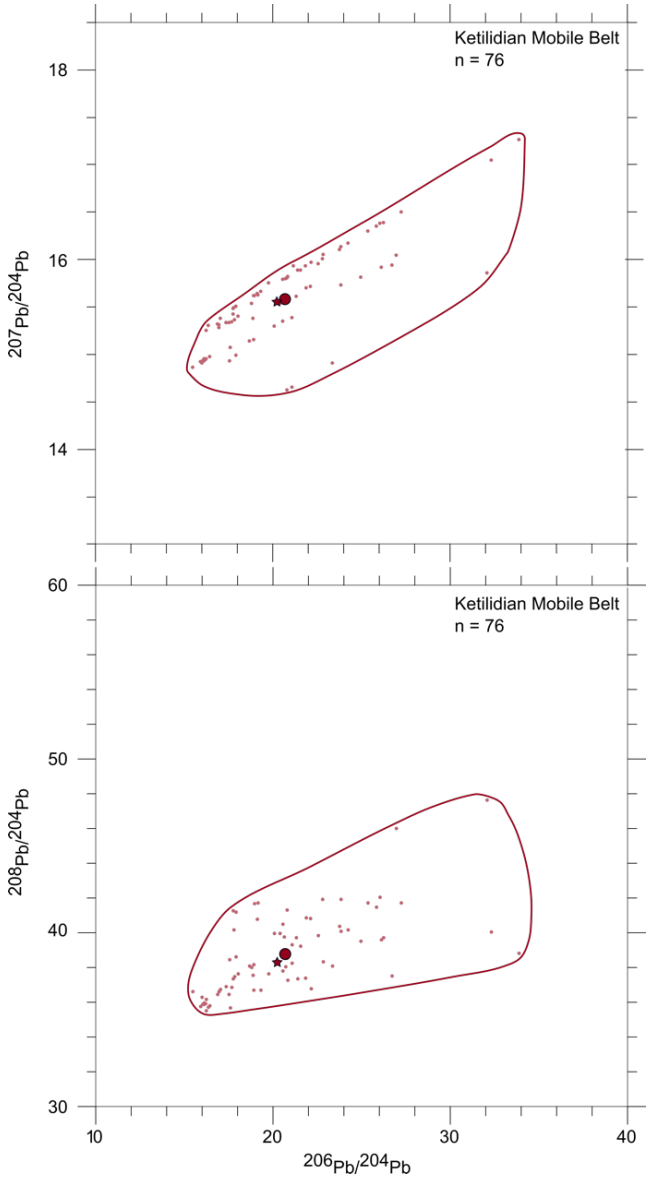

Figure A9: Whole-rock Pb isotope composition of the Ketilidian Mobile Belt. Top panel = $^{206}Pb/^{204}Pb$ vs. $^{207}Pb/^{204}Pb$, bottom panel = $^{206}Pb/^{204}Pb$ vs. $^{208}Pb/^{204}Pb$. Mean = circle and median = star. Envelope highlights range of Pb compositions that characterises the province.

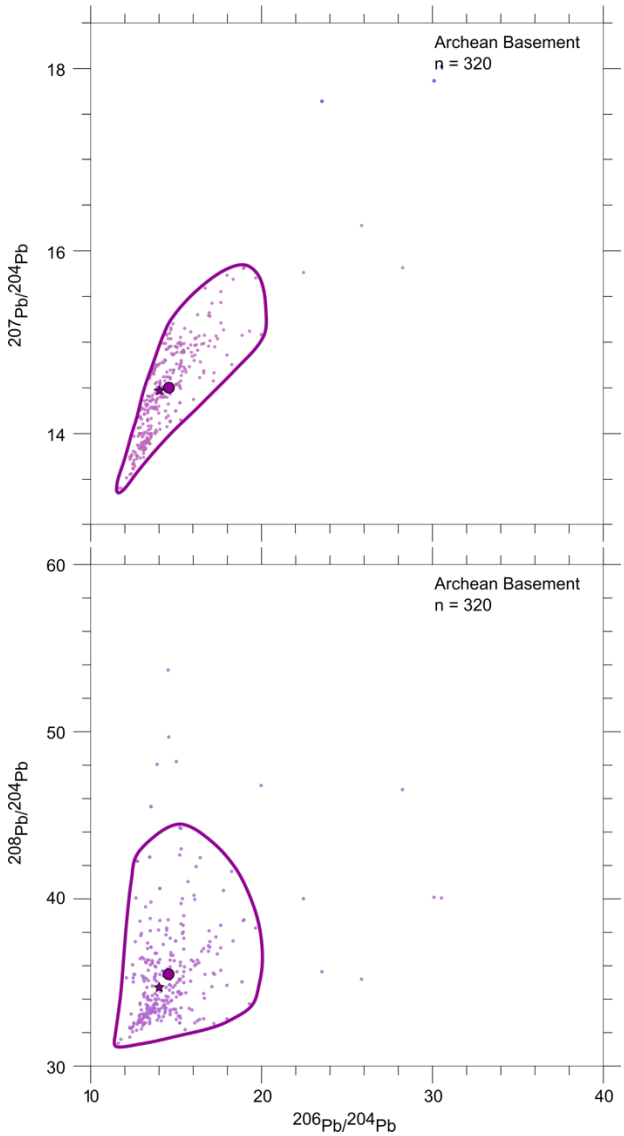

Figure A10: Whole-rock Pb isotope composition of the Archean Basement. Top panel = $^{206}Pb/^{204}Pb$ vs. $^{207}Pb/^{204}Pb$, bottom panel = $^{206}Pb/^{204}Pb$ vs. $^{208}Pb/^{204}Pb$. Mean = circle and median = star. Envelope highlights range of Pb compositions that characterises the basement.

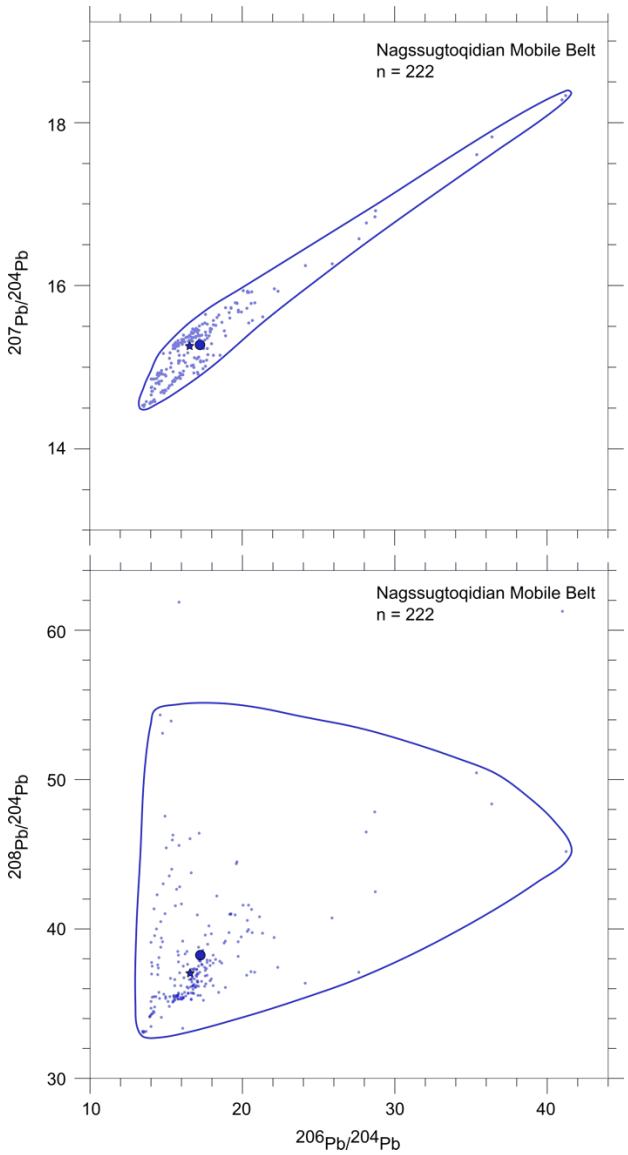

Figure A11: Whole-rock Pb isotope composition of the Nagssugtoqidian Mobile Belt. Top panel = $^{206}Pb/^{204}Pb$ vs. $^{207}Pb/^{204}Pb$, bottom panel = $^{206}Pb/^{204}Pb$ vs. $^{208}Pb/^{204}Pb$. Mean = circle and median = star. Envelope highlights range of Pb compositions that characterises the province.

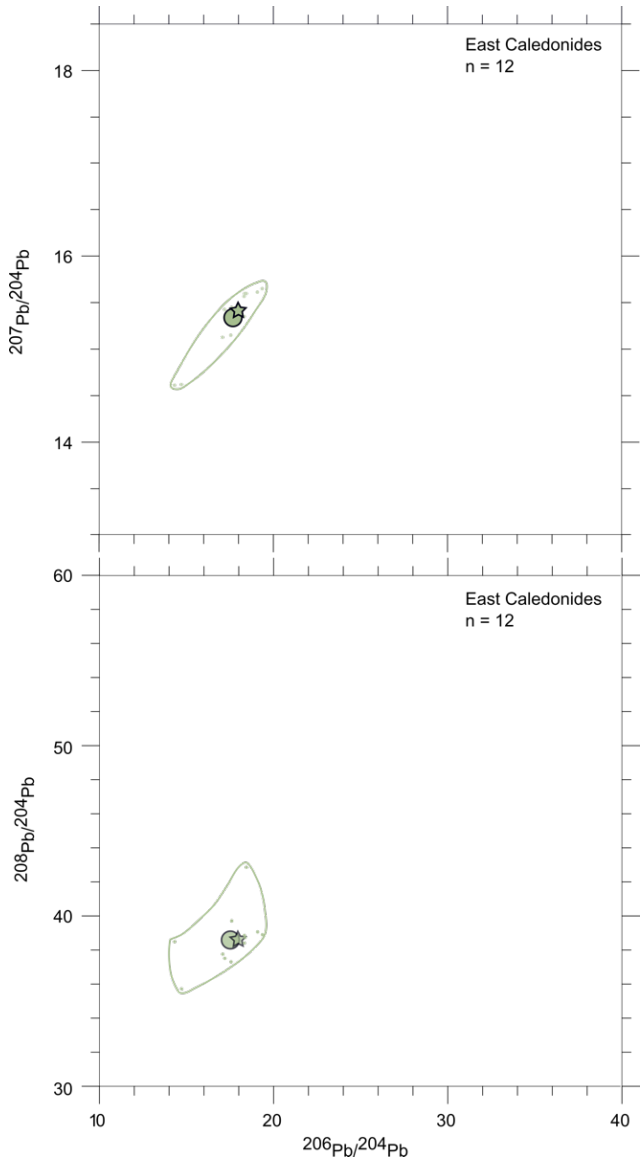

Figure A12: Whole-rock Pb isotope composition of the East Caledonides. Top panel = $^{206}Pb/^{204}Pb$ vs. $^{207}Pb/^{204}Pb$, bottom panel = $^{206}Pb/^{204}Pb$ vs. $^{208}Pb/^{204}Pb$. Mean = circle and median = star. Envelope highlights range of Pb compositions that characterises the province.

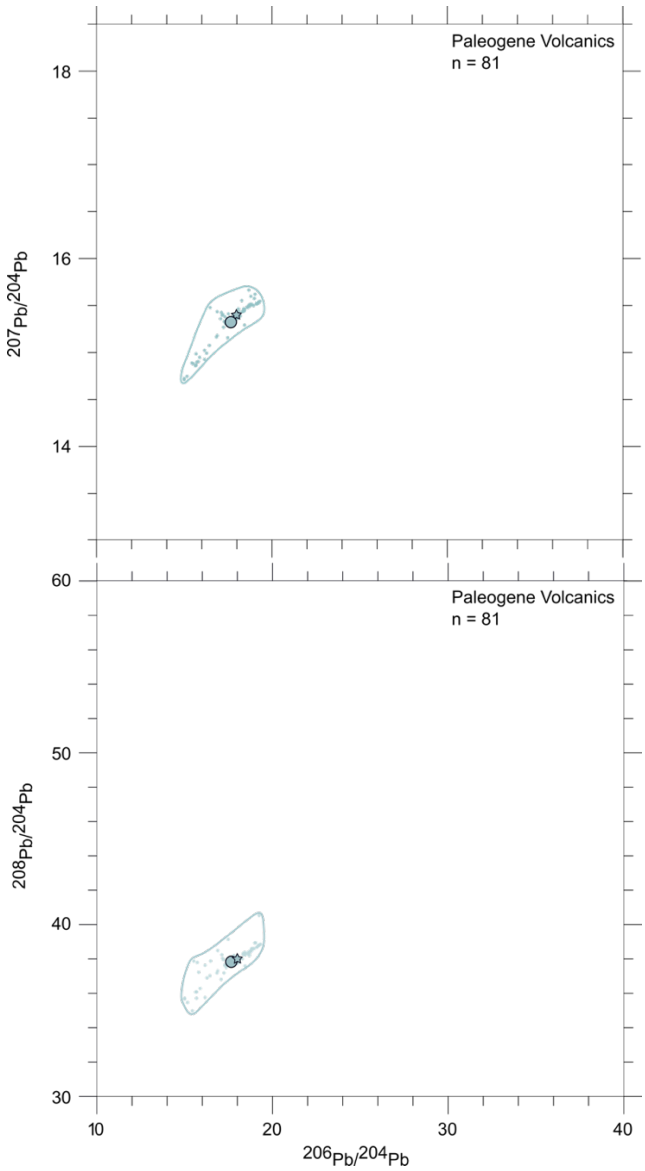

Figure A13: Whole-rock Pb isotope composition of the Paleogene Volcanics. Top panel = $^{206}Pb/^{204}Pb$ vs. $^{207}Pb/^{204}Pb$, bottom panel = $^{206}Pb/^{204}Pb$ vs. $^{208}Pb/^{204}Pb$. Mean = circle and median = star. Envelope highlights range of Pb compositions that characterises the province.

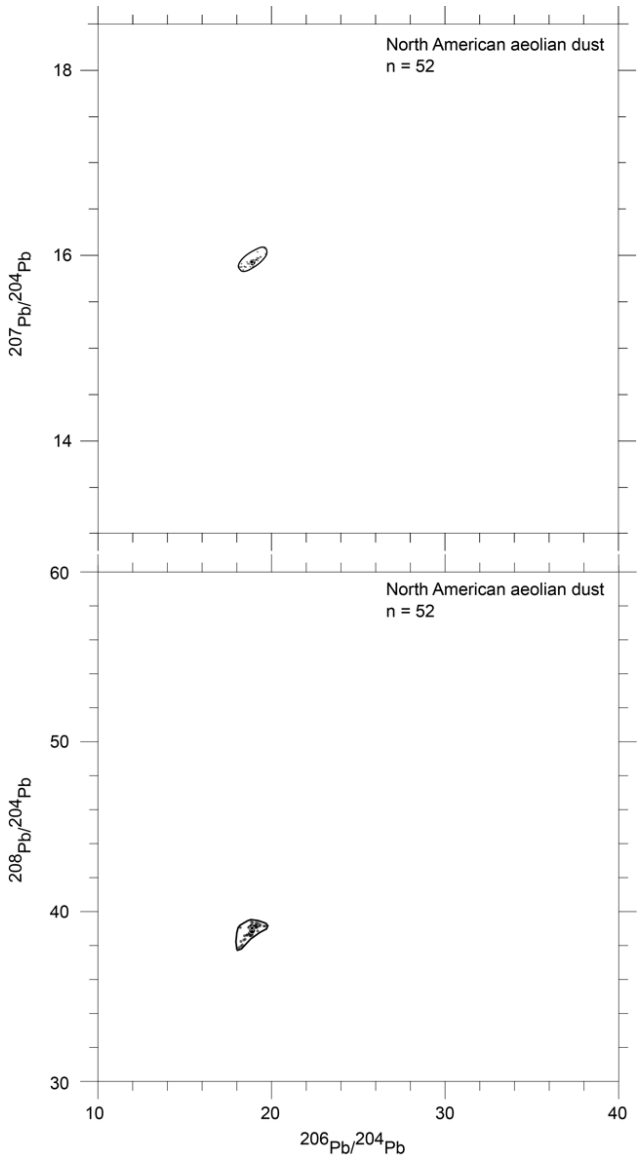

Figure A14: Pb isotope composition of North American aeolian dust. Top panel = $^{206}Pb/^{204}Pb$ vs. $^{207}Pb/^{204}Pb$, bottom panel = $^{206}Pb/^{204}Pb$ vs. $^{208}Pb/^{204}Pb$. Mean = circle and median = star. Envelope highlights range of Pb compositions that characterises aeolian dust.

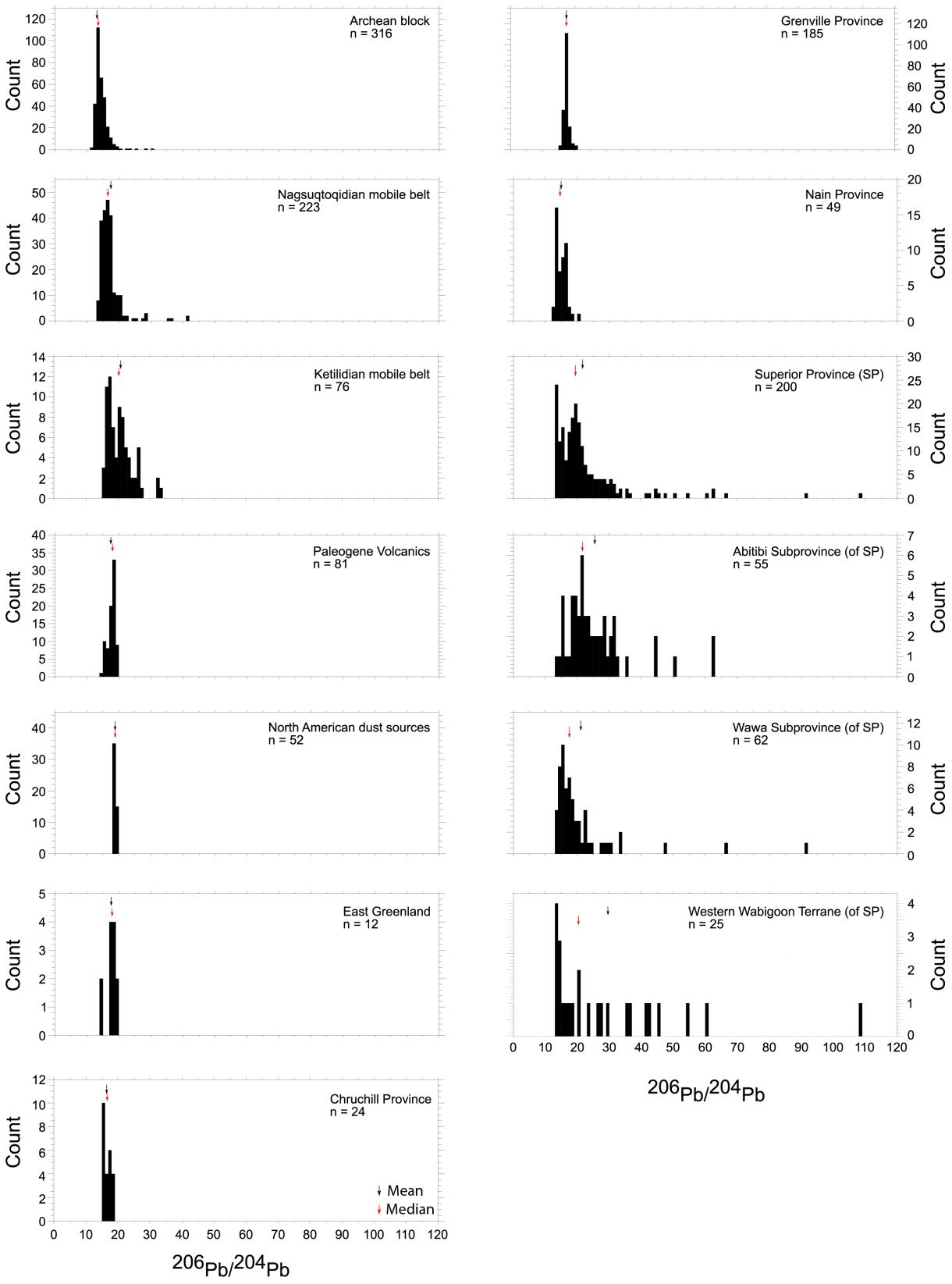

Figure A15: Histograms of raw regional source whole-rock $^{206}Pb/^{204}Pb$ data for each regional source end-member. Mean = red arrow, median = black arrow.

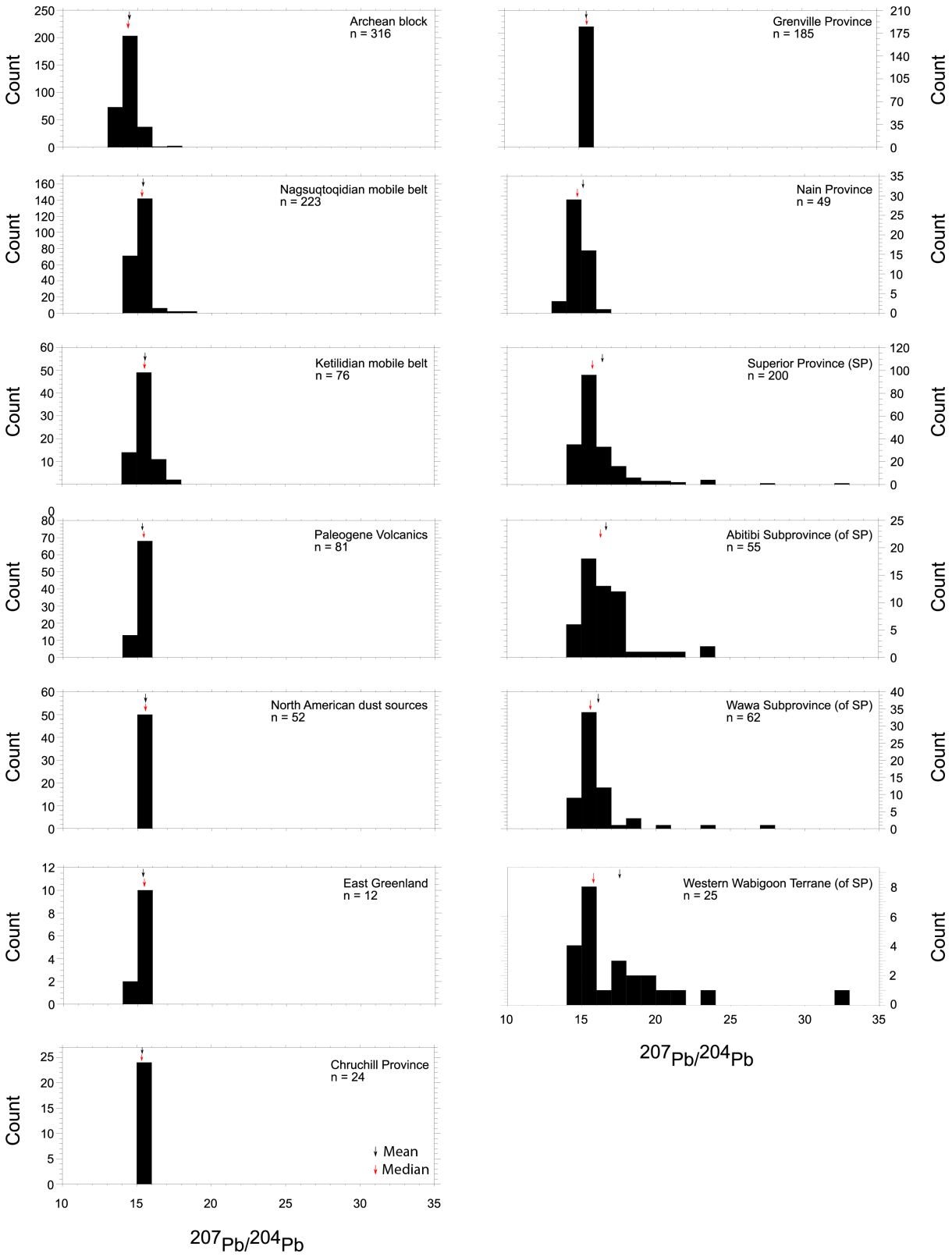

Figure A16: Histograms of raw regional source whole-rock $^{207}Pb/^{204}Pb$ data for each regional source end-member. Mean = red arrow, median = black arrow.

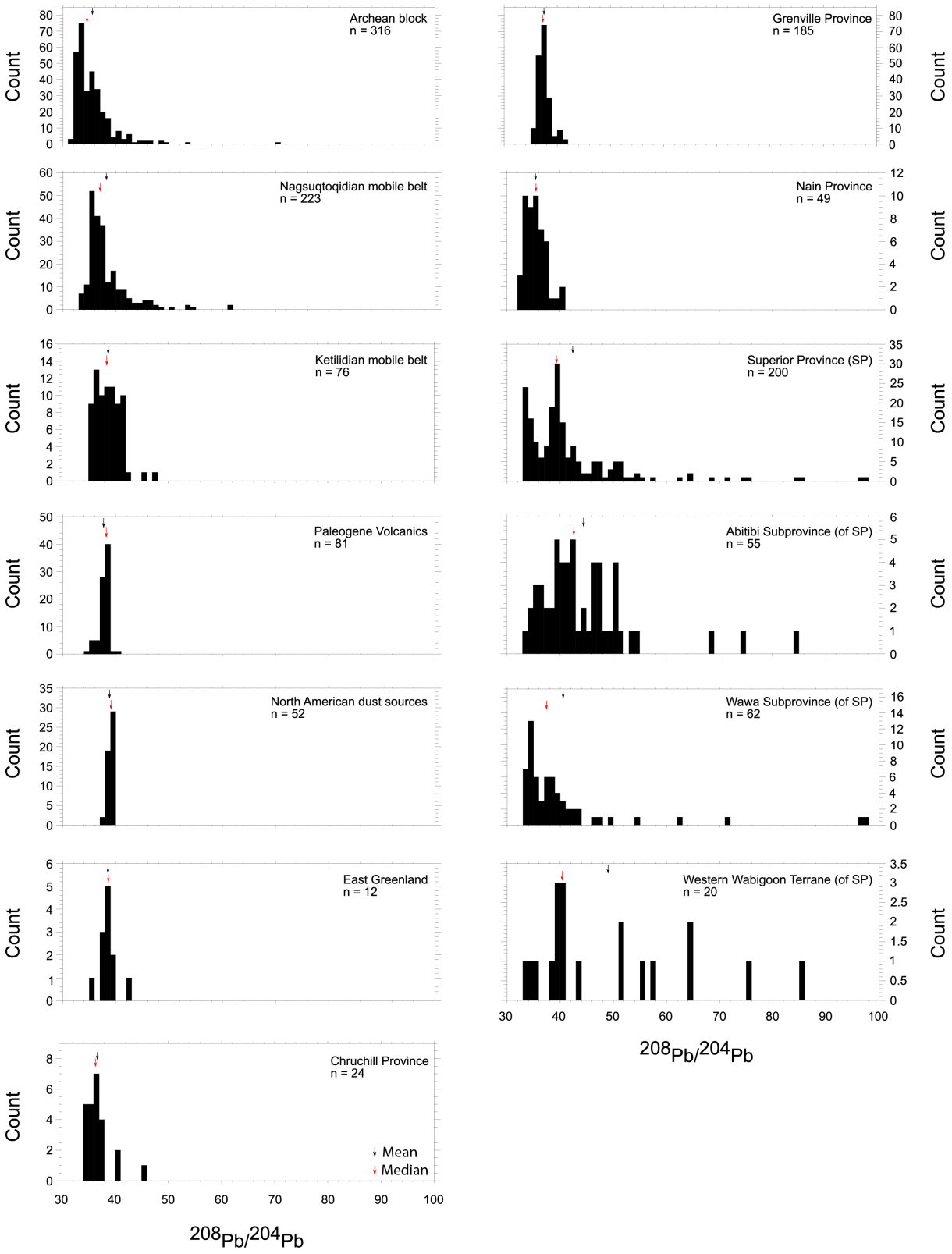

Figure A17: Histograms of raw regional source whole-rock $^{208}Pb/^{204}Pb$ data for each regional source end-members. Mean = red arrow, median = black arrow.

Appendix B: Chapter 5 – ε_{Nd} dataset and LNADW ε_{Nd} composition matrix

B1: IODP Site U1313 ε_{Nd} data – see spreadsheet tab 'B1'.

B2: Lower North Atlantic Deep Water ε_{Nd} composition matrix – see spreadsheet tab 'B2'.